Molecular Insights into New Particle Formation across urban and polar environments

by
James Brean

A thesis submitted to the University of Birmingham for the degree of
DOCTOR OF PHILOSOPHY

School of Geography, Earth & Environmental Sciences
College of Life & Environmental Sciences
University of Birmingham

March 2020

ABSTRACT

New particle formation (NPF) is a process involving formation of thermodynamically stable molecular clusters and their subsequent growth to larger sizes. NPF modulates the earth's radiative budget and poses potentially significant health effects, however, the mechanisms driving NPF globally are still uncertain due to limited molecular scale measurements. Urban measurements in both Beijing and Barcelona show highly oxygenated multifunctional organic molecules in high mixing ratios, arising primarily from anthropogenic VOC precursors. Efficient autoxidation due to high temperatures is offset by rapid peroxy radical termination due to high NO_x mixing ratios. Nucleation is seen to proceed by the nucleation of sulphuric acid, alkylamines, and HOMs in conjunction in Barcelona. An investigation of these mechanisms in the remote polar environment of the Antarctic Peninsula shows nucleation driven by sulphuric acid and amines, with elevations to both the sulphuric acid precursors and amines arising from the melt of sea ice. Particle formation rates are around two orders of magnitude more rapid in the urban environment than in the polar, and particle growth rates are around a single order of magnitude greater. This thesis demonstrates underappreciated roles of both anthropogenic VOC emissions in urban NPF and amine sources in polar regions in facilitating efficient NPF.

ACKNOWLEDGEMENTS

I am extremely grateful to my supervisors, Professor Roy. M. Harrison, and Dr. Zongbo Shi for providing me with the opportunity to pursue this Ph.D., as well as their support and guidance throughout. I would also like to thank Dr. David Beddows for all his guidance and instrumental role in organising and running all the fieldwork throughout the last three and a half years. This project was funded by the National Centre for Atmospheric Science, for which I am most grateful. My gratitude also goes out to Mary Harding, for all the logistical support, and work preparing manuscripts for the papers presented in this thesis, and to Dr. Nicholas Davidson for helping me prepare and send off all instruments for fieldwork (even before it was his job to do so). The advice of the people at Aerodyne Research Inc., and TSI Instruments Ltd. was vital for carrying out high quality measurements throughout this research.

The work of chapter two was assisted by the measurements made by Dr. W. Joe F. Acton and organised by Professor C. Nicholas Hewitt, as well as the gas phase measurements made by Freya A. Squires and Professor James Lee, all of whom also gave advice on the manuscript. The APHH-Beijing campaign was organised by (amongst many others) Dr. Zongbo Shi and Professor Pingqing Fu and conducted at the Institute for Atmospheric Physics in Beijing, who also provided the MET data. The work of chapter three was conducted at the Institute of Environmental Assessment and Water Research of Barcelona. The supporting measurements were organised and carried out by Dr. Brice Temime-Roussel, Dr. Nicolas Marchand, and Dr. María Cruz Minguillón, and the field campaign was organised by Professor Andrés Alastuey and Professor Xavier Querol, all of whom provided feedback and support during preparation of the manuscript. The Antarctic work of chapter four was organised by Dr. Manuel Dall'Osto, and he and Professor Rafel Simo provided great support streamlining and strengthening the manuscript for this paper. This work would also not have been possible without the extensive effort of all staff aboard the BIO Hesperides research vessel, and at Juan Carlos I Antarctic research base.

On a final personal note, I would like to thank Dana Slack, Julie Brean, Rich Piana, and all my friends and colleagues in Birmingham for making my research the last few years so enjoyable.

CONTENTS

LIST OF FIGURES

LIST OF TABLES

PUBLICATIONS

Papers accepted for publication from this doctoral research

- **Paper 1:** Observations of highly oxidised molecules and particle nucleation in the atmosphere of Beijing
  James Brean, Roy M. Harrison, Zongbo Shi, David C. S. Beddows, W. Joe F. Acton, C. Nicholas Hewitt, Freya A. Squires, and James Lee.
  Atmos. Chem. Phys., 19, 14933-14947 https://doi.org/10.5194/acp-19-14933-2019, 2019

- **Paper 2:** Molecular insights into new particle formation in Barcelona, Spain
  James Brean, David C.S. Beddows, Zongbo Shi, Brice Temime-Roussel, Nicolas Marchand, Xavier Querol, Andrés Alastuey, María Cruz Minguillón, and Roy M. Harrison.
  Atmos. Chem. Phys., in review https://doi.org/10.5194/acp-2020-84, 2020

- **Paper 3:** Open ocean and coastal new particle formation from sulphuric acid and amines around the Antarctic peninsula
  James Brean, Manuel Dall'Osto, Rafel Simo, Zongbo Shi, David C.S. Beddows, and Roy M. Harrison

Papers arising from research related to this doctoral research

- Interpretation of particle number size distributions measured across an urban area during the FASTER campaign
  Roy M. Harrison, David C.S. Beddows, Mohammed S. Alam, Ajit Singh, **James Brean**, Ruixin Xu, Simone Kotthaus, and Sue Grimmond
  Atmos. Chem. Phys., 19, 39–55, https://doi.org/10.5194/acp-19-39-2019, 2019.

CHAPTER 1: INTRODUCTION

Theory & Background

New particle formation (NPF) is the generation of new atmospheric particles from gas phase species involving formation and subsequent growth of an embryonic molecular cluster, where rates of formation and growth must outcompete evaporation and coagulational losses. In practical terms, it is typical to conceptualise this in terms of a "two-step" process. (see Figure 1). The first of these steps is nucleation, with the generation of thermodynamically stable molecular clusters. This process is analogous to generation of crystals within a supersaturated liquid. Nucleation processes in solution are under intense study across multiple fields due to the applications of resultant nanoparticles in biomedicine, catalysis, fuel cell, data storage, agriculture and solar cell research[1]. Nucleation processes involve a free energy change, occurring with a decrease in enthalpy, but also result in a decrease in entropy. They are not strongly thermodynamically favourable, but become more favourable at lower temperatures. Gas phase molecules will form clusters held together by intermolecular forces, which form either due to random fluctuations in vapour density, or assisted by irregularities such as ions or small clusters. These will further grow by addition of gas phase molecules and ions. Typically, these involve gases capable of forming strong hydrogen bonded pairs like sulphuric acid and dimethylamine. Once this cluster reaches the critical diameter, typically stated at 1.5 ± 0.4 nm, growth of the cluster to larger sizes becomes a spontaneous process[2,3]

Once this nucleation step has taken place, particles will grow by condensation of low volatility gas phase molecules on the surface of this aerosol (Figure 2), which results in an increase in particle diameter with no decrease in particle number. This occurs when the saturation vapour pressure of a molecule in the gas phase exceeds the saturation vapour pressure over a particle. Early stage particle growth is limited heavily by the Kelvin effect, stating that the vapour pressure over a more curved surface is significantly greater than that over a less curved surface. This greatly increases the saturation vapour pressure demands of molecules necessary to condense down onto the smallest particles, and thus an abundance of low volatility vapours is required for this to proceed rapidly. Such growth can be

explained by nano-Köhler theory, wherein spontaneous growth occurs after activation at a given saturation ratio[4]. This framework adequately explains the condensation of nitric acid and ammonia under sufficiently high saturation ratios[5] Alternatively, particles can grow by the coagulation of two newly generated aerosols, which results in an increase to particle diameter with a decrease in particle number. The former of these is more likely under typical conditions due to the relatively low concentrations of new particles compared to low volatility gas phase compounds[6–10].

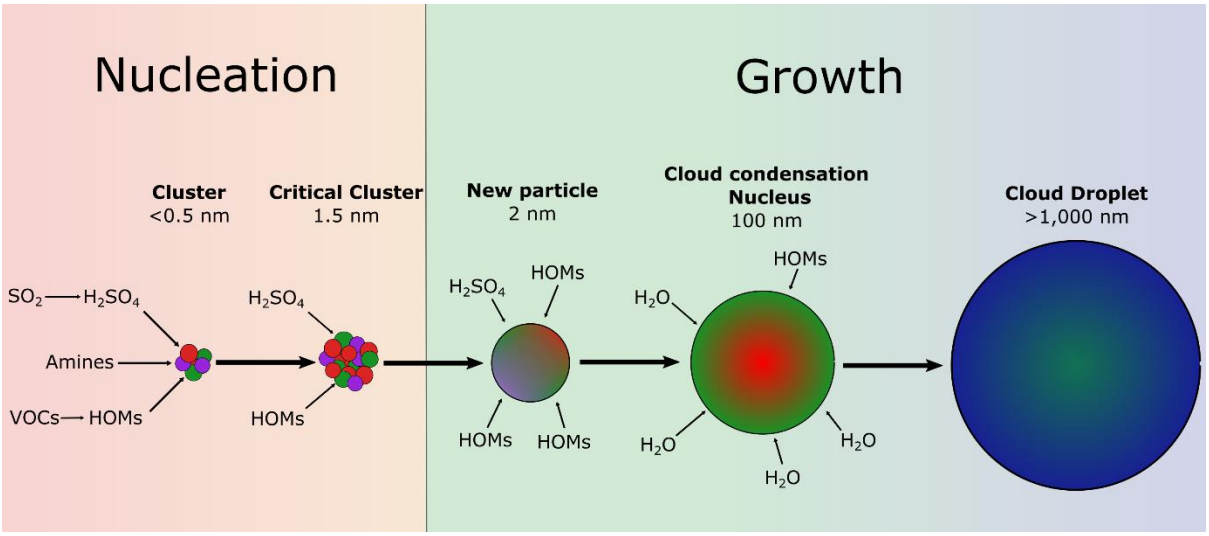

Figure 1: Schematic diagram of new particle formation and growth, resulting in the generation of a CCN particle.

Aerosol particles are found across the troposphere with concentrations ranging from 100 – 10^5 cm^{3}[11], covering diameters from 10^{-9} – 10^{-4} m. While NPF is a significant contributor to particle number, its effect on particle mass is less significant. The majority of particle mass comes from larger particles, which will typically arise as the result of combustion, sea spray or resuspension of dust, which in turn contribute relatively little to particle number. Particle size distributions are comprised of a series of lognormal modes. Such modes cover such a diverse range of particle sizes with distinct chemical and physical characteristics. These are typically separated into the nucleation (1-20 nm), Aitken (20-100 nm), accumulation (100-1000 nm), and coarse (>1000 nm) modes.

As liquid droplets, aerosol particles are capable of both absorbing and scattering incident radiation (direct radiative forcing). Aerosol particles can also act as cloud condensation nuclei (CCN) which affect the microphysical properties of clouds, their coverage and lifetimes, and the likelihood of their

precipitation[12] (the climate forcing portions of these effects are referred to as indirect radiative forcing). The two combined direct and indirect effects provide great uncertainty in global estimates of radiative forcing, with the latter having the greatest effect[13]. Estimates of radiative forcing show that the anthropogenic increase to global aerosol load has offset approximately one third of continental warming by greenhouse gas emissions[14], meanwhile, different estimates of the effect of NPF on global climate range from positive to negative[15,16] depending on the mechanisms involved[17–19]. Proper understanding of global NPF processes on a molecular level is therefore key to understanding the global climate.

A CCN particle is defined as a particle that can become activated at a particular water saturation ratio. Activation is the indefinite growth of a particle due to condensation of water vapour. For particles to act efficiently as CCN, they must be sufficiently large, with ranges for particles to become active at atmospheric water saturation ratios ranging from 50-150 nm[12,20–22]. They must also be sufficiently hygroscopic, a property determined by particle composition[23]. NPF is a significant contributor to CCN due to the high number concentration of resultant particles reaching CCN active sizes (Figure 2), with approximately half of global CCN thought to arise from NPF, down from just under 70% estimated during preindustrial conditions[24]. Physical observations typically show that 10-60% of NPF events lead to an enhancement to CCN count, and these events lead to increases to CCN count ranging from a factor of 0.5 to 11[6]. NPF is therefore a significant modulator of the global climate. Further, despite reductions to SO_2 emissions across Europe, and a reduction in the frequency of NPF events, the CCN production associated with NPF has been found to increase over time due to increased BVOC emissions, and therefore particle growth[25].

Alongside climate forcing effects, airborne particulate matter is the air pollutant believed to have the greatest impact on human health, with airborne particles causing 4.2 million premature deaths in 2015 alone[26]. Most attention is given to the mass concentration of aerosols of diameter less than 2.5 μm, however, the ultrafine fraction can exhibit significant health effects also. Ultrafine particles can initiate inflammation via oxidative stress responses[27–29], and these particles can more easily enter the lung and penetrate the bloodstream due to their more diffuse, gas like behaviour[30–33]. Mouse studies employing diesel exhaust (which is chemically distinct from particles arising from NPF, but exists in similar size

ranges) demonstrate that diesel generated UFP can induce a variety of inflammatory and hyperreactive responses[34–37]. Studies in the urban environment tend to show weak positive associations between UFP concentrations and respiratory mortality[38,39], with UFP exposure associated with increases to blood pressure and decreased expiratory volume[40].

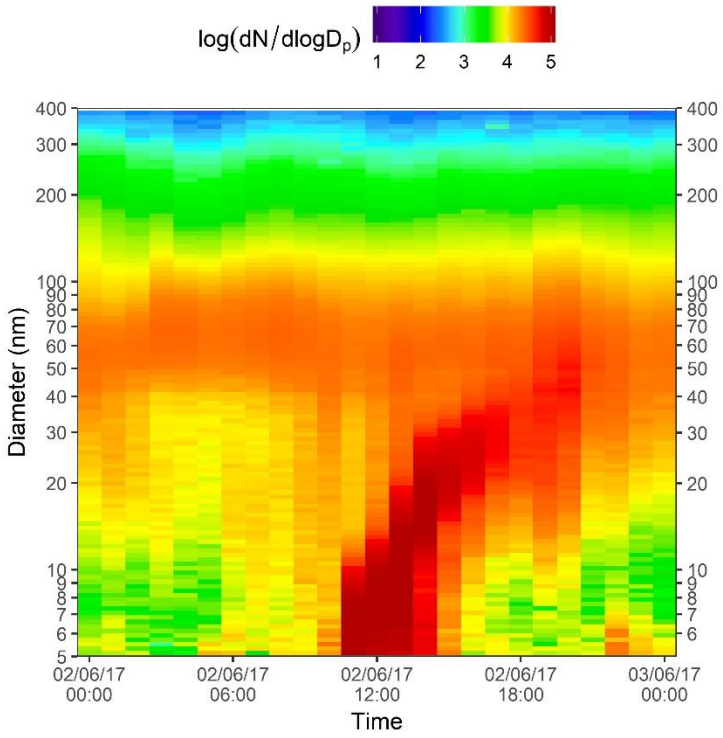

Figure 2: Particle size distribution contour plot for an NPF event day in Beijing

Measurements and models

Background

Early measurements of NPF were made using ion spectrometers and showed midday increases to the number counts of the smallest particles[41]. Subsequent research has found NPF events to occur worldwide, across a diverse range of environments[42], from polluted urban centres[43–46] (where such particle formation was unexpected[47]), to pristine polar[48] and free tropospheric environments[49,50]. NPF exhibits strong seasonality across near all environments, and occurs typically at midday under intense insolation[11] and therefore production of $OH^{\cdot}$ radicals[51,52], with observations of nocturnal or evening time

cluster formation being rare[53,54]. Cluster analysis applied to results from multiple sites across Europe show most frequent NPF can happen at different times of year depending on geographic location[44], with intense wintertime NPF seen in southern Europe and southeast Asia[43,44].

Nucleation of binary sulphuric acid-water systems was initially thought to drive most nucleation observed in the troposphere[55,56]. A role of a ternary stabilising species, ammonia, was suggested by observational studies[57,58], and backed up by computational studies[8], with later studies later suggesting a potential role of oxygenated organic molecules[59], iodic acid[60], methanesulphonic acid (MSA)[61], and amines[62]. These molecules are all either involatile (in the case of acids and large oxygenated organics), or capable of forming strong hydrogen bonded pairs and with molecules that are (in the case of amines and smaller oxygenated organic molecules). Sulphuric acid arises from the $OH^{\cdot}$ oxidation of SO_2, which has natural marine and volcanic sources, and anthropogenic sources in the combustion of sulphur-containing fuels[63]. Sulphuric acid can also be directly emitted by traffic sources[64,65]. Iodic acid arises from the oxidation of biogenic iodine emissions[60,66] (I_2, CH_2I_2), and MSA from the oxidation of dimethylsulphide (DMS), which oxidises to produce SO_2 and MSA at approximately a ratio of 3:1[67]. The majority of biogenic iodine emissions, as well as MSA emissions are from marine sources. $OH^{\cdot}$ arises primarily from the photolysis of ozone, water vapour, HONO, H_2O_2 etc., and thus $OH^{\cdot}$ concentrations tend to track insolation intensity quite closely[51,52], and in combination with O_3 is the main daytime oxidant of most tropospheric vapours. Amines are often co-emitted with ammonia, and have biogenic sources in ocean regions[68,69], and anthropogenic sources in agriculture, waste management, traffic, and food industries[70–73]

High condensation sinks (CS, the rate at which vapours will condense down onto particle surface area) will inhibit NPF, and elevations to CS occur simultaneously with elevations to coagulation sinks (CoagS)[6]. Elevations to CS will result in a reduction to NPF precursor vapours such as sulphuric acid. Elevated CoagS will result in the rapid coagulation of new particles, supressing NPF from occurring. High mixing ratios of isoprene have also been found to supress NPF in forested environments[74], with isoprene, as well as CO and CH_4 capable of acting as a significant $OH^{\cdot}$ sink[75]. Isoprene oxidation products are still generally too volatile to participate efficiently in new particle formation processes,

and $OH^{\cdot}$ scavenging by isoprene inhibits the generation of less volatile monoterpene oxidation products[75–77]. We therefore have mechanisms whereby the oxidation products of biogenic and anthropogenic emissions combine, either synergistically or antagonistically to drive the formation and growth of new particles. Pre-existing particles, either from NPF or primary emissions will supress NPF and thus NPF is expected much more frequently in cleaner environments.

The role sulphuric acid and bases

Sulphuric acid by itself is relatively inefficient at forming large molecular clusters, with concentrations orders of magnitude higher than typically observed in the troposphere required to form particles at appreciable rates at 278 K. In the presence of water vapour, this demand decreases due to the favourable mixing enthalpy of sulphuric acid and water. Evaporation rates of sulphuric acid-water clusters are, however, extremely high, and theoretical nucleation rates from this system failed to match tropospheric observations[78]. Systems involving a ternary stabilising compound are therefore expected. Early results from the CLOUD chamber showed that sulphuric acid, water and ammonia in the presence of ionizing radiation could reproduce tropospheric observations at sufficiently low temperatures. Evaporation of such clusters is still a rapid process, however, with increases to temperature strongly decreasing formation rates[78]. On the basis of earlier studies[62] the role of dimethylamine was studied[78], with extremely rapid particle formation rates observed, largely not influenced by ionising radiation nor temperature[79]. The cluster binding energies between sulphuric acid and amines are significantly higher than those between sulphuric acid and ammonia[62], the latter having roughly similar binding energies than seen between sulphuric acid and organic acids[80]. Recent evidence shows that cluster evaporation becomes significant at temperatures approaching 298 K, and this results in reduced particle formation rates under typical urban conditions[81] Other amines have been shown to be efficient at forming particles in flow tube studies[82], where it was shown that even in the presence of strong bases ammonia increased the nucleation rate, despite the fact amines are expected to efficiently replace ammonia in sulphuric acid clusters[83]. Bases at a few pptv have been shown to accelerate sulphuric acid-water nucleation by over 3 orders of magnitude more than ammonia at 278 K, and can form particles at rates similar to that measured across the troposphere at typical sulphuric acid concentrations[83,84]. Due to the strong bonding

between sulphuric acid and dimethylamine, near-zero evaporation of clusters can be assumed, contrary to what is expected in the sulphuric acid-ammonia system[85], and it is only in the upper atmosphere, or the extremely cold polar regions that nucleation involving sulphuric acid, ammonia and water vapour can be expected to proceed efficiently. Modelling studies oft neglect sulphuric acid-amine nucleation due to the low emission fluxes and short atmospheric lifetime of amines[18,24] despite significant urban, agricultural and oceanic sources[70]. Regardless, these modelling studies found a significant contribution of sulphuric acid-ammonia nucleation (around half), with around 2/3 of this nucleation being ion induced[24].

Highly oxygenated multifunctional organic molecules

Early Work

Highly oxygenated multifunctional organic molecules, or HOMs, are organic molecules containing multiple oxygen containing functionalities, arising from rapidly occurring autoxidation mechanisms. Such mechanisms result in organic molecules with extremely low volatility, with each -OH or -OOH functionality reducing saturation vapour pressure by a two and a half orders of magnitude[86]. The occurrence of such low-volatility organic molecules and their role in new particle formation has been hypothesised for many years[56], however, HOMs were first truly observed in the night-time boreal atmosphere in 2010[87]. This was the first field deployment of the atmospheric pressure interface time of flight mass spectrometer (APi-ToF)[88]. The existence of clusters with extremely high O:C ratios (up to 1.4) were observed, and hypothesised to be the oxidation products of α-pinene, clustered with the nitrate ion (NO_3^-). These results were reproduced in the JPAC chamber, showing ozonolysis to be an efficient HOM formation pathway[89]. The concentration of small, charged clusters were seen to correlate positively with certain HOM during NPF events seen in the remote boreal environment in 2013[9]. This was the first indication that these compounds were involved in nucleation processes. As the negative ion spectra showed many HOM to be clustered with the nitrate ion, it was apparent that the nitrate ion efficiently bound itself to HOM in the atmosphere, and thus a chemical ionization inlet was adapted from the work of Eisele and Tanner[90,91]. This was employed in a later study showing that HOM produced from the ozonolysis of monoterpenes were capable of efficiently forming new particles, and based on

parameterisations of the volatility basis set (VBS), they were dubbed Extremely Low Volatility Organic Compounds (ELVOC)[92]. Later work saw the definition of HOM updated to include three criteria. In order for a molecule to be classed as HOM, it must:

1. Be formed under atmospheric conditions in the gas phase
2. Contain six or more oxygen atoms
3. Be formed via peroxy radical autoxidation

The third of these is especially important, as a growing body of evidence suggests molecules such as aromatics can become highly oxygenated via multiple generations of oxidation[93,94].

Mechanisms of formation & yields

A carbon centred radical in the atmosphere will quickly see O_2 added to it to produce a hydroperoxyl functionality (RO_2·). If a RO_2· has a sufficiently weakly bound hydrogen (for example, aldehydic hydrogens easily abstract[95]), it will undergo a H-shift reaction, producing an –OOH functionality and another carbon centred radical to which another O_2 can add[96] (Figure 3). Autoxidation is a rapid process and can see multiple new functionalities added in a matter of seconds[77], with RO_2· Lifetimes ranging from 0.5 to 1000 s, determined primarily by NO and HO_2· concentrations in the urban and pristine environments respectively, although only closed-shell compounds were measured in the work of this thesis, consistent with prior publications[43]. This process is well studied in combustion chemistry, but was only considered to be atmospherically relevant relatively recently[97]. The number of H-shifts a molecule will undergo is sensitive to the number of loosely bound hydrogens in the correct configurations present in the precursor VOC, as any significant energy barrier decreases the rate of the H-shift reaction by orders of magnitude, and therefore increases the fraction of RO_2· radicals being terminated upon reaction with HO_2·, NO, or another RO_2· before multiple autoxidation cycles. These rates of autoxidation are dependent upon structure of the isomerising radical, and temperature. Computational rate constants of H-shift reactions show changes of near 1 order of magnitude with a 20 K temperature difference[98], and the resultant HOM molar yields (note, mass yields will always be significantly larger than molar yields, but these are not discussed here) have been shown to change by a factor of 50 between 273 and 293 K[99]. Quéléver et al. show that despite this decrease in yield, the

distribution of oxidation states across the products remains similar at different temperatures[99], contrasting results from other work[100–102], where a decrease in temperature reduces the average oxidation state of carbon seen in the products. In the context of early stage particle growth, this is offset by a decrease in effective volatility, and increased condensation of less oxygenated products[103].

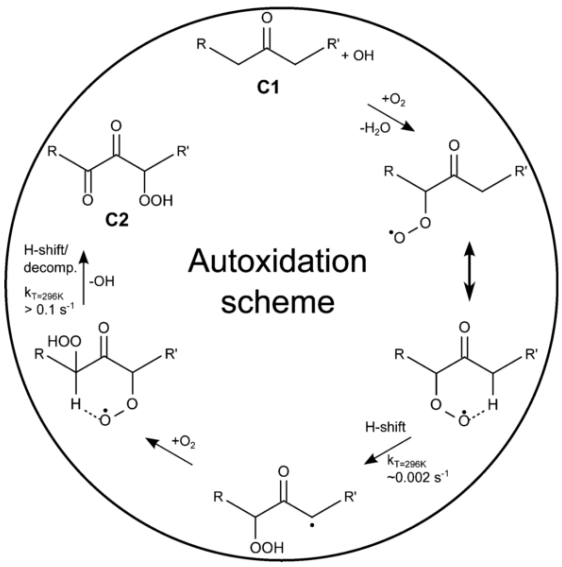

Figure 3: H-shift reactions of a model compound, figure taken from Crounse et al., 2013[97]

Although HOM were initially observed as the products of the ozonolysis of α-pinene, other pathways have been investigated, with $OH^{\cdot}$, $NO_3^{\cdot}$, and Cl producing HOM in chamber studies[104–106]. HOM yields from these pathways vary between near-zero, for the likes of the O_3-isoprene system, and 17%, for the system involving limonene and $O_3 + OH^{\cdot}$. with the mean around 5%[93,105,107–110]. Certain VOCs such as limonene, containing multiple carbon-carbon double bonds, are capable of going through multiple generations of oxidation and thus the apparent HOM yield is higher than that for other molecules[92,93]. Biogenic monoterpenes prove themselves to be (mostly) highly capable of producing HOM, and their double bonds allow for efficient ozonolysis pathways, as well as oxidation by the nitrate or hydroxyl radical. The formation of highly oxygenated molecules from aromatic compounds is less efficient, with yields for small aromatics such as benzene, toluene and ethylbenzene as low as 0.1 and 0.2%. Yields for larger aromatics such as xylenes, mesitylene and polycyclic compounds appears higher, ranging from 0.6 – 2.5%[110]. The oxidation of these compounds will proceed primarily by the $OH^{\cdot}$ oxidation pathway, as no efficient ozonolysis mechanism exists, and thus their oxidation is quite limited to daytime processes, but they are undoubtedly of great significance in urban environments due to their abundance.

Volatility

Further studies have brought the initial assignment of volatility of HOMs as ELVOC from VBS[92] into debate. Constraining the volatility of HOM is essential when constraining their treatment in dynamical growth models, as more volatile HOM will exist in equilibrium between gas and particle phase, while less volatile HOM are more likely to condense irreversibly[111–113]. VBS is based upon composition activity relationships, where the molecular formula is known but structure is not. Average functionalities are assumed, and each of these is presumed to have an effect on volatility. As later studies brought to attention that these highly oxygenated molecules were the result of autoxidation mechanisms, and therefore had multiple –OOH functionalities. The actual number of volatility-reducing functionalities is relatively small compared to initial estimates (according to SIMPOL, the reduction in vapour pressure from an –OOH is roughly similar to that of an –OH, around 2.5 orders of magnitude[86]). Further, effects like intramolecular hydrogen bonding can further increase volatility in certain configurations of HOM, causing further uncertainties. Updated VBS calculations and quantum chemical calculations rendered updated understanding of the vapour pressures of HOM, and more recent work considers only the largest HOM to be ELVOC, typically the dimerization products of two RO_2· radicals[112,114–118]. The result of recent calculations of volatility from α-pinene ozonolysis shows HOM to cover over 20 orders of magnitude[115]. Experimental evidence, although sparse, indicates that models such as SIMPOL under predict saturation vapour pressures[119]. Such experimental studies produce general linear models to predict the volatility of α-pinene HOM, where the volatility depends negatively on the oxygen and, to a lesser extent the hydrogen content, as the former determines the number of oxygen containing functionalities, and the latter is a predictor for how many of these oxygen functionalities will be, for example, hydroxyl rather than carbonyl. Positive association with nitrogen functionalities is consistent with experimental observation of nitrogen containing HOM failing to form new particles, and is likely due to intramolecular H-bonding from an R-O-NO_3 group[119].

Role in nucleation and growth

HOMs from multiple precursors have been shown to participate in nucleation in conjunction with sulphuric acid in several studies[2,120–122]. Clustering between sulphuric acid and organics has been shown

by computation studies to proceed by hydrogen bonding between carboxylic acids in organic molecules and sulphuric acid, a necessary condition of the organic molecule as well as the presence of a carboxylic acid group is also the lack of intramolecular hydrogen bonding within the HOM[80]. HOMs efficiently form particles in this system as they form hydrogen bonds with sulphuric acid, and require only a few additions of large HOMs before a cluster >1.5 nm is formed. This, therefore, proves itself an efficient source of new particles in the real atmosphere.

Nucleation of oxygenated organic molecules in the absence of sulphuric acid requires ionising radiation to proceed efficiently; as otherwise, the requisite functionalities to form intramolecular bonds are not present. It appears to be only the largest HOMs that can participate in these mechanisms (C_{20} dimers in the case of dimers formed from monoterpene oxidation). This was first shown in chambers[123], and consequently in the free troposphere[49] and remote boreal environment[54]. Molecules with sufficiently low saturation vapour pressures to nucleate by themselves fall into a newly dubbed category of ultra-low volatility volatile organic compounds (ULVOC)[124]. This process has been shown to be extremely sensitive to temperatures down to -50 ºC due to the reduced saturation vapour pressures at these temperatures[102]. Such mechanisms involving HOM in the absence of sulphuric acid are rare, as conditions necessary for ionization of HOM also lend themselves to production of sulphuric acid. These mechanisms will, therefore, only occur in environments far from sources of gas phase sulphur[49,54].

Tropospheric measurements of sulphuric acid are insufficient to explain the first few nanometres of particle growth in most environments[4,43], unless strong long range intermolecular forces are taken into account[103], and, until the first measurement of HOMs, there was uncertainty as to what drove much of the observed initial new particle growth. Extremely involatile HOMs have been found to be sufficient to drive early particle growth, and, as HOMs cover several orders of magnitude of volatility, more abundant less volatile HOM (as well as LVOC and SVOC not classified as HOM) will be sufficient to drive later stages of organic new particle growth[112,115].

Other mechanisms

Measurements across the troposphere point towards sulphuric acid, bases and oxygenated organic molecules being the likely candidates to explain most observed nucleation, however, two other

compounds have been the subject of significant investigation. The oxidation products of biogenic iodine emissions such as CH_2I_2 were hypothesised to participate in nucleation in the marine boundary layer, specifically coastal regions[60,125]. A later study saw extremely strong new particle formation in the summer, with concentrations high enough for extremely large clusters to be seen in the CI-APi-ToF spectra > 2,000 m/Q. On the basis of the high gas phase concentrations attributed to HIO_3, and the O:I ratio of the large clusters, sequential addition of HIO_3 followed by formation of I_2O_5 was suggested[66], although current instrumentation is incapable of measuring the sequence in real-time. The potential role of iodine oxides cannot therefore be dismissed across coastal and marine environments globally.

MSA is an oxidation product of DMS, also found plentifully in the marine boundary layer. MSA has been shown to form particles in flow tubes, though rather inefficiently[126–128], and further, quantum computational studies that show that addition of MSA to a nucleating system of sulphuric acid and amines can accelerate particle formation by up to an order of magnitude, but this increase is substantially lower at standard tropospheric temperatures[129]. Global models also show roughly a doubling in particle number concentrations globally if MSA can act as sulphuric acid in ternary nucleation involving ammonia and water vapour, and binary nucleation involving water vapour, and suggest that even if this pathway is not viable, MSA will substantially contribute to total sulphate aerosol mass via condensation[67].

Despite a growing body of knowledge regarding molecular scale evidence for direct mechanisms of particle formation in urban environments[43,130], there still maintains a distinct gap between theory and measurement. Survival parameters (*P*) of new particles are extremely small due to high CS:GR ratios[131]. Theory predicts that P values <50 are required for NPF to take place, yet NPF events occur frequently with P values up to a factor of 4 greater[43,45,132–143]. Possible explanations for this include coagulation sticking probabilities of less than unity, or early stage growth rates significantly higher than currently thought, with measurements of $GR_{1\text{-}3}$ still sparse[4,43,131,144]. Where molecular scale measurements of acids and HOMs have been performed, their condensation seems incapable of explaining rapid early particle growth, even when HOMs are assumed involatile[43]. Several theories attempt to bridge this gap, by describing enhanced growth from long range intermolecular forces[144] or describing yet-unmeasured

organic oxidation products[43], with measurements achieving "carbon closure" only performed in chambers thus far[145]. With regards to HOM production, while there has been a substantial body of research studying HOM production from biogenic monoterpenoids[89,96,100,102,105,107,114,119,123,145–152], studies on HOM arising from aromatic VOC oxidation are relatively few[93,94,109,110,153], despite these being the dominant VOCs in urban environments. There therefore exists a substantial gap in the mechanistic knowledge of new particle formation processes in both urban and remote environments, and a need for further intensive field campaigns to fully understand the processes occurring on a molecular scale.

Methodologies

Particle count measurements

The scanning mobility particle sizer (SMPS) is capable of measuring a size distribution of particles from a few nm up to nearly micron diameters. Such size distributions are typically comprised of two or more lognormal modes. An SMPS is comprised of an electrostatic classifier (EC) which first neutralises, and then charges particles with a known charge distribution, before sizing these particles as according to electrical mobility in the differential mobility analyser. Particles are then counted in each size bin, typically by a condensation particle counter (CPC). The CPC employs condensational growth by mixing a sample aerosol flow with a saturated vapour, typically of water or alcohol. In the most modern cases, butanol is used[154]. Once particles are grown sufficiently, they are then counted by a laser-based optical detector. Both the commercially available CPC and SMPS systems are used routinely globally and are a staple in atmospheric observatories worldwide[11,45,46,133,155,156], as well as being used extensively in detailed chamber studies[78,79,120,121]. These instruments have two limiting factors in new particle formation studies. The first of these is the lack of measurements below 3 nm, due to the limitations of butanol-based counting. This limitation can be circumvented by the use of other working fluids with lower saturation vapour pressures[157], or alternative instruments such as the neutral cluster and air ion spectrometer (NAIS)[158]. The second of these is the lack of differentiation between charged and neutral aerosol, as this changes the dynamics of aerosol formation drastically. Air ion measurements are possible with the NAIS, and it's sibling instrument, the air ion spectrometer (AIS)[158,159].

The particle size magnifier (PSM) was first developed in 2011 and is capable of growing particles from ~1 nm to sizes where they can be detected by conventional CPC instruments[160]. The instrument mixes a turbulently cooled sample flow with a heated flow of air containing a supersaturation of diethylene glycol (DEG). The degree of supersaturation of DEG can be varied within the PSM instrument to vary the D_{50} diameter (the diameter at which 50% detection efficiency is achieved) between ~1-3 nm, allowing a particle size distribution at these diameters to be measured, continuous with SMPS measurements. These data require data inversion to achieve a size distribution[161,162].

Chemical ionisation atmospheric pressure interface time of flight mass spectrometry

Working principals

Measurement of gas phase acids, HOMs, and amines is key to understanding NPF processes. Through this work, the Aerodyne nitrate chemical ionisation atmospheric pressure interface time of flight mass spectrometer (CI-APi-ToF) is used to make measurements of these compounds. A schematic of the nitrate chemical ionisation inlet is shown in Figure 4. The nitrate chemical ionisation inlet charges molecules through two possible mechanisms, proton abstraction or adduct formation, shown in reactions [1] through [3].

$$HNO_{3(g)} + h\nu \rightarrow NO_3^-{}_{(g)} + H^+{}_{(g)} \quad [\,1\,]$$

$$NO_3^-{}_{(g)} + H_2SO_{4(g)} \rightarrow HNO_{3(g)} + HSO_4^-{}_{(g)} \quad [\,2\,]$$

$$NO_3^-{}_{(g)} + C_6H_8O_{7(g)} \rightarrow C_6H_8O_7\text{-}NO_3^-{}_{(g)} \quad [\,3\,]$$

Where the dash represents adduct formation. Adduct formation will occur efficiently between nitrate ions and molecules with multiple hydrogen bond donating groups, such as –OH or –OOH[163], with the latter forming stronger hydrogen bonds[164]. These are frequently produced as the products of autoxidation. Similar sensitivities are presumed for sulphuric acid, HOMs and other species measured in the CI-APi-ToF[165] (dicarboxylic acids, other inorganic acids). If clustering with the nitrate ion is collision-limited, the rates of cluster formation for HOMs and sulphuric acid are similar[92], although inconsistencies likely arise due to different sample line losses, declustering rates within the instrument, and mass discrimination effects[147] . A similar reaction to reaction [3] can occur between charged clusters of nitrate and nitric acid and gas phase bases, due to the acidity of the nitric acid clusters. This

will typically happen with a cluster of two molecules of nitric acid, and one of nitrate (dubbed the "nitrate trimer").

$$(HNO_3)_2NO_3^-{}_{(g)} + C_2H_6NH_{(g)} \rightarrow C_2H_6NH\text{-}(HNO_3)_2NO_3^-{}_{(g)} \quad [4]$$

Such species usually appear in the mass spectra clustered with the nitrate dimer and nitrate trimer, and thus their presence in the mass spectra can be confirmed by comparison of the variation of intensity of the two peaks. The sensitivity of NO_3^- charging to individual bases is likely to vary significantly between different bases, but this is currently uncertain [165,166].

Nitrate ions are generated from the X-ray photolysis of nitric acid vapour, which is entrained from a reservoir of nitric acid liquid (65% w/w). These nitrate ions are then introduced into the instrument sheath flow. Ambient air is pulled into the front end of the chemical ionisation inlet at 10-20 LPM through a ¾" diameter stainless steel inlet of length ~1 meter. The flows are intended to be as fast as possible while maintaining laminar flow to minimise wall losses. Reynolds numbers were used to estimate turbulence for different flowrates throughout this work (typical values were 750 – 1250). Ambient air is then introduced into the reaction chamber. A flow of sheath air containing nitrate ions is ran parallel and concentric to the ambient air, rendering the reaction chamber effectively "wall-less". These nitrate ions are guided into the sample flow by means of a potential difference across the reaction chamber.

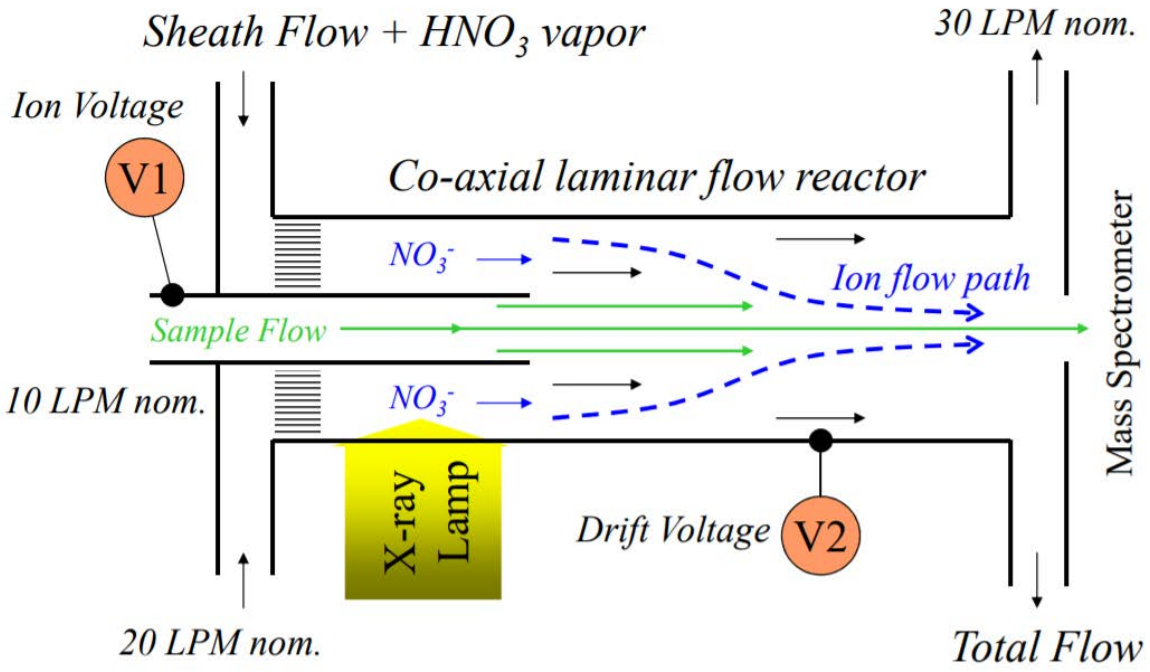

Figure 4: Scheme of nitrate chemical ionisation system. Taken from instrument setup manual, adapted from Eisele and Tanner (1993)[90]

The APi-ToF instrument thereafter contains a series of differentially pumped chambers from a few mbar at the front end through to 10^{-7} mbar in the ToF analyser (extremely low pressures required to ensure minimal collisions within the ToF analyser). The first and second of these chambers are the small segmented quadrupole (SSQ) and big segmented quadrupole (BSQ), which are used to focus the ion beam. The frequency of operation of these quadrupoles can be altered to increase transmissions of certain mass ranges of ions. The third of these is the primary beam (PB), used to focus the ion beam further, and the fourth is the ToF analyser itself. Potential differences across every part of the instrument can be altered to affect transmission of different ions, with the potential differences across the SSQ and BSQ regions mostly affecting transmission (for example, survival of more weakly bound clusters), and the resolution (mostly affected by the potential differences across the ToF region). The ToF itself is a region where ions drift at a velocity inversely proportional to the square root of their mass to charge ratio. Their mass:charge is then recorded as a *time of flight* which can be converted to a m/Q by the following equation:

$$t = k \times \sqrt{\frac{m}{Q}} \quad (1)$$

Where t is time of flight, m is the mass of the ion, Q is the charge of the ion (typically 1) and k is a constant. The value of k can be established using the position of the mass spectra of known ions. With NO_3^- ionisation, there will be distinct peaks belonging to NO_3^-, $(H_2O)NO_3^-$, $(HNO_3)NO_3^-$, and $(HNO_3)_2(NO_3^-)$. The ToF produces mass spectra at around a rate of 50 kHz, and 50,000 mass spectra are aggregated up to represent a 1 second average spectrum. An example of such a mass spectrum is presented in Figure 5. A physical calibration constant to convert from ion intensity (cps) to concentration (cm^{-3}) can be created by calibration with sulphuric acid vapour generated in the gas phase[167]. No such calibration was performed in this work, but calibration can be estimated based upon the comparison of measured signals with a photochemical sulphuric acid proxy, which estimates photochemical production of sulphuric acid from oxidation of SO_2[165,168], presuming the concentration of sulphuric acid to be a function of SO_2 concentration, solar radiation (and therefore $OH^\cdot$ concentration), condensation sink and relative humidity. The gradient of the line of best fit between this proxy against ion counts yields calibration constants in the range $10^{9\text{-}10}$ cm^{-3} in this work. This is applied in chapters 2 and 3 of this thesis, where in paper 1 a comparison with a proxy utilising OH data was also used, although data overlap was sparse.

Data analysis

The mass spectra collected by the CI-APi-ToF represent 1 second time resolution measurements of all gas phase molecules of sufficient acidity, basicity or hydrogen bond donating capacity to achieve charges with NO_3^- ionisation, and therefore the resultant spectra comprise thousands of peaks, often overlapping due to limitations of mass spectral resolution. Further, due to the nature of VOC oxidation, multiple different VOCs can produce HOMs of identical mass, but vastly differing structures and vapour pressures (for example, the oxidation of monoterpenes and the oxidation of C_4-alkylbenzenes can both produce molecules of the formulae $C_{10}H_{14\text{-}16}O_{6\text{-}12}N_{0\text{-}2}$).

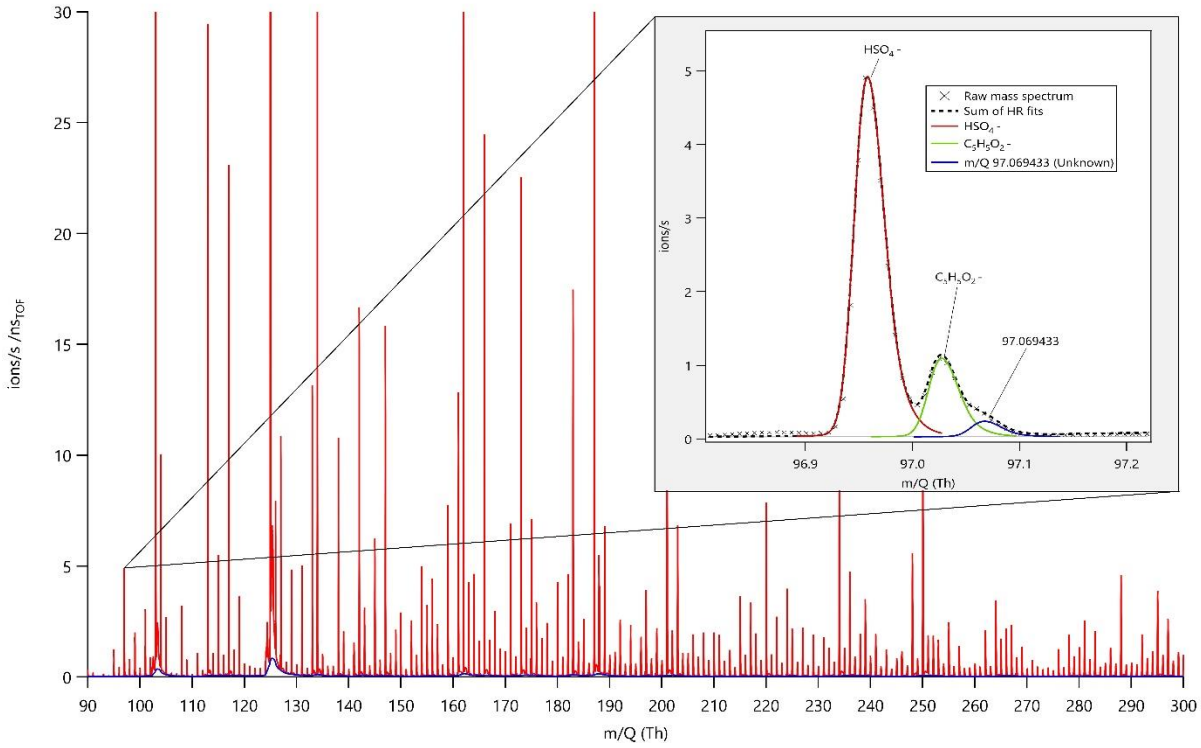

Figure 5: Example mass spectrum from 90-300 m/Q, with region from 96.8 – 97.2 highlighted.

Peaks within the mass spectrum must be assigned manually. Statistical methods exist for deconvolving the mass spectra into sub-spectra by either positive matrix factorization (PMF) or cluster analysis[169–172]. These methods are not widely established for the analysis of these datasets and were not employed in this work. Each peak assignment was made on the basis of both the mass accuracy and the physical viability of the molecule based upon current understanding of oxidation chemistry[77]. An example of peak fits is included in Figure 5. Uncertainty in the assignment of peaks increases with increasing m/Q, due to widening of peaks in the mass spectrum, thus more overlap, as well as an increase to the total number of possible chemical compositions, and uncertainties in the mass calibration increasing with increasing distance from the mass of the heaviest known species. For measurements in complex urban environments, peak assignment at masses much greater than 500 m/Q becomes highly uncertain.

Working advantages & disadvantages

The CI-APi-ToF is the only instrument of its kind capable of making such detailed measurements of NPF precursors. Running the APi-ToF without chemical ionization interface allows for the measurement of atmospheric ions from single molecules up to large clusters with great sensitivity, as their transmission through the instrument is highly efficient[48,54,173,174]. This interface is, however, not

quantitative with respect to neutral species, as the ion signals are dependent upon both the proton affinity of the species and the concentration of the neutral species, with the lowest proton affinity molecules most likely to become negatively charged. The CI-APi-ToF ran with nitrate ionization gives a quantitative description of the neutral species it measures. While still a soft ionization scheme, significant fragmentation of more weakly bound larger clusters occurs upon charging with NO_3^-, resulting in cluster fragmentation, thus, extremely high concentrations of sulphuric acid are required to measure the sulphuric acid trimer $(H_2SO_4)_2HSO_4^-$, and measurements where a stabilising base is also present are equally rare. Instances of measurements of large clusters have been made in chambers[85], but only one instance in the real environment, showing large clusters of HIO_3 resulting from vapour concentrations peaking at over 10^8 cm^{-3} [66]. The quantification and measurements made by CI-APi-ToF are also highly uncertain, with uncertainties on concentrations reported up to 85%, arising from calibration, charging efficiency, mass dependent transmission efficiencies, and sample line losses[66,93,115,123].

Calculations and parameterisations

Parameterisation of NPF events

New particle formation events can be characterised as according to the criteria of Dal Maso et al., (2005)[175]. These events must fulfil the following criteria:

1. The formation of a distinct new mode of particles
2. The mode must start at the nucleation mode (1-20 nm)
3. The mode must survive for a period of multiple hours and show growth.

These criteria satisfactorily explain the well-studied regional NPF events seen across a diverse range of environments[43,46,175–177]; however, these criteria, exclude lines-sources and point-sources of new particles from regions where NPF is dominated by coastal emissions[178], or sources such as traffic[179], as well as events with limited particle growth[54,176,180], and events where particles which have formed and grown several nm in diameter are entrained from the free troposphere to the boundary layer[181]. NPF events classified as according to Dal Maso et al. (2005) describe measurements under conditions with vapour concentrations sufficient to form and grow particles at a rate that outcompetes their loss

processes, resulting in steady growth across the period of several hours, leading to a neglect of other such new particle sources when classifying particle size spectra. The lifetime of sulphuric acid and HOMs is on the order of 20 – 600 s with respect to condensation, their main loss process, and thus the lifetime of these species is significantly less than that of the newly formed particles, with coagulation sinks of 3 nm particles around an order of magnitude lower than vapour condensation sinks, and sinks of larger particles lower again[182]. We therefore run into a possible limitation when events occurring on sub-regional scales are analysed (such as the "burst-events" of chapter 3), where the measured vapour may not represent the conditions under which the measured particles are formed.

Aerosol populations can be described using a few key parameters, a few pertaining specifically to new particle formation. Those that have been used in this work are outlined below.

Condensation sink

The CS represents the rate at which a vapour phase molecule will collide with pre-existing particle surface. If a sticking coefficient of unity is assumed, it can be taken as the rate that gas phase molecules condense onto particle surface and was calculated from the size distribution data as follows:

$$CS = 2\pi D \sum_{d_p} \beta_{m,d_p} d_p N_{d_p} \quad (2)$$

where D is the diffusion coefficient of the diffusing vapour (assumed sulphuric acid), β_m is a transition regime correction[183], d_p is particle diameter, and N_{dp} is the number of particles at diameter d_p. β_m is calculated thus:

$$\beta_{m,d_p} = \frac{Kn + 1}{1 + 1.677Kn + 1.333Kn^2} \quad (3)$$

Where Kn is the Knudsen number, calculated as follows:

$$Kn = \frac{2\lambda}{d_p} \quad (4)$$

Where λ is the mean free path in air, at STP, this is around 68 nm. Increases to condensation sink suppress NPF by acting as a significant sink to sulphuric acid, HOMs and other low volatility species. The condensation sink proves to be a useful metric in describing the likelihood of NPF

occurrence[6,43,46,184], and can predict the physical behaviour of molecules like sulphuric acid, where D is known. If the condensation sink is going to be applied to HOM molecules, some assumptions must be made regarding the diffusion coefficient. A sticking coefficient of unity is typically assumed[112,113], with no proof of a much less than unity coefficient[185]. If a HOM molecule is sufficiently volatile, re-evaporation will be significant and condensational losses will be less efficient. =

Coagulation sink

$CoagS_{dp}$ represents the coagulation sink for particles at d_p, or the rate at which a particle of size d_p will collide and coagulate into a particle of size $\geq d_p$:

$$CoagS_{d_p} = \sum_{d'_p=d_p}^{d'_p=d_p max} K_{(d_p,d'_p)} N_{d_p} \quad (5)$$

Where K is the coagulation coefficient of particles size d_p and d'_p. In the transitional particle regime, this can be expressed as:

$$K_{(d_p,d'_p)} = \frac{K_C^B}{d_{p1,2} \Big/ d_{p1,2} + \sigma_{1,2} + {}^{4D_{1,2}}\Big/ \bar{c}_{1,2} + R_{1,2}} \quad (6)$$

Where $K_B{}^C$ is the cogulation coefficient in the continuum regime:

$$K_C^B = 4\pi(d_{p1} + d_{p2})(D_1 + D_2) \quad (7)$$

And the particle diffusion coefficient is as follows:

$$D_i = \frac{K_B T C_c}{3\pi\mu d_p} \quad (8)$$

Where $D_{1,2}$ is referred to, it is the sum of D at diameters d_{p1} and d_{p2}. K_B is the Boltzmann constant, μ is the dynamic viscosity of gas, and C_c is the Cunningham slip correction factor, and is calculated as follows:

$$C_c = 1 + Kn(\alpha_1 + \alpha_2 \exp(\frac{-\alpha_3}{Kn}) \quad (9)$$

The values of $\alpha_{1,2,3}$ are available in Allen & Raabe (1985)[186]. Further: $\bar{c}$ is the relative mean thermal velocity, and is calculated as the square root of the sum of the squares of the average thermal velocities of the two particles. The average thermal velocity is calculated as follows:

$$\bar{c}_i = \sqrt{\frac{8K_B T}{\pi m_i}} \quad (10)$$

Where m_i refers to the mass of particle i. The mean relative thermal velocity is as follows:

$$\bar{c}_{1,2} = \sqrt{\bar{c}_1^2 + \bar{c}_2^2} \quad (11)$$

The distance at which the mass flux of the two particles are matched is similarly calculated, with the mass flux being:

$$\omega_i = \frac{(d_{p1,2} + \gamma_i)^3 - (d_{p1,2}^2 + \gamma_i^2)^{\frac{3}{2}}}{3 d_{p1,2} \gamma_i} - d_{p1,2} \quad (12)$$

And:

$$\gamma_i = \frac{8D_i}{\pi \bar{c}_i} \quad (13)$$

And therefore the point at which they are matched being:

$$\sigma_{1,2} = \sqrt{\omega_1^2 + \omega_2^2} \quad (14)$$

Above equations pertaining to coagulation adapted from Fuchs (1964)[187], Kulmala et al., (2001)[188] and Kulmala et al. (2012)[3].

Growth rate

The particle growth rate (GR) is the rate at which particles formed grow to larger sizes, and can be represented simply as follows:

$$GR = \frac{\Delta d_p}{\Delta t} \quad (15)$$

Where d_p can be parametised by fitting a lognormal distribution to the mode of newly forming particles in the particle size distribution for every measurement. The rate of change of the geometric mean of these modes is the growth rate. This growth rate includes both the growth by condensation and the growth by coagulation (both self-coagulation between two freshly formed particles, and growth by coagulation scavenging). As the condensational growth is the feature of interest here, we can account for these coagulational effects as below[189]:

$$GR_{selfcoag} = \frac{d_p}{6} k_{selfcoag}(d_p) N \quad (16)$$

Where $k_{selfcoag}$ represents the self-coagulation coefficient for two neutral particles. The significance of self-coagulation increases with increasing particle diameter because both the resultant increase to particle diameter is larger, and the self-coagulation coefficient increases up to a peak at around 20 nm. Diameters below 20 nm were always used to calculate growth rates in this work. The growth rate method cannot be applied to local NPF (i.e., local NPF with growth that cannot be measured over several hours). Growth rates can also be calculated by presuming irreversible condensation onto prexisting particles[190]

$$GR = \frac{\gamma}{2\rho_v}\left(1 + \frac{d_v}{d_p}\right)^2 \left(\frac{8k_b T}{\pi}\right)^{0.5} \left(\frac{1}{m_p} + \frac{1}{m_v}\right)^{0.5} m_p C_v \quad (17)$$

Where ρ_v is the density of the condensing vapour in the particle phase, $m_{p,v}$ refer to the masses of a single particle and vapour molecule respectively, $d_{p,v}$ refer to the diameters of a single particle and vapour molecule respectively, and C_v is the concentration of vapour. γ is a correction factor defined thus:

$$\gamma = \frac{4}{3} Kn\, \beta_m \quad (18)$$

Formation rate

The formation rate of new particles at size d_p is calculated as follows:

$$J_{d_p} = \frac{\Delta N_{d_p}}{\Delta t} + CoagS_{d_p} . N_{d_p} + \frac{GR}{\Delta d_p} . N_{d_p} \quad (19)$$

Where the first term on the right-hand side comprises the rate at which particles enter the size d_p, and the latter two terms represent losses from this size by coagulation and growth respectively. This method cannot predict the rate of formation of charged particles, but an extended version of equation ( ) can estimate the rate of formation of charged particles by accounting for ion-ion recombination and charging of neutral particles as sinks and sources of charged particles respectively. Uncertainties on the calculation of the formation rate dominated by the uncertainty on the detection thresholds in the particle counting instruments. These will be composition dependent and, in the case of the PSM, D_{50} is determined during calibration using NiCr particles, which are likely to have different uptake efficiencies for DEG than a particle comprised of organic material, or sulphuric acid and amines. In the case that the particle size distribution is only measured down to a few nanometers, the rate of particle formation at a lower diameter (J_1) based upon the equations of Korhonen et al. (2014)[191]

$$J_{1.7\,(t)} = J_{x\,(\Delta t+t)} . \exp\left(\frac{CoagS_{d_{p1.7}}}{GR_{1.7}} . d_{p1.7} . \gamma\right) \quad (20)$$

where $J_{1.7}$ is the formation rate to be calculated at 1.7 nm , $CoagS_{dp1.7}$ is the coagulation sink at that size, $GR_{1.7}$ is the growth rate between 1.7 nm and 4.5 nm, J_x is the original particle formation rate, and Δt is determined using a time-delay method using sulphuric acid. *γ is a factor defined as*

$$\gamma = \frac{1}{m-n+1}\left[\left(\frac{d_{pX}}{d_{p1.7}}\right)^{m-n+1} - 1\right] \quad (21)$$

Where m is a coefficient describing the slope of coagulation sink with diameter, dependent upon the background particle population

$$m = \frac{log\left(CoagS_{d_{px}}/CoagS_{d_{p1.7}}\right)}{log\left(d_{px}/d_{p1.7}\right)} \quad (22)$$

and n is dependent upon the slope of the growth rate (GR) with diameter

$$n = \frac{log\left(GR_{d_{px}}/GR_{d_{p1.7}}\right)}{log\left(d_{px}/d_{p1.7}\right)} \quad (23)$$

Systematic uncertainties on our calculated values of $J_{1.7}$ include a factor of +100% / -50% on the calculated growth rates, a factor of ±25% on dp of the NanoSMPS, and ±50% on the established losses due to condensation sink.

HOM properties

The double bond equivalent (DBE) describes the degree of unsaturation of an organic molecule and is defined simply as:

$$DBE = N_C - \frac{N_H}{2} - \frac{N_N}{2} + 1 \quad (24)$$

The saturation vapour pressure at 300 K is defined by within the 2D-volatility basis set (2D-VBS) as follows, if all nitrogen functionality is assumed to take the form $-ONO_2$[111,116,192]

$$Log_{10}(C^*)(300\ K) = (N_{C0} - N_C)b_C - N_O b_O - 2\frac{N_o N_C}{N_C + N_O} b_{CO} - N_n b_N \quad (25)$$

where N_C, N_H, and N_N, are the number of carbon, hydrogen, and nitrogen atoms respectively. N_O is the number of oxygen atoms minus $3N_N$ to account for $-ONO_2$ groups, N_{C0} is 25 (the carbon number of an alkane with a saturation mass concentration of 1 μg m^{-3}), b_C, b_O, b_{CO}, and b_N are 0.475, 0.2, 0.9 and 2.5 respectively, and represent interaction and nonideality terms. The final term of equation (25) accounts for $-ONO_2$ groups, each reducing the saturation vapourpressure by 2.5 orders of magnitude.

The average degree of HOM oxidation can be described using the average carbon oxidation state (OS_c), defined as follows

$$OS_c = 2\ O{:}C - H{:}C \quad (26)$$

Where an additional term at the end (-5 N:C) accounts for nitrogen functionalities. A lack of such a term (such as in chapter 2) can result in overpredictions in the calculation of OS_c

Summary of thesis

The dominant uncertainties in our current understanding of NPF are firstly a lack of understanding of the nature of HOM chemistry in polluted urban centres, and second, comprehensive, molecular scale measurements indicating NPF mechanisms across a diverse range of environments. The above methodology is employed across three diverse environments to attempt to answer these questions. Chapter two first gives an overview of HOMs in a polluted urban centre, Beijing (high insolation, high pollution), and discusses the viability of their contribution to NPF processes, with high temperatures facilitating rapid autoxidation, but high NO_x facilitating rapid peroxy radical termination. These results also provide some insight as to the mechanism behind nucleation in Beijing. The third chapter then presents an investigation of nucleation mechanisms in a similar environment, Barcelona (high insolation, moderate pollution), which is informed by the findings of the prior chapter, and a mechanism involving sulphuric acid and amines is inferred, with evidence for the necessary role of HOMs in particle growth.

Chapter four presents a contrasting study in a remote polar environment of the Antarctic Peninsula (low pollution, moderate insolation) where anthropogenic influence is negligible, but a similar mechanism was found to the polluted urban centres, involving sulphuric acid and small amines. A further investigation into the sources of ions seen in the mass spectra are presented, and it is found that air masses travelling over regions of melting sea ice contain elevated concentrations of amines and sulphuric acid, the latter likely arising from DMS oxidation.

CHAPTER 2: OBSERVATIONS OF HIGHLY OXIDIZED MOLECULES AND PARTICLE NUCLEATION IN THE ATMOSPHERE OF BEIJING

Authors: James Brean, Roy M. Harrison, Zongbo Shi, David C. S. Beddows, W. Joe F. Acton, C. Nicholas Hewitt, Freya A. Squires, and James Lee.

Published in: Atmospheric Chemistry and Physics. DOI: https://doi.org/10.5194/acp-19-14933-2019

Author contributions. The study was conceived and planned by RMH and ZS. DCSB and JB set up and operated the main instrumental measurements, and JB prepared all figures alongside the first draft of the paper and responded to comments from RMH, ZS and referees. CNH and WJFA contributed the hydrocarbon data and provided comments on the draft paper, and FAS and JL contributed the gas-phase pollutant data. R code to produce CS values was provided by DCSB.

Atmos. Chem. Phys., 19, 14933–14947, 2019
https://doi.org/10.5194/acp-19-14933-2019

Atmospheric Chemistry and Physics
Open Access
EGU

Observations of highly oxidized molecules and particle nucleation in the atmosphere of Beijing

James Brean[1], Roy M. Harrison[1,a], Zongbo Shi[1], David C. S. Beddows[1], W. Joe F. Acton[2], C. Nicholas Hewitt[2], Freya A. Squires[3], and James Lee[3]

[1]Division of Environmental Health and Risk Management, School of Geography, Earth and Environmental Sciences, University of Birmingham, Edgbaston, Birmingham B15 2TT, UK
[2]Lancaster Environment Centre, Lancaster University, Lancaster LA1 4YQ, UK
[3]National Centre for Atmospheric Science, Wolfson Atmospheric Chemistry Laboratories, University of York, York YO10 5DD, UK
[a]also at: Department of Environmental Sciences/Center of Excellence in Environmental Studies, King Abdulaziz University, P.O. Box 80203, Jeddah, 21589, Saudi Arabia

Correspondence: Roy M. Harrison (r.m.harrison@bham.ac.uk)

Received: 14 February 2019 – Discussion started: 27 March 2019
Revised: 15 October 2019 – Accepted: 29 October 2019 – Published: 10 December 2019

Abstract. Particle nucleation is one of the main sources of atmospheric particulate matter by number, with new particles having great relevance for human health and climate. Highly oxidized multifunctional organic molecules (HOMs) have been recently identified as key constituents in the growth and, sometimes, in initial formation of new particles. While there have been many studies of HOMs in atmospheric chambers, flow tubes, and clean environments, analyses of data from polluted environments are scarce. Here, measurements of HOMs and particle size distributions down to small molecular clusters are presented alongside volatile organic compounds (VOCs) and trace-gas data from a campaign in June 2017, in Beijing. Many gas-phase HOMs have been characterized and their temporal trends and behaviours analysed in the context of new particle formation. The HOMs identified have a degree of oxidation comparable to that seen in other, cleaner, environments, likely due to an interplay between the higher temperatures facilitating rapid hydrogen abstractions and the higher concentrations of NO_x and other $RO_2^{\bullet}$ terminators ending the autoxidation sequence more rapidly. Our data indicate that alkylbenzenes, monoterpenes, and isoprene are important precursor VOCs for HOMs in Beijing. Many of the C_5 and C_{10} compounds derived from isoprene and monoterpenes have a slightly greater degree of average oxidation state of carbon compared to those from other precursors. Most HOMs except for large dimers have daytime peak concentrations, indicating the importance of $OH^{\bullet}$ chemistry in the formation of HOMs, as O_3 tends to be lower on days with higher HOM concentrations; similarly, VOC concentrations are lower on the days with higher HOM concentrations. The daytime peaks of HOMs coincide with the growth of freshly formed new particles, and their initial formation coincides with the peak in sulfuric acid vapours, suggesting that the nucleation process is sulfuric-acid-dependent, with HOMs contributing to subsequent particle growth.

1 Introduction

Atmospheric particle nucleation, or the formation of solid or liquid particles from vapour-phase precursors, is one of the dominant sources of global aerosol by number, with primary emissions typically dominating the mass loadings (Tomasi et al., 2017). New particle formation (NPF) or the secondary formation of fresh particles is a two-step process comprising initial homogeneous nucleation of thermodynamically stable clusters and their subsequent growth. The rate of growth needs be fast enough to outcompete the loss of these particles by coagulation and condensation processes in order for the new particles to grow, and hence NPF is a function of the competition between source and sink (Gong et al., 2010). New particle formation has been shown to occur across a

wide range of environments (Kulmala et al., 2005). The high particle load in urban environments was thought to suppress new particle formation until measurements in the early 2000s (McMurry et al., 2000; Shi et al., 2001; Alam et al., 2003), with frequent occurrences observed even in the most polluted urban centres. NPF events in Beijing occur on about 40 % of days annually, with the highest rates in the spring (Wu et al., 2007, 2008; Wang et al., 2016). Chu et al. (2019) review many studies of NPF which have taken place in China and highlight the need for long-term observations and mechanistic studies.

NPF can lead to the production of cloud condensation nuclei (CCN) (Wiedensohler et al., 2009; Yu and Luo, 2009; Yue et al., 2011; Kerminen et al., 2012), which influences the radiative atmospheric forcing (Penner et al., 2011). A high particle count, such as that caused by nucleation events, has been shown to precede haze events in environments such as Beijing (Guo et al., 2014). These events are detrimental to health and quality of life. The sub-100 nm fraction of particles to which new particle formation contributes is often referred to as the ultrafine fraction. Ultrafine particles (UFPs) pose risks to human health due to their high number concentration. UFPs exhibit gas-like behaviour and enter all parts of the lung before penetrating the bloodstream (Miller et al., 2017). They can initiate inflammation via oxidative stress responses, progressing conditions such as atherosclerosis and initiating cardiovascular responses such as hypertension and myocardial infarction (Delfino et al., 2005; Brook et al., 2010).

Highly oxidized multifunctional molecules (HOMs), organic molecules with O : C ratios > 0.6, are the result of atmospheric autoxidation and have recently been subject to much investigation, in part because the extremely low volatilities arising from their high O : C ratios favour their condensation into the particulate phase. HOMs are most well characterized as the product of oxidation of the biogenic monoterpenoid compound α-pinene (Riccobono et al., 2014; Tröstl et al., 2016; Bianchi et al., 2017). Although globally biogenic volatile organic compound (BVOC) concentrations far exceed anthropogenic volatile organic compound (AVOC) concentrations, in the urban environment the anthropogenic fraction is far more significant. Formation of HOMs from aromatic compounds has been demonstrated in laboratory studies and these have been hypothesized to be large drivers of NPF in urban environments (Wang et al., 2017; Molteni et al., 2018; Qi et al., 2018). The formation of HOMs through autoxidation processes begins with the reaction of VOCs with $OH^{\bullet}$, O_3, or $NO_3^{\bullet}$; formation of a peroxy radical ($RO_2^{\bullet}$) is followed by rapid O_2 additions and intramolecular hydrogen abstractions (Jokinen et al., 2014; Rissanen et al., 2014; Kurtén et al., 2015). Furthermore, generation of oligomers from stabilized Criegee intermediates arising from short-chain alkenes has been hypothesized as a contributor of extremely low-volatility organic compounds (ELVOCs) and low-volatility organic compounds (LVOCs) (Zhao et al., 2015). The low volatilities of these molecules arise from their numerous oxygen-containing functionalities, and this allows them to make a significant contribution to early stage particle growth where other species cannot due to the Kelvin effect (Tröstl et al., 2016), although the contribution of HOMs to the initial molecular clusters is still debated (Kurtén et al., 2016; Elm et al., 2017; Myllys et al., 2017).

Recent technological advances have facilitated insights into the very first steps of nucleation, which were previously unseen, with mass spectrometric techniques such as the atmospheric-pressure-interface time-of-flight mass spectrometer (APi-ToF-MS) and its chemical ionization counterpart (CI-APi-ToF-MS) allowing for high-mass and high-time-resolution measurements of low-volatility compounds and molecular clusters. Diethylene glycol-based particle counters, such as the particle size magnifier (PSM), allow for measurements of particle size distributions down to the smallest molecular clusters nearing 1 nm. Recent chamber studies have elucidated the contribution of individual species to particle nucleation, ammonia, and amines, greatly enhancing the rate of sulfuric acid nucleation (Kirkby et al., 2011; Almeida et al., 2013). In these studies, HOMs have been identified, formed through autoxidation mechanisms (Schobesberger et al., 2013; Riccobono et al., 2014; Ehn et al., 2014). These are key to early particle growth (Tröstl et al., 2016) and can nucleate even in the absence of sulfuric acid in chambers (Kirkby et al., 2016) and in the free troposphere (Rose et al., 2018). In this paper, we report the results of HOM and particle size measurements during a summer campaign in Beijing, China.

2 Data and methods

2.1 Sampling site

Sampling was performed as part of the Air Pollution and Human Health in a Developing Megacity (APHH-Beijing) campaign, a large international collaborative project examining emissions, processes, and health effects of air pollution. For a comprehensive overview of the programme, see Shi et al. (2019). All sampling was conducted across a 1-month period at the Institute for Atmospheric Physics (IAP), Chinese Academy of Sciences, Beijing (39°58.53′ N, 116°22.69′ E). The sampling was conducted from a shipping container, with sampling inlets 1–2 m above ground level, the nearest road being 30 m away. Meteorological parameters (wind speed, wind direction, relative humidity (RH), and temperature) were measured at the IAP meteorological tower, 20 m away from the sampling site, 30 m from the nearest road at a height of 120 m. Data were continuously taken from the CI-APi-ToF-MS during a 2-week period, but due to data losses only 5 d of data are presented here. Particle size distribution measurements were taken during a 33 d period from 24 May to 26 June 2017.

2.2 Chemical ionization atmospheric-pressure-interface time-of-flight mass spectrometry

The Aerodyne nitrate chemical ionization atmospheric-pressure-interface time-of-flight mass spectrometer (CI-APi-ToF-MS) was used to make measurements of neutral oxidized organic compounds, sulfuric acid, and their molecular clusters at high time resolution with high resolving power. The ionization system charges molecules by adduct formation, such as in the case of organic compounds with two or more hydrogen bond donor groups (Hyttinen et al., 2015), or proton transfer in the case of strong acids like sulfuric acid. Hydroxyl or hydroperoxyl functionalities are both common hydrogen-bond-donating groups, with hydroperoxyl being the more efficient hydrogen bond donor (Møller et al., 2017). This instrument has been explained in great detail elsewhere (Junninen et al., 2010; Jokinen et al., 2012), but briefly the front end consists of a chemical ionization system where a $10\,\mathrm{L\,min^{-1}}$ sample flow is drawn in through the 1 m long 1 in. OD stainless-steel tubing opening. A secondary flow was run parallel and concentric to this sample flow, rendering the reaction chamber effectively wall-less. A $3\,\mathrm{cm^3\,min^{-1}}$ flow of a carrier gas (N_2) is passed over a reservoir of liquid HNO_3, entraining vapour, which is subsequently ionized to NO_3^- via an X-ray source. This flow is then guided into the sample flow. The nitrate ions will then charge molecules by either clustering or proton transfer. The mixed flows travelling at $10\,\mathrm{L\,min^{-1}}$ enter the critical orifice at the front end of the instrument at $0.8\,\mathrm{L\,min^{-1}}$ and are guided through a series of differentially pumped chambers before reaching the ToF analyser. Two of these chambers contain quadrupoles, which can be used to select greater sensitivity for certain mass ranges, and the voltages across each individual chamber can be tuned to maximize sensitivity and resolution for ions of interest. Mass spectra are taken at a frequency of 20 kHz but are recorded at a rate of 1 Hz. All data analysis was carried out in the Tofware package in Igor Pro 6 (Tofwerk AG, Switzerland). A seven-point mass calibration was performed for every minute of data, and all data were normalized to signal at 62, 80, and 125 m/Q to account for fluctuations in ion signal, these masses representing NO_3^-, $H_2ONO_3^-$, and $HNO_3NO_3^-$ respectively. Typical values for calibration coefficients range from 10^9 to $10^{10}\,\mathrm{molec.\,cm^{-3}}$ from these normalized data (Kürten et al., 2012), producing peak sulfuric acid concentrations in the range of $10^6\,\mathrm{molec.\,cm^{-3}}$. From the very limited periods with simultaneous data for SO_2, OH radical, and condensation sink, it was possible to calculate H_2SO_4 concentrations of 10^3 to $10^5\,\mathrm{molec.\,cm^{-3}}$, in which range the calibration constant was $7.0\pm1.6\times10^8\,\mathrm{cm^{-3}}$, which fits well with that expected for this concentration range (Kürten et al., 2012). The nitrate–water cluster is included as the presence of many nitrate–water clusters of the general formula $(H_2O)_x(HNO_3)_yNO_3^-$ were found, where $x = (1, 2, 3, \ldots 20)$ and $y = (0, 1)$. No sensitivity calibration was performed for these measurements, and so all values are reported in normalized signal intensity. Due to the high resolving power of the CI-APi-ToF-MS system (mass resolving power of 3500 $m/\Delta m$ and mass accuracy of 20 ppm at 288 m/Q; resolving power is measured as the mass/charge, termed m divided by the peak width at its half maximum, dubbed Δm), multiple peaks can be fit at the same unit mass and their molecular formulae assigned. These peaks follow the general formula $C_xH_yO_zN_w$, where $x = 2$–20, $y = 2$–32, $z = 4$–16, and $w = 0$–2, spanning from small organic acids like oxalic and malonic acid through to large dimers of oxidized monoterpene $RO_2^\bullet$ radicals such as $C_{20}H_{31}O_9N$. Beyond 500 m/Q, peak fitting and assignment of compositions becomes problematic as signal decreases, mass accuracy decreases, and the total number of chemical compositions increases, so peaks above the C_{20} region have not been assigned, and a number of peaks have been unassigned due to this uncertainty (Cubison and Jimenez, 2015). As proton transfer mostly happens with acids, and nearly all HOM molecules will be charged by adduct formation, it is possible to infer the uncharged formula; therefore all HOMs from here onwards will be listed as their uncharged form.

2.3 Size distribution measurements

Two scanning mobility particle sizer (SMPS) instruments measured particle size distributions at 15 min time resolution, with one long SMPS (TSI 3080 EC, 3082 long DMA, 3775 CPC, TSI, USA) and one nano SMPS (3082 EC, 3082 nano DMA, 3776 CPC, TSI, USA) measuring the ranges 14–615 and 4–65 nm respectively. A particle size magnifier (A10, Airmodus, FN) linked to a CPC (3775, TSI, USA) measured the sub-3 nm size fraction. The PSM was run in stepping mode, operating at four different saturator flows to vary the lowest size cut-off of particles that it will grow (this cut-off is technically a point of 50 % detection efficiency) of < 1.30, 1.36, 1.67, and 2.01 nm. The instrument switched between saturator flows per 2.5 min, giving a sub-2.01 nm size distribution every 10 min. The data were treated with a moving-average filter to account for jumps in total particle count, and due to the similar behaviour of the two upper and two lower size cuts, these have been averaged to two size cuts at 1.30 and 1.84 nm.

2.4 Calculations

The condensation sink (CS) was calculated from the size distribution data as follows:

$$\mathrm{CS} = 4\pi D \sum_{d'_\mathrm{p}} \beta_{m,d'_\mathrm{p}} d'_\mathrm{p} N_{d'_\mathrm{p}}, \quad (1)$$

where D is the diffusion coefficient of the diffusing vapour (assumed sulfuric acid), β_m is a transition regime correction (Kulmala et al., 2012), d'_p is particle diameter, and $N_{d'_\mathrm{p}}$ is the number of particles at diameter d'_p.

2.5 Other measurements

Measurements of the classical air pollutants were measured at the same site and have been reported in the campaign overview paper (Shi et al., 2019). SO_2 was measured using a 43i SO_2 analyser (Thermo Fisher Scientific, USA), O_3 with a 49i O_3 analyser (Thermo Fisher Scientific, USA), and NO_x with a 42i-TL trace NO_x analyser (Thermo Fisher Scientific, USA) and a T500U CAPS NO_2 analyser (Teledyne API, USA). VOC mixing ratios were measured using a proton-transfer-reaction time-of-flight mass spectrometer (PTR-ToF-MS 2000, Ionicon, Austria).

3 Results and discussion

3.1 Characteristics of sampling period

A total of 5 d of CI-API-ToF-MS data were collected successfully, from 21 June 2017 midday through 26 June 2017 midday. New particle formation events were observed on 24 June in the late afternoon and 25 June at midday. Some nighttime formation of molecular clusters was seen earlier in the campaign, as were several peaks in the 1.5–100 nm size range, likely from pollutant plumes containing freshly nucleating condensable materials. The trace gases, O_3, SO_2, NO, and NO_2, are plotted in Fig. S1 in the Supplement. O_3 shows mid-afternoon peaks, around $\sim$ 120 ppb on the first 2 d of the campaign and 50–70 ppb for the later days. SO_2 shows a large peak, reaching 4 ppb on 22 June but $<$ 1 ppb for the rest of campaign. NO shows strong mid-morning rush-hour-related peaks, declining towards midday due to being rapidly consumed by O_3. NO_2 shows large traffic-related peaks. The sulfuric acid signal across this period as measured by NO_3^- CI-APi-ToF-MS showed strong midday peaks, with the highest signal on 24 and 25 June 2017. The meteorological data are shown in Fig. S2 alongside condensation sink (CS). The conditions were generally warm and humid, with temperature reaching its maximum on 25 June 2017, with a peak hourly temperature of 31 °C. High temperatures were also seen on 21 and 24 June, 30 and 26 °C respectively.

3.2 Gas-phase HOM chemistry

3.2.1 Bulk chemical properties

For the peaks that have had chemical formulae assigned, oxidation state of carbon, or OS_c, can be used to describe their bulk oxidation chemistry. OS_c is defined as (Kroll et al., 2011)

$$OS_c = (2 \times O : C) - H : C. \quad (2)$$

This does not account for the presence of nitrate ester groups, which has been accounted for previously by subtracting 5 times the N : C ratio (Massoli et al., 2018), under the assumption that all nitrogen-containing functionality is in the form of nitrate ester ($RONO_2$) groups. In Beijing, multiple sources of nitrate-containing organic compounds are seen, in the forms of amines, nitriles, and heterocycles. The variation in oxidation state with carbon number (C_n) without correction for nitrate esters is plotted in Fig. 1. The average oxidation state of carbon in this dataset tends to decrease with an increase in C_n, highest where $C_n = 5$, attributable to both high O : C and peak area, for the peak assigned to $C_5H_{10}N_2O_8$ at m/Q 288. $C_n = 5$ also shows the greatest distribution of oxidation states, likely due to the high ambient concentration of isoprene and therefore its many oxidation products being of high enough signal for many well-resolved peaks to be seen in this dataset. It is worth noting that some of the ions plotted here may not form through peroxy radical autoxidation, such as $C_5H_{10}N_2O_8$, which may be a second-generation oxidation product of isoprene under high NO_x (Lee et al., 2016). $C_n = 10$ and 15 also see a small increase in average oxidation number compared to their neighbours. The lower oxidation state of the larger products is likely a function of two things. First and foremost, any autoxidation mechanism must undergo more steps in order for a larger molecule to reach an O : C ratio equivalent to that of a smaller one, and the equivalent O : C ratio is ultimately less likely to be reached before the radical is terminated (Massoli et al., 2018). Secondly, the lower vapour pressures of these larger products will lead to their partitioning into the condensed phase more readily than the smaller; thus they are more rapidly lost (Mutzel et al., 2015).

The degrees of OSc observed here are similar to those seen in other environments such as during the SOAS campaign in 2013 in the southern United States, characterized by low NO/NO_2 and high temperatures, where campaign averages of 0.3 ppb, 0.4–0.5 ppb, and 25 °C respectively were measured, although an additional parameter to account for nitrogen-containing VOCs is included in the calculation (Massoli et al., 2018). The OS_c observed in Beijing is also higher than that seen in the boreal forest environment of Hyytiälä, despite extremely low NO_x concentrations, likely due to low temperature conditions dominating in those conditions (Schobesberger et al., 2013). These degrees of oxidation relatively similar to those seen in other, cleaner environments are likely due to an interplay between the higher temperatures facilitating rapid hydrogen abstractions (Crounse et al., 2013; Quéléver et al., 2019) and the higher concentrations of NO_x, $HO_2^\bullet$, and other $RO_2^\bullet$ molecules terminating the autoxidation sequence more efficiently (Praske et al., 2018; Rissanen, 2018; Garmash et al., 2019).

A mass defect plot is shown in Fig. 2, which shows nominal mass plotted against mass defect for all peaks in this dataset. Mass defect is defined as the ion mass minus integer mass. This is shown for two separate daytime periods, one where nucleation was not occurring and HOM concentrations are lower (10:30–12:00 CST 23 June 2017) and one where nucleation was occurring under high HOM concentrations (10:30–12:00 CST 25 June 2017). The band of

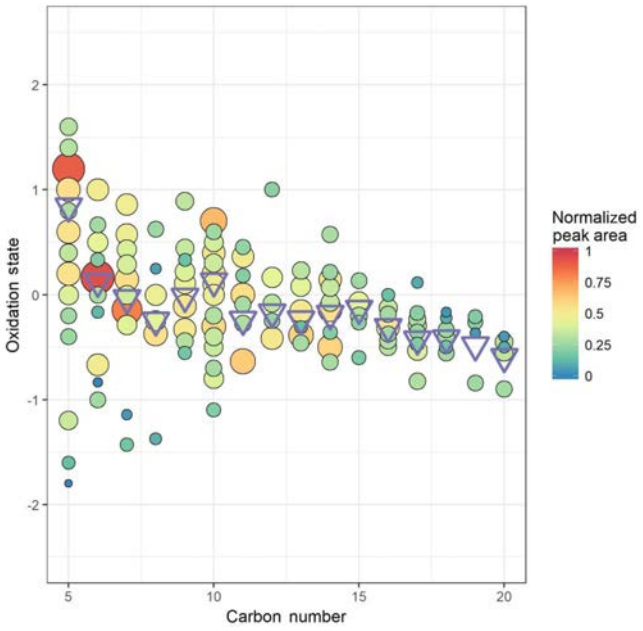

Figure 1. Oxidation state of carbon calculated as 2 times the oxygen-to-carbon ratio minus the hydrogen-to-carbon ratio against carbon number for (coloured) individual ions and (blue circles) signal-weighted average for each carbon number. Area and colour are both proportional to the peak area for each ion.

lower mass defect is characterized by a number of large peaks with high signal, for example, at m/Q 436 the ion $(C_2H_7N)_2(H_2SO_4)_2HSO_4^-$. The upper component of the mass defect is dominated by organic compounds, and the upper end of the more positive mass defect is occupied by molecules with more ^{1}H (mass defect 7.825 mDa) and ^{14}N (mass defect 3.074 mDa). The end of the less positive mass defect has lower ^{1}H and more ^{16}O (mass defect −5.085 mDa); alternatively put, the mass defect reflects the variation in OS_c. The organic components with more positive mass defects will be more volatile than their lower mass defect counterparts as they will contain fewer oxygen functionalities (Tröstl et al., 2016; Stolzenburg et al., 2018). These higher-volatility products may still contribute to larger size particle growth. The more negative mass defect components will be those of greater O : C and therefore lower volatility, LVOCs, and the yet larger and more oxidized components, ELVOCs (Tröstl et al., 2016). During the nucleation period, the signal intensity for the species in the upper band of more negative mass defect have the most marked increase in concentration, with significantly less difference > 500 m/Q. This region 200–400 m/Q will contain most of the $> C_5$ monomer HOMs seen in this dataset.

3.2.2 Diurnal trends of HOMs

Temporal trends of HOMs in the urban atmosphere can reveal their sources and behaviour in the atmosphere. Most of the HOM species peak in the daytime. These species all follow a similar diurnal trend, as shown in Fig. 3. The concentrations of both O_3 and $OH^\bullet$ are high during the summer period in Beijing (although the nitrate chemical ionization technique is not sensitive to all $OH^\bullet$ oxidation products; Berndt et al., 2015). Figure S1 shows the time series of concentrations of NO, which is considered a dominant peroxy radical terminator of particular importance in the polluted urban environment (Khan et al., 2015). Radicals such as $HO_2^\bullet$ and $RO_2^\bullet$ also typically peak during daytime. The HOM components peaking in the daytime are presumed to be the oxidation products of a mixture of anthropogenic and biogenic components, such as alkylbenzenes, monoterpenes, and isoprene. The oxidation of monoterpenes, specifically the monoterpene α-pinene, has been the subject of extensive study recently, with the O_3-initiated autoxidation sequence being the best characterized (Ehn et al., 2014; Jokinen et al., 2014; Kurtén et al., 2015; Kirkby et al., 2016); ozonolysis of α-pinene opens the ring structure and produces a $RO_2^\bullet$ radical (Kirkby et al., 2016). In the case of aromatics, $OH^\bullet$ addition to the ring and the subsequently formed bicyclic peroxy radical are the basis for the autoxidation of compounds such as xylenes and trimethylbenzenes (Molteni et al., 2018; Wu et al., 2017).

The identified compounds have been roughly separated into several categories, each of these plotted in Fig. 3. Figure 3a shows the separation of components into non-nitrogen-containing HOMs and nitrogen-containing HOMs, or organonitrates (ONs). The ON signal is much higher than that of the HOM, attributable in part to a few ions of high signal, such as the isoprene organonitrate $C_5H_{10}N_2O_8$. A few similar structural formulae are seen ($C_5H_{10}N_2O_6$, $C_5H_{11}NO_6$, $C_5H_{11}NO_7$, etc.), some of which have been identified as important gas-phase oxidation products of isoprene under high-NO_x conditions (Xiong et al., 2015), and their contribution to secondary organic aerosol (SOA) has been explored previously (Lee et al., 2016). A high nitrophenol signal is also seen, $C_6H_5NO_3$. The signal for HOM compounds is less dominated by a few large ions. The prevalence of ON compounds points towards the important role of NO_x as a peroxy radical terminator, with the probability of the $RO_2^\bullet + NO_x$ reaction producing nitrate ester compounds increasing with the size of the $RO_2^\bullet$ molecule (Atkinson et al., 1982). The NO_x concentrations in urban Beijing are approximately a factor of 10 higher than seen at the Hyytiälä station in Finland as reported by Yan et al. (2016), and hence it is expected to be a more significant peroxy radical terminator.

Despite the very large fluxes of anthropogenic organic pollutants in Beijing, biogenic emissions are still an important source of reactive VOCs in the city, with abundant isoprene oxidation products observed (see above), as well as monoter-

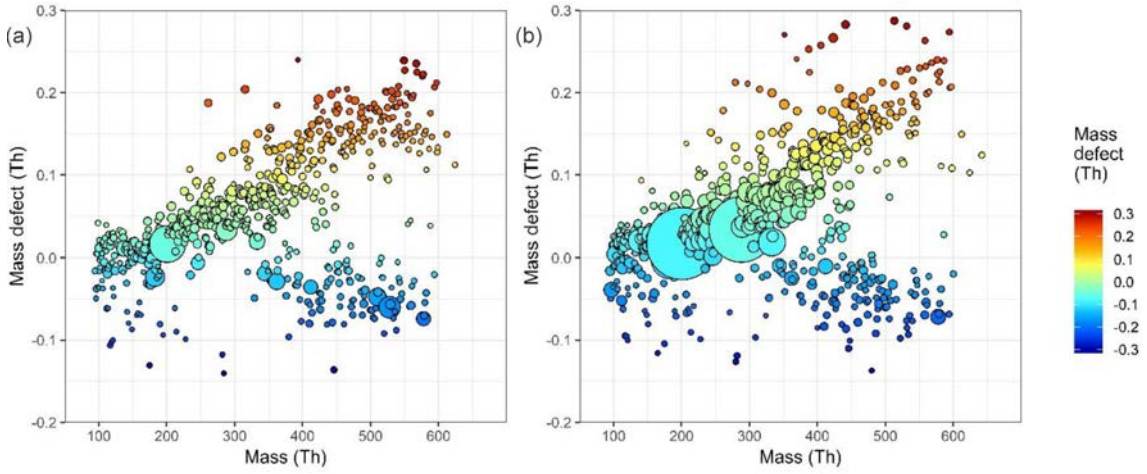

Figure 2. Mass defect plot of fitted mass spectral peaks between 100 and 600 mass units at **(a)** 10:30–12:00 CST on 23 June 2017, a non-nucleation day, and **(b)** at 10:30–12:00 CST on 25 June 2017, a nucleation day. Mass defect can be defined as the mass – integer mass. The size of point is proportional to the signal intensity. As ^{1}H has a positive mass defect (1.007276 Da), the upward trend along the horizontal indicates increasing carbon chain length, and differences at similar masses are due to increasing oxygen functionality and clustering with species such as sulfuric acid (negative mass defect) and ammonia (positive mass defect), as ^{16}O and ^{32}S have negative mass defects (15.9949 and 31.9721 Da respectively), while ^{14}N has a positive mass defect at 14.0031 Da. The two large peaks seen at 201 and 288 m/Q are the nitrophenol–nitrate cluster and a $C_5H_{10}N_2O_8$–nitrate cluster respectively.

pene monomers ($C_{10}H_{16}O_9$, $C_{10}H_{15}O_9N$) and some dimer products ($C_{20}H_{30}O_{11}$, $C_{20}H_{31}O_{11}N$). The time series of the signals of all C_5, C_{10}, and C_{20} molecules is plotted in Fig. 3b, with C_5 species assumed to be isoprene-dominated and C_{10} and C_{20} assumed to be monoterpene-dominated. Signals for isoprene oxidation products are higher, with abundant isoprene nitrate and dinitrate products. C_{10} products show similar behaviour, with, for example, several $C_{10}H_{15}O_xN$ $x = 5$–9 compounds seen. The C_{20} signal intensities are low and follow the general formula $C_{20}H_xO_yN_z$, where $x = 26$–32, $y = 7$–11, and $z = 0$–2; in Fig. 3 the signal for C_{20} compounds has been multiplied by a factor of 50 for visibility. The low signals reflect the lack of $RO_2^{\bullet}$ cross reactions necessary for the production of these accretion products.

Other identified peaks are plotted in Fig. 3c. The C_2–C_4 components are summed together, these being small organic acids such as malonic acid and oxalic acid, as well as products such as $C_4H_7O_6N$. Malonic acid is the most prominent here, seen as both an NO_3^- adduct ($C_3H_4O_4NO_3^-$) and a proton transfer product ($C_3H_3O_4^-$) at a ratio of around 2 : 3. Measurements of particle-phase dicarboxylic acids in cities typically show greater concentrations of oxalic acid than malonic acid (Ho et al., 2010), and these acids are primarily produced in the aqueous phase (Bikkina et al., 2014). Primary sources of dicarboxylic acid include fossil fuel combustion (Kawamura and Kaplan, 1987) and biomass burning (Narukawa et al., 1999), which are both plentiful in urban Beijing. The C_6–C_9 components are assumed to be dominated by oxidation products of alkylbenzenes such as $C_8H_{12}O_5$, although fragments of other compounds, i.e. monoterpenes, can also occupy this region (Isaacman-Vanwertz et al., 2018). It is assumed the majority of the signal for these peaks come from alkylbenzenes. This assumption is supported by the relative signal intensity ratios of the oxygen numbers of monomer $C_8H_{12}O_n$ compounds being similar to those seen for xylene oxidation products in previous work (Molteni et al., 2018). The largest fraction, C_{11} through C_{18}, includes the larger compounds, oxidation products of larger aromatics, or products of the cross reaction of smaller $RO_2^{\bullet}$ radicals. Here they are grouped without more sophisticated disaggregation as they all follow much the same time series, with species such as $C_{11}H_{11}O_8N$ following the same temporal trends as $C_{15}H_{16}O_9$ and $C_{16}H_{24}O_{12}$.

Nearly all ions with the exception of the larger compounds attributed to the cross reaction of C_{10} monomers follow similar temporal patterns, with the majority of peaks occurring in the daytime. This reflects the importance of the concentration of atmospheric oxidants. Some selected oxidation products are plotted against their precursor VOCs in Fig. 4. The concentration of isoprene is plotted against the signal of a nitrate HOM product, $C_5H_9NO_6$ (Xiong et al., 2015; Lee et al., 2016), while monoterpenes are plotted against $C_{10}H_{16}O_9$ (Ehn et al., 2014; Berndt et al., 2016; Yan et al., 2016; Kirkby et al., 2016; Massoli et al., 2018) and C_2 benzenes against $C_8H_{12}O_6$ (Molteni et al., 2018; Wang et al., 2017). The first half of the time series shows little correlation between the VOC species and the resultant oxidation products, while isoprene, monoterpenes, and C_2 benzenes follow their usual diurnal cycles, with isoprene having the most distinct cycle with a strong midday peak. The last 2 d, however, show sim-

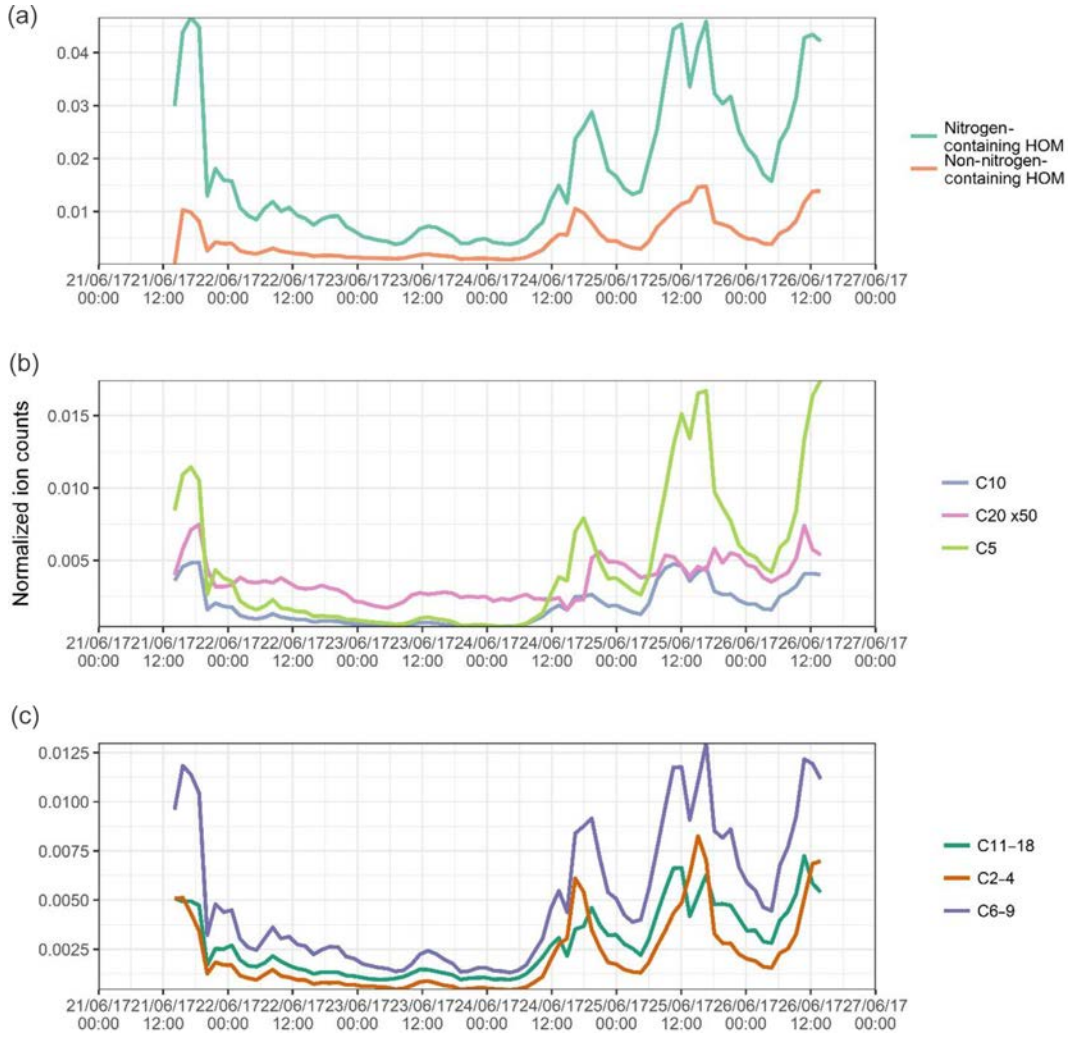

Figure 3. Summed time series of the normalized signals of **(a)** all non-nitrogen-containing HOMs and all organonitrates identified; **(b)** C_5, C_{10}, and C_{20} components, assumed to be dominated by isoprene, monoterpene monomer, and monoterpene dimers, and signal for C_{20} multiplied 50 times to fit scale; and **(c)** summed C_6–C_9 components and summed C_{11}–C_{18} components, assumed to be dominated by alkylbenzenes and other larger components respectively.

ilar and coinciding peaks in both the VOCs and HOMs – HOMs show afternoon peaks on both days and an initial shelf on the final half day. The $C_5H_9NO_6$ peak follows some of the peaks of the isoprene, but not all (e.g. morning shelf of isoprene on 24 June). Concentrations of isoprene do not seem to determine directly the signal of HOM, as the day with the lowest isoprene of all is the day with the highest $C_5H_9NO_6$. The $C_{10}H_{16}O_9$ trace also has coincidental peaks with the monoterpene trace, including two 4 h separated simultaneous peaks on 25 June. The peaks in the concentrations of C_2 benzenes are nearly synchronous with the peaks in $C_8H_{12}O_6$, for which the data exhibit a strong mid-afternoon peak likely due to the lack of an efficient ozonolysis reaction pathway; the main oxidant of C_2 benzenes is the $OH^{\bullet}$ radical. Trends of both C_3 benzenes and their HOMs are much the same as C_2 benzenes as discussed above, pointing to similar sources and oxidation chemistries. The concentration of precursor VOC is likely a driving force in the identity and quantity of various HOM products, but not the sole determinant, as while there are simultaneous peaks of VOCs and HOMs, both the condensation sink and oxidant concentrations also influence HOM product signals.

The first half of campaign measurements are marked by an episode of low HOM signals. A diurnal cycle still exists but it is weak. The radiation intensity was significantly lower on these prior days than it was on 24 June. No data are available for the final period of measurement. Ozone is higher on the prior measurement days with lower HOM signals (see Fig. S1). Little agreement is seen between VOC concentration and HOM signals on these days. The condensational sinks are roughly similar to those on days of higher HOM concentrations, but temperature and solar radi-

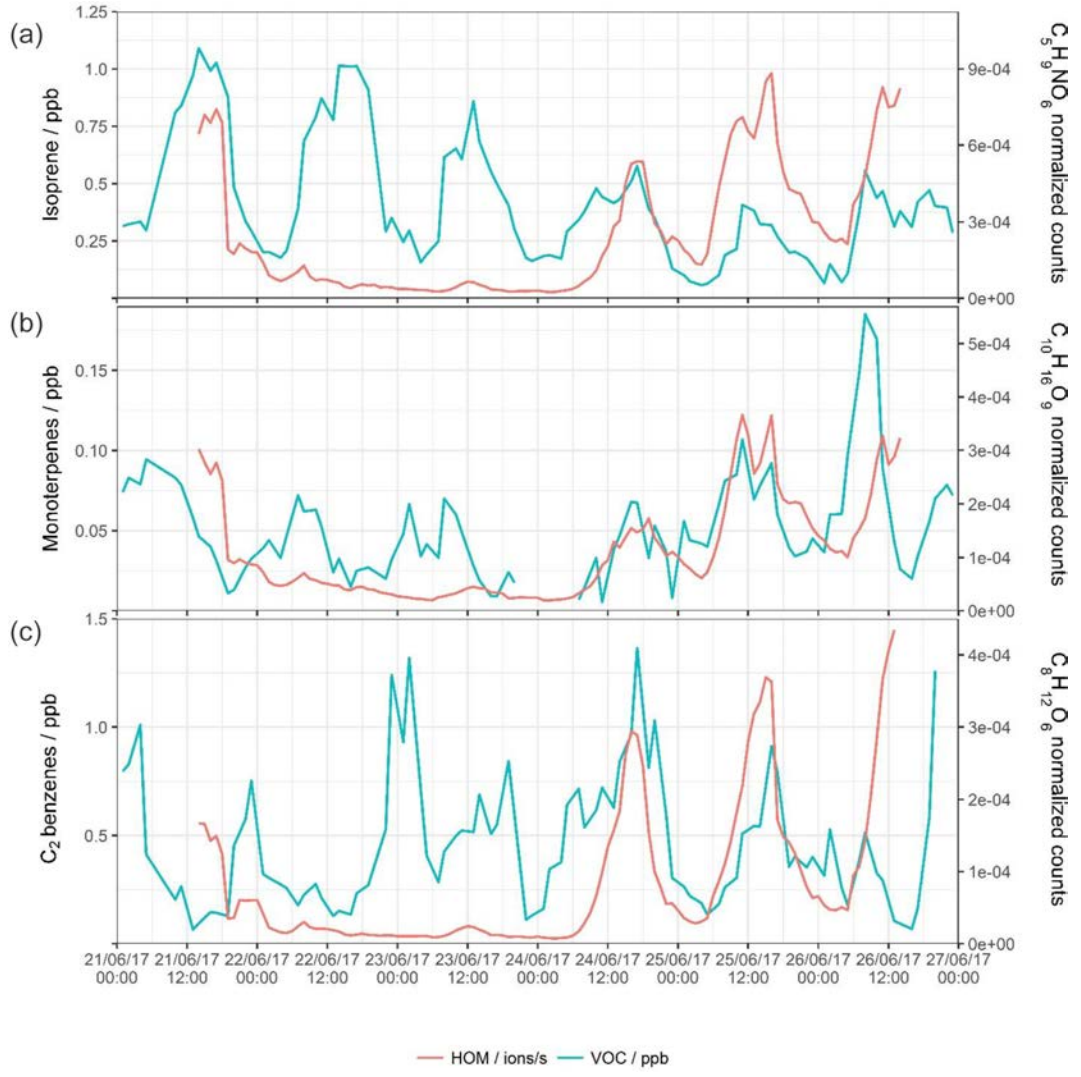

Figure 4. Time series for the whole sampling campaign for the concentrations of (left axis) VOCs as measured by PTR-ToF-MS and (right axis) a selected HOM product associated with that precursor.

ation are much lower. HOM formation is largely dependent upon VOC concentration, oxidant concentration (which will be lower if solar radiation is lower, especially in the case of $OH^{\bullet}$, the main oxidant of aromatic species especially), and temperature (as H shifts are highly temperature-dependent) (Quéléver et al., 2019), as well as losses by $RO_2^{\bullet}$ termination before a molecule can become HOM and losses to condensational sink. The low HOM concentration is likely due to these lower temperatures and weaker solar radiation not facilitating HOM formation.

The C_{20} compounds plotted in Fig. 3b show no strong diurnal sequence, contrasting with other HOMs. We can presume that all C_{20} compounds identified are the result of the reaction of two monoterpenoid C_{10} $RO_2^{\bullet}$ radicals, a reasonable assumption as all identified C_{20} species follow the general formula outlined for these reactions ($C_{20}H_{28-32}O_{6-16}$). The formation of C_{20} dimers is dependent upon two processes, initial oxidation of monoterpenes and RO_2–RO_2 termination. Initial oxidation is contingent upon oxidant concentration, which is highest in the daytime, and $RO_2^{\bullet}$–$RO_2^{\bullet}$ termination is contingent upon the probability of the molecular collision between the $RO_2^{\bullet}$ molecules occurring before other radical termination (i.e. $RO_2^{\bullet}$–NO_x or $RO_2^{\bullet}$–$HO_2^{\bullet}$). There is likely a strong diurnal sequence in the dominant $RO_2^{\bullet}$ termination mechanisms across the daytime period, and the combination of the two factors discussed above results in there being no strong diurnal trend in these molecules. A lower oxidant concentration at night results in fewer $RO_2^{\bullet}$ molecules, but less NO and $HO_2^{\bullet}$ results in a greater chance for those $RO_2^{\bullet}$ molecules to dimerise (Rissanen, 2018; Garmash et al., 2019). As the levels of NO_x in Beijing fall, the peroxy radical termination reactions will be less probable

compared to continued autoxidation (Praske et al., 2018), and it is expected that more oxidized HOM products will be seen with lower volatilities and therefore a greater potential contribution to earlier stage particle formation and growth.

3.3 New particle formation

Nearly all the signal intensity in the CI-APi-ToF-MS instrument arises from molecules charged by NO_3^-; therefore plotting the unit mass resolution data (the data gained by integrating over the entire area at each m/Q integer) against time simply describes the evolution of oxidized organic molecules, acids, and their molecular clusters with both each other and stabilizing amine species. This is done in Fig. 5. As the signal intensity varies by factors of 10 from mass to mass, each value has been normalized so they have maxima at 1. This has been done separately for 2 d for clarity, as the signal intensity also varies from day to day. PSM data for these 2 d is also plotted in Fig. 5, with both total particle count > 1.30 nm in black and the number difference between the lower and upper size cuts (1.30 and 1.84 nm) in blue, which shows the number of particles between these sizes. The relationship between mass and electrical mobility diameter can be defined thus (Tammet, 1995)

$$d_e = \left(\frac{6m}{\pi\rho}\right)^{\frac{1}{3}} + d_g, \quad (3)$$

where d_e is the electrical mobility diameter of the cluster or particle, m is the mass of the cluster or particle expressed in kilogrammes, ρ is the density, and d_g is the effective gas diameter, determined to be 0.3 nm for smaller particles (Larriba et al., 2011). We can use this to draw a comparison between the PSM and CI-APi-ToF-MS measurements. If a density of $1.2\,g\,cm^{-3}$ is assumed, then once molecular clusters reach the > 400 m/Q range, they will be seen in the lowest size cut of the PSM, or > 700 m/Q if a density of $2.0\,g\,cm^{-3}$ is assumed. A full table of densities is provided in the Supplement.

A burst in the signal seen by the CI-APi-ToF-MS occurs first in the late morning in Fig. 5a, and this is at the same time as peaks begin to rise in the identified HOMs (see Fig. 3). Here, the PSM is not available due to an instrumental fault until 16:00 CST; however, at that point, an elevation to particle count and a large elevation to cluster count can be seen. Moving into the evening period, the mass contour shows peaks in larger masses > 400 m/Q. These are likely dimerized compounds and products of $NO_3^{\bullet}$ chemistry with little contribution to newly forming particles but still sensitive to chemical ionization by NO_3^-. Many of these peaks cannot be assigned due to uncertainties in the structural formula assignment for higher mass peaks, as the number of possible dimerized compounds is many, being the combination of most possible RO_2 radicals. Graphically, these are over-represented in Fig. 5 due to the normalization, and their signals (especially > 500 m/Q) are much lower than the signals < 400 m/Q.

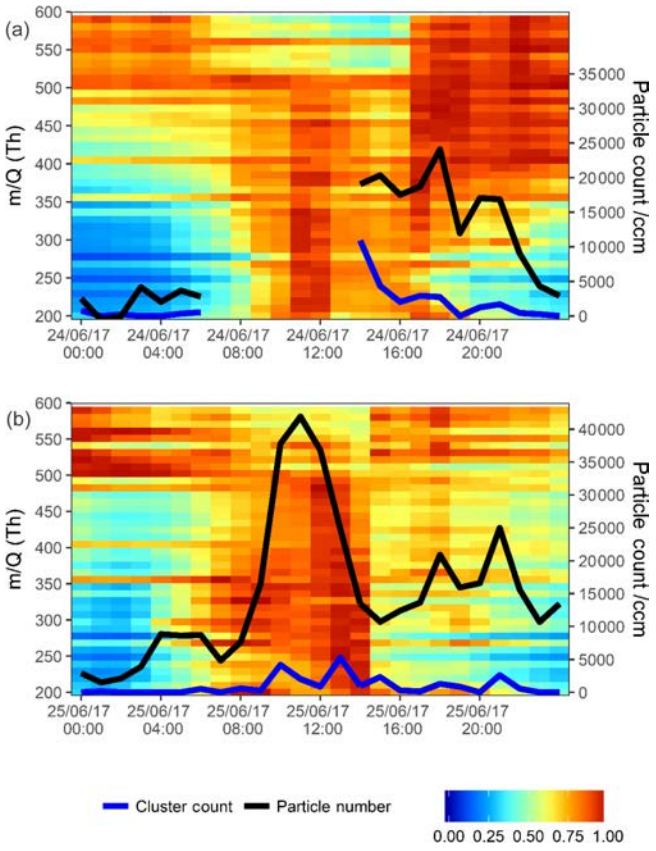

Figure 5. Normalized unit mass NO_3^- CI-APi-ToF-MS signal intensity on 24 June 2017 **(a)** and 25 June 2017 **(b)**. Each individual unit mass was normalized to a maximum of 1. Each period is normalized separately so the individual signal maxima on each day are visible. The graph is plotted between 200 and 600 mass units, with every 10 mass units averaged for simplicity. On the secondary axis PSM data are plotted, both total particle count > 1.30 nm (black trace) and total clusters between 1.30 and 1.84 nm (blue trace). Data are plotted at 1 h time resolution.

The second day plotted in Fig. 5b (25 June 2017) shows a strong afternoon peak to the HOMs (for most HOMs, stronger than that on the day prior). Particle formation is shown in the PSM data. A strong midday peak to particle number is seen with two distinct peaks in cluster count. These two peaks are not coincidental with the two peaks in HOM signal (i.e. nitrogen-containing HOMs in Fig. 3a peaking at 11:00 and 16:00 CST). Sulfuric acid, however, does peak synchronously with the particle number count. Sulfuric acid is plotted across the contour plot in Fig. 6, where PSM data are also shown in the bottom panel. The peak in CI-APi-ToF-MS mass signal, visible in Fig. 5, occurs at around 12:00–13:00 CST; peaks in the PSM cluster count occur at 10:00 and 13:00 CST. Peaks in mass up to 550 m/Q are seen in the CI-APi-ToF-MS at 13:00 CST. Assuming the density of these species is $\leq 1.6\,g\,cm^{-3}$, then these will be suitably sized to be grown in the PSM saturator. These newly formed

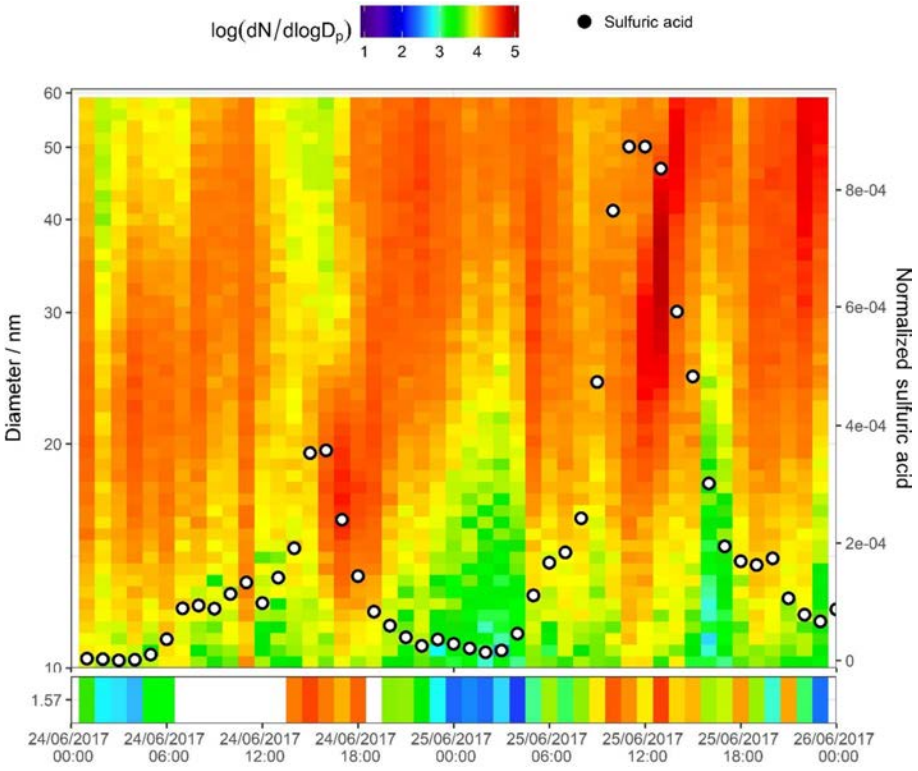

Figure 6. SMPS + PSM contour plot for two nucleation days on 24 and 25 June 2017. Data in the bottom panel are from the PSM instrument, and the top panel from the nano SMPS; units in the colour bar are $\log_{10}$ ($\mathrm{d}N/\log D_\mathrm{p}$) for N in reciprocal cubic centimetres. Points signify normalized sulfuric acid concentration (right axis) as measured by CI-APi-ToF-MS.

particles then go on to grow and contribute significantly to the larger particle count (Fig. S3). As initial particle formation coincides with sulfuric acid signal peaks and before HOM signals peak, it can be assumed on these days that the HOM contribution to the initial particle formation is modest.

There is recent strong evidence to suggest that the driving force of the earliest stages of particle formation in urban Shanghai is sulfuric acid and C_2 amines (Yao et al., 2018), and the coincidental peaks of sulfuric acid with new particles as seen in Fig. 6 suggest a similar behaviour. Dimethylamine (DMA) can efficiently stabilize the sulfuric acid clusters (Almeida et al., 2013). Here, few larger sulfuric acid–DMA clusters were visible in the dataset, as seen in the work by Yao et al. (2018). Although five sulfuric acid–dimethylamine (SA–DMA) ions were observed, the others were likely too low in signal to be confidently resolved from their neighbouring peaks; however, clusters of up to four sulfuric acid molecules and three dimethylamine molecules were seen, with similar diurnal trends in sulfuric acid. The scarcity of SA–DMA clusters is likely due to instrumental conditions, rather than their absence in the atmosphere. The nitrate chemical ionization system tends to evaporate amine compounds upon charging, and as specific voltage-tuning setups can lend themselves towards preservation or breakage of molecular clusters, the signal for larger sulfuric acid clusters was also very weak. The formation of HOM–sulfuric acid clusters is unlikely under atmospheric conditions (Elm et al., 2017) and few of these were observed. Signals of HOMs seem to coincide with later particle growth; it can be expected that HOM molecules make a more significant contribution to particle growth than to early particle formation, with the largest and most oxidized being involved in early growth and the smaller and less oxidized contributing to later growth as the necessary vapour pressure properties become less demanding.

4 Conclusions

The average degree of HOM oxidation in Beijing is comparable with that seen in other environments. Rapid intramolecular hydrogen shifts during autoxidation due to the higher temperatures are probably offset by the frequent termination reactions due to high NO_x concentrations. OS_c values seem to be marginally higher for biogenic species.

The temporal trend of nearly every HOM shows afternoon or evening maxima. Both O_3 and $OH^\bullet$ have high daytime concentrations, and these likely drive the initial oxidation steps. The species arising from alkylbenzene precursors show sharper afternoon peaks, probably since their oxidation

is $OH^{\bullet}$-dominated. Many of the rest of the peaks, coming from largely BVOC precursors, show broader daytime peaks, being influenced by O_3 also. There seems to be no direct link between VOC concentrations and HOM signals, with days of lower precursor VOC sometimes having higher HOM signals and vice versa.

Initial particle formation coincides with peak sulfuric acid signals, while the growth of the particles correlates more closely with the signals of HOMs. This is very similar to behaviour observed in a study of NPF in Shanghai which was attributed to sulfuric acid–dimethylamine–water nucleation with condensing organic species contributing to particle growth (Yao et al., 2018), and this is further backed up by numerous SA–DMA clusters present in this dataset. The freshly formed particles grow and contribute significantly to total particle loading. This is visible when the unit mass CI-APi-ToF-MS data are plotted as a contour plot, and further this is visible in the PSM data, with bursts in both total number count > 1.30 nm and the number of molecular clusters between 1.30 and 1.84 nm. As NO_x levels fall in Beijing due to traffic emission control measures being enforced, it is likely that autoxidation will become increasingly significant in the new particle formation processes. The number of molecules detected by the NO_3^- CI-APi-ToF-MS is undoubtedly many more than have had formulae assigned here, but to identify more requires a more sophisticated data deconvolution.

Data availability. Data supporting this publication are openly available from the UBIRA eData repository at https://doi.org/10.25500/edata.bham.00000304 (Brean and Harrison, 2019).

Supplement. The supplement related to this article is available online at: https://doi.org/10.5194/acp-19-14933-2019-supplement.

Author contributions. The study was conceived and planned by RMH and ZS. DCSB and JB set up and operated the main instrumental measurements, and JB prepared the first draft of the paper and responded to comments from RMH and ZS. CNH and WJFA contributed the hydrocarbon data and provided comments on the draft paper, and FAS and JL contributed the gas-phase pollutant data.

Competing interests. The authors declare that they have no conflict of interest.

Special issue statement. This article is part of the special issue "In-depth study of air pollution sources and processes within Beijing and its surrounding region (APHH-Beijing) (ACP/AMT inter-journal SI)". It is not associated with a conference.

Acknowledgements. This was part of the APHH-Beijing programme funded by the UK Natural Environmental Research Council, the National Centre for Atmospheric Science, and the Natural Sciences Funding Council of China. We thank Xinming Wang from the Guangzhou Institute of Geochemistry, Chinese Academy of Sciences; Brian Davison from Lancaster University; and Ben Langford, Eiko Nemitz, Neil Mullinger, and other staff from the Centre for Ecology and Hydrology, Edinburgh for assistance with the VOC measurements and associated infrastructure.

Financial support. This research has been supported by the Natural Environmental Research Council (grant no. NE/N007190/1) and the Natural Sciences Funding Council of China. It was additionally facilitated by the National Centre for Atmospheric Science ODA national capability programme ACREW (NE/R000034/1), which is supported by NERC and the GCRF.

Review statement. This paper was edited by Kimitaka Kawamura and reviewed by three anonymous referees.

References

Alam, A., Shi, J. P., and Harrison R. M.: Observations of new particle formation in urban air, J. Geophys. Res., 108, 4093–4107, https://doi.org/10.1029/2001JD001417, 2003.

Almeida, J., Schobesberger, S., Kürten, A., Ortega, I. K., Kupiainen-Määttä, O., Praplan, A. P., Adamov, A., Amorim, A., Bianchi, F., Breitenlechner, M., David, A., Dommen, J., Donahue, N. M., Downard, A., Dunne, E., Duplissy, J., Ehrhart, S., Flagan, R. C., Franchin, A., Guida, R., Hakala, J., Hansel, A., Heinritzi, M., Henschel, H., Jokinen, T., Junninen, H., Kajos, M., Kangasluoma, J., Keskinen, H., Kupc, A., Kurtén, T., Kvashin, A. N., Laaksonen, A., Lehtipalo, K., Leiminger, M., Leppä, J., Loukonen, V., Makhmutov, V., Mathot, S., McGrath, M. J., Nieminen, T., Olenius, T., Onnela, A., Petäjä, T., Riccobono, F., Riipinen, I., Rissanen, M., Rondo, L., Ruuskanen, T., Santos, F. D., Sarnela, N., Schallhart, S., Schnitzhofer, R., Seinfeld, J. H., Simon, M., Sipilä, M., Stozhkov, Y., Stratmann, F., Tomé, A., Tröstl, J., Tsagkogeorgas, G., Vaattovaara, P., Viisanen, Y., Virtanen, A., Vrtala, A., Wagner, P. E., Weingartner, E., Wex, H., Williamson, C., Wimmer, D., Ye, P., Yli-Juuti, T., Carslaw, K. S., Kulmala, M., Curtius, J., Baltensperger, U., Worsnop, D. R., Vehkamäki, H., and Kirkby, J.: Molecular understanding of sulphuric acid-amine particle nucleation in the atmosphere, Nature, 502, 359–363, 2013.

Atkinson, R., Aschmann, S. M., Carter, W. P. L., Winer, A. M., and Pitts, J. N.: Alkyl nitrate formation from the nitrogen oxide (NO_x) air photooxidations of C_2–C_8 n-alkanes, J. Phys. Chem., 86, 4563–4569, 1982.

Berndt, T., Richters, S., Kaethner, R., Voigtländer, J., Stratmann, F., Sipilä, M., Kulmala, M., and Herrmann, H.: Gas-Phase Ozonolysis of Cycloalkenes: Formation of Highly Oxidized RO_2 Radicals and Their Reactions with NO, NO_2, SO_2, and Other RO_2 Radicals, J. Phys. Chem. A., 119, 10336–10348, 2015.

Berndt, T., Richters, S., Jokinen, T., Hyttinen, N., Kurtén, T., Otkjær, R. V., Kjaergaard, H. G., Stratmann, F., Herrmann,

H., Sipilä, M., Kulmala, M., and Ehn, M.: Hydroxyl radical-induced formation of highly oxidized organic compounds, Nature Comm., 7, 13677, https://doi.org/10.1038/ncomms13677, 2016.

Bianchi, F., Garmash, O., He, X., Yan, C., Iyer, S., Rosendahl, I., Xu, Z., Rissanen, M. P., Riva, M., Taipale, R., Sarnela, N., Petäjä, T., Worsnop, D. R., Kulmala, M., Ehn, M., and Junninen, H.: The role of highly oxygenated molecules (HOMs) in determining the composition of ambient ions in the boreal forest, Atmos. Chem. Phys., 17, 13819–13831, https://doi.org/10.5194/acp-17-13819-2017, 2017.

Bikkina, S., Kawamura, K., Miyazaki, Y., and Fu, P.: High abundances of oxalic, azelaic, and glyoxylic acids and methylglyoxal in the open ocean with high biological activity: Implication for secondary OA formation from isoprene, Geophys. Res. Lett., 41, 3649–3657, https://doi.org/10.1002/2014GL059913, 2014.

Brean, J. and Harrison, R. M.: HOMS measured by APi-ToF in Beijing, University of Birmingham, https://doi.org/10.25500/edata.bham.00000304, 2019.

Brook, R. D., Rajagopalan, S., Pope, C. A., Brook, J. R., Bhatnagar, A., Diez-Roux, A. V., Holguin, F., Hong, Y., Luepker, R. V., Mittleman, M. A., Peters, A., Siscovick, D., Smith, S. C., Whitsel, L., and Kaufman, J. D.: Particulate matter air pollution and cardiovascular disease: An update to the scientific statement from the american heart association, Circulation, 121, 2331–2378, 2010.

Chu, B., Kerminen, V.-M., Bianchi, F., Yan, C., Petäjä, T., and Kulmala, M.: Atmospheric new particle formation in China, Atmos. Chem. Phys., 19, 115–138, https://doi.org/10.5194/acp-19-115-2019, 2019.

Crounse, J. D., Nielsen, L. B., Jørgensen, S., Kjaergaard, H. G., and Wennberg, P. O.: Autoxidation of organic compounds in the atmosphere, J. Phys. Chem. Lett., 4, 3513–3520, 2013.

Cubison, M. J. and Jimenez, J. L.: Statistical precision of the intensities retrieved from constrained fitting of overlapping peaks in high-resolution mass spectra, Atmos. Meas. Tech., 8, 2333–2345, https://doi.org/10.5194/amt-8-2333-2015, 2015.

Delfino, R. J., Sioutas, C., and Malik, S.: Potential role of ultrafine particles in associations between airborne particle mass and cardiovascular health, Environ. Health Perspect., 113, 934–946, 2005.

Ehn, M., Thornton, J. A., Kleist, E., Sipilä, M., Junninen, H., Pullinen, I., Springer, M., Rubach, F., Tillmann, R., Lee, B., Lopez-Hilfiker, F., Andres, S., Acir, I.-H., Rissanen, M., Jokinen, T., Schobesberger, S., Kangasluoma, J., Kontkanen, J., Nieminen, T., Kurtén, T., Nielsen,L. B., Jørgensen, S., Kjaergaard, H. G., Canagaratna, M., Maso, M. D., Berndt, T., Petäjä, T., Wahner, A., Kerminen, V.-M., Kulmala, M., Worsnop, D. R., Wildt, J., and Mentel, T. F.: A large source of low-volatility secondary organic aerosol, Nature, 506, 476–479, 2014.

Elm, J., Myllys, N., and Kurtén, T.: What is Required for Highly Oxidized Molecules to Form Clusters with Sulfuric Acid?, J. Phys. Chem. A, 121, 4578–4587, 2017.

Garmash, O., Rissanen, M. P., Pullinen, I., Schmitt, S., Kausiala, O., Tillmann, R., Percival, C., Bannan, T. J., Priestley, M., Hallquist, Å. M., Kleist, E., Kiendler-Scharr, A., Hallquist, M., Berndt, T., McFiggans, G., Wildt, J., Mentel, T., and Ehn, M.: Multi-generation OH oxidation as a source for highly oxygenated organic molecules from aromatics, Atmos. Chem. Phys. Discuss., https://doi.org/10.5194/acp-2019-582, in review, 2019.

Gong, Y., Hu, M., Cheng, Y., Su, H., Yue, D., Liu, F., Wiedensohler, A., Wang, Z., Kalesse, H., Liu, S., Wu, Z., Xiao, K., Mi, P., and Zhang, Y.: Competition of coagulation sink and source rate: New particle formation in the Pearl River Delta of China, Atmos. Environ., 44, 3278–3285, 2010.

Guo, S., Hu, M., Zamora, M. L., Peng, J., Shang, D., Zheng, J., Du, Z., Wu, Z., Shao, M., Zeng, L., Molina, M. J., and Zhang, R.: Elucidating severe urban haze formation in China, P. Natl. Acad. Sci. USA, 111, 17373–17378, 2014.

Ho, K. F., Lee, S. C., Ho, S. S. H., Kawamura, K., Tachibana, E., Cheng, Y., and Zhu, T.: Dicarboxylic acids, ketocarboxylic acids, α-dicarbonyls, fatty acids, and benzoic acid in urban aerosols collected during the 2006 Campaign of Air Quality Research in Beijing (CAREBeijing-2006), J. Geophys. Res.-Atmos., 115, D19312, https://doi.org/10.1029/2009JD013304, 2010.

Hyttinen, N., Kupiainen-Määttä, O., Rissanen, M. P., Muuronen, M., Ehn, M., and Kurtén, T.: Modeling the Charging of Highly Oxidized Cyclohexene Ozonolysis Products Using Nitrate-Based Chemical Ionization, J. Phys. Chem., A, 119, 6339–6345, 2015.

Isaacman-Vanwertz, G., Massoli, P., O'Brien, R., Lim, C., Franklin, J. P., Moss, J. A., Hunter, J. F., Nowak, J. B., Canagaratna, M. R., Misztal,P. K., Arata, C., Roscioli, J. R., Herndon, S. T., Onasch, T. B., Lambe, A. T., Jayne, J. T., Su, L., Knopf, D. A., Goldstein, A. H., Worsnop, D. R., and Kroll, J. H.: Chemical evolution of atmospheric organic carbon over multiple generations of oxidation, Nat. Chem., 10, 462–468, https://doi.org/10.1038/s41557-018-0002-2, 2018

Jokinen, T., Sipilä, M., Junninen, H., Ehn, M., Lönn, G., Hakala, J., Petäjä, T., Mauldin III, R. L., Kulmala, M., and Worsnop, D. R.: Atmospheric sulphuric acid and neutral cluster measurements using CI-APi-TOF, Atmos. Chem. Phys., 12, 4117–4125, https://doi.org/10.5194/acp-12-4117-2012, 2012.

Jokinen, T., Sipilä, M., Richters, S., Kerminen, V. M., Paasonen, P., Stratmann, F., Worsnop, D., Kulmala, M., Ehn, M., Herrmann, H., and Berndt, T.: Rapid autoxidation forms highly oxidized RO_2 radicals in the atmosphere, Angew. Chem. Int. Edit., 53, 14596–14600, https://doi.org/10.1002/anie.201408566, 2014.

Junninen, H., Ehn, M., Petäjä, T., Luosujärvi, L., Kotiaho, T., Kostiainen, R., Rohner, U., Gonin, M., Fuhrer, K., Kulmala, M., and Worsnop, D. R.: A high-resolution mass spectrometer to measure atmospheric ion composition, Atmos. Meas. Tech., 3, 1039–1053, https://doi.org/10.5194/amt-3-1039-2010, 2010.

Kawamura, K. and Kaplan, I. R.: Motor Exhaust Emissions as a Primary Source for Dicarboxylic Acids in Los Angeles Ambient Air, Environ. Sci. Technol., 21, 105–110, https://doi.org/10.1021/es00155a014, 1987.

Kerminen, V.-M., Paramonov, M., Anttila, T., Riipinen, I., Fountoukis, C., Korhonen, H., Asmi, E., Laakso, L., Lihavainen, H., Swietlicki, E., Svenningsson, B., Asmi, A., Pandis, S. N., Kulmala, M., and Petäjä, T.: Cloud condensation nuclei production associated with atmospheric nucleation: a synthesis based on existing literature and new results, Atmos. Chem. Phys., 12, 12037–12059, https://doi.org/10.5194/acp-12-12037-2012, 2012.

Khan, M., Cooke M, Utembe, S., Archibald A., Derwent, R., Jenkin, M., Morris, W., South, N., Hansen, J., Francisco, J., Percival, C., and Shallcross, D.: Global analysis of peroxy radicals and peroxy radical-water complexation using the STOCHEM-CRI

global chemistry and transport model, Atmos. Environ., 106, 278–287, 2015.

Kirkby, J., Curtius, J., Almeida, J., Dunne, E., Duplissy, J., Ehrhart, S., Franchin, A., Gagné, S., Ickes, L., Kürten, A., Kupc, A., Metzger, A., Riccobono, F., Rondo, L., Schobesberger, S., Tsagkogeorgas, G., Wimmer, D., Amorim, A., Bianchi, F., Breitenlechner, M., David, A., Dommen, J., Downard, A., Ehn, M., Flagan, R. C., Haider, S., Hansel, A., Hauser, D., Jud, W., Junninen, H., Kreissl, F., Kvashin, A., Laaksonen, A., Lehtipalo, K., Lima, J., Lovejoy, E. R., Makhmutov, V., Mathot, S., Mikkilä, J., Minginette, P., Mogo, S., Nieminen, T., Onnela, A., Pereira, P., Petäjä, T., Schnitzhofer, R., Seinfeld, J. H., Sipilä, M., Stozhkov, Y., Stratmann, F., Tomé, A., Vanhanen, J., Viisanen, Y., Vrtala, A., Wagner, P. E., Walther, H., Weingartner, E., Wex, H., Winkler, P. M., Carslaw, K. S., Worsnop, D. R., Baltensperger, U., and Kulmala, M.: Role of sulphuric acid, ammonia and galactic cosmic rays in atmospheric aerosol nucleation, Nature, 476, 429–435, https://doi.org/10.1038/nature10343, 2011.

Kirkby, J., Duplissy, J., Sengupta, K., Frege, C., Gordon, H., Williamson, C., Heinritzi, M., Simon, M., Yan, C., Almeida, J., Trostl, J., Nieminen, T., Ortega, I. K., Wagner, R., Adamov, A., Amorim, A., Bernhammer, A. K., Bianchi, F., Breitenlechner, M., Brilke, S., Chen, X., Craven, J., Dias, A., Ehrhart, S., Flagan, R. C., Franchin, A., Fuchs, C., Guida, R., Hakala, J., Hoyle, C. R., Jokinen, T., Junninen, H., Kangasluoma, J., Kim, J., Krapf, M., Kurten, A., Laaksonen, A., Lehtipalo, K., Makhmutov, V., Mathot, S., Molteni, U., Onnela, A., Perakyla, O., Piel, F., Petaja, T., Praplan, A. P., Pringle, K., Rap, A., Richards, N. A., Riipinen, I., Rissanen, M. P., Rondo, L., Sarnela, N., Schobesberger, S., Scott, C. E., Seinfeld, J. H., Sipila, M., Steiner, G., Stozhkov, Y., Stratmann, F., Tomé, A., Virtanen, A., Vogel, A. L., Wagner, A. C., Wagner, P. E., Weingartner, E., Wimmer, D., Winkler, P. M., Ye, P., Zhang, X., Hansel, A., Dommen, J., Donahue, N. M., Worsnop, D. R., Baltensperger, U., Kulmala, M., Carslaw, K. S., and Curtius, J.: Ion-induced nucleation of pure biogenic particles, Nature, 533, 521–526, https://doi.org/10.1038/nature17953, 2016.

Kroll, J. H., Donahue, N. M., Jimenez, J. L., Kessler, S. H., Canagaratna, M. R., Wilson, K. R., Altieri, K. E., Mazzoleni, L. R., Wozniak, A. S., Bluhm, H., Mysak, E. R., Smith, J. D., Kolb, C. E., and Worsnop, D. R.: Carbon oxidation state as a metric for describing the chemistry of atmospheric organic aerosol, Nat. Chem., 3, 133–139, https://doi.org/10.1038/nchem.948, 2011.

Kulmala, M., Petäjä, T., Mönkkönen, P., Koponen, I. K., Dal Maso, M., Aalto, P. P., Lehtinen, K. E. J., and Kerminen, V.-M.: On the growth of nucleation mode particles: source rates of condensable vapor in polluted and clean environments, Atmos. Chem. Phys., 5, 409–416, https://doi.org/10.5194/acp-5-409-2005, 2005.

Kulmala, M., Petäjä, T., Nieminen, T., Sipilä, M., Manninen, H. E., Lehtipalo, K., Dal Maso, M., Aalto, P. P., Junninen, H., Paasonen, P.,Riipinen, I., Lehtinen, K. E. J., Laaksonen, A., and Kerminen, V.-M.: Measurement of the nucleation of atmospheric aerosol particles, Nat. Protoc., 7, 1651–1667, https://doi.org/10.1038/nprot.2012.091, 2012.

Kürten, A., Rondo, L., Ehrhart, S., and Curtius, J.: Calibration of a chemical ionization mass spectrometer for the measurement of gaseous sulfuric acid, J. Phys. Chem., A, 116, 6375–6386, 2012.

Kurtén, T., Rissanen, M. P., Mackeprang, K., Thornton, J. A., Hyttinen, N., Jørgensen, S., Ehn, M., and Kjaergaard, H. G.: Computational Study of Hydrogen Shifts and Ring-Opening Mechanisms in α-Pinene Ozonolysis Products, J. Phys. Chem., A, 119, 11366–11375, 2015.

Kurtén, T., Tiusanen, K., Roldin, P., Rissanen, M., Luy, J. N., Boy, M., Ehn, M., and Donahue, N.: α-Pinene autoxidation products may not have extremely low saturation vapor pressures despite high O : C ratios, J. Phys. Chem., A, 120, 2569–2582, 2016.

Larriba, C., Hogan, C. J., Attoui, M., Borrajo, R., Garcia, J. F., and De La Mora, J. F.: The mobility-volume relationship below 3.0 nm examined by tandem mobility-mass measurement, Aerosol Sci. Tech., 45, 453–467, 2011.

Lee, B. H., Mohr, C., Lopez-Hilfiker, F. D., Lutz, A., Hallquist, M., Lee, L., Romer, P., Cohen, R. C., Iyer, S., Kurtén, T., Hu, W., Day, D. A., Campuzano-Jost, P., Jimenez, J. L., Xu, L., Ng, N. L., Guo, H., Weber, R. J., Wild, R. J., Brown, S. S., Koss, A., de Gouw, J., Olson, K., Goldstein, A. H., Seco, R., Kim, S., McAvey, K., Shepson, P. B., Starn, T., Baumann, K., Edgerton, E. S., Liu, J., Shilling, J. E., Miller, D. O., Brune, W., Schobesberger, S., D'Ambro, E. L., and Thornton, J. A.: Highly functionalized organic nitrates in the southeast United States: Contribution to secondary organic aerosol and reactive nitrogen budgets, P. Natl. Acad. Sci. USA, 113, 1516–1521, 2016.

Massoli, P., Stark, H., Canagaratna, M. R., Krechmer, J. E., Xu, L., Ng, N. L., Mauldin, R. L., Yan, C., Kimmel, J., Misztal, P. K., Jimenez, J. L., Jayne, J. T., and Worsnop, D. R.: Ambient Measurements of Highly Oxidized Gas-Phase Molecules during the Southern Oxidant and Aerosol Study (SOAS) 2013, ACS Earth Space Chem., 2, 653–672, 2018.

McMurry, P. H., Shan Woo, K., Weber, R., Chen, D.-R., and Pui, D. Y. H.: Size distributions of 3–10 nm atmospheric particles: implications for nucleation mechanisms, Philos. T. Roy. Soc. A, 358, 2625–2642, 2000.

Miller, M. R., Raftis, J. B., Langrish, J. P., McLean, S. G., Samutrtai, P., Connell, S. P., Wilson, S., Vesey, A. T., Fokkens, P. H., Boere, A. J. F., Krystek, P., Campbell, C. J., Hadoke, P. W., Donaldson, K., Cassee, F. R., Newby, D. E., Duffin, R., and Mills, N. L.: Inhaled nanoparticles accumulate at sites of vascular disease, ACS Nano, 11, 4542–4552, 2017.

Møller, K. H., Tram, C. M., and Kjaergaard, H. G.: Side-by-Side Comparison of Hydroperoxide and Corresponding Alcohol as HydrogenBond Donors, J. Phys. Chem. A, 121, 2951–2959, 2017.

Molteni, U., Bianchi, F., Klein, F., El Haddad, I., Frege, C., Rossi, M. J., Dommen, J., and Baltensperger, U.: Formation of highly oxygenated organic molecules from aromatic compounds, Atmos. Chem. Phys., 18, 1909–1921, https://doi.org/10.5194/acp-18-1909-2018, 2018.

Mutzel, A., Poulain, L., Berndt, T., Iinuma, Y., Rodigast, M., Böge, O., Richters, S., Spindler, G., Sipila, M., Jokinen, T., Kulmala, M., and Herrmann, H.: Highly oxidized multifunctional organic compounds observed in tropospheric particles: A field and laboratory study, Environ. Sci. Technol., 49, 7754–7761, 2015.

Myllys, N., Olenius, T., Kurtén, T., Vehkamäki, H., Riipinen, I., and Elm, J.: Effect of Bisulfate, Ammonia, and Ammonium on the Clustering of Organic Acids and Sulfuric Acid, J. Phys. Chem. A, 121, 4812–4824, 2017.

Narukawa, M., Kawamura, K., Takeuchi, N., and Nakajima, T.: Distribution of dicarboxylic acids and carbon isotopic ratios in

aerosols from 1997 Indonesian forest fires, Geophys. Res. Lett., 26, 3101–3104, 1999.

Penner, J. E., Xu, L., and Wang, M.: Satellite methods underestimate indirect climate forcing by aerosols, P. Natl. Acad. Sci. USA, 108, 13404–13408, 2011.

Praske, E., Otkjær, R. V., Crounse, J. D., Hethcox, J. C., Stoltz, B. M., Kjaergaard, H. G., and Wennberg, P. O.: Atmospheric autoxidation is increasingly important in urban and suburban North America, P. Natl. Acad. Sci. USA, 115, 64–69, 2018.

Qi, X., Ding, A., Roldin, P., Xu, Z., Zhou, P., Sarnela, N., Nie, W., Huang, X., Rusanen, A., Ehn, M., Rissanen, M. P., Petäjä, T., Kulmala, M., and Boy, M.: Modelling studies of HOMs and their contributions to new particle formation and growth: comparison of boreal forest in Finland and a polluted environment in China, Atmos. Chem. Phys., 18, 11779–11791, https://doi.org/10.5194/acp-18-11779-2018, 2018.

Quéléver, L. L. J., Kristensen, K., Normann Jensen, L., Rosati, B., Teiwes, R., Daellenbach, K. R., Peräkylä, O., Roldin, P., Bossi, R., Pedersen, H. B., Glasius, M., Bilde, M., and Ehn, M.: Effect of temperature on the formation of highly oxygenated organic molecules (HOMs) from alpha-pinene ozonolysis, Atmos. Chem. Phys., 19, 7609–7625, https://doi.org/10.5194/acp-19-7609-2019, 2019.

Riccobono, F., Schobesberger, S., Scott, C., Dommen, J., Ortega, I., Rondo, L., Almeida, J., Amorim, A., Bianchi, F., Breitenlechner, M., David, A., Downard, A., Dunne, E., Duplissy, J., Ehrhart, S., Flagan, R., Franchin, A., Hansel, A., Junninen, H., Kajos, M., Keskinen, H., Kupc, A., Kürten, A., Kvashin, A., Laaksonen, A., Lehtipalo, K., Makhmutov, V., Mathot, S., Nieminen, T., Onnela, A., Petäjä, T., Praplan, A., Santos, F., Schallhart, S., Seinfeld, J., Sipilä, M., Van Spracklen, D., Stozhkov, Y., Stratmann, F., Tomé, A., Tsagkogeorgas, G., Vaattovaara, P., Viisanen, Y., Vrtala, A., Wagner, P., Weingartner, E., Wex, H., Wimmer, D., Carslaw, K., Curtius, J., Donahue, N., Kirkby, J., Kulmala, M., Worsnop, D., and Baltensperger, U.: Oxidation products of biogenic emissions contribute to nucleation of atmospheric particles, Science, 344, 717–721, 2014.

Rissanen, M. P.: NO_2 Suppression of Autoxidation–Inhibition of Gas-Phase Highly Oxidized Dimer Product Formation, ACS Earth Space Chem., 2, 1211–1219, https://doi.org/10.1021/acsearthspacechem.8b00123, 2018.

Rissanen, M. P., Kurtén, T., Sipilä, M., Thornton, J. A., Kangasluoma, J., Sarnela, N., Junninen, H., Jørgensen, S., Schallhart, S., Kajos, M. K., Taipale, R., Springer, M., Mentel, T. F., Ruuskanen, T., Petäjä, T., Worsnop, D. R., Kjaergaard, H. G., and Ehn, M.: The formation of highly oxidized multifunctional products in the ozonolysis of cyclohexene, J. Am. Chem. Soc., 136, 15596–15606, 2014.

Rose, C., Zha, Q., Dada, L., Yan, C., Lehtipalo, K., Junninen, H., Mazon, S. B., Jokinen, T., Sarnela, N., Sipilä, M., Petäjä, T., Kerminen, V.-M., Bianchi, F., and Kulmala, M.: Observations of biogenic ion-induced cluster formation in the atmosphere, Sci. Adv., 4, eaar5218, https://doi.org/10.1126/sciadv.aar5218, 2018.

Schobesberger, S., Junninen, H., Bianchi, F., Lönn, G., Ehn, M., Lehtipalo, K., Dommen, J., Ehrhart, S., Ortega, I. K., Franchin, A., Nieminen, T., Riccobono, F., Hutterli, M., Duplissy, J., Almeida, J., Amorim, A., Breitenlechner, M., Downard, A. J., Dunne, E. M., Flagan, R. C., Kajos, M., Keskinen, H., Kirkby, J., Kupc, A., Kürten, A., Kurtén, T., Laaksonen, A., Mathot, S., Onnela, A., Praplan, A. P., Rondo, L., Santos, F. D., Schallhart, S., Schnitzhofer, R., Sipilä, M., Tomé, A., Tsagkogeorgas, G., Vehkamäki, H., Wimmer, D., Baltensperger, U., Carslaw, K. S., Curtius, J., Hansel, A., Petäjä, T., Kulmala, M., Donahue, N. M., and Worsnop, D. R.: Molecular understanding of atmospheric particle formation from sulfuric acid and large oxidized organic molecules., P. Natl. Acad. Sci. USA, 110, 17223–17228, 2013.

Shi, J. P., Evans, D. E., Khan, A. A., and Harrison, R. M.: Sources and concentration of nanoparticles (< 10 nm diameter) in the urban atmosphere, Atmos. Environ., 35, 1193–1202, 2001.

Shi, Z., Vu, T., Kotthaus, S., Harrison, R. M., Grimmond, S., Yue, S., Zhu, T., Lee, J., Han, Y., Demuzere, M., Dunmore, R. E., Ren, L., Liu, D., Wang, Y., Wild, O., Allan, J., Acton, W. J., Barlow, J., Barratt, B., Beddows, D., Bloss, W. J., Calzolai, G., Carruthers, D., Carslaw, D. C., Chan, Q., Chatzidiakou, L., Chen, Y., Crilley, L., Coe, H., Dai, T., Doherty, R., Duan, F., Fu, P., Ge, B., Ge, M., Guan, D., Hamilton, J. F., He, K., Heal, M., Heard, D., Hewitt, C. N., Hollaway, M., Hu, M., Ji, D., Jiang, X., Jones, R., Kalberer, M., Kelly, F. J., Kramer, L., Langford, B., Lin, C., Lewis, A. C., Li, J., Li, W., Liu, H., Liu, J., Loh, M., Lu, K., Lucarelli, F., Mann, G., McFiggans, G., Miller, M. R., Mills, G., Monk, P., Nemitz, E., O'Connor, F., Ouyang, B., Palmer, P. I., Percival, C., Popoola, O., Reeves, C., Rickard, A. R., Shao, L., Shi, G., Spracklen, D., Stevenson, D., Sun, Y., Sun, Z., Tao, S., Tong, S., Wang, Q., Wang, W., Wang, X., Wang, X., Wang, Z., Wei, L., Whalley, L., Wu, X., Wu, Z., Xie, P., Yang, F., Zhang, Q., Zhang, Y., Zhang, Y., and Zheng, M.: Introduction to the special issue "In-depth study of air pollution sources and processes within Beijing and its surrounding region (APHH-Beijing)", Atmos. Chem. Phys., 19, 7519–7546, https://doi.org/10.5194/acp-19-7519-2019, 2019.

Stolzenburg, D, Fischer, L., Vogel, A., Heinritzi, M., Schervish, M., Simon, M., Wagner, A., Dada, L., Ahonen, L., Amorim, A., Baccarini, A., Bauer, P., Baumgartner, B., Bergen, A., Bianchi, F., Breitenlechner, M., Brilke, S., Buenrostro Mazon, S., Chen, D., Dias, A., Draper, D., Duplissy, J., El Haddad, I., Finkenzeller, H., Frege, C., Fuchs, C., Garmash, O., Gordon, H., He, X., Helm, J., Hofbauer, V., Hoyle, C., Kim, C., Kirkby, J., Kontkanen, J., Kürten, A., Lampilahti, J., Lawler, M., Lehtipalo, K., Leiminger, M., Mai, H., Mathot, S., Mentler, B., Molteni, U., Nie, W., Nieminen, T., Nowak, J., Ojdanic, A., Onnela, A., Passananti, M., Petäjä, T., Quéléver, L., Rissanen, M., Sarnela, N., Schallhart, S., Tauber, C., Tomé, A., Wagner, R., Wang, M., Weitz, L., Wimmer, D., Xiao, M., Yan, C., Ye, P., Zha, Q., Baltensperger, U., Curtius, J., Dommen, J., Flagan, R., Kulmala, M., Smith, J., Worsnop, D., Hansel, A., Donahue, N., and Winkler, P.: Rapid growth of organic aerosol nanoparticles over a wide tropospheric temperature range, P. Natl. Acad. Sci. USA, 115, 9122–9127, 2018.

Tammet, H.: Size and mobility of nanometer particles, clusters and ions, J. Aerosol Sci., 26, 459–475, 1995.

Tomasi, C., Fuzzi, S., and Kokhanovsky, A.: Atmospheric Aerosols: Life Cycles and Effects on Air Quality and Climate, John Wiley & Sons, Weinheim, Germany, 2017.

Tröstl, J., Chuang, W. K., Gordon, H., Heinritzi, M., Yan, C., Molteni, U., Ahlm, L., Frege, C., Bianchi, F., Wagner, R., Simon, M., Lehtipalo, K., Williamson, C., Craven, J. S., Duplissy, J., Adamov, A., Almeida, J., Bernhammer, A. K., Breitenlechner, M., Brilke, S., Dias, A., Ehrhart, S., Flagan, R. C., Franchin, A., Fuchs, C., Guida, R., Gysel, M., Hansel, A.,

Hoyle, C. R., Jokinen, T., Junninen, H., Kangasluoma, J., Keskinen, H., Kim, J., Krapf, M., Kürten, A., Laaksonen, A., Lawler, M., Leiminger, M., Mathot, S., Möhler, O., Nieminen, T., Onnela, A., Petäjä, T., Piel, F. M., Miettinen, P., Rissanen, M. P., Rondo, L., Sarnela, N., Schobesberger, S., Sengupta, K., Sipilä, M., Smith, J. N., Steiner, G., Tomè, A., Virtanen, A., Wagner, A. C., Weingartner, E., Wimmer, D., Winkler, P. M., Ye, P., Carslaw, K. S., Curtius, J., Dommen, J., Kirkby, J., Kulmala, M., Riipinen, I., Worsnop, D. R., Donahue, N. M., and Baltensperger, U.: The role of low-volatility organic compounds in initial particle growth in the atmosphere, Nature, 533, 527–531, https://doi.org/10.1038/nature18271, 2016.

Wang, S., Wu, R., Berndt, T., Ehn, M., and Wang, L.: Formation of Highly Oxidized Radicals and Multifunctional Products from the Atmospheric Oxidation of Alkylbenzenes, Environ. Sci. Techn., 51, 8442–8449, 2017.

Wang, Z., Wu, Z., Yue, D., Shang, D., Guo, S., Sun, J., Ding, A., Wang, L., Jiang, J., Guo, H., Gao, J., Cheung, H. C., Morawska, L., Keywood, M., and Hu, M.: New particle formation in China: Current knowledge and further directions, Sci. Total Environ., 577, 258–266, 2016.

Wiedensohler, A., Cheng, Y. F., Nowak, A., Wehner, B., Achtelt, P., Berghof, M., Birmili, W., Wu, Z. J., Hu, M., Zhu, T., Takegawa, N., Kita, K., Kondo, Y., Lou, S. R., Hofeumahaus, A., Holland, F., Wahner, A., Gunthe, S. S., Rose, D., Su, H., and Pöschl, U.: Rapid aerosol particle growth and increase of cloud condensation nucleus activity by secondary aerosol formation and condensation: A case study for regionalair pollution in northeastern China, J. Geophys. Res.-Atmos., 114, 1–13, https://doi.org/10.1029/2008JD010884, 2009.

Wu, Z., Hu, M., Liu, S., Wehner, B., Bauer, S., Massling, A., Wiedensohler, A., Petäjä, T., Dal Maso, M., and Kulmala, M.: New particle formation in Beijing, China: Statistical analysis of a 1-year data set, J. Geophys. Res.-Atmos., 112, D09209, https://doi.org/10.1029/2006JD007406, 2007.

Wu, Z., Hu, M., Lin, P., Liu, S., Wehner, B., and Wiedensohler, A.: Particle number size distribution in the urban atmosphere of Beijing, China, Atmos. Environ., 42, 7967–7980, 2008.

Wu, Z., Ma, N., Größ, J., Kecorius, S., Lu, K., Shang, D., Wang, Y., Wu, Y., Zeng, L., Hu, M., Wiedensohler, A., and Zhang, Y.: Thermodynamic properties of nanoparticles during new particle formation events in the atmosphere of North China Plain, Atmos. Res., 188, 55–63, 2017.

Xiong, F., McAvey, K. M., Pratt, K. A., Groff, C. J., Hostetler, M. A., Lipton, M. A., Starn, T. K., Seeley, J. V., Bertman, S. B., Teng, A. P., Crounse, J. D., Nguyen, T. B., Wennberg, P. O., Misztal, P. K., Goldstein, A. H., Guenther, A. B., Koss, A. R., Olson, K. F., de Gouw, J. A., Baumann, K., Edgerton, E. S., Feiner, P. A., Zhang, L., Miller, D. O., Brune, W. H., and Shepson, P. B.: Observation of isoprene hydroxynitrates in the southeastern United States and implications for the fate of NO_x, Atmos. Chem. Phys., 15, 11257–11272, https://doi.org/10.5194/acp-15-11257-2015, 2015.

Yan, C., Nie, W., Äijälä, M., Rissanen, M. P., Canagaratna, M. R., Massoli, P., Junninen, H., Jokinen, T., Sarnela, N., Häme, S. A. K., Schobesberger, S., Canonaco, F., Yao, L., Prévôt, A. S. H., Petäjä, T., Kulmala, M., Sipilä, M., Worsnop, D. R., and Ehn, M.: Source characterization of highly oxidized multifunctional compounds in a boreal forest environment using positive matrix factorization, Atmos. Chem. Phys., 16, 12715–12731, https://doi.org/10.5194/acp-16-12715-2016, 2016.

Yao, L., Garmash, O., Bianchi, F., Zheng, J., Yan, C., Kontkanen, J., Junninen, H., Mazon, S. B., Ehn, M., Paasonen, P., Sipilä, M., Wang, M., Wang, X., Xiao, S., Chen, H., Lu, Y., Zhang, B., Wang, D., Fu, Q., Geng, F., Li, L., Wang, H., Qiao, L., Yang, X., Chen, J., Kerminen, V. M., Petäjä, T., Worsnop, D. R., Kulmala, M., and Wang, L.: Atmospheric new particle formation from sulfuric acid and amines in a Chinese megacity, Science, 361, 278–281, 2018.

Yu, F. and Luo, G.: Simulation of particle size distribution with a global aerosol model: contribution of nucleation to aerosol and CCN number concentrations, Atmos. Chem. Phys., 9, 7691–7710, https://doi.org/10.5194/acp-9-7691-2009, 2009.

Yue, D. L., Hu, M., Zhang, R. Y., Wu, Z. J., Su, H., Wang, Z. B., Peng, J. F., He, L. Y., Huang, X. F., Gong, Y. G., and Wiedensohler, A.: Potential contribution of new particle formation to cloud condensation nuclei in Beijing, Atmos. Environ., 45, 6070–6077, 2011.

Zhao, Y., Wingen, L. M., Perraud, V., Greaves, J., and Finlayson-Pitts, B. J.: Role of the reaction of stabilized Criegee intermediates with peroxy radicals in particle formation and growth in air, Phys. Chem. Chem. Phys., 17, 12500–12514, 2015.

Supplement of Atmos. Chem. Phys., 19, 14933–14947, 2019
https://doi.org/10.5194/acp-19-14933-2019-supplement

Atmospheric Chemistry and Physics
Open Access
EGU

Supplement of

Observations of highly oxidized molecules and particle nucleation in the atmosphere of Beijing

James Brean et al.

Correspondence to: Roy M. Harrison (r.m.harrison@bham.ac.uk)

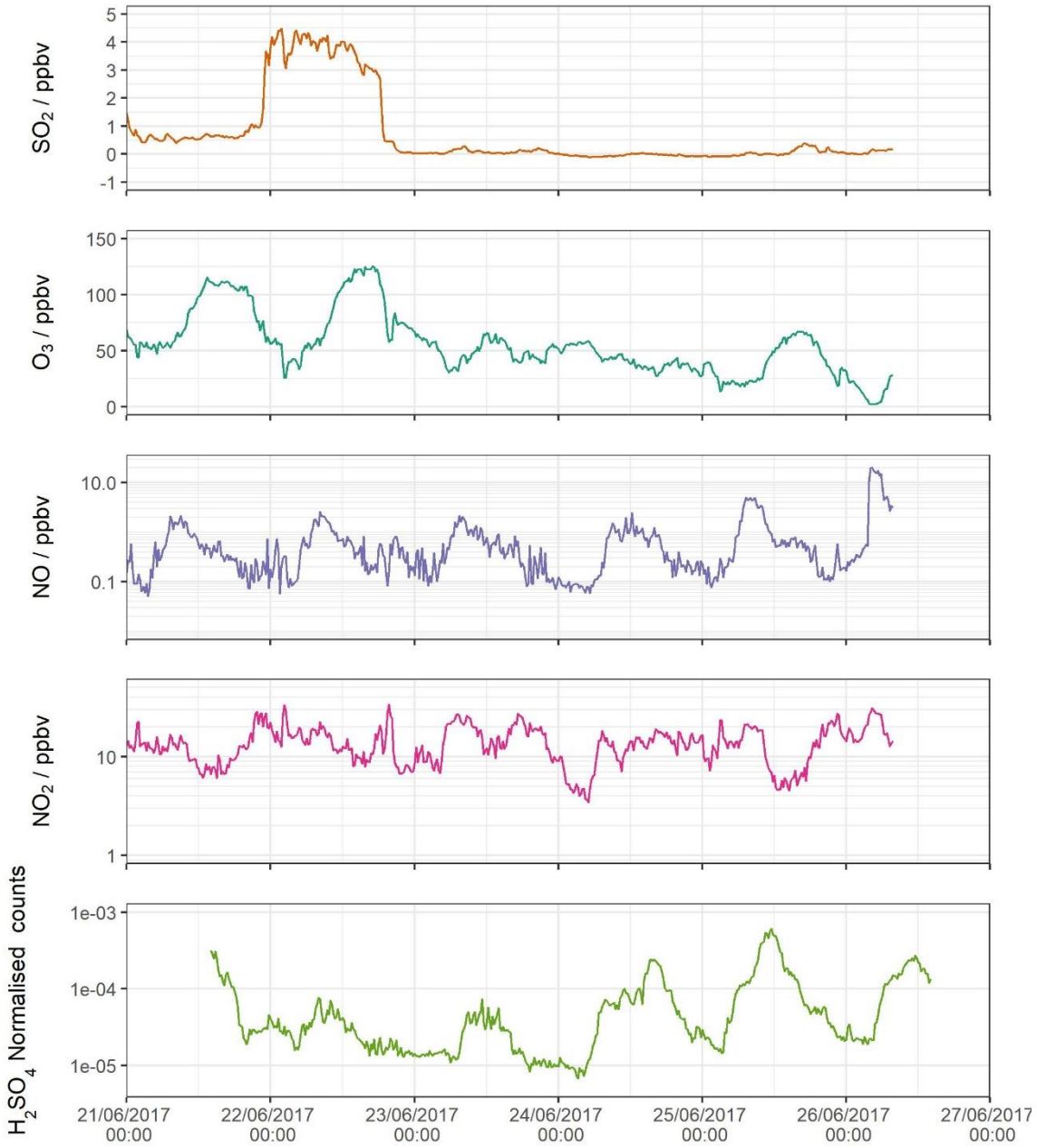

Figure S1. Time series for (from top downwards), SO_2, O_3, NO, NO_2 and H_2SO_4.

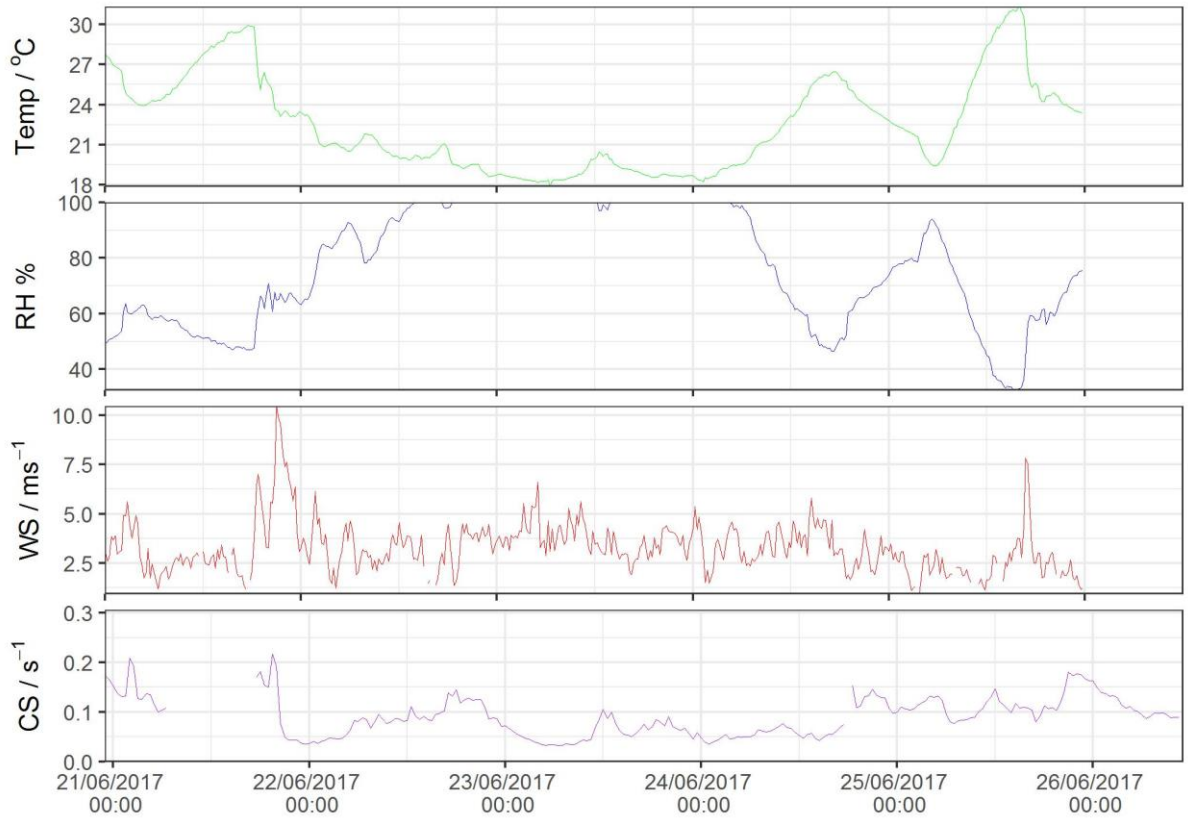

Figure S2. MET data for the sampling period. Temperature, relative humidity and wind speed were collected at 120 m on the meteorological tower at the sampling site. The particle size distribution from which condensation sink was calculated was measured at 2 metres.

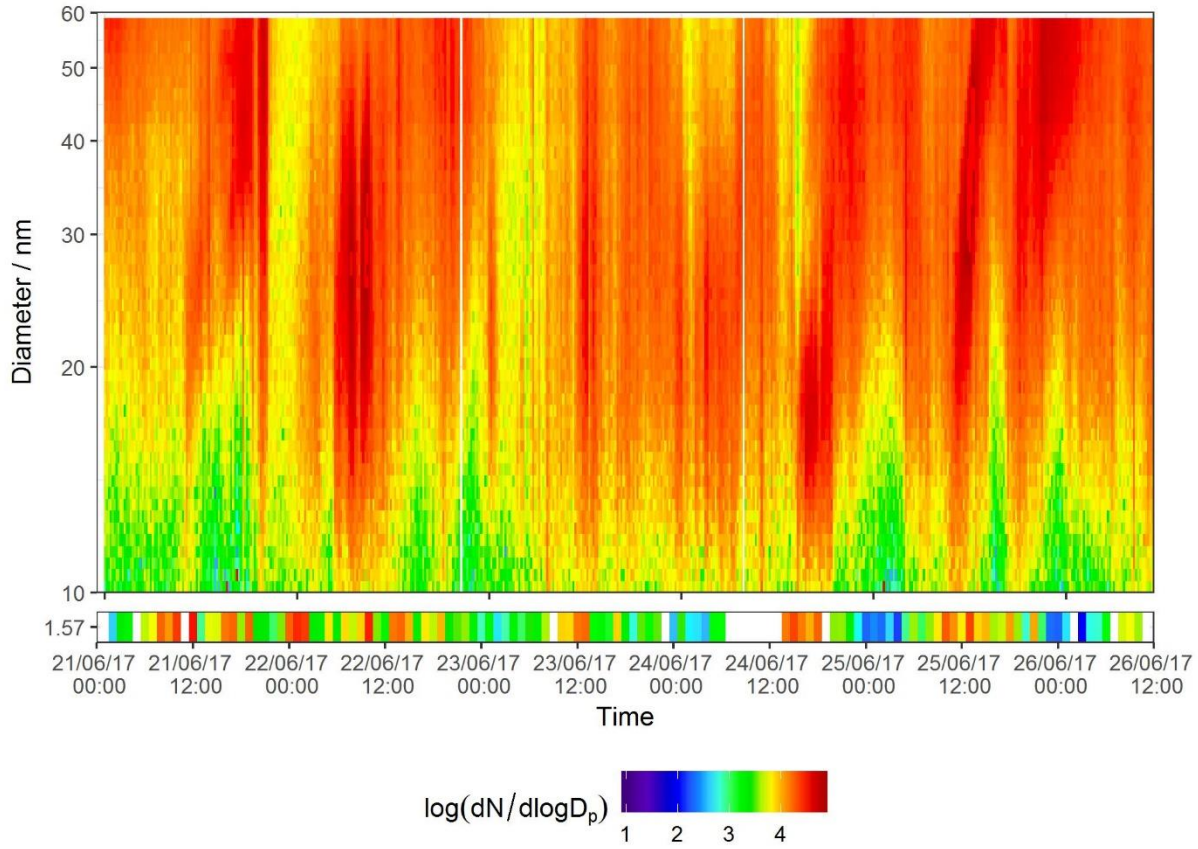

Figure S3. SMPS + PSM contour plot for all days of sampling period. Data, from top panel to bottom, from long column SMPS, nano column SMPS and PSM instruments, units in colour bar are $\log_{10}$ ($dN/\log D_p$) for N in cm^{-3}.

Table S1. Relationship between molecular mass and calculated electrical mobility diameter (nm) for multiple masses up to 800 Da and densities , as calculated according to Tammet (1995), and corrected according to Larriba et al. (2011).

Mass / Da	ρ g/cm^3					
	1.0	1.2	1.4	1.6	1.8	2.0
200	1.159	1.109	1.068	1.035	1.006	0.982
300	1.284	1.226	1.179	1.141	1.109	1.081
400	1.383	1.319	1.268	1.226	1.19	1.159
500	1.466	1.397	1.342	1.297	1.259	1.226
600	1.539	1.466	1.408	1.359	1.319	1.284
700	1.605	1.528	1.466	1.415	1.372	1.335
800	1.664	1.583	1.519	1.466	1.421	1.383

Table S2. All peaks identified by NO3- CIMS

Ion	Mass
$C_2HO_3O^-$	88.988
$C_3H_5O_2O^-$	89.025
$CH_3SO_3^-$	94.98
HSO_4^-	96.96
$C_4H_3O_2O^-$	99.009
$C_4H_5O_2O^-$	101.024
$C_3H_3O_3O^-$	103.004
SO_4O^-	111.947
$C_6H_4NO_3^-$	138.019
$SO_3NO_3^-$	141.945
$C_5H_9O_4O^-$	149.046
$H_2SO_4NO_3^-$	159.956
$C_3H_5NO_3NO_3^-$	165.015
$C_3H_4O_4NO_3^-$	165.999
$C_8H_{11}O_3O^-$	171.066
$C_7H_{10}NO_3O^-$	172.062
IO_3^-	174.89
$C_4H_6O_4NO_3^-$	180.015
$C_3H_6NO_4NO_3^-$	182.018
$C_4H_6O_2HSO_4^-$	182.997
$C_3H_6O_5NO_3^-$	184.01
$C_3H_5O_3HSO_4^-$	185.984
$C_5H_6NO_3NO_3^-$	191.031
$C_5H_8O_4NO_3^-$	194.031
$H_2SO_4HSO_4^-$	194.926

Table S2 continued

Ion	Mass
$C_4H_8O_5NO_3^-$	198.026
$C_5H_{10}O_2HSO_4^-$	199.028
$C_6H_5NO_3NO_3^-$	201.015
$HNO_3SO_3NO_3^-$	204.941
$C_6H_{12}NO_3NO_3^-$	208.07
$C_5H_9NO_4NO_3^-$	209.042
$C_5H_8O_5NO_3^-$	210.026
$C_4H_7NO_5NO_3^-$	211.021
$C_5H_{10}O_5NO_3^-$	212.041
$C_4H_8O_6NO_3^-$	214.02
$C_7H_7NO_3NO_3^-$	215.031
$C_4H_{10}O_6NO_3^-$	216.036
$C_7H_8O_4NO_3^-$	218.031
$C_6H_7NO_4NO_3^-$	219.026
$C_7H_{10}O_4NO_3^-$	220.046
$C_6H_9NO_4NO_3^-$	221.042
$C_5H_7NO_5NO_3^-$	223.021
$C_9H_9NO_2NO_3^-$	225.052
$C_{10}H_{13}NONO_3^-$	225.088
$C_4H_7NO_6NO_3^-$	227.016
$C_8H_9NO_3NO_3^-$	229.047
$C_5H_{12}O_6NO_3^-$	230.052
$C_7H_7NO_4NO_3^-$	231.026

Table S2 continued

Ion	Mass
$C_8H_{10}O_4NO_3^-$	232.046
$C_7H_9NO_4NO_3^-$	233.042
$C_7H_8O_5NO_3^-$	234.026
$C_7H_{10}O_5NO_3^-$	236.041
$C_5H_5NO_6NO_3^-$	237.000
$C_6H_9NO_5NO_3^-$	237.036
$C_6H_8O_6NO_3^-$	238.020
$C_7H_{12}O_5NO_3^-$	238.057
$C_5H_7NO_6NO_3^-$	239.016
$C_{10}H_{11}NO_2NO_3^-$	239.067
$C_6H_{10}O_6NO_3^-$	240.036
$C_5H_9NO_6NO_3^-$	241.031
$C_5H_{11}NO_6NO_3^-$	243.047
$C_5H_{10}O_7NO_3^-$	244.031
$C_{10}H_{14}O_3NO_3^-$	244.083
$C_3H_7NO_8NO_3^-$	247.006
$C_8H_{10}O_5NO_3^-$	248.041
$C_7H_9NO_5NO_3^-$	249.036
$C_8H_{12}O_5NO_3^-$	250.057
$C_6H_9NO_6NO_3^-$	253.031
$C_5H_8N_2O_6NO_3^-$	254.027

Table S2 continued

Ion	Mass
$C_{10}H_{11}NO_2NO_3^-$	239.067
$C_6H_{10}O_6NO_3^-$	240.036
$C_5H_9NO_6NO_3^-$	241.031
$C_5H_{11}NO_6NO_3^-$	243.047
$C_5H_{10}O_7NO_3^-$	244.031
$C_{10}H_{14}O_3NO_3^-$	244.083
$C_3H_7NO_8NO_3^-$	247.006
$C_8H_{10}O_5NO_3^-$	248.041
$C_7H_9NO_5NO_3^-$	249.036
$C_8H_{12}O_5NO_3^-$	250.057
$C_6H_9NO_6NO_3^-$	253.031
$C_8H_{12}O_6NO_3^-$	266.052
$C_5H_{10}O_9NO_3^-$	276.021
$C_{10}H_{14}O_5NO_3^-$	276.072
$C_7H_7NO_3HNO_3NO_3^-$	278.027
$C_8H_{12}O_7NO_3^-$	282.047
$C_6H_{10}N_2O_7NO_3^-$	284.037
$C_{10}H_9NO_5NO_3^-$	285.036
$C_{10}H_8O_6NO_3^-$	286.02
$C_5H_{10}N_2O_8NO_3^-$	288.032
$C_{10}H_{15}NO_5NO_3^-$	291.083
$C_{10}H_{14}O_6NO_3^-$	292.067
$C_9H_{13}NO_6NO_3^-$	293.063
$C_{10}H_{16}O_6NO_3^-$	294.083
$C_9H_{15}NO_6NO_3^-$	295.078
$C_2H_7NHNO_3NO_3^-$	296.033
$C_{12}H_{13}NO_4NO_3^-$	297.073
$C_6H_{10}N_2O_8NO_3^-$	300.032
$C_7H_{13}NO_8NO_3^-$	301.052

Table S2 continued

Ion	Mass
$C_7H_{12}O_9NO_3^-$	302.036
$C_5H_{10}N_2O_9NO_3^-$	304.027
$C_{11}H_{17}NO_5NO_3^-$	305.099
$C_{10}H_{15}NO_6NO_3^-$	307.078
$HSO_5H_2SO_4HSO_4^-$	307.882
$C_{10}H_{14}O_7NO_3^-$	308.062
$C_{13}H_{13}NO_4NO_3^-$	309.073
$C_{13}H_{14}NO_4NO_3^-$	310.081
$C_9H_{15}NO_7NO_3^-$	311.073
$C_9H_{14}O_8NO_3^-$	312.057
$C_7H_{12}N_2O_8NO_3^-$	314.048
$C_{10}H_9NO_7NO_3^-$	317.026
$C_{11}H_{12}O_7NO_3^-$	318.047
$C_{10}H_{15}N_2O_6NO_3^-$	321.081
$C_{10}H_{14}O_8NO_3^-$	324.057
$C_{10}H_{17}NO_7NO_3^-$	325.089
$C_{10}H_{16}O_8NO_3^-$	326.073
$C_9H_{15}NO_8NO_3^-$	327.068
$C_{13}H_{14}O_6NO_3^-$	328.067
$C_{12}H_{13}NO_6NO_3^-$	329.063
$C_{11}H_{12}N_2O_6NO_3^-$	330.058
$(C_2H_7N)_3H_2SO_4HSO_4^-$	330.101
$C_{10}H_9NO_8NO_3^-$	333.021

Table S2 continued

Ion	Mass
$C_9H_8N_2O_8NO_3^-$	334.016
$C_{10}H_{11}NO_8NO_3^-$	335.037
$C_{11}H_{17}NO_7NO_3^-$	337.089
$C_{11}H_{16}O_8NO_3^-$	338.073
$C_{10}H_{15}NO_8NO_3^-$	339.068
$C_{14}H_{14}O_6NO_3^-$	340.067
$C_{10}H_{16}O_9NO_3^-$	342.068
$C_{13}H_{17}NO_6NO_3^-$	345.094
$C_2H_7NHNO_3(HSO_5)_2NO_3^-$	345.992
$C_{11}H_{11}NO_8NO_3^-$	347.037
$C_{10}H_{14}N_2O_8NO_3^-$	352.063
$C_{11}H_{17}NO_8NO_3^-$	353.084
$C_{14}H_{14}NO_6NO_3^-$	354.07
$C_{10}H_{15}NO_9NO_3^-$	355.063
$C_{11}H_{18}O_9NO_3^-$	356.083
$C_{12}H_{12}N_2O_7NO_3^-$	358.053
$C_{14}H_{19}NO_6NO_3^-$	359.11
$C_{13}H_{19}NO_7NO_3^-$	363.105
$C_{13}H_{18}O_8NO_3^-$	364.089
$C_{13}H_{20}O_8NO_3^-$	366.104
$C_{12}H_{19}NO_8NO_3^-$	367.099

Table S2 continued

Ion	Mass
$C_{11}H_{16}O_{10}NO_3^-$	370.063
$C_{14}H_{15}NO_7NO_3^-$	371.073
$C_{14}H_{14}O_8NO_3^-$	372.057
$C_{13}H_{13}NO_8NO_3^-$	373.052
$C_{10}H_{16}O_{11}NO_3^-$	374.058
$(C_2H_7N)_2(H_2SO_4)_2HSO_4^-$	383.011
$C_{13}H_{15}NO_8NO_3^-$	375.068
$C_{14}H_{23}NO_7NO_3^-$	379.136
$C_{13}H_{21}NO_8NO_3^-$	381.115
$C_{16}H_{18}NO_6NO_3^-$	382.102
$C_{16}H_{19}NO_6NO_3^-$	383.11
$C_{14}H_{15}NO_8NO_3^-$	387.068
$C_{10}H_{17}NO_{11}NO_3^-$	389.069
$C_{15}H_{23}NO_7NO_3^-$	391.136
$C_{14}H_{21}NO_8NO_3^-$	393.115
$C_{17}H_{21}NO_6NO_3^-$	397.125

Table S2 continued

Ion	Mass
$C_{16}H_{20}N_2O_6NO_3^-$	398.121
$C_{16}H_{19}NO_7NO_3^-$	399.105
$C_{16}H_{18}O_8NO_3^-$	400.089
$C_{15}H_{17}NO_8NO_3^-$	401.084
$C_{15}H_{16}O_9NO_3^-$	402.068
$C_{14}H_{15}NO_9NO_3^-$	403.063
$C_{17}H_{28}O_7NO_3^-$	406.172
$C_{17}H_{18}N_2O_6NO_3^-$	408.105
$C_{18}H_{21}NO_6NO_3^-$	409.125
$C_{17}H_{19}NO_7NO_3^-$	411.105
$C_{17}H_{20}O_8NO_3^-$	414.104
$C_{16}H_{19}NO_8NO_3^-$	415.099
$C_{16}H_{21}NO_8NO_3^-$	417.115
$C_{14}H_{14}O_{11}NO_3^-$	420.042
$C_{18}H_{21}NO_7NO_3^-$	425.12
$C_{15}H_{24}O_{10}NO_3^-$	426.125
$(C_2H_7N)_2(H_2SO_4)_2HSO_4^-$	428.068
$C_{18}H_{22}O_8NO_3^-$	428.12
$C_{17}H_{21}NO_8NO_3^-$	429.115
$C_{16}H_{23}NO_9NO_3^-$	435.126
$C_2H_7N(H_2SO_4)_3HSO_4^-$	435.919

Table S2 continued

Ion	Mass
$C_{15}H_{23}NO_{10}NO_3^-$	439.121
$C_{18}H_{23}NO_8NO_3^-$	443.131
$C_{12}H_{16}O_{14}NO_3^-$	446.042
$C_{17}H_{27}NO_9NO_3^-$	451.157
$C_{16}H_{25}NO_{10}NO_3^-$	453.136
$C_{17}H_{28}O_{10}NO_3^-$	454.157
$C_{16}H_{27}NO_{10}NO_3^-$	455.152
$C_{19}H_{22}O_9NO_3^-$	456.115
$C_{15}H_{25}NO_{11}NO_3^-$	457.131
$C_{20}H_{32}NO_7NO_3^-$	460.206
$C_{17}H_{25}NO_{10}NO_3^-$	465.136
$C_{17}H_{29}NO_{10}NO_3^-$	469.168
$C_{16}H_{24}O_{12}NO_3^-$	470.115
$C_{16}H_{27}NO_{11}NO_3^-$	471.147
$C_{16}H_{26}O_{12}NO_3^-$	472.131
$(C_2H_7N)_4(H_2SO_4)_2HSO_4^-$	473.126
$C_{15}H_{27}NO_{12}NO_3^-$	475.142

Table S2 continued

Ion	Mass
$(C_2H_7N)_2(H_2SO_4)_3HSO_4^-$	480.978
$C_{17}H_{25}NO_{11}NO_3^-$	481.131
$C_{18}H_{28}O_{11}NO_3^-$	482.152
$C_{17}H_{27}NO_{11}NO_3^-$	483.147
$C_{20}H_{26}N_2O_8NO_3^-$	484.157
$C_{20}H_{27}NO_9NO_3^-$	487.157
$C_{20}H_{29}NO_9NO_3^-$	489.173

CHAPTER 3: MOLECULAR INSIGHTS INTO NEW PARTICLE FORMATION IN BARCELONA, SPAIN

Authors: James Brean, David C.S. Beddows, Zongbo Shi, Brice Temime-Roussel, Nicolas Marchand, Xavier Querol, Andrés Alastuey, María Cruz Minguillón, and Roy M. Harrison.

Published in: Atmospheric Chemistry and Physics Discussions. DOI: https://doi.org/10.5194/acp-2020-84

Author contributions: RMH and XQ conceived the study, JB and DCSB carried out the CI-APi-TOF and related measurements with assistance from AA and MCM. The VOC measurements were proposed by NM and collected by BT-R. JB prepared all figures and wrote the first draft of the paper with feedback throughout from RMH and ZS, the final version was enhanced by contributions from the co-authors and three referees. R code to produce HYSPLIT back trajectories and CS values was provided by DCSB.

Molecular Insights into New Particle Formation in Barcelona, Spain

James Brean[1], David C.S. Beddows[1], Zongbo Shi[1], Brice Temime-Roussel[2], Nicolas Marchand[2], Xavier Querol[3], Andrés Alastuey[3], María Cruz Minguillón[3], and Roy M. Harrison[1a*]

[1]Division of Environmental Health and Risk Management School of Geography, Earth and Environmental Sciences University of Birmingham, Edgbaston, Birmingham B15 2TT United Kingdom

[2]Aix Marseille Univ, CNRS, LCE Marseille, 13003, France

[3]Institute of Environmental Assessment and Water Research (IDAEA-CSIC), Barcelona, 08034 Spain

[a]Also at: Department of Environmental Sciences / Center of Excellence in Environmental Studies, King Abdulaziz University, PO Box 80203, Jeddah, 21589, Saudi Arabia

[*] To whom correspondence should be addressed (Email: r.m.harrison@bham.ac.uk)

ABSTRACT

Atmospheric aerosols contribute some of the greatest uncertainties to estimates of global radiative forcing, and have significant effects on human health. New particle formation (NPF) is the process by which new aerosols of sub-2 nm diameter form from gas-phase precursors and contributes significantly to particle numbers in the atmosphere, accounting for approximately 50% of cloud condensation nuclei globally. Here, we study summertime NPF in urban Barcelona in NE Spain utilising particle counting instruments down to 1.9 nm and a Nitrate CI-APi-ToF. The rate of formation of new particles is seen to increase linearly with sulphuric acid concentration, although particle formation rates fall short of chamber studies of H_2SO_4-DMA-H_2O, while exceeding those of H_2SO_4-BioOxOrg-H_2O nucleation, although a role of highly oxygenated molecules (HOMs) cannot be ruled out. The sulphuric acid dimer:monomer ratio is significantly lower than that seen in experiments involving sulphuric acid and DMA in chambers, indicating that stabilization of sulphuric acid clusters by bases is weaker in this dataset than in chambers, either due to rapid evaporation due to high summertime temperatures, or limited pools of stabilising amines. Such a mechanism cannot be verified in this data, as no higher-order H_2SO_4-amine clusters, nor H_2SO_4-HOM clusters were measured. The high concentrations of HOMs arise from isoprene, alkylbenzene, monoterpene and PAH oxidation, with alkylbenzenes providing greater concentrations of HOMs due to significant local sources. The concentration of these HOMs shows a dependence on temperature. The organic compounds measured primarily fall into the SVOC volatility class arising from alkylbenzene and isoprene oxidation. LVOC largely arise from oxidation of alkylbenzenes, PAHs and monoterpenes, whereas ELVOC arise from primarily PAH and monoterpene oxidation. New particle formation without growth past 10 nm is also observed, and on these days oxygenated organic concentrations are lower than on days with growth by a factor of 1.6, and thus high concentrations of low volatility oxygenated organics which primarily derive from traffic-emitted VOCs appear to be a necessary condition for the growth of newly formed particles in Barcelona. These results are consistent with prior observations of new particle formation from sulphuric acid-

amine reactions in both chambers and the real atmosphere, and are likely representative of the urban background of many European Mediterranean cities. A role for HOMs in the nucleation process cannot be confirmed or ruled out, and there is strong circumstantial evidence for the participation of HOMs across multiple volatility classes in particle growth.

1. INTRODUCTION

Atmospheric aerosols, defined as liquid or solid droplets suspended in a gas, affect the climate both directly by scattering and absorbing radiation, and indirectly by acting as cloud condensation nuclei (CCN) (Penner et al., 2011), providing great uncertainties in estimates of global radiative forcing (IPCC, 2014). Further, fine ambient aerosols (defined as those with diameter below 2.5 μm) are the fifth greatest global mortality risk factor, resulting in 103.1 million disability-adjusted life year loss in 2015 (Cohen et al., 2017). The number concentration of the ultrafine fraction of these (aerosols with diameter below 0.1 μm, referred to as ultrafine particles or UFP) pose potentially significant health risks also, due to their high concentration and surface area. The more diffuse, gas-like behaviour of UFP allows them to penetrate into the deep lung and enter the bloodstream (Miller et al., 2017). Ultrafine particles occur in the urban environment either as primary emissions (e.g., from car exhaust (Harrison et al., 2018)) or secondarily as the product of new particle formation (NPF) (Brines et al., 2015; Guo et al., 2014; Kulmala et al., 2017; Lee et al,. 2019)

NPF is the formation of aerosol particles from gas-phase precursors. NPF can be considered a two-step process involving initial formation of a cluster of gas molecules at the critical diameter at around 1.5 nm - the diameter at which a free-energy barrier must be overcome to allow the spontaneous phase transition from gas to liquid or solid (Zhang et al., 2012), and the subsequent growth of this droplet to a larger aerosol particle. The first step of this process is dependent upon the stability and abundance of the clustering molecules. Sulphuric acid, water, and dimethylamine (DMA), for example, efficiently form particles as the strong hydrogen bonding between the acid base pair produces near negligible evaporation, much lower than the evaporation rate seen for the more weakly bound sulphuric acid-ammonia-water system. Nucleation of sulphuric acid, DMA and water proceeds at, or near to the kinetic limit in a chamber at 278 K when DMA mixing ratios are sufficient (Almeida et al., 2013; Kürten et al., 2014). Once past this 1.5 nm diameter, condensation and coagulation will drive particle growth. Both the abundance of condensable gases and their

vapour pressures limit condensational growth. Vapour pressures are especially important for the initial growth stages, as the Kelvin effect barrier impairs condensation of more volatile species, with this condition of low vapour pressures becoming less significant as the diameter of the particle increases (Tröstl et al., 2016). Once sufficiently large (>50 nm), the loss processes of coagulation and evaporation of these particles become inefficient, resulting in a significant atmospheric lifetime. It is from these these diameters onwards the climate forcing effects of these particles become most pronounced.

NPF processes happen globally, across a diverse range of environments from pristine polar regions, to polluted urban megacities (Kerminen et al., 2018), and represent a significant source of CCN, with 10-60% of NPF events shown to produce CCN and enhancement factors to CCN count ranging from 0.5 – 11 (Lee et al., 2019 and references within). Strong NPF events are observed across a range of urban environments, despite high condensation sinks $>10^{-2}$ s^{-1} (Bousiotis et al., 2019; Yu et al., 2016), and can act as a precursor to strong haze events (Guo et al., 2014). The occurrence of urban NPF has only been partially explained by growing understanding from recent in-depth studies (Yao et al., 2018). Recent advances in instrumentation allow for the measurement of particles down to the critical diameter with instruments such as the particle size magnifier (PSM), and (Neutral) Air Ion Spectrometer (NAIS/AIS) (Lee et al., 2019), and mass spectral techniques for measuring the abundance and composition of neutral (Jokinen et al., 2012) and charged (Junninen et al., 2010) clusters. Elucidated mechanisms with these techniques involve sulphuric acid and ammonia in remote environments (Jokinen et al., 2018; Yan, 2018), monoterpene derived highly oxygenated molecules (HOM) in remote environments (Rose et al., 2018), iodic acid in coastal environments (Sipilä et al., 2016), and sulphuric acid and DMA in polluted urban environments (Yao et al., 2018).

Urban Barcelona sees frequent, strong summer-time NPF events occurring on 28% of days. These events are associated with high insolation and elevated ozone (~60 $\mu g\ m^{-3}$) when considering the

whole year (Brines et al., 2014, 2015).Ground-level observations report NPF events starting typically at midday, and either occurring in urban Barcelona and the surrounding regional background simultaneously, or isolated to eitherurban Barcelona or just the regional background (Dall'Osto et al., 2013). Vertical profiles over urban Barcelona reveal that NPF occurs at higher altitudes, and starts earlier in the day, as at a given altitude these events are not suppressed by early traffic peaks contributing to particle load (Minguillón et al., 2015). Here, we examine gas phase mass spectral evidence and particle formation rates at the critical diameter from sulphuric acid in Barcelona, with possible contribution from strong bases and highly oxygenated organic molecules (HOMs), as well as factors influencing subsequent particle growth.

2. METHODS

2.1 Sampling Site

The Palau Reial site in Barcelona (41°23'15" N, 2°6'53.64" E) is representative of the urban background of Barcelona, located at the Institute of Environmental Assessment and Water Research (IDAEA-CSIC) in the north-west of the city. Sampling was performed from a container 20 m from a low traffic road, and 200 m from the nearest main road (Avinguda Diagonal). Data were taken from 2018/06/28 through 2018/07/18.

2.2 Chemical Ionisation Atmospheric Pressure Interface Time of Flight Mass Spectrometry

The Aerodyne Nitrate Chemical Ionisation Atmospheric Pressure interface Time of Flight Mass Spectrometer (CI-APi-ToF) was used to make measurements of neutral oxygenated organic compounds, organic and inorganic acids, bases, and their molecular clusters at high time resolution with high resolving power. The ionization system charges molecules by adduct formation, such as in the case of organic compounds with two or more hydrogen bond donor groups (Hyttinen et al., 2015), or proton transfer in the case of strong acids like sulphuric acid (Jokinen et al., 2012).

Hydroxyl or hydroperoxyl functionalities are both common hydrogen bond donating groups, with hydroperoxyl being the more efficient hydrogen bond donor (Møller et al., 2017). This instrument has been explained in great detail elsewhere (Jokinen et al., 2012; Junninen et al., 2010), but briefly, the front end consists of a chemical ionisation system where a 10 L min^{-1} sample flow is drawn in through the 1 m length 1" OD stainless steel tubing opening. A secondary flow was run parallel and concentric to this sample flow, rendering the reaction chamber effectively wall-less. A 3 cm^3 min^{-1} flow of a carrier gas (N_2) is passed over a reservoir of liquid HNO_3, entraining vapour which is subsequently ionised to NO_3^- via an X-ray source. Ions are then guided into the sample flow. The nitrate ions will then charge molecules either by clustering or proton transfer. The mixed flows travelling at 10 L min^{-1} enter the critical orifice at the front end of the instrument at 0.8 L min^{-1} and are guided through a series of differentially pumped chambers before reaching the ToF analyser. All data analysis was carried out in the Tofware package in Igor Pro 7 (Tofwerk AG, Switzerland). Signals except for those of amines and ammonia are divided by the sum of reagent ion signals and multiplied by a calibration coefficient to produce a concentration. A calibration coefficient of 3×10^9 cm^{-3} was established based upon comparison with a sulphuric acid proxy (Mikkonen et al., 2011) and is in line with a prior calibration with our instrument (Brean et al., 2020). Uniform sensitivity between H_2SO_4 and all other species measured by CI-APi-ToF bar amines and ammonia was assumed in this work. This introduces some uncertainties, as it relies upon both collision rates and charging efficiencies to be the same within the ionisation source for all species. Amine and ammonia signals are normalised to the nitrate trimer signal (Simon et al., 2016). Prior reports of ammonia and amines as measured by CI-APi-ToF employed corona discharge systems, which utilise higher concentrations of nitric acid, thus we report normalised signals. We present correlations of each of these bases clustered with the nitrate dimer plotted against measurements with the nitrate trimer, as well as their intercorrelations and example peak fits across Figure S1. C_2 amines, C_4 amines and ammonia were the only molecules of this kind found in our mass spectra. Systematic uncertainties of +100% / -50 % arising from this method are assumed.

Due to the high resolving power of the CI-APi-ToF system (mass resolving power of 3000, and mass accuracy of 20 ppm at 201 m/Q), multiple peaks can be fit at the same unit mass and their molecular formulae assigned. Beyond 500 m/Q, peak fitting and assignment of compositions becomes problematic as signal decreases, mass accuracy decreases, and the total number of possible chemical compositions increases, so peaks above the C_{20} region have not been assigned (Cubison and Jimenez, 2015), however, signals past this region tended to be extremely low. All ions identified are listed in Table S1. As proton transfer mostly happens with acids, and nearly all HOM molecules will be charged by adduct formation it is possible to infer the uncharged formula; therefore, all HOMs from here onwards will be listed as their uncharged form. The CI-APi-ToF inlet was placed approximately 1.5 m a.g.l. CI-APi-ToF data is only available between the dates 2018/07/06 and 2018/07/17.

2.2 Particle Size and Number Measurements

Two Scanning Mobility Particle Sizer (SMPS) instruments measured particle size distributions at 5 minute time resolution, one Long Column SMPS (TSI 3080 EC, 3082 Long DMA, 3772 CPC, TSI, USA) and one NanoSMPS (3082 EC, 3082 Nano DMA, 3776 CPC, TSI, USA) measuring the ranges 10.9 – 478.3 nm and 4.5 – 65.3 nm respectively. A Particle Size Magnifier (A10, Airmodus, FN) linked to a CPC (3775, TSI, USA) measured the sub-3 nm size fraction. The PSM was run in stepping mode, operating at four different saturator flows to vary the lower size cut of particles that it will grow (defined as the point of 50% efficiency, D_{50}). The instrument provided D_{50} from 1.4 to 2.4 nm. The instrument switched between saturator flows each 2.5 minutes, giving a sub-2.4 nm size distribution every 10 minutes. Aerosol sampling inlets were placed approximately 2 m a.g.l.

2.3 Other Measurements

Mixing ratios of non-methane VOC with proton affinity greater than H_3O^+ were made using the proton transfer reaction time of flight mass spectrometer (PTR-ToF-MS 8000, Ionicon Analytik

GmbH, Austria). A detailed description of the instrument is provided by Graus et al., (2010) The sampling set up, operating conditions, and quantification procedures are similar to those described in Minguillón et al. (2016). Continual monitoring of composition and mass of submicron aerosol >75 nm was carried out with an Aerosol Chemical Speciation Monitor (ACSM, Aerodyne, USA) (Ng et al., 2011). Ozone, NO, and NO_2 were measured by conventional ultraviolet and chemiluminiscence air quality instrumentation. Meteorological data were supplied by the Faculty of Physics of University of Barcelona, from a nearby (200 m from the measurement site) meteorological station located at the roof of an 8 floor building.

2.4 Condensation Sink and Particle Growth Rate

The condensation sink (CS) represents the rate at which a vapour phase molecule will collide with pre-existing particle surface, and was calculated from the size distribution data as follows (Kulmala et al., 2012):

$$CS = 2\pi D \sum_{d_p} \beta_{m,d_p} d_p N_{d_p} , \quad (1)$$

where D is the diffusion coefficient of the diffusing vapour (assumed sulphuric acid), β_m is a transition regime correction (Kulmala et al., 2001), d_p is particle diameter, and N_{dp} is the number of particles at diameter d_p. The formation rate of new particles at size d_p is calculated as follows:

$$J_{d_p} = \frac{dN_{d_p}}{dt} + CoagS_{d_p} . N_{d_p} + \frac{GR}{\Delta d_p} . N_{d_p} \quad (2)$$

where the first term on the right-hand side comprises the rate at which particles enter the size d_p, and the latter two terms represent losses from this size by coagulation and growth respectively. J_5 was calculated using the data in the range of 5 – 10 nm, and $J_{1.9}$ was calculated using the measurements in the range of 1.9 – 4.5 nm. We also calculated $J_{1.9}$ from our NanoSMPS data,

employing the equations of Lehtinen et al. (2007). $J_{1.9}$ from both methods showed reasonable agreement (R^2 = 0.34). Agreement between J_5 and $J_{1.9}$ for each method was similar (R^2 = 0.37 and R^2 = 0.38 for $J_{1.9}$ calculated from PSM data and from Lehtinen et al. (2019) respectively). $J_{1.9}$ is greater than J_5 as predicted from equation (2) by around a factor of 20. See Kulmala et al. (2001) for more information on calculation of coagulation sinks and formation rates. Growth rates in the range of 4.5 – 20 nm were calculated according to the lognormal distribution function method (Kulmala et al., 2012), whereas those in the range of 1.9 – 4.5 nm were calculated from PSM data using a time-delay method between PSM and NanoSMPS data. Systematic uncertainties on our calculated $J_{1.9}$ values include 25% method uncertainty (Yli-Juuti et al., 2017), with a further 25% arising from uncertainties in PSM cutoff (± 0.5 nm), as well as a 10% uncertainty in counting errors. A 50% error arising from calculated coagulation sink is also applied (Kürtenet al., 2016). The above calculations rely on the assumption of homogeneous air masses, and while air mass advection, as well as primary particle emissions can cause errors in estimations of temporal changes in particle count and diameter, the appearance and persistence of a new mode of particles across a period of several hours is typically indicative of a regional process.

Growth rates from irreversible condensation of various vapours were calculated as according to Nieminen et al. (2010). At our measured relative humidity, sulphuric acid favours binding to 2 H_2O molecules (Kurtén et al., 2007). As amine concentrations are likely limited, we presume no mass from amines in the condensing species. H_2SO_4 was assigned a density of 1.8 g cm^{-3}. For simplicity, the properties of MSA regarding density and hydration were presumed the same as H_2SO_4, and HIO_3 was presumed to have the same hydration as H_2SO_4, with a density of 4.98 g cm^{-3}. The density of condensing organic vapours was assumed 1.5 g cm^{-3}, and concentration-weighted mean mass (~276 g mol^{-1} for LVOC) and atomic weighted diffusion volumes of organic compounds were used to calculate GRs.

2.4 DBE and 2D-VBS

The double bond equivalent (DBE) describes the degree of unsaturation of an organic molecule and is defined simply as:

$$DBE = N_C - \frac{N_H}{2} - \frac{N_N}{2} + 1 \quad (3)$$

The saturation vapour pressure at 300 K is defined by the 2D-volatility basis set (2D-VBS) as follows, if all nitrogen functionality is assumed to take the form -ONO_2 (Bianchi 2019; Donahue 2011; Schervish and Donahue, 2020):

$$Log_{10}(C^*)(300\ K) = (N_{C0} - N_C)b_C - N_O b_O - 2\frac{N_O N_C}{N_C + N_O} b_{CO} - N_n b_N \quad (4)$$

where N_C, N_H, and N_N, are the number of carbon, hydrogen, and nitrogen atoms respectively. N_O is the number of oxygen atoms minus $3N_N$ to account for -ONO_2 groups, N_{C0} is 25 (the carbon number of an alkane with a saturation mass concentration of 1 μg m^{-3}), b_C, b_O, b_{CO}, and b_N are 0.475, 0.2, 0.9 and 2.5 respectively, and represent interaction and nonideality terms. The final term of equation (4) accounts for -ONO_2 groups, each reducing the saturation vapour pressure by 2.5 orders of magnitude. C* values are calculated at 300 K and not corrected for temperature, as 300 K is within 1 K of the campaign average temperature.

3. RESULTS AND DISCUSSION

3.1 General Conditions of NPF Events

Summer NPF events in the regional background around Barcelona are associated with high insolation, relatively low ozone concentration (high compared with the rest of the year), and lower particulate matter load (Brines et al., 2014; Carnerero et al., 2019). Figure 1 shows an example of a day with no NPF in panel (a), referred to as “non-event” here, where two traffic-associated peaks in

particle number are seen during rush hours. Midday traffic peaks are also seen on certain days, but these are easily distinguished from nucleation processes due to the lack of a significant <10 nm mode. Figure 1(b) shows a nucleation day with growth to larger sizes >10 nm, termed "full-event", showing the growth through the course of the day. These fulfil all the criteria of Dal Maso et al. (2005). 4 events of this type were observed with CI-APi-ToF data coverage. Figure 1(c) shows a day with nucleation occurring, but no growth past 10 nm. These days are referred to as "burst-event" days. Here, NPF is seen to occur, but particles fail to grow past the nucleation mode. 2 such events were seen in this data with CI-Api-ToF data coverage, and both are accompanied by a distinct mode appearing beforehand in the range of ~20 – 40 nm. Condensation sinks were not significantly higher than on full event days, so this failure of particles to grow further cannot be attributed to condensational (or coagulational) losses. $GR_{4.5\text{-}20}$ ranged between 2.47 and 7.31 nm h^{-1} (4.69 ± 2.03 nm h^{-1}), $GR_{1.9\text{-}4.5}$ ranged between 3.12 and 5.20 nm h^{-1} (4.36 ± 1.02 nm h^{-1}). The survival parameter (P) as suggested by Kulmala et al. (2017) is defined as $CS \cdot 10^{-4}$ / GR, and for this data is equal to 41, higher than other European cities.

Figure 2 contains box plots showing condensation sink, temperature and global radiation for all 3 NPF types across the entire day (diurnal profiles plotted in Figure S2). Condensation sinks during NPF periods of both types (Figures 1(b) & 1(c)) were not significantly lower than in non-event periods. Condensation sinks were supressed prior to the beginning of an event for full-events, increasing relative to non-events through the afternoon period. Of the two burst-events, one was similarly characterised by a suppression to condensation sink, whereas the other showed a sharp rise in the midday. Global radiation and temperature were higher for full-events, most significantly for temperature. Figure 3 is as Figure 2 but for sulphuric acid, ammonia and amines, and HOMs as measured by CI-Api-ToF (HOM criteria are discussed in section 3.3.1). Sulphuric acid is elevated during both full-event and burst-event periods. In urban Barcelona, sulphuric acid will primarily arise from oxidation of SO_2 by the $OH^{\cdot}$ radical, with anthropogenic emissions such as shipping

emissions from the port areas being significant sources of SO_2 (Henschel et al., 2013). Direct traffic emissions have been shown to be a significant primary sulphuric acid source (Olin et al., 2020), but our sulphuric acid data show no traffic peaks. Ammonia and amines show enhancement for full-event periods, but not burst-event periods. Nucleation rates (at typical tropospheric sulphuric acid concentrations) are sensitive to amine concentrations in the range of a few pptv, with enhancements to amine mixing ratios past this point increasing the nucleation rate marginally (Almeida et al., 2013), while typical concentrations of DMA and other alkylamines vary from zero to a few pptv in the boundary layer (Ge et al., 2011a).

Barcelona has been shown to contain ppbv levels of ammonia (Pandolfi et al., 2012), arising from both agriculture to the north (Van Damme et al., 2018), and anthropogenic activities such as waste management and traffic, with waste management being the primary ammonia source. Highest ammonia mixing ratios are found in the densely populated old city centre (Reche et al., 2015). Agriculture, waste management, and traffic are also all significant sources of low molecular weight alkylamines, such as DMA (Ábalos et al., 1999; Cadle and Mulawa, 1980; Hutchinson et al., 1982; Ge et al., 2011a), and are likely the source of amines found in this dataset. Activities such as composting and food industry are especially strong sources of trimethylamine (TMA) (Ge et al., 2011a). Although high emission fluxes of TMA are expected in this environment, they are not present in our spectra. The TMA ion has been reported previously with a similar ionisation setup to that utilised in this study (Kürten et al., 2016). On full-event days, the signal for C_2 and C_4 amines has a midday elevation concurrent with peaks to solar radiation (Figure S2), and can help explain the high formation rates we see in this dataset (see section 3.2). The relative strength of these signals are shown in Figure S3, with significantly higher signals attributed to ammonia compared to amines, despite a likely lower sensitivity (Simon et al., 2016).

HOM concentrations were greatly enhanced during full-event periods (factor of 1.5 higher compared to non-NPF mean), but lower during burst-event periods (factor of 1.2 lower compared to non-NPF mean), implying their necessity for growth. The sources and implications of these HOMs are discussed in section 3.3. Further, concentrations of iodine and DMS-derived acids such as iodic acid (HIO_3) and methanesulphonic acid (MSA) are low ($7.8 \cdot 10^5$ and $3.3 \cdot 10^5$ cm^{-3} respectively), indicating a small influence of oceanic emissions on particle nucleation/growth. Extended box plots as Figures 2 & 3 are presented in Figure S4, and HYSPLIT back trajectories per event in Figure S5.

3.2 Mechanisms of New Particle Formation

The correlation between $J_{1.9}$ and concentration of sulphuric acid is plotted in Figure 4. A close relationship between nucleation rates and sulphuric acid concentrations ($R^2 = 0.49$) are consistent with observations globally (Lee et al., 2019). This relationship is not dependent upon condensation sink. These NPF rates have no dependence on other ions as measured by CI-Api-ToF, including HIO_3, MSA, ammonia, amines or HOMs (R^2 for all <0.1). This is not to say that all of these molecules are not involved in the nucleation process, rather that elevations or reductions to their concentrations during nucleation periods do not have significant impact on nucleation rates. In the example of alkylamines, their gas phase concentration may decrease due to clustering with elevated sulphuric acid, as they cluster at around a 1:1 ratio at high amine mixing ratios (Kürten et al., 2014) (and therefore they will not be detectable as free amines). Further, if amines are present at a few pptv, their mixing ratios are significantly higher than our ambient measured sulphuric acid concentrations, and will be sufficient to accelerate nucleation rates (Almeida et al., 2013). Photochemical losses will also be greater during the periods of highest NPF rate (Ge et al., 2011b). The strength of the relationship between sulphuric acid and nucleation rate has been quantitatively reproduced in chamber studies involving the H_2SO_4-H_2O-DMA, and H_2SO_4-H_2O-BioOxOrg system, accurately reproducing tropospheric observations of nucleation rates (Almeida et al., 2013; Riccobono et al., 2014), although a later revision of the former shows nucleation rates at 278 K

exceeding typical tropospheric observations in the presence of high mixing ratios of DMA (Kürten et al., 2018). A comparison between our data and results from the CLOUD chamber is presented in Figure 5; included are the H_2SO_4-H_2O, H_2SO_4-NH_3-H_2O (Kirkby et al., 2011), H_2SO_4-H_2O-DMA (Kürten et al., 2018) and H_2SO_4-BioOxOrg-H_2O systems (Riccobono et al., 2014) – BioOxOrg refers to the oxidation products of pinanediol ($C_{10}H_{18}O_2$) and $OH^{\cdot}$. Data from these chamber experiments is for 278 K and 38 – 39 % relative humidity. Nucleation rates measured in Barcelona ($J_{1.9}$ 178 ± 190 cm^{-3} s^{-1} at [H_2SO_4] $7.1 \cdot 10^6 \pm 2.7 \cdot 10^6$ cm^{-3}) are around an order of magnitude lower than that seen for the H_2SO_4-DMA-H_2SO_4 system , but exceed that of the H_2SO_4-BioOxOrg-H_2O system by ~1 order of magnitude, and that of the H_2SO_4-NH_3-H_2O and H_2SO_4-H_2O system multiple orders of magnitude. No dissimilarity is seen between the data points corresponding to full or burst type nucleation, indicating similar mechanisms of formation, despite lower HOM concentrations on burst-event days. Conversely, research in remote boreal environments show that the mechanism of nucleation can modulate dependent upon the H_2SO_4:HOM ratio (Yan et al., 2018). Model studies of sulphuric acid-amine nucleation show a decline in nucleation rate with an increasing temperature (Almeida et al., 2013; Olenius et al., 2017), as the evaporation rate of sulphuric acid-amine clusters will increase with temperature (Paasonen et al., 2012). Conversely, evaporation rates of such small clusters, and resultant nucleation rates tend to increase modestly with increases in relative humidity, most pronounced at lower amine concentrations (Almeida et al., 2013; Paasonen et al., 2012). Despite this, high nucleation rates at temperatures nearing 300 K have been reported previously (Kuang et al., 2008; Kürten et al., 2016), although these tend to show a temperature dependence (Yu et al., 2016). No higher-order sulphuric acid clusters, sulphuric acid-base clusters, nor sulphuric acid-HOM clusters were visible in the mass spectral data, likely due to these being below the limit of detection of the instrument (Jokinen et al., 2012), so cluster identity cannot be directly identified. Sulfuric acid trimer stabilisation is dependent upon base abundance (Ortega et al 2012), and conversely, sensitivity of nitrate CI-APi-ToF to sulfuric acid-base clusters is reduced due to the high base content of such clusters (Jen et al., 2016).

To further explore the relationship between sulphuric acid clusters and the rate of nucleation, the sulphuric acid dimer:monomer ratio is plotted in Figure 6. The sulphuric acid dimer:monomer ratio is elevated by the presence of gas-phase bases such as DMA, and this elevation is dependent upon both the abundances and proton affinities of such bases (Olenius et al., 2017). Upon charging, evaporation of water and bases from sulphuric acid clusters occurs, and thus these are detected as sulphuric acid dimer (Ortega et al., 2012, 2014). The binding energy of the bisulphate-H_2SO_4 ion is in excess of 40 kcal mol^{-1} (Curtius et al., 2001), and thus minimal declustering of the dimer is expected within the CI-Api-ToF instrument – however, declustering of higher order sulphuric acid clusters has been shown to be sensitive to voltage tune (Passananti et al., 2019), and this likely extends to the dimer also, and as such discrepancies between sets of results due to instrument setup cannot be ruled out. The ratio of sulphuric acid dimer:monomer is also highly sensitive to condensation sinks, with a difference in dimer concentration of approximately a factor of 4 expected at 10^7 cm^{-3} between 0.001 s^{-1} (a clean environment) and 0.03 s^{-1} (condensation sinks during these NPF events measured in this dataset) (Yao et al., 2018) and thus our low dimer:monomer ratio can, in part, be explained by elevated condensation sinks. The dashed line represents the ratio that would be seen due to ion induced clustering (IIC) in the nitrate chemical ionisation system for a 50 ms reaction time (Zhao et al., 2010). The sulphuric acid dimer:monomer ratio seen in the CLOUD H_2SO_4-DMA-H_2O system is plotted, alongside our own data from Barcelona. The ratio from our own data is seen to be much lower than that for the system purely involving DMA as a ternary stabilising species. Similarly, this ratio is lower than for reports of H_2SO_4-DMA-H_2O nucleation in Shanghai (Yao et al., 2018), but is markedly similar to reports in central rural Germany (Kürten et al., 2016). Similar to central Germany, this ratio increases at lower sulphuric acid concentrations to a ratio more similar to the H_2SO_4-DMA-H_2O system. A possible explanation for this is that at higher sulphuric acid concentrations, the concentrations of stronger stabilising bases are insufficient to stabilise all present sulphuric acid, with the higher end of the sulphuric acid concentrations seen in this data roughly equivalent to 1 pptv sulphuric acid (3×10^7

396 cm^{-3} = 1.2 pptv sulphuric acid). We also cannot account for clustering due to naturally charged
397 sulphuric acid in the atmosphere, but ion concentrations in urban environments tend to be small due
398 to efficient sink processes (Hirsikko et al., 2011). Particle formation plausibly operates by sulphuric
399 acid-amine nucleation involving the measured C_2 and C_4 amines in our data, with nucleation rates
400 hindered relative to those measured in the CLOUD experiments by elevated temperatures, and a
401 decline to the sulphuric acid dimer:monomer ratio indicates that base concentrations may be
402 limited. We cannot rule out an involvement of HOMs in particle formation processes, and, as no
403 higher-order clusters were observed, we cannot establish sulphuric acid-amine nucleation with
404 certainty.
405
406 **3.3 HOMs and Growth**
407 **3.3.1 HOM composition and sources**
408 Barcelona, as a densely populated urban agglomerate, is distinct from the remote conditions under
409 which HOMs have primarily been studied (Bianchi et al., 2016, 2017; Schobesberger et al., 2013;
410 Yan et al., 2016), and is characterised by elevated temperatures, insolation and NO_x mixing ratios,
411 as well as a diverse host of potential precursor VOC. The first of these affects HOM yields
412 significantly, as yields are highly dependent upon temperature (Quéléver et al., 2019; Stolzenburg et
413 al., 2018). Lower temperatures result in slower H-abstractions, which will result in the likelihood of
414 an RO_2· To undergo a different reaction pathway, such as termination with HO_2· To increase (Praske
415 et al., 2018). This is particularly important in this study if there is a large energy barrier for the first
416 or second H-abstraction taking place, as this will determine the number of hydrogen bond donating
417 groups, and therefore whether the NO_3^- CI-Api-ToF is sensitive to a molecule or not. Elevated
418 insolation will result in enhanced photochemistry, and thus more rapid RO_2· Formation rates,
419 whereas elevated NO_x will produce more HOM with nitrate ester functionality (Garmash et al.,
420 2020; Rissanen, 2018), which tend towards higher volatilities, and less efficient participation in
421 particle formation (Ehn et al., 2014; Lehtipalo et al., 2018), and growth (Yan et al., 2020).

Oxygenated volatile organic compounds (OVOC) are defined as species visible in the nitrate CI-APi-ToF that do not classify as HOM. Here, the first of the three criteria provided by Bianchi et al. (2019), that HOM must be formed by peroxy radical autoxidation, cannot be applied to define HOM, as knowledge as to whether a molecule is a result of autoxidation requires sound knowledge of the structure of the precursors, oxidants and peroxy radical terminators present, however, the number of molecules observed with $N_n = 2$ is around an order of magnitude lower than that for $N_n = 1$, where the primary source of multiple nitrogen functionalities would be multiple peroxy radical termination reactions from NO_x, and therefore while multiple generations of oxidation have been shown to occur in aromatics (Garmash et al., 2020), it is a small contributor to the concentration of what is classed as HOM here. The second criterion to define HOM are that they must be formed in the gas phase under atmospherically relevant conditions, which we deem appropriately fulfilled as all CI-APi-ToF measurements are of gas phase compounds, and the final criterion is that HOM must contain more than 6 oxygen atoms. To attempt to satisfy these criteria as best possible, the criteria of both containing 6 oxygen atoms and 5 carbon atoms or greater and having an O:C ratio >0.6 is applied.

The diversified range of HOM precursors in Barcelona will be primarily anthropogenic in origin. Averaged PTR-MS mixing ratios of different VOCs are presented in Figure S6. Figure 7(a) shows HOM concentration plotted against temperature, showing a dependence of HOM concentrations on temperature, with a lesser dependence on global radiation. The precursors for these HOMs are presumed to be largely isoprene, alkylbenzenes, monoterpenes, and PAHs. The mean peak intensities assigned to alkylbenzene derived HOMs are approximately a factor of two higher than those assigned to isoprene and monoterpene oxidation across this entire campaign. In this data these VOC mixing ratios are, with the exception of isoprene, not largely temperature dependent, with many of these HOMs forming under negligible or zero insolation, and therefore very low $OH^{\cdot}$ concentrations. These night-time HOMs will not be derived from the oxidation of aromatics,

448 however, as rates of oxidation of alkylbenzenes by O_3 and $NO_3^{\cdot}$ are negligible (Molteni et al, 2018).
449 These night-time HOMs will therefore mostly be derived from biogenic emissions which undergo
450 more rapid nocturnal oxidation, and are likely transported from inland by the land breeze during
451 night (Millán, 2014; Querol et al., 2017). Monoterpene derived HOMs and OVOCs peak in the
452 night-time, with the ratio of $C_{10}H_{15}NO_x$:$C_{10}H_{16}O_x$ with O = 4-11 increasing by almost a factor of 4
453 during the night (Figure S7). Such an increase is indicative of nocturnal monoterpene oxidation by
454 $NO_3^{\cdot}$.
455
456 Operating under the assumption that C_5, C_6, C_7, C_8, and C_9 HOMs primarily arise from isoprene,
457 benzene toluene, C_2-alkylbenzene C_3-alkylbenzene oxidation respectively (Massoli et al., 2018;
458 Molteni et al., 2018; Wang et al., 2017), HOM signals plotted against parent VOC concentration
459 indicate their dependence upon that VOC. Here, a C_7 HOM is thought to follow the formula $C_7H_{8-12}O_{5-10}N_{0-2}$. We have plotted HOM concentrations against VOC concentrations in Figure 7(b). C_{10}
461 HOMs are not included in these analyses as these may primarily arise from $C_{10}H_{12-14}$ alkylbenzene,
462 or monoterpene oxidation. HOM concentration appears mostly independent of VOC concentration,
463 with the exception of isoprene, for which emissions are highly temperature dependent, and thus this
464 is likely a function of the effect of temperature on HOM formation (Figure 7(a)). A lack of
465 correlation between other VOCs and their HOMs confirms that this relationship between HOMs
466 and temperature is not a function of enhanced VOC emission fluxes from, for example, evaporation,
467 except in the instance of isoprene. Fragmented monoterpene oxidation products will also contribute
468 to the total number of C_9 HOMs, and similarly, other VOCs can fragment upon oxidation. However,
469 these results indicate that HOM concentrations are elevated by temperature, and operate quite
470 independent of precursor VOC concentration.
471
472 DBE as calculated by equation 3 is equal to the number of pi bonds and rings within a molecule.
473 Benzene, toluene, and similar aromatics have DBE = 4, naphthalene = 7 and monoterpenes = 3.

DBE can be used as an indicator of sources when considering HOM in bulk. Saturation mass concentration as calculated by equation 4 can help describe capacity of a molecule to both condense onto newly formed particles and participate in nucleation. Figure 8 shows concentrations of HOMs and other oxygenated organic molecules binned to the nearest integer $Log_{10}(C^*)(300\ K)$, coloured by DBE. Mean ion signals per carbon number are shown in Figure S8. Most measured molecules fall into the SVOC class ($0.3 < C^*(300\ K) < 300\ \mu g\ m^{-3}$) which will mostly exist in equilibrium between gas and particle phase. Highest SVOC concentrations arise from fingerprint molecules for isoprene oxidation under high NO_x concentrations ($C_5H_{10}N_2O_8$) (Brean et al., 2020), and oxidation of small alkylbenzenes ($C_7H_8O_5$, $C_8H_{10}O_5$). LVOC and ELVOC ($3{\cdot}10^{-5} < C^* < 0.3\ \mu g\ m^{-3}$ and $3{\cdot}10^{-9} < C^*(300\ K) < 3{\cdot}10^{-5}\ \mu g\ m^{-3}$ respectively) have a greater contribution from molecules with higher DBE, i.e., $C_{10}H_{10}O_8$ arising most likely from PAH oxidation (Molteni et al., 2018), and $C_{10}H_{15}O_7N$, a common molecule arising from monoterpene oxidation in the presence of NO_x. The contribution of molecules with carbon number ≤ 9 to these LVOC is modest, and ELVOCs are entirely comprised of molecules with carbon numbers ≥ 10, and is dominated by DBEs of 8 and 4, attributable to PAH and monoterpene oxidation respectively. No molecules classed as ultra-low volatility organic compounds (ULVOC, $C^*(300\ K) < 3{\cdot}10^{-9}\ \mu g\ m^{-3}$) were observed in our data, and thus any pure HOM nucleation is unlikely.

3.3.2 HOMs and NPF

As shown in Figure 3, an elevated HOM concentration appears to be a necessary condition for particle growth past 10 nm during NPF events. These days are associated with elevated temperatures, solar radiation, higher ozone, and lower $NO:NO_2$ ratio. HIO_3 is also significantly higher on burst-event days. A recent study in a remote environment reports growth rates matching condensation rates without accounting for aqueous phase chemistry (Mohr et al., 2019). From 2D-VBS volatility calculations discussed in the previous section, is it shown that LVOC and ELVOC measured in Barcelona plausibly arise from the oxidation of aromatics (particularly PAHs in the case of ELVOC)

and monoterpenes. Calculated growth rates according to the method of Nieminen et al. (2010) are presented in Figure S9 for both $GR_{1.9–5}$ and $GR_{5\text{-}20}$. Best agreement for $GR_{5\text{-}20}$ is when condensation of SVOC, LVOC, ELVOC, MSA, HIO_3 and H_2SO_4 is considered, and best agreement for $GR_{1.9\text{-}5}$ is seen for condensation of all these except SVOC. This SIMPOL based estimate of volatility neglects effects of the flexible -OOH groups to participate in internal H-bonding. This will limit the ability of a molecule to participate in intermolecular bonding, and therefore underpredicts C^* (Kúrten et al., 2016). Conversely, evidence from chamber studies suggests that oxidation of aromatics may proceed by multi-generational $OH^{\cdot}$ oxidation, possibly resulting in an overprediction of C^* (Garmash et al., 2020; Wang et al., 2020). The application of our volatility estimates here therefore come with some uncertainties, with previous work applying an order of magnitude systematic error on the saturation mass concentration (Stolzenburg et al., 2018). Despite such uncertainty, these results indicate an essential role of the condensation of organic compounds to produce high growth rates observed in urban environments.

Figure 9 shows three mass-defect plots for a non-event period, full-event period, and burst-event period. The non-event day included in Figure 8 was characterised by lower solar radiation and temperatures than average, so lower signals for oxygenated species are seen due to weaker photochemistry (i.e., $OH^{\cdot}$ concentration), and slower autoxidation due to slower H-shift reactions (Frege et al., 2018; Quéléver et al., 2019; Stolzenburg et al., 2018). The full-event day sees enhancements to smaller OVOCs and HOMs compared to the non-event day, especially around 150-200 m/Q, which contains peaks corresponding to dicarboxylic acids and isoprene oxidation products. Some of the largest peaks in the mass spectra correspond to formulae seen arising from the enhanced $OH^{\cdot}$ oxidation of alkylbenzenes (such as $C_7H_7NO_6$) (Molteni et al., 2018; Wang et al., 2017). Larger HOMs see a less significant enhancement to smaller alkylbenzene derived HOMs. The presence of larger, unidentified HOMs >400 m/Q is enhanced during full-events, these peaks will comprise the largest compounds, most likely of class ELVOC, arising from the oxidation of

large VOCs, or RO_2·-RO_2· accretion reactions, and thus, we likely underpredict ELVOC concentrations and resultant impacts on particle growth in Figure S9. These unidentified peaks >400 m/Q are both more numerous and larger during full-event periods, with a factor of two difference in total peak area. The burst-event day has significantly lower concentrations of OVOCs and HOMs, and to a lesser degree, their nitrogen containing counterparts (N-OVOCs and N-HOMs), with significantly fewer compounds >400 m/Q. The most significant difference between full and burst-event days is in the SVOCs, accounting for a factor of two difference in concentration. The sulphur containing acids all have similar peak areas to the full-event day. These elevations to condensable OVOCs and HOMs on particle formation days with growth are consistent with particle composition data as measured by ACSM (Figure S10). Particle composition on full-event days shows an elevation to organic mass concentration in the late evening and night around when new particles from NPF will reach sizes detectable by the ACSM (~75 nm, Ng et al., 2011). Organic mass between 16:00 and 23:00 is 3.5 μg m^{-3} on burst-event days, versus 7.8 μg m^{-3} on full-event days.

4. CONCLUSIONS

We show new particle formation rates in Barcelona are linearly dependent upon the sulphuric acid concentrations, and while formation rates far exceed that of H_2SO_4-BioOxOrg-H_2O nucleation, they fall short of those of H_2SO_4-DMA-H_2O nucleation at 278 K, as does the sulphuric acid dimer:monomer ratio, possibly explained by cluster evaporation due to high temperatures in summertime Barcelona (303 K during events), and limited pools of gas-phase amines. These results are similar to reports of nucleation rates in rural Germany (Kürten et al., 2016). As no higher-order clusters were directly measured, we cannot determine nucleation mechanisms with certainty, and an involvement of HOMs in nucleation is plausible.

High concentrations of OVOCs and HOMs were measured by CI-APi-ToF. Of these, the SVOC arose from mostly isoprene and alkylbenzene oxidation, whereas LVOC and ELVOC arose from alkylbenzene, monoterpene and PAH oxidation together, with a dependence of their concentration on temperature. Concentrations of species associated with coastal and oceanic sources such as MSA and HIO_3 were low. High HOM concentrations are seen to be a necessary condition for new particle growth past 10 nm, with the most significant difference between days with and without particle growth being SVOC concentrations (factor of 2 difference), while modelled growth rates from condensation of these organic compounds, alongside H_2SO_4, MSA and HIO_3 were shown to match growth rates within measurement error. Thus, oxidation of traffic derived alkylbenzenes and PAHs, and to a lesser degree, isoprene and monoterpene emissions is a significant determinant of new particle growth in this environment.

These results are consistent with extensive chamber and flow tube studies on particle formation from sulphuric acid, amines and HOMs, and further, nucleation rates relative to sulphuric acid are similar to many tropospheric observations. Barcelona is representative of many Mediterranean urban environments, with moderate pollution, influence of shipping emissions, and high insolation, and the present study reveals the complexity of NPF mechanisms in these environments.

DATA AVAILABILITY

Data supporting this publication are openly available from the UBIRA eData repository at https://doi.org/10.25500/edata.bham.00000434

AUTHOR CONTRIBUTIONS

RMH and XQ conceived the study, JB and DCSB carried out the CI-APi-TOF and related measurements with assistance from AA and MCM. The VOC measurements were proposed by NM

and collected by BT-R. JB wrote the first draft of the manuscript which was enhanced by contributions from the co-authors.

COMPETING INTERESTS

The authors have no conflict of interests.

ACKNOWLEDGEMENTS

Financial assistance from the Spanish Ministry of Science, Innovation and Universities and Competitiveness and FEDER funds under the project HOUSE (CGL2016-78594-R), and by the Generalitat de Catalunya (AGAUR 2017 SGR41) is gratefully acknowledged. MCM acknowledges the Ramón y Cajal Fellowship awarded by the Spanish Ministry. Financial support of the UK scientists by the Natural Environment Research Council through the National Centre for Atmospheric Science is also acknowledged (R8/H12/83/011).

FIGURE LEGENDS:

Figure 1: Average SMPS contour plots for (a) non-event days, (b) full-event days and (c) burst-event days.

Figure 2: Box plots for days of non-event, full-event and burst-event, showing (a) condensation sink, (b) temperature, and (c) global radiation from hourly data. "Full-event" and "burst-event" include data across the entire day.

Figure 3: Box plots for days of non-event, full-event and burst-event, showing (a) sulphuric acid, (b) C_2 and C_4 amines, as clustered with the nitrate dimer and trimer, and (c) summed HOM concentration from C_5+ from hourly data. Units for ammonia + amines are normalised counts, as no calibration was performed. Event days include data across the full event day.

Figure 4: Formation rate ($J_{1.9}$) plotted against sulphuric acid monomer concentration, coloured by condensation sink. Circles represent burst-events, squares represent full events. Data is for hourly averages across NPF periods, typically within the hours 08:00 – 16:00. Slope of the line = $4.9 \cdot 10^{-5}$ s^{-1}. Error bars represent systematic uncertainties on [H_2SO4] and $J_{1.9}$

Figure 5: Formation rate plotted against sulphuric acid monomer concentration for data collected from Barcelona. Tan circles represent burst-events, purple squares represent full events. as well as that for the H_2SO_4-H_2O (blue inverted triangles), H_2SO_4-NH_3-H_2O (yellow inverted triangles), H_2SO_4-DMA-H_2O (pink triangles), and H_2SO_4-BioOxOrg-H_2O (brown diamonds) systems from the CLOUD chamber (Kürten et al., 2018 Kirkby et al., 2011; Riccobono et al., 2014). CLOUD chamber experiments were performed at 278 K and 38 – 39 % RH. Data is for hourly averages across NPF periods, typically within the hours 08:00 – 16:00. Error bars represent systematic uncertainties on [H_2SO_4] and $J_{1.9}$.

Figure 6: Sulphuric acid dimer concentration plotted against monomer concentration, showing burst-event periods (tan circles), full event periods (purple squares), non-event periods (green inverted triangles), and the ratio of sulphuric acid dimer:monomer in the CLOUD chamber for the H_2SO_4-H_2O-DMA system (pink triangles) (Almeida et al., 2013). Dashed line represents the dimer concentration produced by ion induced clustering in the chemical ionization unit (Zhao et al., 2010). CLOUD chamber experiments were performed at 278 K and 38 – 39 % RH. Data is for hourly averages across NPF periods, typically within the hours 08:00 – 16:00. Error bars represent systematic uncertainties on [H_2SO_4] and [$(H_2SO_4)_2$].

Figure 7: Influencing factors on HOM concentration, showing (a) $C_{5\text{-}10}$ HOM concentration plotted against temperature, coloured by global radiation. Ellipsis shows 95% confidence on a multivariate t-distribution. (b) HOM concentration by carbon number potted against parent VOC mixing ratio. These are segregated by carbon number/VOC, i.e, C_7 HOMs plotted against toluene, under the assumption that toluene oxidation is the main producer of C_7 HOMs. Time for both plots is of hourly time resolution.

Figure 8: Concentrations of all oxygenated organic molecules and HOMs binned to integer $Log_{10}(C^*)$ values, coloured by DBE.

Figure 9: Mass defect plots for (a) non-event, (b) full-event, and (c) burst-event periods, data taken from 10:00 – 15:00 on the days 11/07/2018, 16/07/2018 and 15/07/2018 respectively. Size corresponds to mass spectral peak area. Ions are coloured according to identified chemical composition. *Blue* points correspond to HOMs containing all organic species with ≥5 carbon atoms and ≥6 oxygen atoms, and an O:C ratio of >0.6. *Purple* points correspond to the same but for species containing 1-2 nitrogen atoms. Species not meeting this HOM criterea were classed generally as OVOCs which are coloured *brown,* with the nitrogen containing OVOCs coloured *orange*. Sulphur acids (*red*) include ions HSO_4^-, $CH_3SO_3^-$ and SO_5^-, as well as the sulphuric acid dimer. Iodine acids (*green*) contains both IO_3^- and I^- (the latter presumably deprotonated hydrogen iodide). Unidentified points are left uncoloured.

REFERENCES

Ábalos, M., Bayona, J. M. and Ventura, F.: Development of a solid-phase microextraction GC-NPD procedure for the determination of free volatile amines in wastewater and sewage-polluted waters, Anal. Chem., 71(16), 3531–3537, doi:10.1021/ac990197h, 1999.

Almeida, J., Schobesberger, S., Kürten, A., Ortega, I. K., Kupiainen-Määttä, O., Praplan, A. P., Adamov, A., Amorim, A., Bianchi, F., Breitenlechner, M., David, A., Dommen, J., Donahue, N. M., Downard, A., Dunne, E., Duplissy, J., Ehrhart, S., Flagan, R. C., Franchin, A., Guida, R., Hakala, J., Hansel, A., Heinritzi, M., Henschel, H., Jokinen, T., Junninen, H., Kajos, M., Kangasluoma, J., Keskinen, H., Kupc, A., Kurtén, T., Kvashin, A. N., Laaksonen, A., Lehtipalo, K., Leiminger, M., Leppä, J., Loukonen, V., Makhmutov, V., Mathot, S., McGrath, M. J., Nieminen, T., Olenius, T., Onnela, A., Petäjä, T., Riccobono, F., Riipinen, I., Rissanen, M., Rondo, L., Ruuskanen, T., Santos, F. D., Sarnela, N., Schallhart, S., Schnitzhofer, R., Seinfeld, J. H., Simon, M., Sipilä, M., Stozhkov, Y., Stratmann, F., Tomé, A., Tröstl, J., Tsagkogeorgas, G., Vaattovaara, P., Viisanen, Y., Virtanen, A., Vrtala, A., Wagner, P. E., Weingartner, E., Wex, H., Williamson, C., Wimmer, D., Ye, P., Yli-Juuti, T., Carslaw, K. S., Kulmala, M., Curtius, J., Baltensperger, U., Worsnop, D. R., Vehkamäki, H. and Kirkby, J.: Molecular understanding of sulphuric acid-amine particle nucleation in the atmosphere, Nature, 502(7471), 359–363, doi:10.1038/nature12663, 2013.

Bianchi, F., Tröstl, J., Junninen, H., Frege, C., Henne, S., Hoyle, C. R., Molteni, U., Herrmann, E., Bukowiecki, N., Chen, X., Duplissy, J., Gysel, M., Hutterli, M., Kangasluoma, J., Kontkanen, J., Manninen, H. E., Münch, S., Peräkylä, O., Petäjä, T., Rondo, L., Williamson, C., Weingartner, E., Worsnop, D. R., Kulmala, M., Dommen, J. and Baltensperger, U.: New particle formation in the free troposphere : A question of chemistry and timing, Science, 5456(May), 1–11, 2016.

Bianchi, F., Garmash, O., He, X., Yan, C., Iyer, S., Rosendahl, I., Xu, Z., Rissanen, M. P., Riva, M., Taipale, R., Sarnela, N., Petäjä, T., Worsnop, D. R., Kulmala, M., Ehn, M. and Junninen, H.: The role of highly oxygenated molecules (HOMs) in determining the composition of ambient ions in the boreal forest, Atmos. Chem. Phys., 17(22), 13819–13831, doi:10.5194/acp-17-13819-2017, 2017.

Bianchi, F., Kurtén, T., Riva, M., Mohr, C., Rissanen, M. P., Roldin, P., Berndt, T., Crounse, J. D., Wennberg, P. O., Mentel, T. F., Wildt, J., Junninen, H., Jokinen, T., Kulmala, M., Worsnop, D. R., Thornton, J. A., Donahue, N., Kjaergaard, H. G. and Ehn, M.: Highly Oxygenated Organic Molecules (HOM) from Gas-Phase Autoxidation Involving Peroxy Radicals: A Key Contributor to Atmospheric Aerosol, Chem. Rev., 2019.

Bousiotis, D., Dall'osto, M., Beddows, D. C. S., Pope, F. D. and Harrison, R. M.: Analysis of new particle formation (NPF) events at nearby rural, urban background and urban roadside sites, Atmos. Chem. Phys, 19, 5679–5694, doi:10.5194/acp-19-5679-2019, 2019.

Brean, J., Harrison, R. M., Shi, Z., Beddows, D. C. S., Acton, W. J. F., Hewitt, C. N., Squires, F. A., and Lee, J.: Observations of highly oxidized molecules and particle nucleation in the atmosphere of Beijing, Atmos. Chem. Phys., 19, 14933–14947, https://doi.org/10.5194/acp-19-14933-2019, 2019.

Brines, M., Dall'Osto, M., Beddows, D. C. S., Harrison, R. M., and Querol, X.: Simplifying aerosol size distributions modes simultaneously detected at four monitoring sites during SAPUSS, Atmos. Chem. Phys., 14, 2973–2986, https://doi.org/10.5194/acp-14-2973-2014, 2014.

Brines, M., Dall'Osto, M., Beddows, D. C. S., Harrison, R. M., Gómez-Moreno, F., Núñez, L., Artíñano, B., Costabile, F., Gobbi, G. P., Salimi, F., Morawska, L., Sioutas, C., and Querol, X.: Traffic and nucleation events as main sources of ultrafine particles in high-insolation developed world cities, Atmos. Chem. Phys., 15, 5929–5945, https://doi.org/10.5194/acp-15-5929-2015, 2015.

Cadle, S. H. and Mulawa, P. A.: Low-molecular-weight aliphatic amines in exhaust from catalyst-equipped cars, Environ. Sci. Technol., 14(6), 718–723, doi:10.1021/es60166a011, 1980.

Carnerero, C., Pérez, N., Petäjä, T., Laurila, T. M., Ahonen, L. R., Kontkanen, J., Ahn, K. H., Alastuey, A. and Querol, X.: Relating high ozone, ultrafine particles, and new particle formation episodes using cluster analysis, Atmos. Environ. X, 4(May), 1–20, doi:10.1016/j.aeaoa.2019.100051, 2019.

Cohen, A. J., Brauer, M., Burnett, R., Anderson, H. R., Frostad, J., Estep, K., Balakrishnan, K., Brunekreef, B., Dandona, L., Dandona, R., Feigin, V., Freedman, G., Hubbell, B., Jobling, A., Kan, H., Knibbs, L., Liu, Y., Martin, R., Morawska, L., Pope, C. A., Shin, H., Straif, K., Shaddick, G., Thomas, M., van Dingenen, R., van Donkelaar, A., Vos, T., Murray, C. J. L. and Forouzanfar, M. H.: Estimates and 25-year trends of the global burden of disease attributable to ambient air pollution: an analysis of data from the Global Burden of Diseases Study 2015, Lancet, 389(10082), 1907–1918, doi:10.1016/S0140-6736(17)30505-6, 2017.

Cubison, M. J. and Jimenez, J. L.: Statistical precision of the intensities retrieved from constrained fitting of overlapping peaks in high-resolution mass spectra, Atmos. Meas. Tech., 8(6), 2333–2345, doi:10.5194/amt-8-2333-2015, 2015.

Curtius, J., Froyd, K. D. and Lovejoy, E. R.: Cluster ion thermal decomposition (I): Experimental kinetics study and ab initio calculations for $HSO_4^-(H_2SO_4)_x(HNO_3)_y$, J. Phys. Chem. A, 105(48), 10867–10873, doi:10.1021/jp0124950, 2001.

Dal Maso, M., Kulmala, M., Riipinen, I., Wagner, R., Hussein, T., Aalto, P. P. and Lehtinen, K. E. J.: Formation and growth of fresh atmospheric aerosols: Eight years of aerosol size distribution data from SMEAR II, Hyytiälä, Finland, Boreal Environ. Res., 10(5), 323–336, 2005.

Dall'Osto, M., Querol, X., Alastuey, A., O'Dowd, C., Harrison, R. M., Wenger, J. and Gómez-Moreno, F. J.: On the spatial distribution and evolution of ultrafine particles in Barcelona, Atmos. Chem. Phys., 13(2), 741–759, doi:10.5194/acp-13-741-2013, 2013.

Donahue, N. M., Epstein, S. A., Pandis, S. N. and Robinson, A. L.: Atmospheric Chemistry and Physics A two-dimensional volatility basis set: 1. organic-aerosol mixing thermodynamics, Atmos. Chem. Phys, 11, 3303–3318, doi:10.5194/acp-11-3303-2011, 2011.

Ehn, M., Thornton, J. A., Kleist, E., Sipilä, M., Junninen, H., Pullinen, I., Springer, M., Rubach, F., Tillmann, R., Lee, B., Lopez-Hilfiker, F., Andres, S., Acir, I.-H., Rissanen, M., Jokinen, T., Schobesberger, S., Kangasluoma, J., Kontkanen, J., Nieminen, T., Kurtén, T., Nielsen, L. B., Jørgensen, S., Kjaergaard, H. G., Canagaratna, M., Maso, M. D., Berndt, T., Petäjä, T., Wahner, A., Kerminen, V.-M., Kulmala, M., Worsnop, D. R., Wildt, J. and Mentel, T. F.: A large source of low-volatility secondary organic aerosol, Nature, 506(7489), 476–479, doi:10.1038/nature13032, 2014.

Elm, J., Myllys, N. and Kurtén, T.: What is Required for Highly Oxidized Molecules to Form Clusters with Sulphuric Acid?, J. Phys. Chem. A, 121(23), 4578–4587, doi:10.1021/acs.jpca.7b03759, 2017.

Frege, C., Ortega, I. K., Rissanen, M. P., Praplan, A. P., Steiner, G., Heinritzi, M., Ahonen, L., Amorim, A., Bernhammer, A. K., Bianchi, F., Brilke, S., Breitenlechner, M., Dada, L., Dias, A., Duplissy, J., Ehrhart, S., El-Haddad, I., Fischer, L., Fuchs, C., Garmash, O., Gonin, M., Hansel, A., Hoyle, C. R., Jokinen, T., Junninen, H., Kirkby, J., Kürten, A., Lehtipalo, K., Leiminger, M., Lee Mauldin, R., Molteni, U., Nichman, L., Petäjä, T., Sarnela, N., Schobesberger, S., Simon, M., Sipilä,

M., Stolzenburg, D., Tomé, A., Vogel, A. L., Wagner, A. C., Wagner, R., Xiao, M., Yan, C., Ye, P., Curtius, J., Donahue, N. M., Flagan, R. C., Kulmala, M., Worsnop, D. R., Winkler, P., Dommen, J. and Baltensperger, U.: Influence of temperature on the molecular composition of ions and charged clusters during pure biogenic nucleation, Atmos. Chem. Phys., 18(1), 65–79, doi:10.5194/acp-18-65-2018, 2018.

Garmash, O., Rissanen, M. P., Pullinen, I., Schmitt, S., Kausiala, O., Tillmann, R., Zhao, D., Percival, C., Bannan, T. J., Priestley, M., Hallquist, Å. M., Kleist, E., Kiendler-Scharr, A., Hallquist, M., Berndt, T., McFiggans, G., Wildt, J., Mentel, T. F., and Ehn, M.: Multi-generation OH oxidation as a source for highly oxygenated organic molecules from aromatics, Atmos. Chem. Phys., 20, 515–537, doi:10.5194/acp-20-515-2020, 2020.

Ge, X., Wexler, A. S. and Clegg, S. L.: Atmospheric amines – Part I. A review, Atmos. Environ., 45(3), 524–546, doi:10.1016/j.atmosenv.2010.10.012, 2011a.

Ge, X., Wexler, A. S. and Clegg, S. L.: Atmospheric amines – Part II. Thermodynamic properties and gas/particle partitioning, Atmos. Environ., 45(3), 561–577, doi:10.1016/j.atmosenv.2010.10.013, 2011b.

Graus, M., Müller, M. and Hansel, A.: High resolution PTR-TOF: Quantification and Formula Confirmation of VOC in Real Time, J. Am. Soc. Mass Spectrom., 21(6), 1037–1044, doi:10.1016/j.jasms.2010.02.006, 2010.

Guo, S., Hu, M., Zamora, M. L., Peng, J., Shang, D., Zheng, J., Du, Z., Wu, Z., Shao, M., Zeng, L., Molina, M. J. and Zhang, R.: Elucidating severe urban haze formation in China., Proc. Natl. Acad. Sci. U. S. A., 111(49), 17373–8, doi:10.1073/pnas.1419604111, 2014.

Harrison, R. M., Rob Mackenzie, A., Xu, H., Alam, M. S., Nikolova, I., Zhong, J., Singh, A., Zeraati-Rezaei, S., Stark, C., Beddows, D. C. S., Liang, Z., Xu, R. and Cai, X.: Diesel exhaust nanoparticles and their behaviour in the atmosphere, Proc. R. Soc. A Math. Phys. Eng. Sci., 474(2220), doi:10.1098/rspa.2018.0492, 2018.

Henschel, S., Querol, X., Atkinson, R., Pandolfi, M., Zeka, A., Tertre, A. L., Analistis, A., Katsouyanni, K., Chanel, O., Pascal, M., Bouland, C., Haluza, D., Medina, S., and Goodman, P. G.: Ambient air SO_2 patterns in 6 European cities, Atmos. Environ., 79, 236–247, doi:10.1016/j.atmosenv.2013.06.008, 2013.

Hirsikko, A., Nieminen, T., Gagné, S., Lehtipalo, K., Manninen, H. E., Ehn, M., Hõrrak, U., Kerminen, V.-M., Laakso, L., Mcmurry, P. H., Mirme, A., Mirme, S., Petäjä, T., Tammet, H., Vakkari, V., Vana, M. and Kulmala, M.: Atmospheric ions and nucleation: a review of observations, Atmos. Chem. Phys, 11, 767–798, doi:10.5194/acp-11-767-2011, 2011.

Hutchinson, G. L., Mosier, A. R. and Andre, C. E.: Ammonia and Amine Emissions from a Large Cattle Feedlot, J. Environ. Qual., 11(2), 288–293, 1982.

Hyttinen, N., Kupiainen-M tta, O., Rissanen, M. P., Muuronen, M., Ehn, M. and Kurtén, T.: Modeling the Charging of Highly Oxidized Cyclohexene Ozonolysis Products Using Nitrate-Based Chemical Ionization, J. Phys. Chem. A, 119(24), 6339–6345, doi:10.1021/acs.jpca.5b01818, 2015.

IPCC, 2013: Climate Change 2013: The Physical Science Basis. Contribution of Working Group I to the Fifth Assessment Report of the Intergovernmental Panel on Climate Change, edited by V. B. and

P. M. M. Stocker, T.F., D. Qin, G.-K. Plattner, M. Tignor, S.K. Allen, J. Boschung, A. Nauels, Y. Xia, Cambridge University Press, Cambridge., 2014.

Jen, C. N., Zhao, J., McMurry, P. H., and Hanson, D. R.: Chemical ionization of clusters formed from sulfuric acid and dimethylamine or diamines, Atmos. Chem. Phys., 16, 12513–12529, doi:10.5194/acp-16-12513-2016, 2016.

Jokinen, T., Sipilä, M., Junninen, H., Ehn, M., Lönn, G., Hakala, J., Petäjä, T., Mauldin, R. L., Kulmala, M. and Worsnop, D. R.: Atmospheric sulphuric acid and neutral cluster measurements using CI-Api-TOF, Atmos. Chem. Phys., 12(9), 4117–4125, doi:10.5194/acp-12-4117-2012, 2012.

Jokinen, T., Sipilä, M., Kontkanen, J., Vakkari, V., Tisler, P., Duplissy, E.-M., Junninen, H., Kangasluoma, J., Manninen, H. E., Petäjä, T., Kulmala, M., Worsnop, D. R., Kirkby, J., Virkkula, A. and Kerminen, V.-M.: Ion-induced sulphuric acid–ammonia nucleation drives particle formation in coastal Antarctica, Sci. Adv., 4(11), eaat9744, doi:10.1126/sciadv.aat9744, 2018.

Junninen, H., Ehn, M., Petäjä, Luosujärvi, L., Kotiaho, T., Kostiainen, R., Rohner, U., Gonin, M., Fuhrer, K., Kulmala, M. and Worsnop, D. R.: A high-resolution mass spectrometer to measure atmospheric ion composition, Atmos. Meas. Tech., 3(4), 1039–1053, doi:10.5194/amt-3-1039-2010, 2010.

Kerminen, V. M., Chen, X., Vakkari, V., Petäjä, T., Kulmala, M. and Bianchi, F.: Atmospheric new particle formation and growth: Review of field observations, Environ. Res. Lett., 13(10), doi:10.1088/1748-9326/aadf3c, 2018.

Kirkby, J., Curtius, J., Almeida, J., Dunne, E., Duplissy, J., Ehrhart, S., Franchin, A., Gagné, S., Ickes, L., Kürten, A., Kupc, A., Metzger, A., Riccobono, F., Rondo, L., Schobesberger, S., Tsagkogeorgas, G., Wimmer, D., Amorim, A., Bianchi, F., Breitenlechner, M., David, A., Dommen, J., Downard, A., Ehn, M., Flagan, R. C., Haider, S., Hansel, A., Hauser, D., Jud, W., Junninen, H., Kreissl, F., Kvashin, A., Laaksonen, A., Lehtipalo, K., Lima, J., Lovejoy, E. R., Makhmutov, V., Mathot, S., Mikkilä, J., Minginette, P., Mogo, S., Nieminen, T., Onnela, A., Pereira, P., Petäjä, T., Schnitzhofer, R., Seinfeld, J. H., Sipilä, M., Stozhkov, Y., Stratmann, F., Tomé, A., Vanhanen, J., Viisanen, Y., Vrtala, A., Wagner, P. E., Walther, H., Weingartner, E., Wex, H., Winkler, P. M., Carslaw, K. S., Worsnop, D. R., Baltensperger, U. and Kulmala, M.: Role of sulphuric acid, ammonia and galactic cosmic rays in atmospheric aerosol nucleation, Nature, 476(7361), 429–435, doi:10.1038/nature10343, 2011.

Kirkby, J., Duplissy, J., Sengupta, K., Frege, C., Gordon, H., Williamson, C., Heinritzi, M., Simon, M., Yan, C., Almeida, J., Trostl, J., Nieminen, T., Ortega, I. K., Wagner, R., Adamov, A., Amorim, A., Bernhammer, A. K., Bianchi, F., Breitenlechner, M., Brilke, S., Chen, X., Craven, J., Dias, A., Ehrhart, S., Flagan, R. C., Franchin, A., Fuchs, C., Guida, R., Hakala, J., Hoyle, C. R., Jokinen, T., Junninen, H., Kangasluoma, J., Kim, J., Krapf, M., Kürten, A., Laaksonen, A., Lehtipalo, K., Makhmutov, V., Mathot, S., Molteni, U., Onnela, A., Perakyla, O., Piel, F., Petaja, T., Praplan, A. P., Pringle, K., Rap, A., Richards, N. A. D., Riipinen, I., Rissanen, M. P., Rondo, L., Sarnela, N., Schobesberger, S., Scott, C. E., Seinfeld, J. H., Sipila, M., Steiner, G., Stozhkov, Y., Stratmann, F., Tomé, A., Virtanen, A., Vogel, A. L., Wagner, A. C., Wagner, P. E., Weingartner, E., Wimmer, D., Winkler, P. M., Ye, P., Zhang, X., Hansel, A., Dommen, J., Donahue, N. M., Worsnop, D. R., Baltensperger, U., Kulmala, M., Carslaw, K. S. and Curtius, J.: Ion-induced nucleation of pure biogenic particles, Nature, 533(7604), 521–526, doi:10.1038/nature17953, 2016.

Kuang, C., McMurry, P. H., McCormick, A. V. and Eisele, F. L.: Dependence of nucleation rates on sulfuric acid vapor concentration in diverse atmospheric locations, J. Geophys. Res. Atmos., 113(10), 1–9, doi:10.1029/2007JD009253, 2008.

Kulmala, M., Dal Maso, M., Mäkelä, J. M., Pirjola, L., Väkevä, M., Aalto, P., Miikkulainen, P., meri, K. and O'Dowd, C. D.: On the formation, growth and composition of nucleation mode particles, Tellus, Ser. B Chem. Phys. Meteorol., 53(4), 479–490, doi:10.1034/j.1600-0889.2001.d01-33.x, 2001.

Kulmala, M., Petäjä, T., Nieminen, T., Sipilä, M., Manninen, H. E., Lehtipalo, K., Dal Maso, M., Aalto, P. P., Junninen, H., Paasonen, P., Riipinen, I., Lehtinen, K. E. J., Laaksonen, A. and Kerminen, V.-M.: Measurement of the nucleation of atmospheric aerosol particles, Nat. Protoc., 7(9), 1651–1667, doi:10.1038/nprot.2012.091, 2012.

Kulmala, M., Kerminen, V. M., Petäjä, T., Ding, A. J. and Wang, L.: Atmospheric gas-to-particle conversion: Why NPF events are observed in megacities?, Faraday Discuss., 200, 271–288, doi:10.1039/c6fd00257a, 2017.

Kürten, A., Jokinen, T., Simon, M., Sipilä, M., Sarnela, N., Junninen, H., Adamov, A., Almeida, J., Amorim, A., Bianchi, F., Breitenlechner, M., Dommen, J., Donahue, N. M., Duplissy, J., Ehrhart, S., Flagan, R. C., Franchin, A., Hakala, J., Hansel, A., Heinritzi, M., Hutterli, M., Kangasluoma, J., Kirkby, J., Laaksonen, A., Lehtipalo, K., Leiminger, M., Makhmutov, V., Mathot, S., Onnela, A., Petäjä, T., Praplan, A. P., Riccobono, F., Rissanen, M. P., Rondo, L., Schobesberger, S., Seinfeld, J. H., Steiner, G., Tomé, A., Tröstl, J., Winkler, P. M., Williamson, C., Wimmer, D., Ye, P., Baltensperger, U., Carslaw, K. S., Kulmala, M., Worsnop, D. R. and Curtius, J.: Neutral molecular cluster formation of sulfuric acid–dimethylamine observed in real time under atmospheric conditions, Proc. Natl. Acad. Sci., 111(42), 15019–15024, doi:10.1073/pnas.1404853111, 2014.

Kürten, A., Münch, S., Rondo, L., Bianchi, F., Duplissy, J., Jokinen, T., Junninen, H., Sarnela, N., Schobesberger, S., Simon, M., Sipilä, M., Almeida, J., Amorim, A., Dommen, J., Donahue, N. M., Dunne, E. M., Flagan, R. C., Franchin, A., Kirkby, J., Kupc, A., Makhmutov, V., Petäjä, T., Praplan, A. P., Riccobono, F., Steiner, G., Tomé, A., Tsagkogeorgas, G., Wagner, P. E., Wimmer, D., Baltensperger, U., Kulmala, M., Worsnop, D. R. and Curtius, J.: Thermodynamics of the formation of sulfuric acid dimers in the binary (H_2SO_4-H_2O) and ternary (H_2SO_4-H_2O-NH_3) system, Atmos. Chem. Phys., 15(18), 10701–10721, doi:10.5194/acp-15-10701-2015, 2015.

Kürten, A., Bergen, A., Heinritzi, M., Leiminger, M., Lorenz, V., Piel, F., Simon, M., Sitals, R., Wagner, A. C. and Curtius, J.: Observation of new particle formation and measurement of sulphuric acid, ammonia, amines and highly oxidized organic molecules at a rural site in central Germany, Atmos. Chem. Phys., 16(19), 12793–12813, doi:10.5194/acp-16-12793-2016, 2016.

Kürten, A., Li, C., Bianchi, F., Curtius, J., Dias, A., Donahue, N. M., Duplissy, J., Flagan, R. C., Hakala, J., Jokinen, T., Kirkby, J., Kulmala, M., Laaksonen, A., Lehtipalo, K., Makhmutov, V., Onnela, A., Rissanen, M. P., Simon, M., Sipilä, M., Stozhkov, Y., Tröstl, J., Ye, P. and McMurry, P. H.: New particle formation in the sulfuric acid-dimethylamine-water system: Reevaluation of CLOUD chamber measurements and comparison to an aerosol nucleation and growth model, Atmos. Chem. Phys., 18(2), 845–863, doi:10.5194/acp-18-845-2018, 2018.

Kurtén, T., Noppel, M., Vehkamäki, H., Salonen, M. and Kulmala, M.: Quantum chemical studies of hydrate formation of H_2SO_4 and HSO_4^-, Boreal Environ. Res., 12(3), 431–453, 2007.

Kurtén, T., Loukonen, V., Vehkaméki, H. and Kulmala, M.: Amines are likely to enhance neutral and ion-induced sulphuric acid-water nucleation in the atmosphere more effectively than ammonia, Atmos. Chem. Phys., 8(14), 4095–4103, doi:10.5194/acp-8-4095-2008, 2008.

Kurtén, T., Tiusanen, K., Roldin, P., Rissanen, M., Luy, J. N., Boy, M., Ehn, M. and Donahue, N.: α-Pinene Autoxidation Products May Not Have Extremely Low Saturation Vapor Pressures Despite High O:C Ratios, J. Phys. Chem. A, 120(16), 2569–2582, doi:10.1021/acs.jpca.6b02196, 2016.

Lee, S. H., Gordon, H., Yu, H., Lehtipalo, K., Haley, R., Li, Y. and Zhang, R.: New Particle Formation in the Atmosphere: From Molecular Clusters to Global Climate, J. Geophys. Res. Atmos., doi:10.1029/2018JD029356, 2019.

Lehtinen, K. E. J., Dal Maso, M., Kulmala, M. and Kerminen, V. M.: Estimating nucleation rates from apparent particle formation rates and vice versa: Revised formulation of the Kerminen-Kulmala equation, J. Aerosol Sci., 38(9), 988–994, doi:10.1016/j.jaerosci.2007.06.009, 2007.

Lehtinen, K. E. J., Dal Maso, M., Kulmala, M. and Kerminen, V. M.: Estimating nucleation rates from apparent particle formation rates and vice versa: Revised formulation of the Kerminen-Kulmala equation, J. Aerosol Sci., 38(9), 988–994, doi:10.1016/j.jaerosci.2007.06.009, 2007.

Lehtipalo, K., Yan, C., Dada, L., Bianchi, F., Xiao, M., Wagner, R., Stolzenburg, D., Ahonen, L. R., Amorim, A., Baccarini, A., Bauer, P. S., Baumgartner, B., Bergen, A., Bernhammer, A.-K., Breitenlechner, M., Brilke, S., Buchholz, A., Mazon, S. B., Chen, D., Chen, X., Dias, A., Dommen, J., Draper, D. C., Duplissy, J., Ehn, M., Finkenzeller, H., Fischer, L., Frege, C., Fuchs, C., Garmash, O., Gordon, H., Hakala, J., He, X., Heikkinen, L., Heinritzi, M., Helm, J. C., Hofbauer, V., Hoyle, C. R., Jokinen, T., Kangasluoma, J., Kerminen, V.-M., Kim, C., Kirkby, J., Kontkanen, J., Kürten, A., Lawler, M. J., Mai, H., Mathot, S., Mauldin, R. L., Molteni, U., Nichman, L., Nie, W., Nieminen, T., Ojdanic, A., Onnela, A., Passananti, M., Petäjä, T., Piel, F., Pospisilova, V., Quéléver, L. L. J., Rissanen, M. P., Rose, C., Sarnela, N., Schallhart, S., Schuchmann, S., Sengupta, K., Simon, M., Sipilä, M., Tauber, C., Tomé, A., Tröstl, J., Väisänen, O., Vogel, A. L., Volkamer, R., Wagner, A. C., Wang, M., Weitz, L., Wimmer, D., Ye, P., Ylisirniö, A., Zha, Q., Carslaw, K. S., Curtius, J., Donahue, N. M., Flagan, R. C., Hansel, A., Riipinen, I., Virtanen, A., Winkler, P. M., Baltensperger, U., Kulmala, M. and Worsnop, D. R.: Multicomponent new particle formation from sulphuric acid, ammonia, and biogenic vapors, Sci. Adv., 4(12), eaau5363, doi:10.1126/sciadv.aau5363, 2018.

Massoli, P., Stark, H., Canagaratna, M. R., Krechmer, J. E., Xu, L., Ng, N. L., Mauldin, R. L., Yan, C., Kimmel, J., Misztal, P. K., Jimenez, J. L., Jayne, J. T. and Worsnop, D. R.: Ambient Measurements of Highly Oxidized Gas-Phase Molecules during the Southern Oxidant and Aerosol Study (SOAS) 2013, ACS Earth Sp. Chem., 2(7), 653–672, doi:10.1021/acsearthspacechem.8b00028, 2018.

Mikkonen, S., Romakkaniemi, S., Smith, J. N., Korhonen, H., Petäjä, T., Plass-Duelmer, C., Boy, M., McMurry, P. H., Lehtinen, K. E. J., Joutsensaari, J., Hamed, A., Mauldin, R. L., Birmili, W., Spindler, G., Arnold, F., Kulmala, M. and Laaksonen, A.: A statistical proxy for sulphuric acid concentration, Atmos. Chem. Phys., 11(21), 11319–11334, doi:10.5194/acp-11-11319-2011, 2011.

Millán, M.: Extreme hydrometeorological events and climate change predictions in Europe, J. Hydrol., 518(PB), 206–224, doi:10.1016/j.jhydrol.2013.12.041, 2014.

Miller, M. R., Raftis, J. B., Langrish, J. P., McLean, S. G., Samutrtai, P., Connell, S. P., Wilson, S., Vesey, A. T., Fokkens, P. H. B., Boere, A. J. F., Krystek, P., Campbell, C. J., Hadoke, P. W. F., Donaldson, K., Cassee, F. R., Newby, D. E., Duffin, R. and Mills, N. L.: Inhaled Nanoparticles Accumulate at Sites of Vascular Disease, ACS Nano, 11(5), 4542–4552, doi:10.1021/acsnano.6b08551, 2017.

Minguillón, M. C., Brines, M., Pérez, N., Reche, C., Pandol, M., Fonseca, A. S., Amato, F., Alastuey,

A., Lyasota, A., Codina, B., Lee, H., Eun, H., Ahn, K. and Querol, X.: New particle formation at ground level and in the vertical column over the Barcelona area, 165, 118–130, doi:10.1016/j.atmosres.2015.05.003, 2015.

Minguillón, M.C., Pérez, N., Marchand, N., Bertrand, A., Temime-Roussel, B., Agrios, K., Szidat, S., van Drooge, B.L., Sylvestre, A., Alastuey, A., Reche, C., Ripoll, A., Marco, E., Grimalt, J.O., Querol, X.: Secondary organic aerosol origin in an urban environment. Influence of biogenic and fuel combustion precursors. Faraday Discuss., 189, 337-359, 2016.

Mohr, C., Thornton, J. A., Heitto, A., Lopez-Hilfiker, F. D., Lutz, A., Riipinen, I., Hong, J., Donahue, N. M., Hallquist, M., Petäjä, T., Kulmala, M. and Yli-Juuti, T.: Molecular identification of organic vapors driving atmospheric nanoparticle growth, Nat. Commun., 10(1), 1–7, doi:10.1038/s41467-019-12473-2, 2019.

Møller, K. H., Tram, C. M. and Kjaergaard, H. G.: Side-by-Side Comparison of Hydroperoxide and Corresponding Alcohol as Hydrogen-Bond Donors, J. Phys. Chem. A, 121(15), 2951–2959, doi:10.1021/acs.jpca.7b01323, 2017.

Molteni, U., Bianchi, F., Klein, F., El Haddad, I., Frege, C., Rossi, M. J., Dommen, J. and Baltensperger, U.: Formation of highly oxygenated organic molecules from aromatic compounds, Atmos. Chem. Phys., 18(3), 1909–1921, doi:10.5194/acp-18-1909-2018, 2018.

Ng, N. L., Herndon, S. C., Trimborn, A., Canagaratna, M. R., Croteau, P. L., Onasch, T. B., Sueper, D., Worsnop, D. R., Zhang, Q., Sun, Y. L. and Jayne, J. T.: An Aerosol Chemical Speciation Monitor (ACSM) for routine monitoring of the composition and mass concentrations of ambient aerosol, Aerosol Sci. Technol., 45(7), 770–784, doi:10.1080/02786826.2011.560211, 2011.

Nieminen, T., Lehtinen, K. E. J., and Kulmala, M.: Sub-10 nm particle growth by vapor condensation – effects of vapor molecule size and particle thermal speed, Atmos. Chem. Phys., 10, 9773–9779, doi:10.5194/acp-10-9773-2010, 2010

Olenius, T., Halonen, R., Kurtén, T., Henschel, H., Kupiainen-Määttä, O., Ortega, I. K., Jen, C. N., Vehkamäki, H. and Riipinen, I.: New particle formation from sulfuric acid and amines: Comparison of monomethylamine, dimethylamine, and trimethylamine, J. Geophys. Res., 122(13), 7103–7118, doi:10.1002/2017JD026501, 2017.

Olin, M., Kuuluvainen, H., Aurela, M., Kalliokoski, J., Kuittinen, N., Isotalo, M., Timonen, H. J., Niemi, J. V., Rönkkö, T., and Dal Maso, M.: Traffic-originated nanocluster emission exceeds H_2SO_4-driven photochemical new particle formation in an urban area, Atmos. Chem. Phys., 20, 1–13, https://doi.org/10.5194/acp-20-1-2020, 2020.

Ortega, I. K., Olenius, T., Kupiainen-Määttä, O., Loukonen, V., Kurtén, T., and Vehkamäki, H.: Electrical charging changes the composition of sulfuric acid–ammonia/dimethylamine clusters, Atmos. Chem. Phys., 14, 7995–8007, https://doi.org/10.5194/acp-14-7995-2014, 2014.

Paasonen, P., Olenius, T., Kupiainen, O., Kurtén, T., Petäjä, T., Birmili, W., Hamed, A., Hu, M., Huey, L. G., Plass-Duelmer, C., Smith, J. N., Wiedensohler, A., Loukonen, V., McGrath, M. J., Ortega, I. K., Laaksonen, A., Vehkamäki, H. and Kulmala, M.: On the formation of sulphuric acid – Amine clusters in varying atmospheric conditions and its influence on atmospheric new particle formation, Atmos. Chem. Phys., 12(19), 9113–9133, doi:10.5194/acp-12-9113-2012, 2012.

Pandolfi, M., Amato, F., Reche, C., Alastuey, A., Otjes, R. P., Blom, M. J. and Querol, X.: Summer ammonia measurements in a densely populated Mediterranean city, Atmos. Chem. Phys., 12(16), 7557–7575, doi:10.5194/acp-12-7557-2012, 2012.

Passananti, M., Zapadinsky, E., Zanca, T., Kangasluoma, J., Myllys, N., Rissanen, M. P., Kurtén, T., Ehn, M., Attoui, M. and Vehkamäki, H.: How well can we predict cluster fragmentation inside a mass spectrometer?, Chem. Commun., 55(42), 5946–5949, doi:10.1039/c9cc02896j, 2019.

Penner, J. E., Xu, L. and Wang, M.: Satellite methods underestimate indirect climate forcing by aerosols., Proc. Natl. Acad. Sci. U. S. A., 108(33), 13404–13408, doi:10.1073/pnas.1018526108, 2011.

Praske, E., Otkjær, R. V., Crounse, J. D., Hethcox, J. C., Stoltz, B. M., Kjaergaard, H. G. and Wennberg, P. O.: Atmospheric autoxidation is increasingly important in urban and suburban North America, Proc. Natl. Acad. Sci., 115(1), 64–69, doi:10.1073/pnas.1715540115, 2018.

Quéléver, L. L. J., Kristensen, K., Normann Jensen, L., Rosati, B., Teiwes, R., Daellenbach, K. R., Peräkylä, O., Roldin, P., Bossi, R., Pedersen, H. B., Glasius, M., Bilde, M. and Ehn, M.: Effect of temperature on the formation of highly oxygenated organic molecules (HOMs) from alpha-pinene ozonolysis, Atmos. Chem. Phys, 19, 7609–7625, doi:10.5194/acp-19-7609-2019, 2019.

Querol, X., Gangoiti, G., Mantilla, E., Alastuey, A., Minguillón, M. C., Amato, F., Reche, C., Viana, M., Moreno, T., Karanasiou, A., Rivas, I., Pérez, N., Ripoll, A., Brines, M., Ealo, M., Pandolfi, M., Lee, H. K., Eun, H. R., Park, Y. H., Escudero, M., Beddows, D., Harrison, R. M., Bertrand, A., Marchand, N., Lyasota, A., Codina, B., Olid, M., Udina, M., Jiménez-Esteve, B., Jiménez-Esteve, B. B., Alonso, L., Millán, M. and Ahn, K. H.: Phenomenology of high-ozone episodes in NE Spain, Atmos. Chem. Phys., 17(4), 2817–2838, doi:10.5194/acp-17-2817-2017, 2017.

Reche, C., Viana, M., Karanasiou, A., Cusack, M., Alastuey, A., Artiñano, B., Revuelta, M. A., López-Mahía, P., Blanco-Heras, G., Rodríguez, S., Sánchez de la Campa, A. M., Fernández-Camacho, R., González-Castanedo, Y., Mantilla, E., Tang, Y. S. and Querol, X.: Urban NH_3 levels and sources in six major Spanish cities, Chemosphere, 119, 769–777, doi:10.1016/j.chemosphere.2014.07.097, 2015.

Riccobono, F., Schobesberger, S., Scott, C., Dommen, J., Ortega, I., Rondo, L., Almeida, J., Amorim, A., Bianchi, F., Breitenlechner, M., David, A., Downard, A., Dunne, E., Duplissy, J., Ehrhart, S., Flagan, R., Franchin, A., Hansel, A., Junninen, H., Kajos, M., Keskinen, H., Kupc, A., Kürten, A., Kvashin, A., Laaksonen, A., Lehtipalo, K., Makhmutov, V., Mathot, S., Nieminen, T., Onnela, A., Petäjä, T., Praplan, A., Santos, F., Schallhart, S., Seinfeld, J., Sipilä, M., Van Spracklen, D., Stozhkov, Y., Stratmann, F., Tomé, A., Tsagkogeorgas, G., Vaattovaara, P., Viisanen, Y., Vrtala, A., Wagner, P., Weingartner, E., Wex, H., Wimmer, D., Carslaw, K., Curtius, J., Donahue, N., Kirkby, J., Kulmala, M., Worsnop, D. and Baltensperger, U.: Oxidation products of biogenic emissions contribute to nucleation of atmospheric particles., Science, 344(6185), 717–721, doi:10.1126/science.1243527, 2014.

Rissanen, M. P.: NO2 Suppression of Autoxidation-Inhibition of Gas-Phase Highly Oxidized Dimer Product Formation, ACS Earth Sp. Chem., 2(11), 1211–1219, doi:10.1021/acsearthspacechem.8b00123, 2018.

Rose, C., Zha, Q., Dada, L., Yan, C., Lehtipalo, K., Junninen, H., Mazon, S. B., Jokinen, T., Sarnela, N., Sipilä, M., Petäjä, T., Kerminen, V.-M., Bianchi, F. and Kulmala, M.: Observations of biogenic

ion-induced cluster formation in the atmosphere, Sci. Adv., 4(4), 5218, doi:10.1126/sciadv.aar5218, 2018.

Schervish, M. and Donahue, N. M.: Peroxy radical chemistry and the volatility basis set, Atmos. Chem. Phys., 20(2), 1183–1199, doi:10.5194/acp-20-1183-2020, 2020.

Schobesberger, S., Junninen, H., Bianchi, F., Lönn, G., Ehn, M., Lehtipalo, K., Dommen, J., Ehrhart, S., Ortega, I. K., Franchin, A., Nieminen, T., Riccobono, F., Hutterli, M., Duplissy, J., Almeida, J., Amorim, A., Breitenlechner, M., Downard, A. J., Dunne, E. M., Flagan, R. C., Kajos, M., Keskinen, H., Kirkby, J., Kupc, A., Kürten, A., Kurtén, T., Laaksonen, A., Mathot, S., Onnela, A., Praplan, A. P., Rondo, L., Santos, F. D., Schallhart, S., Schnitzhofer, R., Sipilä, M., Tomé, A., Tsagkogeorgas, G., Vehkamäki, H., Wimmer, D., Baltensperger, U., Carslaw, K. S., Curtius, J., Hansel, A., Petäjä, T., Kulmala, M., Donahue, N. M. and Worsnop, D. R.: Molecular understanding of atmospheric particle formation from sulphuric acid and large oxidized organic molecules., Proc. Natl. Acad. Sci. U. S. A., 110(43), 17223–17228, doi:10.1073/pnas.1306973110, 2013.

Simon, M., Heinritzi, M., Herzog, S., Leiminger, M., Bianchi, F., Praplan, A., Dommen, J., Curtius, J. and Kürten, A.: Detection of dimethylamine in the low pptv range using nitrate chemical ionization atmospheric pressure interface time-of-flight (CI-APi-TOF) mass spectrometry, Atmos. Meas. Tech., 9(5), 2135–2145, doi:10.5194/amt-9-2135-2016, 2016.

Sipilä, M., Sarnela, N., Jokinen, T., Henschel, H., Junninen, H., Kontkanen, J., Richters, S., Kangasluoma, J., Franchin, A., Peräkylä, O., Rissanen, M. P., Ehn, M., Vehkamäki, H., Kürten, T., Berndt, T., Pe , T., Worsnop, D., Ceburnis, D., Kerminen, V. M., Kulmala, M. and O'Dowd, C.: Molecular-scale evidence of aerosol particle formation via sequential addition of HIO_3, Nature, 537(7621), 532–534, doi:10.1038/nature19314, 2016.

Stolzenburg, D., Fischer, L., Vogel, A. L., Heinritzi, M., Schervish, M., Simon, M., Wagner, A. C., Dada, L., Ahonen, L. R., Amorim, A., Baccarini, A., Bauer, P. S., Baumgartner, B., Bergen, A., Bianchi, F., Breitenlechner, M., Brilke, S., Buenrostro Mazon, S., Chen, D., Dias, A., Draper, D. C., Duplissy, J., El Haddad, I., Finkenzeller, H., Frege, C., Fuchs, C., Garmash, O., Gordon, H., He, X., Helm, J., Hofbauer, V., Hoyle, C. R., Kim, C., Kirkby, J., Kontkanen, J., Kürten, A., Lampilahti, J., Lawler, M., Lehtipalo, K., Leiminger, M., Mai, H., Mathot, S., Mentler, B., Molteni, U., Nie, W., Nieminen, T., Nowak, J. B., Ojdanic, A., Onnela, A., Passananti, M., Petäjä, T., Quéléver, L. L. J., Rissanen, M. P., Sarnela, N., Schallhart, S., Tauber, C., Tomé, A., Wagner, R., Wang, M., Weitz, L., Wimmer, D., Xiao, M., Yan, C., Ye, P., Zha, Q., Baltensperger, U., Curtius, J., Dommen, J., Flagan, R. C., Kulmala, M., Smith, J. N., Worsnop, D. R., Hansel, A., Donahue, N. M. and Winkler, P. M.: Rapid growth of organic aerosol nanoparticles over a wide tropospheric temperature range, P. Natl. Acad. Sci. USA, 115, 9122–9127, 2018.

Tröstl, J., Chuang, W. K., Gordon, H., Heinritzi, M., Yan, C., Molteni, U., Ahlm, L., Frege, C., Bianchi, F., Wagner, R., Simon, M., Lehtipalo, K., Williamson, C., Craven, J. S., Duplissy, J., Adamov, A., Almeida, J., Bernhammer, A. K., Breitenlechner, M., Brilke, S., Dias, A., Ehrhart, S., Flagan, R. C., Franchin, A., Fuchs, C., Guida, R., Gysel, M., Hansel, A., Hoyle, C. R., Jokinen, T., Junninen, H., Kangasluoma, J., Keskinen, H., Kim, J., Krapf, M., Kürten, A., Laaksonen, A., Lawler, M., Leiminger, M., Mathot, S., Möhler, O., Nieminen, T., Onnela, A., Petäjä, T., Piel, F. M., Miettinen, P., Rissanen, M. P., Rondo, L., Sarnela, N., Schobesberger, S., Sengupta, K., Sipilä, M., Smith, J. N., Steiner, G., Tomè, A., Virtanen, A., Wagner, A. C., Weingartner, E., Wimmer, D., Winkler, P. M., Ye, P., Carslaw, K. S., Curtius, J., Dommen, J., Kirkby, J., Kulmala, M., Riipinen, I., Worsnop, D. R., Donahue, N. M. and Baltensperger, U.: The role of low-volatility organic compounds

in initial particle growth in the atmosphere, Nature, 533(7604), 527–531, doi:10.1038/nature18271, 2016.

Van Damme, M., Clarisse, L., Whitburn, S., Hadji-Lazaro, J., Hurtmans, D., Clerbaux, C. and Coheur, P. F.: Industrial and agricultural ammonia point sources exposed, Nature, 564(7734), 99–103, doi:10.1038/s41586-018-0747-1, 2018.

Wang, M., Chen, D., Xiao, M., Ye, Q., Stolzenburg, D., Hofbauer, V., Ye, P., Vogel, A.L., Mauldin., R.L., Amorim, A., Baccarini, A., Baumgartner B., Brilke S., Dada L., Dias A., Duplissy J., Finkenzeller, H., Garmash, O., He X., Hoyle, C.R., Kim, C., Kvashnin, C., Lehtipalo, K., Fischer, L., Molteni, U., Petäjä, T., Pospisilova V., Quéléver, L.L.J., Rissanen, M., Simon, M., Tauber, C., Wagner A.C., Weitz, L., Volkamer, R., Winkler P.M., Kirkby, J., Worsnop, D.R., Kulmala, M., Baltensperger, U., Dommen, J., El-Haddad, I., and Donahue, N.M.: Photo-oxidation of Aromatic Hydrocarbons Produces Low-Volatility Organic Compounds, Environmental Science & Technology 54(13), 7911-7921, doi:10.1021/acs.est.0c02100

Wang, S., Wu, R., Berndt, T., Ehn, M. and Wang, L.: Formation of Highly Oxidized Radicals and Multifunctional Products from the Atmospheric Oxidation of Alkylbenzenes, Environ. Sci. Technol., 51(15), 8442–8449, doi:10.1021/acs.est.7b02374, 2017.

Yan, C., Nie, W., Äijälä, M., Rissanen, M. P., Canagaratna, M. R., Massoli, P., Junninen, H., Jokinen, T., Sarnela, N., Häme, S. A. K., Schobesberger, S., Canonaco, F., Yao, L., Prévôt, A. S. H., Petäjä, T., Kulmala, M., Sipilä, M., Worsnop, D. R. and Ehn, M.: Source characterization of highly oxidized multifunctional compounds in a boreal forest environment using positive matrix factorization, Atmos. Chem. Phys., 16(19), 12715–12731, doi:10.5194/acp-16-12715-2016, 2016.

Yan, C., Dada, L., Rose, C., Jokinen, T., Nie, W., Schobesberger, S., Junninen, H., Lehtipalo, K., Sarnela, N., Makkonen, U., Garmash, O., Wang, Y., Zha, Q., Paasonen, P., Bianchi, F., Sipilä, M., Ehn, M., Petäjä, T., Kerminen, V.-M., Worsnop, D. R., and Kulmala, M.: The role of H2SO4-NH3 anion clusters in ion-induced aerosol nucleation mechanisms in the boreal forest, Atmos. Chem. Phys., 18, 13231–13243, https://doi.org/10.5194/acp-18-13231-2018, 2018.

Yan, C., Nie, W., Vogel, A. L., Dada, L., Lehtipalo, K., Stolzenburg, D., Wagner, R., Rissanen, M. P., Xiao, M., Ahonen, L., Fischer, L., Rose, C., Bianchi, F., Gordon, H., Simon, M., Heinritzi, M., Garmash, O., Roldin, P., Dias, A., Ye, P., Hofbauer, V., Amorim, A., Bauer, P. S., Bergen, A., Bernhammer, A.-K., Breitenlechner, M., Brilke, S., Buchholz, A., Mazon, S. B., Canagaratna, M. R., Chen, X., Ding, A., Dommen, J., Draper, D. C., Duplissy, J., Frege, C., Heyn, C., Guida, R., Hakala, J., Heikkinen, L., Hoyle, C. R., Jokinen, T., Kangasluoma, J., Kirkby, J., Kontkanen, J., Kürten, A., Lawler, M. J., Mai, H., Mathot, S., Mauldin, R. L., Molteni, U., Nichman, L., Nieminen, T., Nowak, J., Ojdanic, A., Onnela, A., Pajunoja, A., Petäjä, T., Piel, F., Quéléver, L. L. J., Sarnela, N., Schallhart, S., Sengupta, K., Sipilä, M., Tomé, A., Tröstl, J., Väisänen, O., Wagner, A. C., Ylisirniö, A., Zha, Q., Baltensperger, U., Carslaw, K. S., Curtius, J., Flagan, R. C., Hansel, A., Riipinen, I., Smith, J. N., Virtanen, A., Winkler, P. M., Donahue, N. M., Kerminen, V.-M., Kulmala, M., Ehn, M. and Worsnop, D. R.: Size-dependent influence of NO_x on the growth rates of organic aerosol particles , Sci. Adv., 6(22), eaay4945, doi:10.1126/sciadv.aay4945, 2020.

Yao, L., Garmash, O., Bianchi, F., Zheng, J., Yan, C., Kontkanen, J., Junninen, H., Mazon, S. B., Ehn, M., Paasonen, P., Sipilä, M., Wang, M., Wang, X., Xiao, S., Chen, H., Lu, Y., Zhang, B., Wang, D., Fu, Q., Geng, F., Li, L., Wang, H., Qiao, L., Yang, X., Chen, J., Kerminen, V. M., Petäjä, T., Worsnop, D. R., Kulmala, M. and Wang, L.: Atmospheric new particle formation from sulphuric acid and amines in a Chinese megacity, Science, 361(6399), 278–281, doi:10.1126/science.aao4839,

2018.

Yli-Juuti, T., Pajunoja, A., Tikkanen, O. P., Buchholz, A., Faiola, C., Väisänen, O., Hao, L., Kari, E., Peräkylä, O., Garmash, O., Shiraiwa, M., Ehn, M., Lehtinen, K. and Virtanen, A.: Factors controlling the evaporation of secondary organic aerosol from α-pinene ozonolysis, Geophys. Res. Lett., 44(5), 2562–2570, doi:10.1002/2016GL072364, 2017.

Yu, H., Zhou, L., Dai, L., Shen, W., Dai, W., Zheng, J., Ma, Y. and Chen, M.: Nucleation and growth of sub-3 nm particles in the polluted urban atmosphere of a megacity in China, Atmos. Chem. Phys., 16(4), 2641–2657, doi:10.5194/acp-16-2641-2016, 2016.

Zhang, R., Khalizov, A., Wang, L., Hu, M. and Xu, W.: Nucleation and growth of nanoparticles in the atmosphere, Chem. Rev., 112(3), 1957–2011, doi:10.1021/cr2001756, 2012.

Zhao, J., Eisele, F. L., Titcombe, M., Kuang, C. and McMurry, P. H.: Chemical ionization mass spectrometric measurements of atmospheric neutral clusters using the cluster-CIMS, J. Geophys. Res., 115(D8), 1–19, doi:10.1029/2009jd012606, 2010.

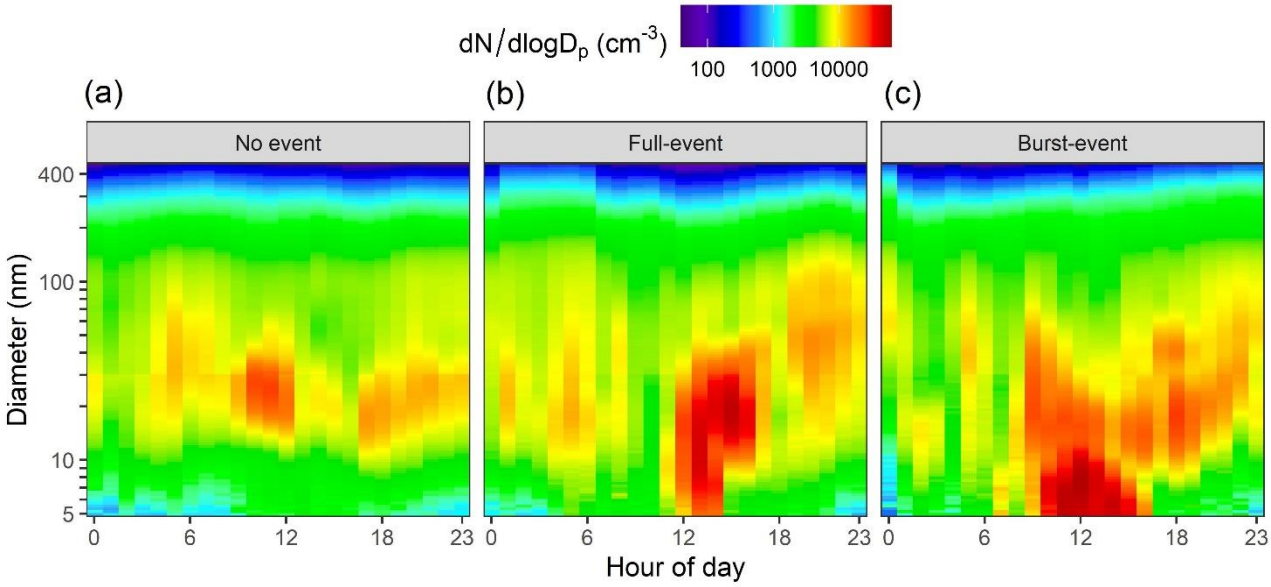

Figure 1: Average SMPS contour plots for (a) non-event days, (b) full-event days and (c) burst-event days.

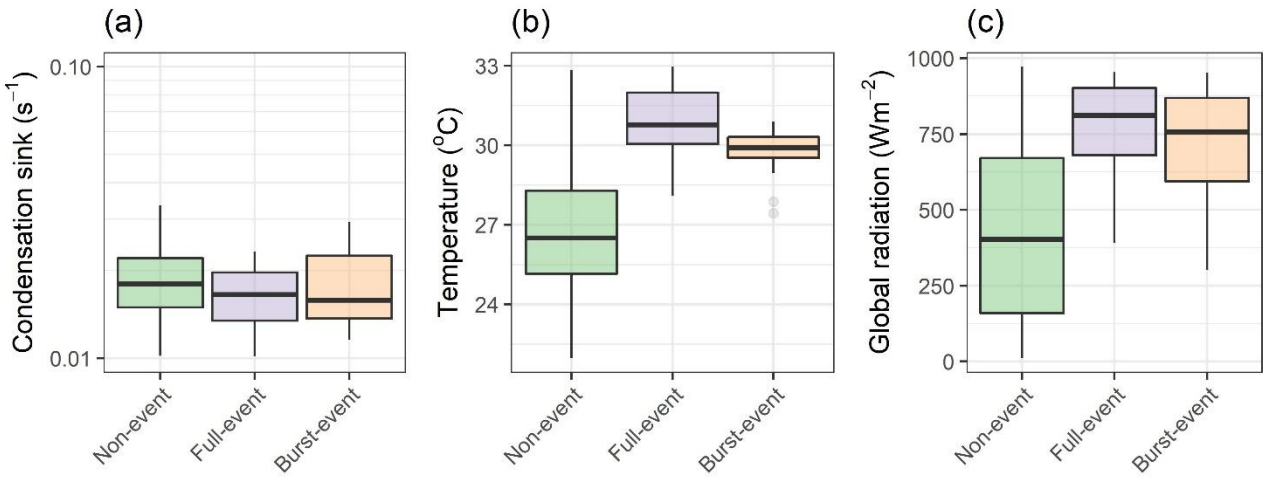

Figure 2: Box plots for days of non-event, full-event and burst-event, showing (a) condensation sink, (b) temperature, and (c) global radiation from hourly data. "Full-event" and "burst-event" include data across the entire day.

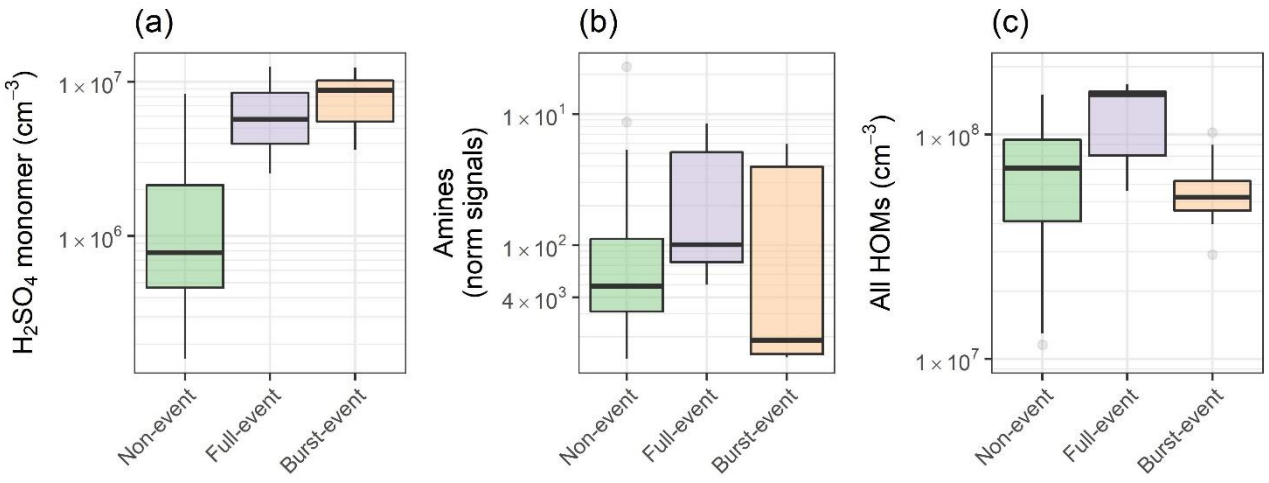

Figure 3: Box plots for days of non-event, full-event and burst-event, showing (a) sulphuric acid, (b) C_2 and C_4 amines, as clustered with the nitrate dimer and trimer, and (c) summed HOM concentration from C_5+ from hourly data. Units for ammonia + amines are normalised counts, as no calibration was performed. Event days include data across the full event day.

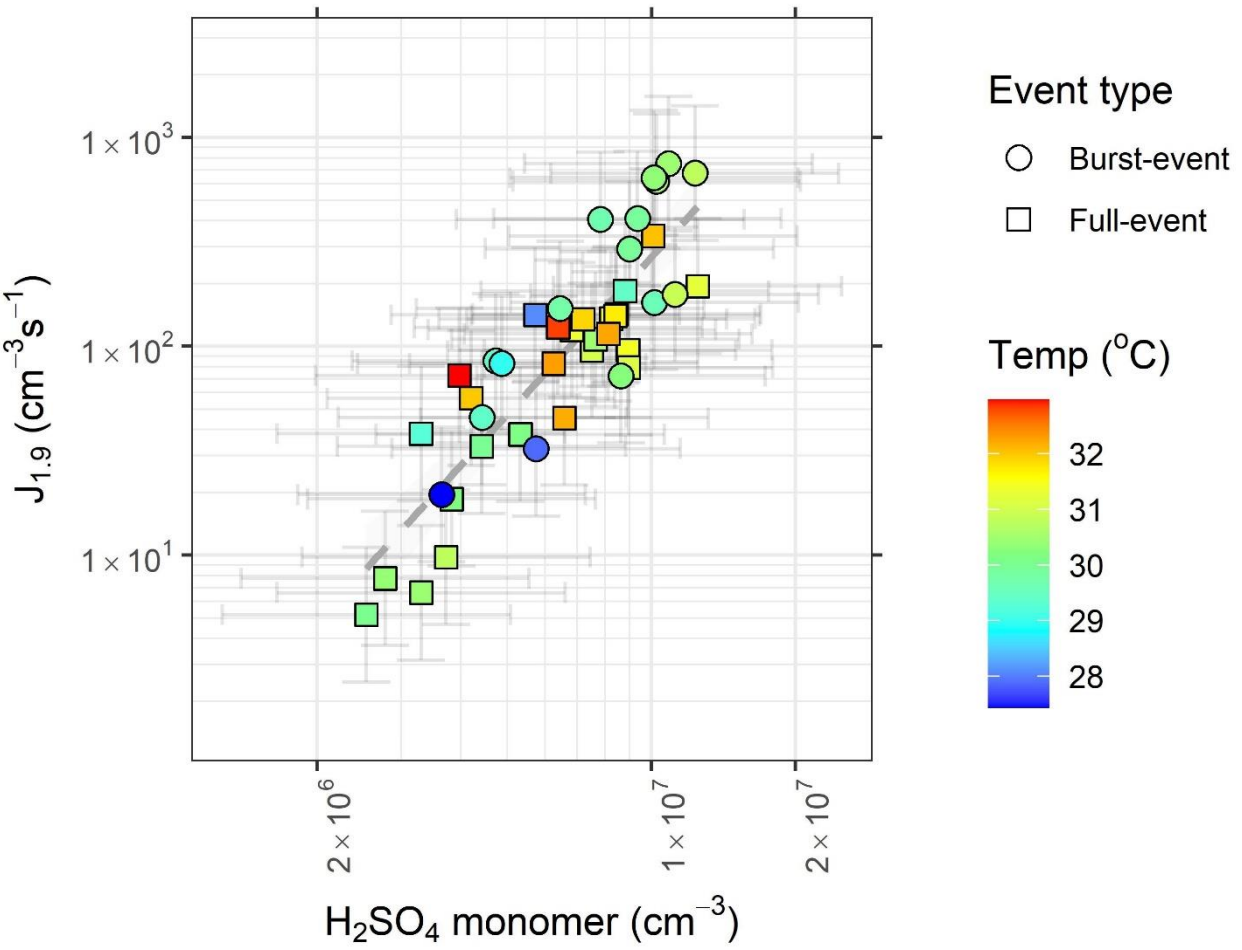

Figure 4: Formation rate ($J_{1.9}$) plotted against sulphuric acid monomer concentration, coloured by condensation sink. Circles represent burst-events, squares represent full events. Data is for hourly averages across NPF periods, typically within the hours 08:00 – 16:00. Slope of the line = $4.9 \cdot 10^{-5}$ s^{-1}. Error bars represent systematic uncertainties on [H_2SO4] and $J_{1.9}$

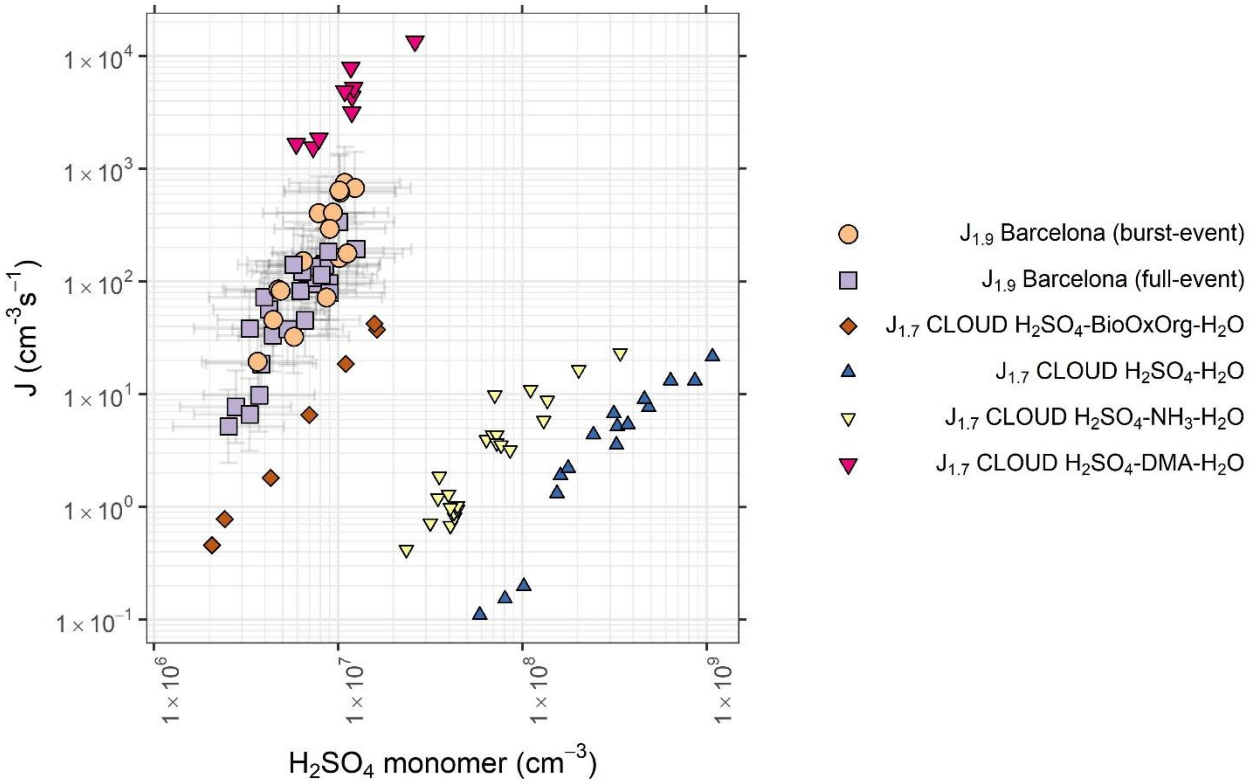

Figure 5: Formation rate plotted against sulphuric acid monomer concentration for data collected from Barcelona. Tan circles represent burst-events, purple squares represent full events. as well as that for the H_2SO_4-H_2O (blue inverted triangles), H_2SO_4-NH_3-H_2O (yellow inverted triangles), H_2SO_4-DMA-H_2O (pink triangles), and H_2SO_4-BioOxOrg-H_2O (brown diamonds) systems from the CLOUD chamber (Kürten et al., 2018 Kirkby et al., 2011; Riccobono et al., 2014). CLOUD chamber experiments were performed at 278 K and 38 – 39 % RH. Data is for hourly averages across NPF periods, typically within the hours 08:00 – 16:00. Error bars represent systematic uncertainties on [H_2SO_4] and $J_{1.9}$.

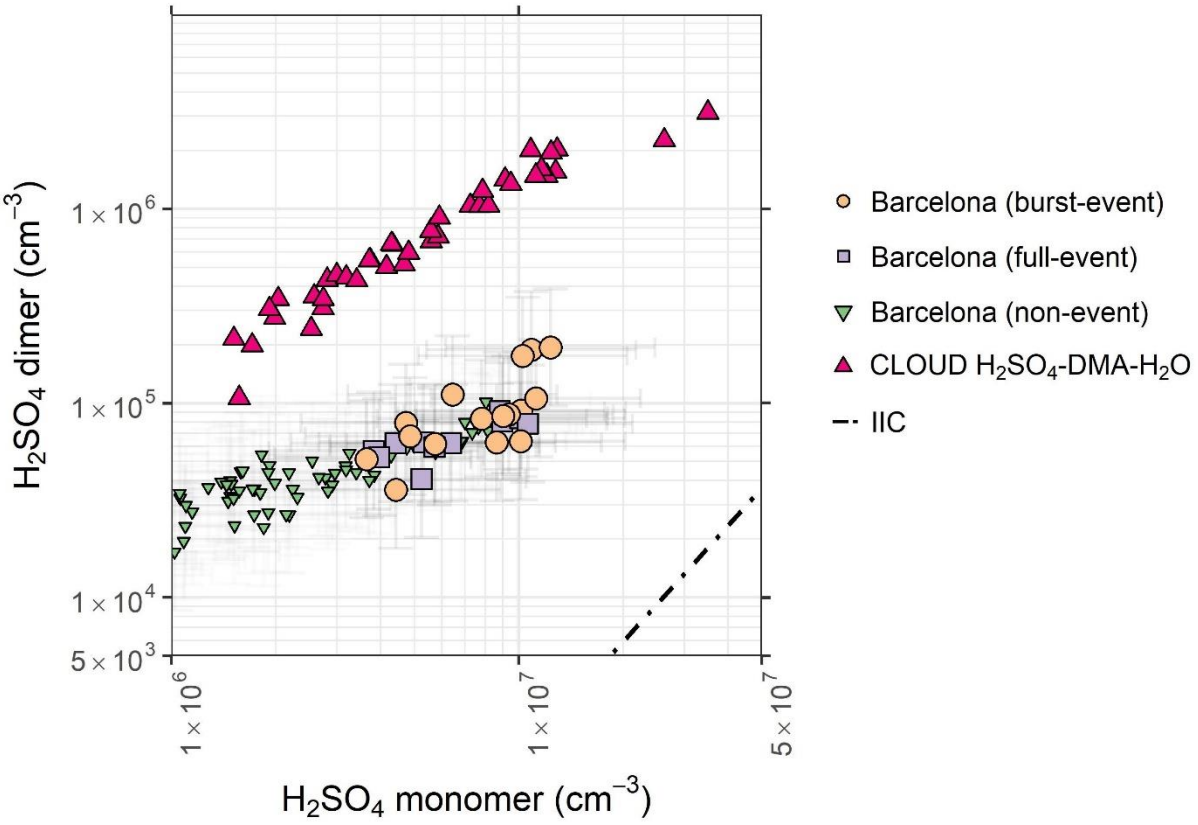

Figure 6: Sulphuric acid dimer concentration plotted against monomer concentration, showing burst-event periods (tan circles), full event periods (purple squares), non-event periods (green inverted triangles), and the ratio of sulphuric acid dimer:monomer in the CLOUD chamber for the H_2SO_4-H_2O-DMA system (pink triangles) (Almeida et al., 2013). Dashed line represents the dimer concentration produced by ion induced clustering in the chemical ionization unit (Zhao et al., 2010). CLOUD chamber experiments were performed at 278 K and 38 – 39 % RH. Data is for hourly averages across NPF periods, typically within the hours 08:00 – 16:00. Error bars represent systematic uncertainties on [H_2SO_4] and [$(H_2SO_4)_2$].

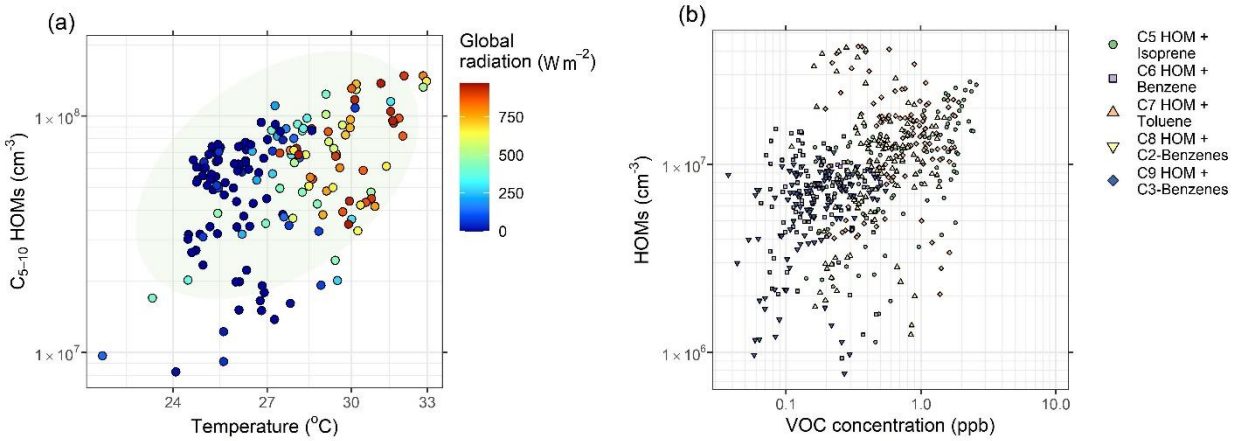

Figure 7: Influencing factors on HOM concentration, showing (a) $C_{5\text{-}10}$ HOM concentration plotted against temperature, coloured by global radiation. Ellipsis shows 95% confidence on a multivariate t-distribution. (b) HOM concentration by carbon number potted against parent VOC mixing ratio. These are segregated by carbon number/VOC, i.e, C_7 HOMs plotted against toluene, under the assumption that toluene oxidation is the main producer of C_7 HOMs. Time for both plots is of hourly time resolution.

1244

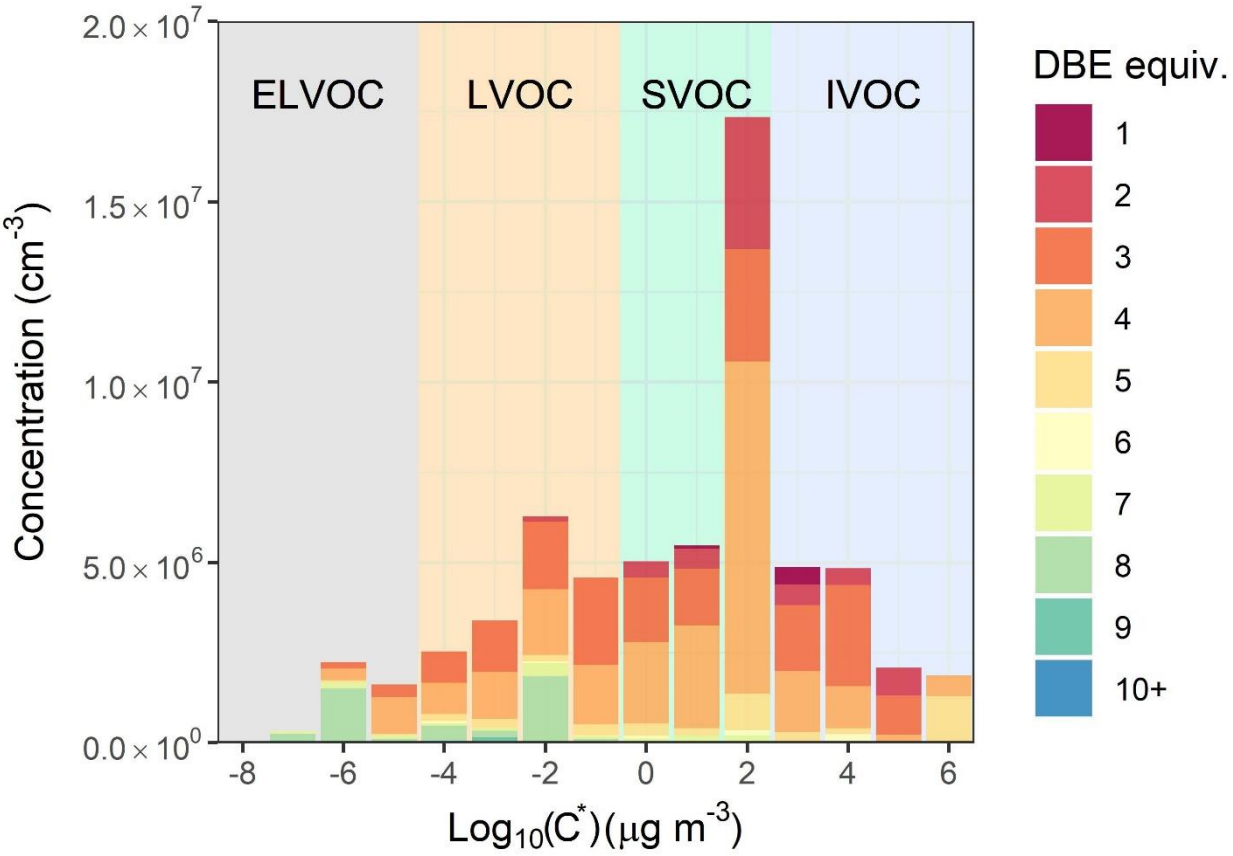

1245

1246 **Figure 8**: Concentrations of all oxygenated organic molecules and HOMs binned to integer $Log_{10}(C^*)$
1247 values, coloured by DBE.

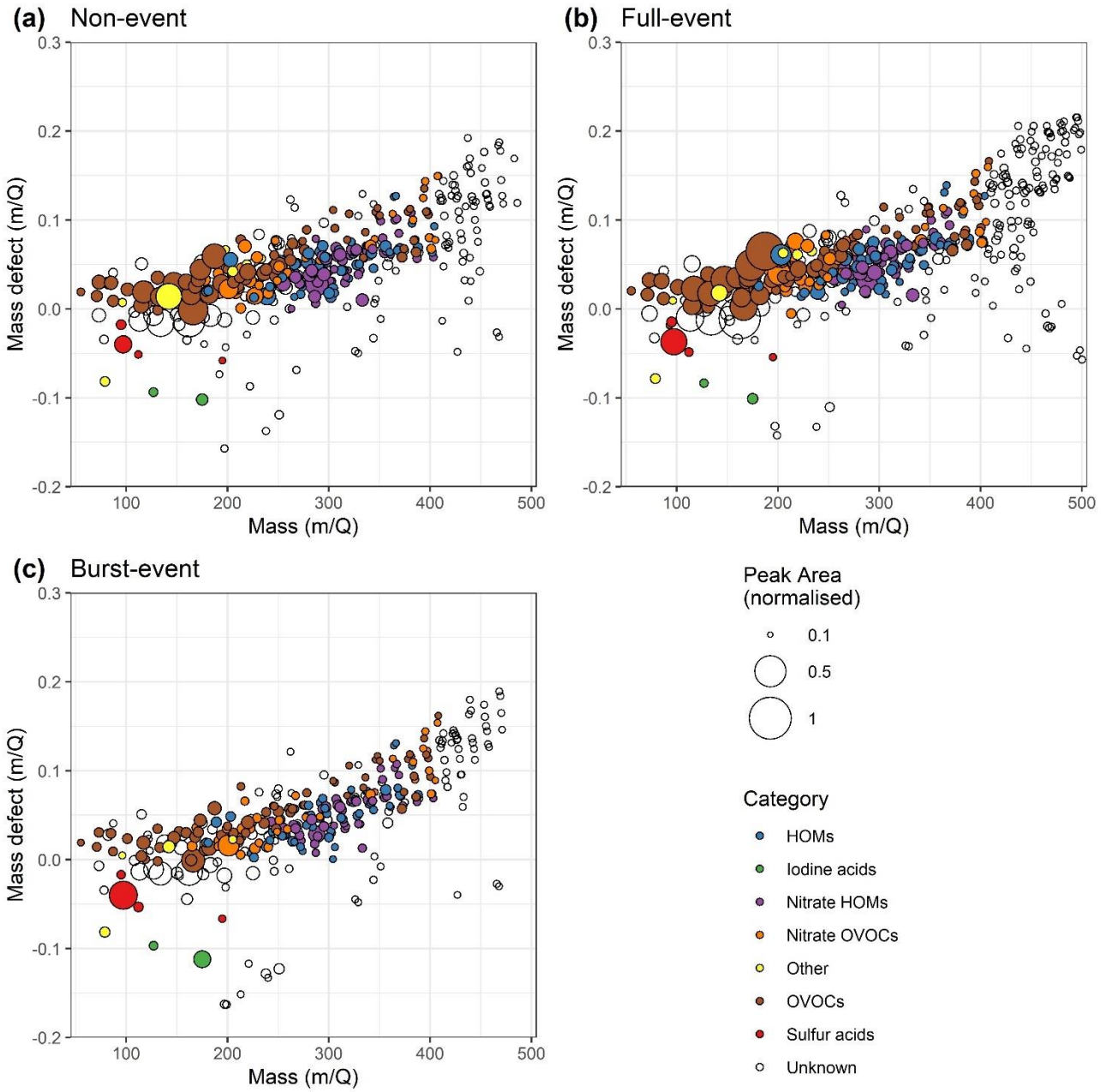

Figure 9: Mass defect plots for (a) non-event, (b) full-event, and (c) burst-event periods, data taken from 10:00 – 15:00 on the days 11/07/2018, 16/07/2018 and 15/07/2018 respectively. Size corresponds to mass spectral peak area. Ions are coloured according to identified chemical composition. *Blue* points correspond to HOMs containing all organic species with ≥5 carbon atoms and ≥6 oxygen atoms, and an O:C ratio of >0.6. *Purple* points correspond to the same but for species containing 1-2 nitrogen atoms. Species not meeting this HOM criterea were classed generally as OVOCs which are coloured *brown,* with the nitrogen containing OVOCs coloured *orange*. Sulphur acids (*red*) include ions HSO_4^-, $CH_3SO_3^-$ and SO_5^-, as well as the sulphuric acid dimer. Iodine acids (*green*) contains both IO_3^- and I^- (the latter presumably deprotonated hydrogen iodide). Unidentified points are left uncoloured.

Supplementary Information

Molecular Insights into New Particle Formation in Barcelona, Spain

James Brean, David C.S. Beddows, Zongbo Shi, Brice Temime-Roussel, Nicolas Marchand, Xavier Querol, Andrés Alastuey, María Cruz Minguillón, and Roy M. Harrison

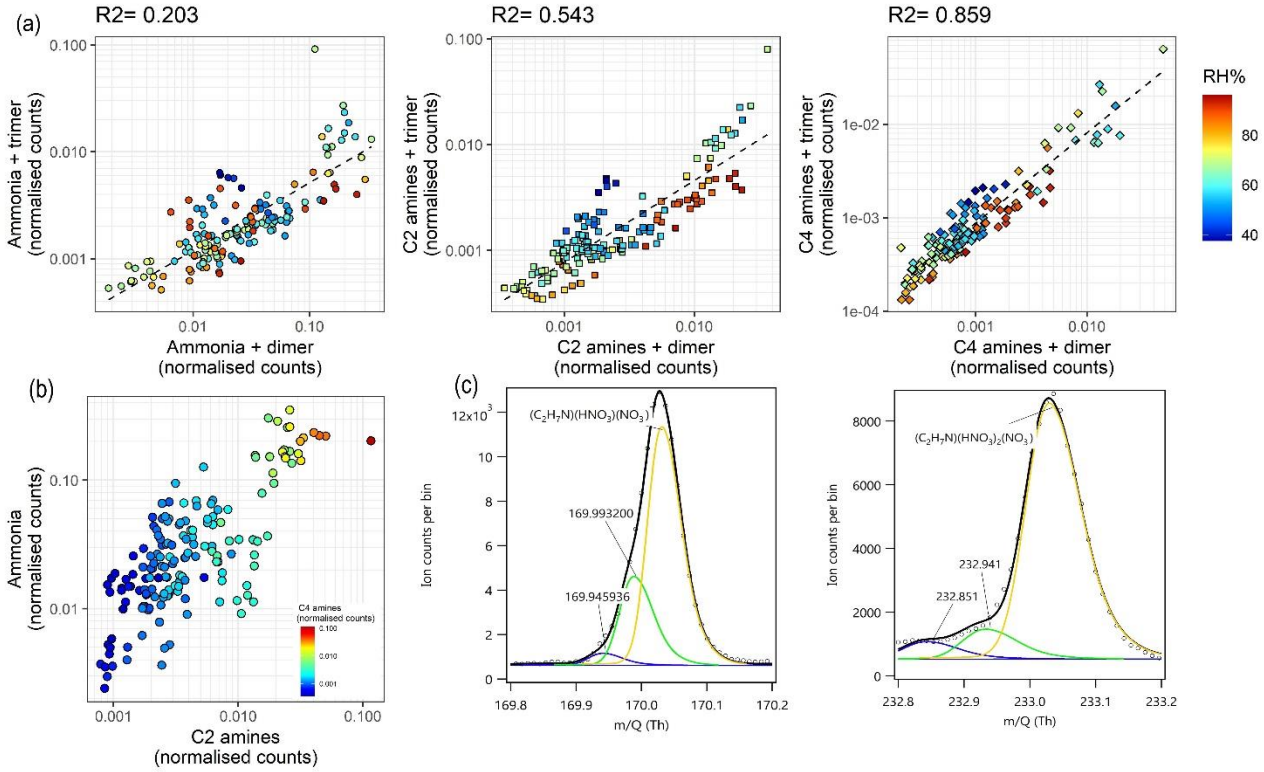

Figure S1: Ammonia and amine measurements via CI-APi-ToF, showing (a) ammonia, C_2 and C_4 amines as measured clustered with the nitrate dimer and trimer. Colour scale shows an RH dependence. (b) Ammonia plotted against C_2 amines, coloured by C_4 amine concentration, and (c) peak fits for the C_2 amine ion as clustered with the nitrate dimer and trimer.

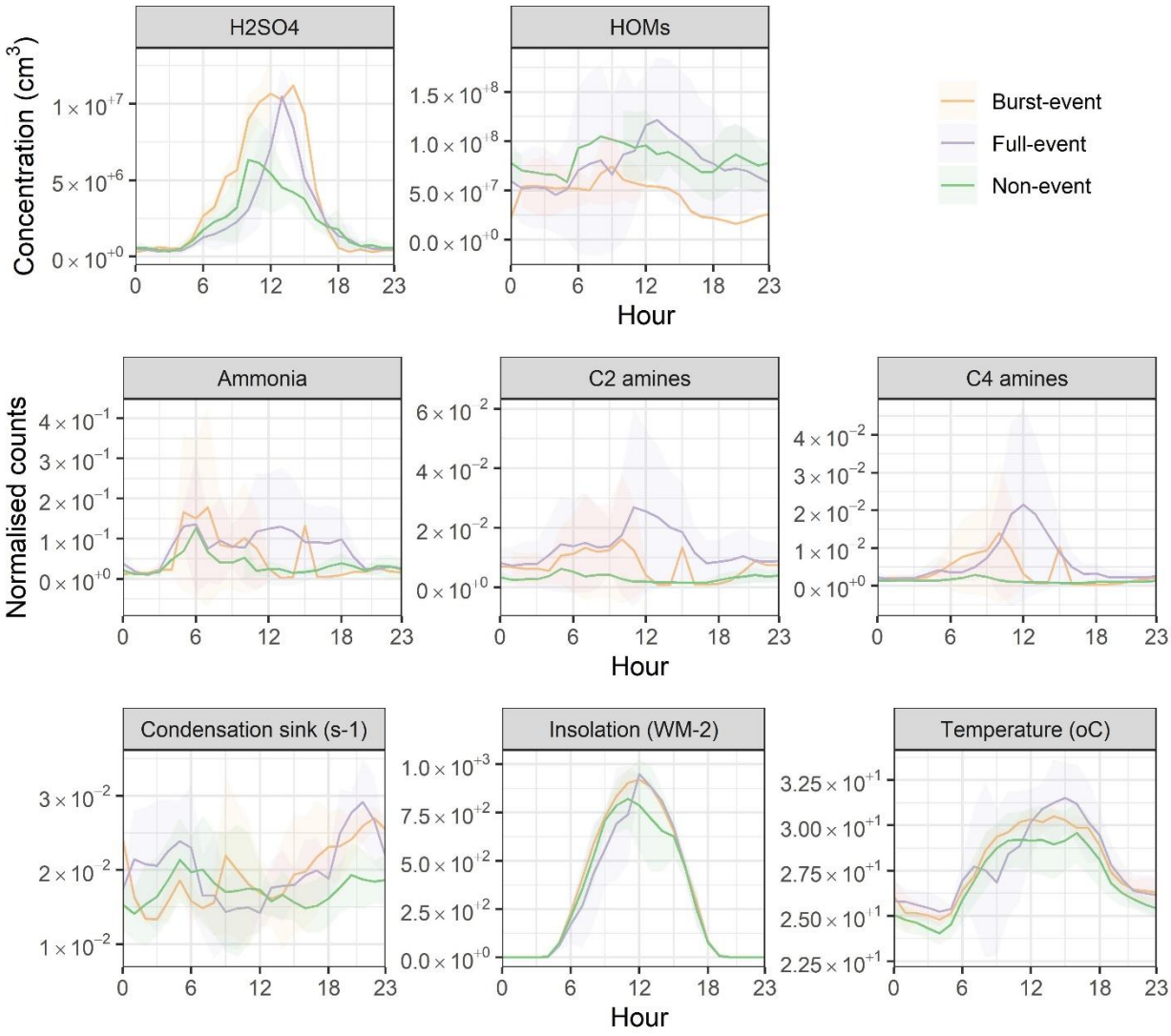

Figure S2: Diurnal profiles of (from top left through bottom right), H_2SO_4, HOMs, NH_3, C_2 amines, C_4 amines, condensation sink, insolation and temperature. Shaded regions show 1 standard deviation on the mean.

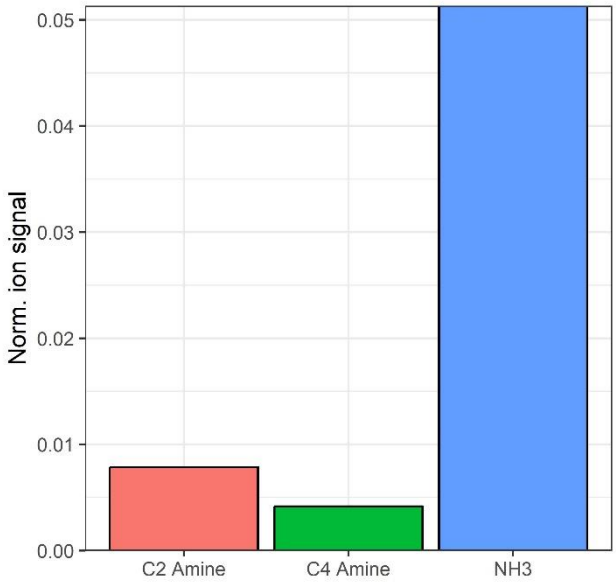

Figure S3: Mean ammonia and amine signals across the campaign as measured by CI-APi-ToF. Units of normalised ion counts.

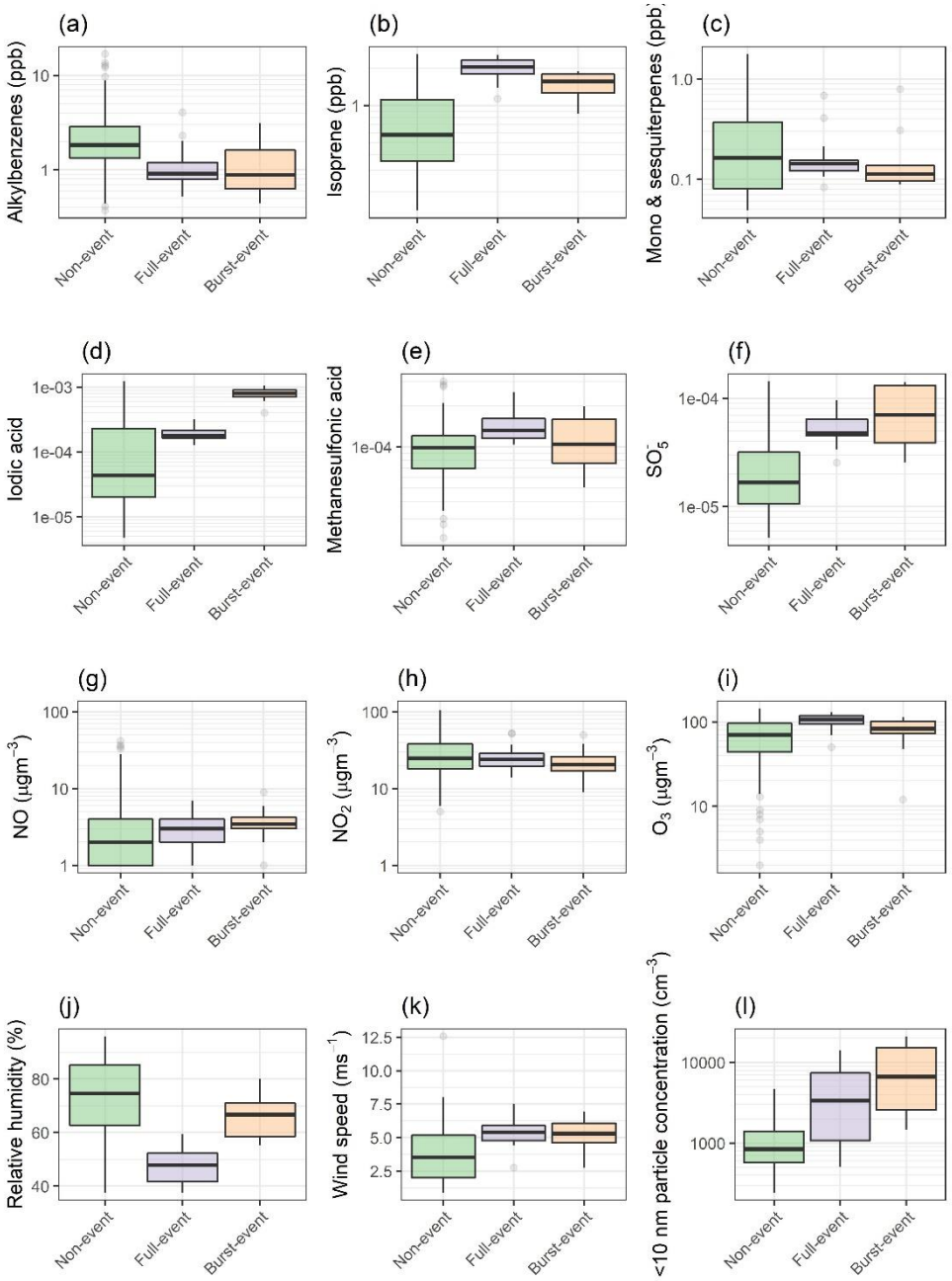

Figure S4: Box plots as figures 2 & 3 for (a-c) VOCs as measured by PTR-ToF-MS, (d-f) other ions as measured by CI-APi-ToF (units of norm. counts) (g-i) trace gases, and (j-l) meteorological and <10 nm particle count parameters.

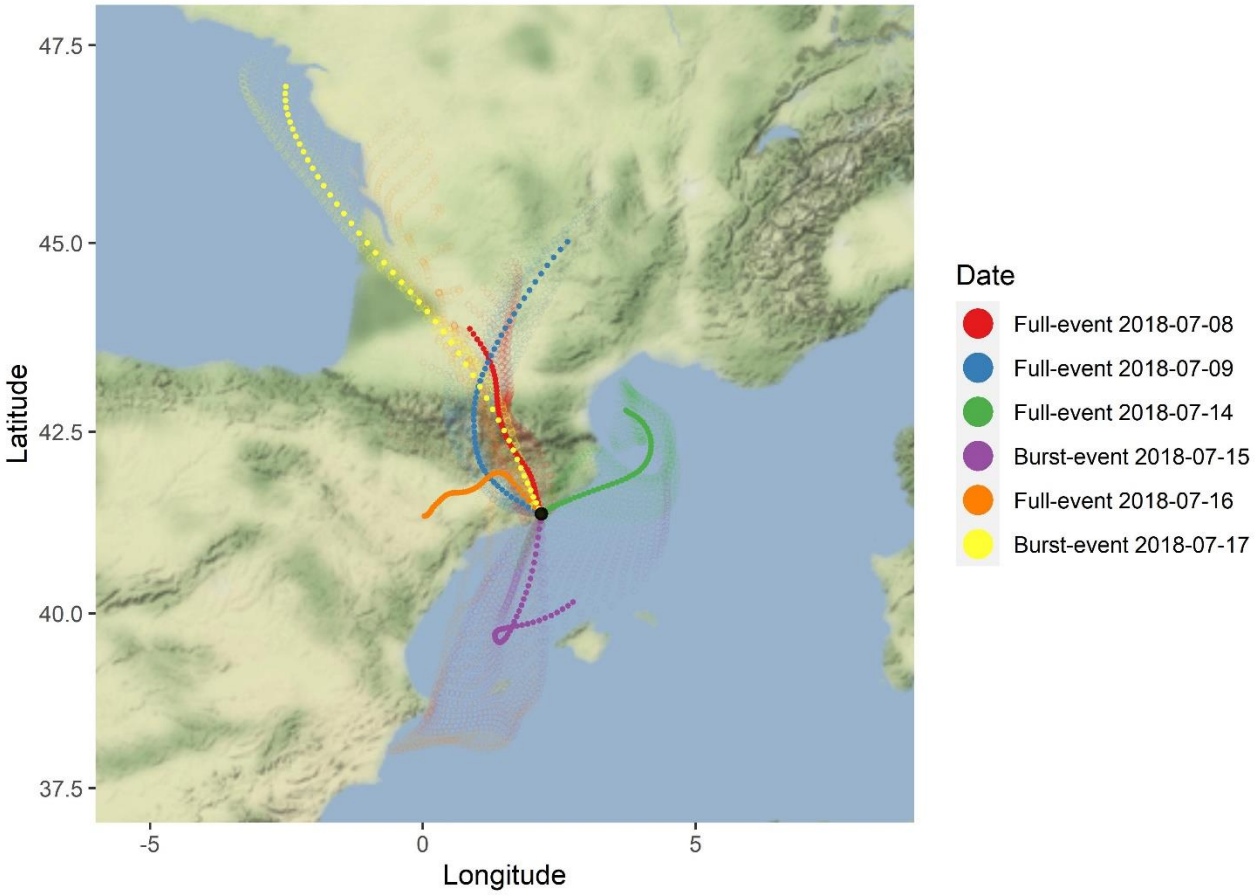

Figure S5: HYSPLIT 96 hour back trajectories per nucleation event. Dark dashed lines show mean trajectory per event, light dashed lines show hourly trajectories from which mean is calculated.

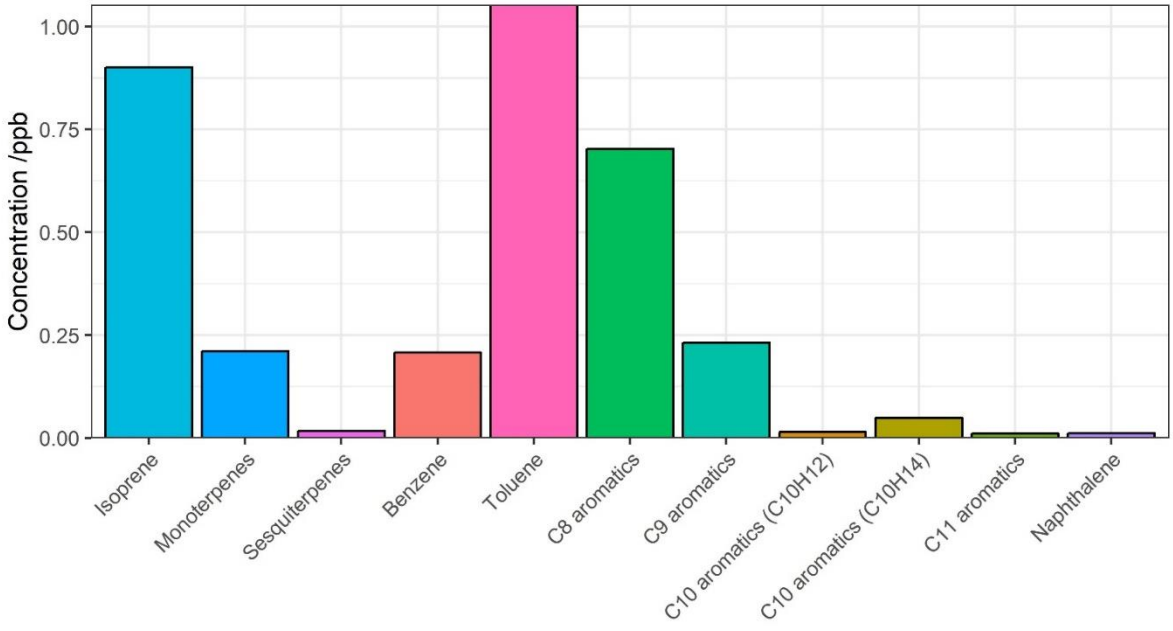

Figure S6: Mean selected VOC concentrations across the campaign as measured by PTR-ToF-MS.

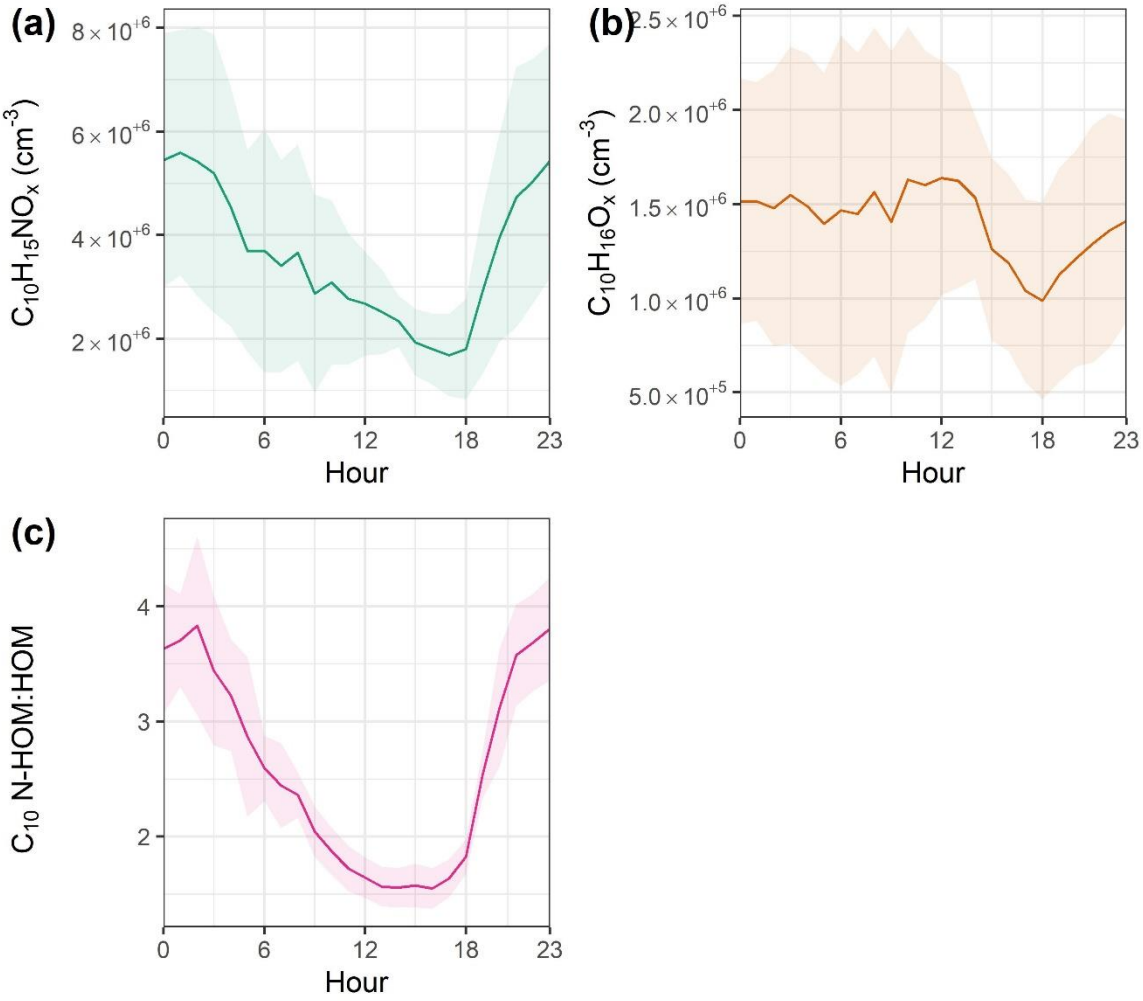

Figure S7: Diurnal pattern of (a) nitrate containing monoterpene HOMs and OVOCs following the formula $C_{10}H_{15}NO_x$, (b) non-nitrate containing monoterpene HOMs and OVOCs following the formula $C_{10}H_{16}O_x$, and (c) the ratio of nitrate:non-nitrate containing monoterpene HOMs and OVOCs, where O = 4-11

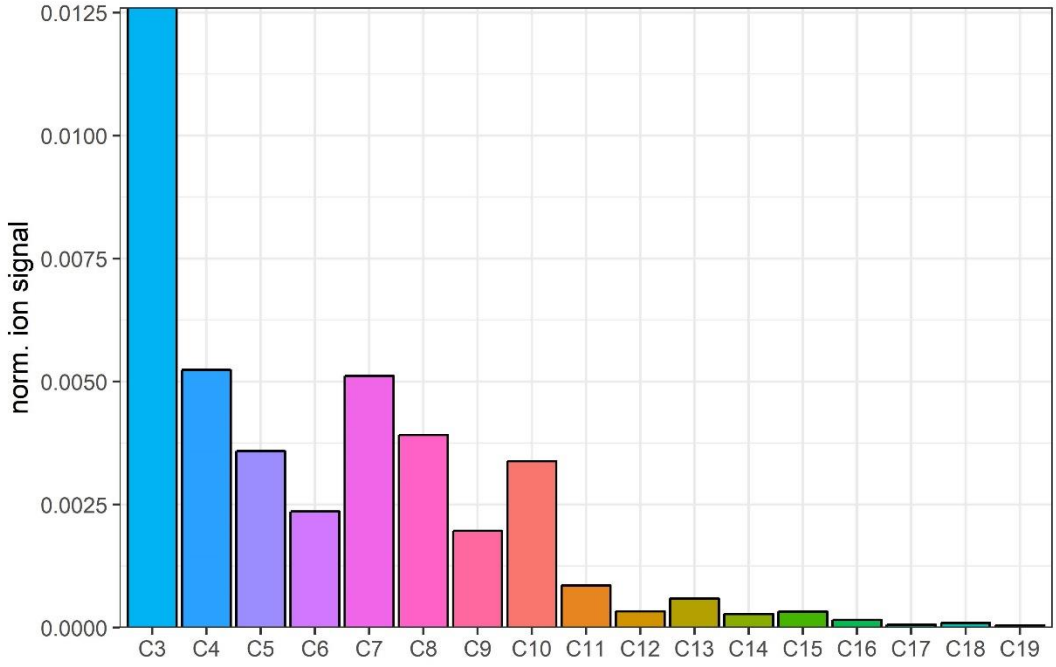

Figure S8: Mean ion signals per carbon number across the campaign as measured by CI-APi-ToF. Units of normalised ion counts.

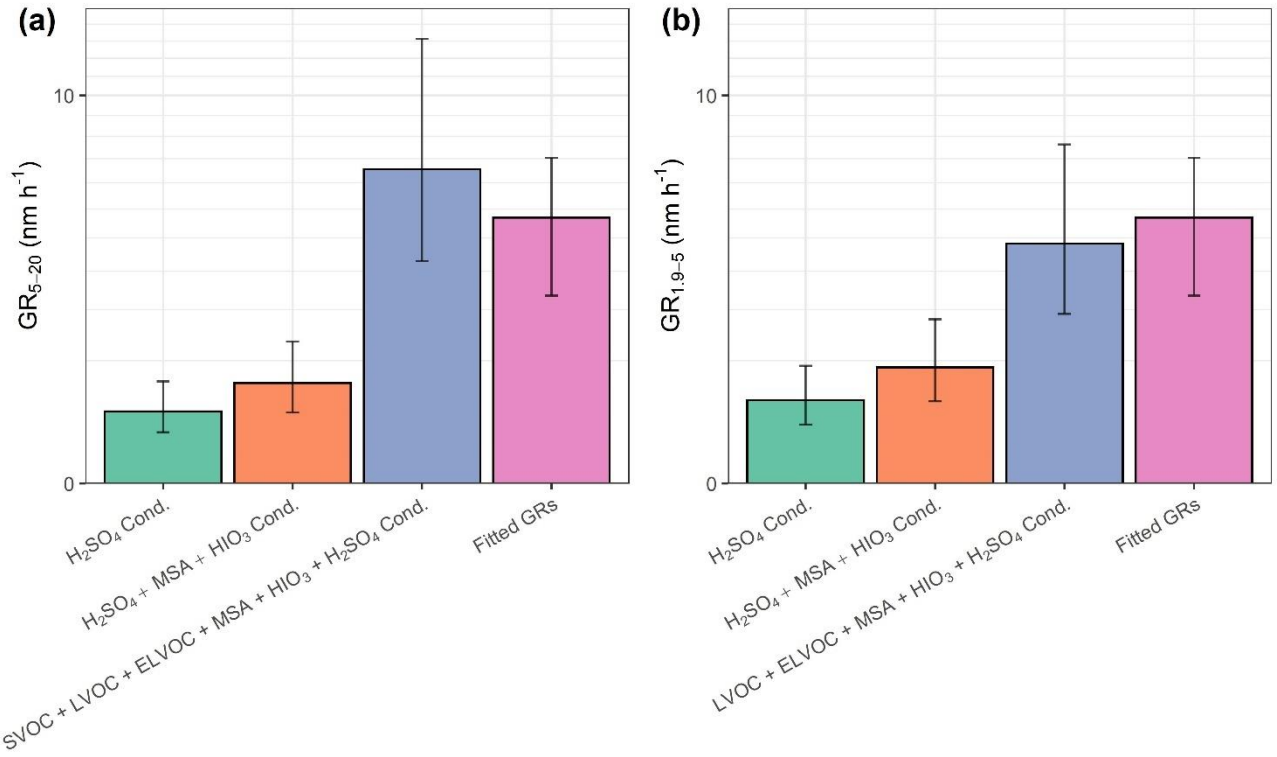

Figure S9: Condensational growth rates in the ranges (a) 5 - 20 nm and (b) 1.9 – 5 nm, calculated from H_2SO_4 condensation, H_2SO_4, MSA, and HIO_3 condensation, and SVOC, LVOC, ELVOC, H_2SO_4, MSA and HIO_3 in (a), and LVOC, ELVOC, H_2SO_4, MSA and HIO_3 in (b). Also presented are growth rates from particle count data. Error bars represent uncertainties on the concentration of species measured by CI-APi-ToF, and the uncertainties from GR calculations. Systematic uncertainties from the methods of Nieminen et al. (2010) are not included.

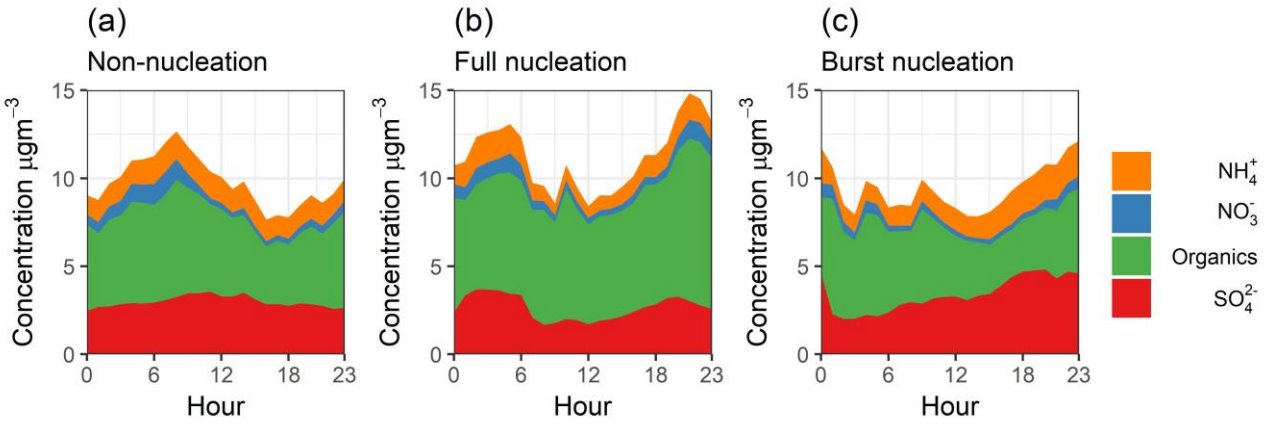

Figure S10: Average diurnals of particle composition as measured by ACSM on (a) non-nucleation, (b) full-nucleation and (c) burst-nucleation days.

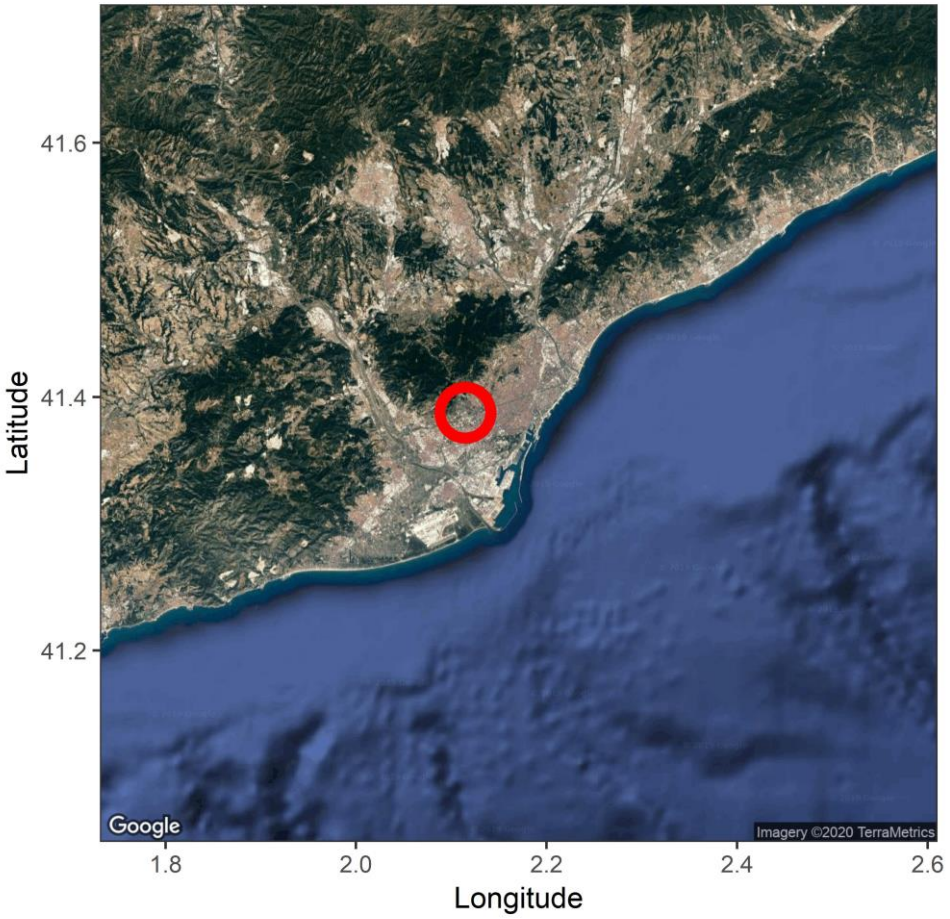

Figure S11: Location of sampling site.

Table 1: Ions identified by CI-APi-ToF

Ion	m/Q
Cl^-	34.97
NO_2^-	45.99
$C_3H_3O^-$	55.02
$(NO_3)^-$	61.99
$C_3H_3O_2^-$	71.01
$C_3H_5O_2^-$	73.03
Br^-	78.92
$H_2O(NO_3)^-$	80.00
$C_4H_5O_2^-$	85.03
$C_3H_3O_3^-$	87.01
$CH_3SO_3^-$	94.98
$CFH_3(NO3)^-$	96.01
HSO_4^-	96.96
$HCl(NO3)^-$	97.97
$H_4O_2(NO3)^-$	98.01
$C_4H_5O_3^-$	101.02
$C_3H_3O_4^-$	103.00
SO_5^-	111.95
$C_4H_3O_4^-$	115.00
$C_4H_5O_4^-$	117.02
$C_3H_4O(NO_3)^-$	118.01
$C_3H_3O_5^-$	119.00
$HNO_3NO_3^-$	124.98
I^-	126.91
$C_4H_3O_5^-$	131.00
$C_5H_7O_4^-$	131.03
$C_4H_5O_5^-$	133.01
$NH_3(HNO_3)(NO_3)^-$	142.01
$C_5H_5O_5^-$	145.01
$C_5H_7O_5^-$	147.03
$C_3H_6O_3(NO_3)^-$	152.02
$C_6H_7O_5^-$	159.03
$C_4H_6O_3(NO_3)^-$	164.02

$C_3H_5NO_3(NO_3)^-$	165.02
$C_3H_4O_4(NO_3)^-$	166.00
$C_6H_5NO(NO_3)^-$	169.03
$C_2H_7N(HNO_3)(NO_3)^-$	170.04
$C_7H_7O_5^-$	171.03
$C_7H_9O_5^-$	173.05
IO_3^-	174.89
$C_4H_5NO_3(NO_3)^-$	177.02
$C_4H_4O_4(NO_3)^-$	178.00
$C_5H_7O_7^-$	179.02
$C_4H_6O_4(NO_3)^-$	180.01
$C_5H_9O_7^-$	181.04
$C_4H_8O_4(NO_3)^-$	182.03
$C_8H_{11}O_5^-$	187.06
$(HNO_3)_2(NO_3)^-$	187.98
$C_7H_9O_6^-$	189.04
$C_5H_7NO_3(NO_3)^-$	191.03
$C_4H_6N_2O_3(NO_3)^-$	192.03
$C_4H_5NO_4(NO_3)^-$	193.01
$C_5H_8O_4(NO_3)^-$	194.03
$H_2SO_4HSO_4^-$	194.93
$C_5H_7O_8^-$	195.01
$C_3H_6N_2O_4(NO_3)^-$	196.02
$C_4H_8O_5(NO_3)^-$	198.03
$C_4H_{11}N(HNO_3)(NO_3)^-$	198.07
$C_7H_7NO_2(NO_3)^-$	199.04
$C_6H_5NO_3(NO_3)^-$	201.02
$C_8H_{11}O_6^-$	203.06
$C_6H_6O_4(NO_3)^-$	204.01
$NH_3(HNO3)_2(NO_3)^-$	205.01
$C_6H_8O_4(NO_3)^-$	206.03
$C_5H_7NO_4(NO_3)^-$	207.03
$C_4H_6N_2O_4(NO_3)^-$	208.02
$C_5H_8O_5(NO_3)^-$	210.03
$C_4H_7NO_5(NO_3)^-$	211.02
$C_8H_6O_3(NO_3)^-$	212.02

$C_3H_5NO_6(NO_3)^-$	213.00
$C_{10}H_{13}O_5^-$	213.08
$C_4H_8O_6(NO_3)^-$	214.02
$C_7H_7NO_3(NO_3)^-$	215.03
$C_7H_6O_4(NO_3)^-$	216.01
$C_7H_9NO_3(NO_3)^-$	217.05
$C_7H_8O_4(NO_3)^-$	218.03
$C_7H_{10}O_4(NO_3)^-$	220.05
$C_6H_9NO_4(NO_3)^-$	221.04
$C_5H_8N_2O_4(NO_3)^-$	222.04
$C_{10}H_7O_6^-$	223.02
$C_5H_8O_6(NO_3)^-$	226.02
$C_4H_7NO_6(NO_3)^-$	227.02
$C_4H_6O_7(NO_3)^-$	228.00
$C_8H_9NO_3(NO_3)^-$	229.05
$C_7H_7NO_4(NO_3)^-$	231.03
$C_2H_7N(HNO3)_2(NO_3)^-$	233.04
$C_7H_{10}O_5(NO_3)^-$	236.04
$C_7H_{12}O_5(NO_3)^-$	238.06
$C_{10}H_7O_7^-$	239.02
$C_4H_6N_2O_6(NO_3)^-$	240.01
$C_5H_8O_7(NO_3)^-$	242.02
$C_5H_{11}NO_6(NO_3)^-$	243.05
$C_5H_{10}O_7(NO_3)^-$	244.03
$C_9H_{12}O_4(NO_3)^-$	246.06
$C_7H_7NO_5(NO_3)^-$	247.02
$C_8H_{10}O_5(NO_3)^-$	248.04
$C_7H_9NO_5(NO_3)^-$	249.04
$C_8H_{12}O_5(NO_3)^-$	250.06
$C_7H_{11}NO_5(NO_3)^-$	251.05
$C_7H_{10}O_6(NO_3)^-$	252.04
$C_7H_{12}O_6(NO_3)^-$	254.05
$C_6H_{11}NO_6(NO_3)^-$	255.05
$C_6H_{10}O_7(NO_3)^-$	256.03
$C_5H_8O_8(NO_3)^-$	258.01
$C_8H_7NO_5(NO_3)^-$	259.02

$C_9H_{10}O_5(NO_3)^-$	260.04
$C_4H_{11}N(HNO3)_2(NO3)^-$	261.07
$C_9H_{12}O_5(NO_3)^-$	262.06
$C_7H_7NO_6(NO_3)^-$	263.02
$C_8H_{11}NO_5(NO_3)^-$	263.05
$C_8H_{10}O_6(NO_3)^-$	264.04
$C_9H_{14}O_5(NO_3)^-$	264.07
$C_7H_9NO_6^-(NO_3)^-$	265.03
$C_7H_8O_7(NO_3)^-$	266.01
$C_8H_{12}O_6(NO_3)^-$	266.05
$C_7H_{11}NO_6(NO_3)^-$	267.05
$C_8H_{15}NO_5(NO_3)^-$	267.08
$C_7H_{10}O_7(NO_3)^-$	268.03
$C_6H_{11}NO_7(NO_3)^-$	271.04
$C_6H_{10}O_8(NO_3)^-$	272.03
$C_5H_9NO_8(NO_3)^-$	273.02
$C_5H_8O_9(NO_3)^-$	274.01
$C_{10}H_{12}O_5(NO_3)^-$	274.06
$C_{10}H_{14}O_5(NO_3)^-$	276.07
$C_9H_{13}NO_5(NO_3)^-$	277.07
$C_9H_{12}O_6(NO_3)^-$	278.05
$C_{10}H_{16}O_5(NO_3)^-$	278.09
$C_8H_{11}NO_6^-(NO_3)^-$	279.05
$C_9H_{14}O_6(NO_3)^-$	280.07
$C_7H_9NO_7(NO_3)^-$	281.03
$C_8H_{12}O_7(NO_3)^-$	282.05
$C_7H_{11}NO_7(NO_3)^-$	283.04
$C_8H_{14}O_7(NO_3)^-$	284.06
$C_{10}H_9NO_5(NO_3)^-$	285.04
$C_5H_8N_2O_8(NO_3)^-$	286.02
$C_5H_7NO_9(NO_3)^-$	287.00
$C_7H_{15}NO_7(NO_3)^-$	287.07
$C_5H_{10}N_2O_8(NO_3)^-$	288.03
$C_5H_9NO_9(NO_3)^-$	289.02
$C_{10}H_{12}O_6(NO_3)^-$	290.05
$C_{10}H_{15}NO_5(NO_3)^-$	291.08

$C_{10}H_{14}O_6(NO_3)^-$	292.07
$C_9H_{13}NO_6(NO_3)^-$	293.06
$C_{10}H_{16}O_6(NO_3)^-$	294.08
$C_8H_{11}NO_7(NO_3)^-$	295.04
$C_9H_{14}O_7(NO_3)^-$	296.06
$C_8H_{13}NO_7(NO_3)^-$	297.06
$C_8H_{12}O_8(NO_3)^-$	298.04
$C_7H_{10}O_9(NO_3)^-$	300.02
$C_{10}H_9NO_6(NO_3)^-$	301.03
$C_7H_{12}O_9(NO_3)^-$	302.04
$C_{10}H_{11}NO_6(NO_3)^-$	303.05
$C_6H_{10}O_{10}(NO_3)^-$	304.02
$C_{12}H_{18}O_5(NO_3)^-$	304.10
$C_9H_9NO_7(NO_3)^-$	305.03
$C_9H_8O_8(NO_3)^-$	306.01
$C_{11}H_{16}O_6(NO_3)^-$	306.08
$C_{10}H_{15}NO_6(NO_3)^-$	307.08
$C_{10}H_{14}O_7(NO_3)^-$	308.06
$C_9H_{13}NO_7(NO_3)^-$	309.06
$C_{10}H_{16}O_7(NO_3)^-$	310.08
$C_9H_{15}NO_7(NO_3)^-$	311.07
$C_9H_{14}O_8(NO_3)^-$	312.06
$C_8H_{13}NO_8(NO_3)^-$	313.05
$C_8H_{12}O_9(NO_3)^-$	314.04
$C_7H_{11}NO_9(NO_3)^-$	315.03
$C_{10}H_{10}N_2O_6(NO_3)^-$	316.04
$C_{10}H_9NO_7(NO_3)^-$	317.03
$C_{12}H_{16}O_6(NO_3)^-$	318.08
$C_{10}H_{11}NO_7(NO_3)^-$	319.04
$C_{10}H_{10}O_8(NO_3)^-$	320.03
$C_{12}H_{18}O_6(NO_3)^-$	320.10
$C_{10}H_{13}NO_7(NO_3)^-$	321.06
$C_{11}H_{16}O_7(NO_3)^-$	322.08
$C_{10}H_{15}NO_7(NO_3)^-$	323.07
$C_{10}H_{14}O_8(NO_3)^-$	324.06
$C_{10}H_{16}O_8(NO_3)^-$	326.07

$C_9H_{15}NO_8(NO_3)^-$	327.07
$C_9H_{14}O_9(NO_3)^-$	328.05
$C_8H_{13}NO_9(NO_3)^-$	329.05
$C_9H_{16}O_9(NO_3)^-$	330.07
$C_{11}H_{11}NO_7(NO_3)^-$	331.04
$C_{10}H_9NO_8(NO_3)^-$	333.02
$C_{12}H_{16}O_7(NO_3)^-$	334.08
$C_{12}H_{18}O_7(NO_3)^-$	336.09
$C_{10}H_{13}NO_8(NO_3)^-$	337.05
$C_{11}H_{16}O_8(NO_3)^-$	338.07
$C_{10}H_{15}NO_8(NO_3)^-$	339.07
$C_{10}H_{14}O_9(NO_3)^-$	340.05
$C_{13}H_{13}NO_6(NO_3)^-$	341.06
$C_{10}H_{16}O_9(NO_3)^-$	342.07
$C_9H_{15}NO_9(NO_3)^-$	343.06
$C_9H_{14}O_{10}(NO_3)^-$	344.05
$C_{12}H_{13}NO_7(NO_3)^-$	345.06
$C_{13}H_{16}O_7(NO_3)^-$	346.08
$C_{13}H_{18}O_7(NO_3)^-$	348.09
$C_{12}H_{17}NO_7(NO_3)^-$	349.09
$C_{13}H_{20}O_7(NO_3)^-$	350.11
$C_{11}H_{15}NO_8(NO_3)^-$	351.07
$C_{11}H_{17}NO_8(NO_3)^-$	353.08
$C_{10}H_{15}NO_9(NO_3)^-$	355.06
$C_{11}H_{18}O_9(NO_3)^-$	356.08
$C_{10}H_{17}NO_9(NO_3)^-$	357.08
$C_{13}H_{14}O_8(NO_3)^-$	360.06
$C_{12}H_{13}NO_8(NO_3)^-$	361.05
$C_{13}H_{19}NO_7(NO_3)^-$	363.10
$C_{13}H_{18}O_8(NO_3)^-$	364.09
$C_{12}H_{17}NO_8(NO_3)^-$	365.08
$C_{13}H_{20}O_8(NO_3)^-$	366.10
$C_{12}H_{19}NO_8(NO_3)^-$	367.10
$C_{12}H_{18}O_9(NO_3)^-$	368.08
$C_{11}H_{17}NO_9(NO_3)^-$	369.08
$C_{11}H_{16}O_{10}(NO_3)^-$	370.06

$C_{10}H_{15}NO_{10}(NO_3)^-$	371.06
$C_{14}H_{14}O_8(NO_3)^-$	372.06
$C_{13}H_{13}NO_8(NO_3)^-$	373.05
$C_{14}H_{16}O_8(NO_3)^-$	374.07
$C_{14}H_{20}O_8(NO_3)^-$	378.10
$C_{13}H_{19}NO_8(NO_3)^-$	379.10
$C_{14}H_{22}O_8(NO_3)^-$	380.12
$C_{13}H_{21}NO_8(NO_3)^-$	381.12
$C_{13}H_{20}O_9(NO_3)^-$	382.10
$C_{16}H_{19}NO_6(NO_3)^-$	383.11
$C_{16}H_{18}O_7(NO_3)^-$	384.09
$C_{15}H_{17}NO_7(NO_3)^-$	385.09
$C_{15}H_{16}O_8(NO_3)^-$	386.07
$C_{10}H_{15}NO_{11}(NO_3)^-$	387.05
$C_{11}H_{18}O_{11}(NO_3)^-$	388.07
$C_{18}H_{21}N(NO_3)O_5^-$	393.13
$C_{15}H_{24}(NO_3)O_8^-$	394.14
$C_{18}H_{23}N(NO_3)O_5^-$	395.15
$C_{18}H_{22}(NO_3)O_6^-$	396.13
$C_{17}H_{21}N(NO_3)O_6^-$	397.13
$C_{17}H_{20}(NO_3)O_7^-$	398.11
$C_{16}H_{19}N(NO_3)O_7^-$	399.10
$C_{16}H_{18}(NO_3)O_8^-$	400.09
$C_{15}H_{17}N(NO_3)O_8^-$	401.08
$C_{12}H_{20}(NO_3)O_{11}^-$	402.09
$C_{10}H_{15}N(NO_3)O_{12}^-$	403.05
$C_{15}H_{18}(NO_3)O_9^-$	404.08
$C_{18}H_{17}N(NO_3)O_6^-$	405.09
$C_{19}H_{23}N(NO_3)O_5^-$	407.15
$C_{19}H_{22}(NO_3)O_6^-$	408.13

63
64

CHAPTER 4: OPEN OCEAN AND COASTAL NEW PARTICLE FORMATION FROM SULPHURIC ACID AND AMINES AROUND THE ANTARCTIC PENINSULA

Authors: James Brean, Manuel Dall'Osto, Rafel Simo, Zongbo Shi, David C.S. Beddows, and Roy M. Harrison

Author contributions: MDO, JB and DCSB made the field measurements. RS and MD'O organised the campaign and the cruise. JB processed the data and led the data interpretation, and produced the first draft of the paper. Further contributions to the paper were made by RMH, ZS and RS. R code to produce HYSPLIT back trajectories and CS values was provided by DCSB, alongside sea ice concentrations and Figure 4a.

OPEN OCEAN AND COASTAL NEW PARTICLE FORMATION FROM SULPHURIC ACID AND AMINES AROUND THE ANTARCTIC PENINSULA

James Brean[1], Manuel Dall'Osto[2], Rafel Simo[2], Zongbo Shi[1], David C.S. Beddows[1] and Roy M. Harrison[1*†]

[1]Division of Environmental Health and Risk Management
School of Geography, Earth and Environmental Sciences
University of Birmingham, Edgbaston
Birmingham B15 2TT, United Kingdom

[2]Institute of Marine Science
Consejo Superior de Investigaciones Científicas (CSIC)
Barcelona, Spain

Short title: New Particle Formation in the Antarctic Peninsula

Classification: Physical Sciences: Earth, Atmospheric and Planetary Sciences

* To whom correspondence should be addressed.
† Also at: Department of Environmental Sciences / Center of Excellence in Environmental Studies, King Abdulaziz University, PO Box 80203, Jeddah, 21589, Saudi Arabia

Abstract page

New particle formation is globally one of the major sources of aerosol by number, and therefore a leading factor controlling cloud condensation nuclei (CCN) concentrations. Antarctica is experiencing drastic and variable climate change, and modelling estimates of the regional feedbacks through aerosol direct and indirect radiative forcing are highly uncertain as they are limited by knowledge of the aerosol formation mechanisms. Here, we study summertime open ocean and coastal new particle formation in the Antarctic Peninsula region. Nucleation events occurred under elevated sulphuric acid concentrations in the presence of high alkylamine signals. The rates of particle formation relative to sulphuric acid concentration as well as the sulphuric acid dimer:monomer ratios were similar to those seen for sulphuric acid-dimethylamine-water nucleation both in chamber studies and an urban environment, evidencing that alkylamines were the bases that facilitated sulphuric acid nucleation. Most new particle formation events occurred in air masses arriving from the ice-covered Weddell Sea and its marginal ice zone, indicating that sea ice-influenced ocean regions are a significant source of volatile sulphur and alkylamines. This amine-mediated mechanism is more efficient than the ion-induced sulphuric acid-ammonia nucleation pathway previously described in Antarctica, and one that can occur rapidly under neutral conditions. This hitherto overlooked pathway to biologically-driven aerosol formation must be considered for a correct estimation of aerosol and CCN numbers in ocean – sea ice – aerosols – climate feedback models.

Keywords: New particle formation; Antarctic; nucleation; sulphuric acid; alkylamines

Significance Statement

The climate of the Antarctic is changing rapidly and the full causation is uncertain. Airborne particles (aerosol) exert a significant effect upon climate both through direct interaction (absorption and scattering) with incoming solar radiation, and by influencing the albedo (reflectivity) of clouds. New particle formation in the atmosphere increases the number of cloud condensation nuclei, which in turn has a direct influence on the cloud albedo. This work has demonstrated a mechanism of new particle formation occurring over both sea and coastal land which is more rapid than the only previously observed mechanism active in the Antarctic.

Introduction

The Antarctic Peninsula has shown some of the largest increases in near-surface air temperature measured globally across the last 50 years[1], despite a pause to this increase within the last two decades[2]. Climate models struggle to accurately predict the temperature of the Antarctic Peninsula[3], and this is due to uncertainties in both meteorology[4,5] and the gas and aerosol processes governing radiative forcing[6]. One of the largest areas of uncertainty in the latter is the direct and indirect radiative forcing due to aerosols and clouds[7]. Model studies suggest that natural aerosols contribute disproportionately to uncertainty in indirect forcing[8]. Unlike the Arctic, where anthropogenic contributions to aerosol loadings are considerable[9] the Antarctic is remote from major emission sources, and particles of natural origin dominate the aerosol population[10]. In such a pristine environment, new particle formation (NPF) makes a major contribution both to the condensation nuclei (CN) count, and more critically to the number of cloud condensation nuclei (CCN), hence influencing both the direct and the indirect radiative forcing. NPF processes in Antarctica have been associated with marine air masses and high fluxes of the trace gas dimethylsulphide (DMS)[11]. Indeed, early studies of Antarctic submicron particles found their composition dominated by sulphuric acid (H_2SO_4), largely accompanied by ammonium[11,12]. Later studies have found a contribution of low molecular weight alkylamines to aerosol mass, arising from air masses passing over areas of melting sea ice[13]. Measurements of amines in seawater further suggest high alkylamine content in or near sea ice, and on-line analysis of Antarctic aerosols show that a significant fraction of aerosol phase alkylamines are secondary in origin, rather than primary[14]. Long term measurements in the Arctic show that sea ice melt significantly affect NPF frequency[15]. A similar time series in Antarctica has served to link NPF frequency and faster growth rates of nascent aerosols to upwind emissions of DMS by phytoplankton[16]. DMS in the atmosphere oxidises to both H_2SO_4 and methanesulphonic acid (CH_3SO_3H, MSA). H_2SO_4 is thought to be responsible for most nucleation observed in the atmosphere[17]. MSA can also form new particles in the presence of bases[18] and has been shown to

accelerate nucleation of H_2SO_4 and dimethylamine (DMA) with which it forms stable clusters in the H_2SO_4-DMA-MSA system[19,20].

Recent advances in instrumentation have provided new insight into the fundamental steps of NPF in remote boreal forest[21], coastal[22], pristine polar[23] and urban environments[24]. This is backed up by a host of chamber experiments that have revealed the role of ammonia[25,26] and amines [27] in accelerating H_2SO_4-water nucleation, the roles of highly oxygenated multifunctional organic molecules (HOMs) in accelerating nucleation and growth (and nucleating even in the absence of H_2SO_4[28]), the influence of galactic cosmic rays (GCR)[26], as well as the effects of temperature[29].

While there have been a number of studies of NPF in Antarctica[10,30,31], only one study[23] has investigated the particle nucleation process at a fundamental level. They reported ion-induced H_2SO_4-ammonia nucleation, similar to that observed in laboratory experiments for H_2SO_4-ammonia where GCR were seen to significantly enhance the nucleation rates[26], most markedly at higher temperatures[29], but dissimilar to H_2SO_4-dimethylamine nucleation where GCR were less influential[27]. Here we present evidence for a parallel process in particle nucleation involving H_2SO_4 and small alkylamines that can proceed rapidly under charged or neutral conditions. The study involved air sampling both on coastal land and over the open ocean, providing the first ship-borne data on nucleation processes at the molecular level.

Results

Characteristics of new particle formation events

NPF events, defined using the criteria of Dal Maso et al. (2005)[32], were observed at the research station on Livingston Island on 5 of 29 measurement days (17.2 %). Events happened under elevated H_2SO_4 concentrations, with no difference in MSA concentrations (Fig. 1a). Iodic acid (HIO_3) was slightly elevated on NPF days, though HIO_3 concentrations were around an order of magnitude lower

than those for H_2SO_4 and MSA. The high concentrations of oxygenated organic compounds, including small ($\leq C_4$) dicarboxylic acids and larger C_{5-7} oxygenated organics were slightly lower on NPF days. These organic molecules are too volatile to contribute to nucleation or early stage growth, and the presence of dicarboxylic acids only marginally increases particle formation rates[33]. High isoprene mixing ratios can, however, act as $OH^{\cdot}$ sinks resulting in supressed NPF[34], thus slight elevations of oxygenated organics on non-event days may indicate the role of their precursors as $OH^{\cdot}$ scavengers. Several low molecular weight alkylamines were identified, alongside ammonia. The C_2 and C_4 amine signals were much higher than methylamine and ammonia (Fig. 1b, Supplementary Fig. 1), yet the difference could be enhanced by sensitivity issues. In any case, low mixing ratios of alkylamines (in the range of a few pptv) are sufficiently to substitute ammonia in H_2SO_4-ammonia clusters[35] and enhance nucleation rates significantly[27]. C_2 and C_4 amine signals were slightly higher on event days also (Fig. 1b).

Two NPF events were observed during the cruise aboard the RV Hesperides, one occurring in close proximity to the research station and the other one just slightly south (Supplementary Fig. 2). Here, NPF also occurred under significant elevations of H_2SO_4 and amines, most notably C_4 amines (Supplementary Fig. 3). C_2 and C_4 amines were the only bases measurable aboard the cruise. Events occurred under depletions of both MSA and HIO_3, and unchanged concentrations of oxygenated organics, compared to non-event periods.

NPF events typically occurred under elevated temperature and solar radiation (Supplementary Fig. 4). Condensation sinks were not significantly different between event and non-event days and, in any case, were extremely low (10^{-3}-10^{-4} s^{-1}) compared to values around 10^{-3}-10^{-2} s^{-1} observed in rural and urban UK[36] and in the boreal forest[21]. The newly formed particles in nucleation events generally underwent growth to around 10-20 nm (Supplementary Fig. 5), a common feature of events in the northern Antarctic Peninsula[37].

Counts of particles <10 nm were much higher on NPF event days than non-event days (Fig. 2), with a significant peak at midday and afternoon that corresponded to the formation of new particles, and subsequent loss from the <10 nm mode by either growth or coagulation. Across the whole range of particle sizes NPF events increased particle numbers from a median background of 229 cm^{-3} to 1625 cm^{-3} (Supplementary Fig. 6). The photochemically induced midday peaks of H_2SO_4 concentration were nearly a factor of 3 higher on event days (Fig. 2). Particle numbers began to rise around 09:00, three hours after the first rise of H_2SO_4 concentrations (06:00). This is consistent with the slow particle growth rates measured, which can be presumed to be slightly more rapid at small radii as H_2SO_4 will be driving most of this early particle growth. Conversely, the diurnal patterns of MSA were less pronounced and the mean concentrations on event and non-event days were markedly similar. MSA has been shown to form particles in flow reactors at ppb concentrations[18,38], with the number of particles formed increasing at lower temperatures; however, maximum MSA concentrations in the absence of H_2SO_4 did not result in NPF events in our data, indicating MSA alone could not form particles at an appreciable rate compared to H_2SO_4. A modelling study[39] showed a significant increase in global particle number count when MSA could participate in ternary nucleation in a manner the same as H_2SO_4; however, our results suggest this was not the case. Rather, MSA could have doubled the rates of particle formation from H_2SO_4 and amines at the ambient temperatures encountered[20], or had an effect on particle size distribution by condensation on newly formed particles[39].

Our observed elevation of H_2SO_4 relative to MSA and HIO_3 (Fig. 1, Supplementary Figs. 3, & 7), as well as the absence of organics that would qualify as extremely low volatility organic compounds (ELVOC) capable of forming new particles in the absence of other acids, suggest that H_2SO_4 was the main driver of NPF in the entire dataset, both at the station and on board the ship. The presence of C_2 and C_4 amines at such high signal relative to NH_3 and methylamine (Supplementary Figs. 1 & 8) imply the former two may be of greater importance in stabilising H_2SO_4 clusters.

New particle formation from sulphuric acid and amines

Fig. 3a shows particle formation rates plotted against H_2SO_4 monomer concentration. Measurements are compared to the results of the CLOUD consortium experiments in the presence/absence of galactic cosmic rays (GCR)[26,27,40]. Particle formation rates of up to 12 cm^{-3} s^{-1} occurred at over an order of magnitude lower H_2SO_4 concentration than would be expected for H_2SO_4-NH_3-H_2O nucleation at 278 K, and formation rates were faster than those previously observed in Antarctica at higher H_2SO_4 concentrations[23].

Fig. 3b shows measured H_2SO_4 dimer against H_2SO_4 monomer concentrations, with the H_2SO_4 dimer concentration in the CI-APi-ToF being elevated by the presence of stabilising bases (H_2SO_4 clusters lose base upon charging by nitrate ions[27]). Also plotted are the ratios seen in the CLOUD chamber for H_2SO_4-DMA-H_2O nucleation experiments[40] as well as the estimated H_2SO_4 dimer formed purely from ion induced clustering (IIC) of H_2SO_4 monomer in the NO_3^- chemical ionisation inlet[24]. The positioning of the H_2SO_4 dimer:monomer ratio above the lower IIC limit indicates that there was a secondary stabilising species present in the system, and likely H_2O as a ternary species. This ratio also sits below that calculated for the ternary H_2SO_4–DMA–H_2O system, but is similar to that seen for DMA-H_2SO_4 nucleation in Shanghai[24]. We can presume that the stabilising compound was not solely DMA but included one or more less efficient bases. Further, while base abundance is of great importance in ion induced particle formation, neutral pathways depend more heavily on base strength[41]. As stabilising bases are only stable enough to not evaporate upon charging with NO_3^- in the H_2SO_4 trimer, tetramer or larger, we cannot search for H_2SO_4-amine peaks in the mass spectrum, so there is some uncertainty as to the nature of the stabilising bases present. Signals for NH_3 and methylamine were extremely low, while signals for C_2 and C_4 amines were higher. C_3 and $C_{\geq 5}$ amines were not present at all in the mass spectra. Taking all of this into account, we suggest that the nucleation events we observed in the Antarctic Peninsula were driven by H_2SO_4-amine clusters of C_2

and C_4 amines, with H_2O as a ternary stabilising species. The role of ions cannot be ruled out, but is seen to be minimal when nucleation involves a strong alkylamine base[27,41].

These results are in contrast to prior evidence for H_2SO_4-NH_3-H_2O nucleation on the coast of mainland Antarctica[23], where no alkylamines were detected in the clusters and formation rates were in agreement with prior chamber work for H_2SO_4-NH_3-H_2O nucleation. Our nucleation rates were faster, and we note that this rate of ternary nucleation involving ammonia would be further reduced at the higher temperatures of our study[26].

Links to air mass trajectories

Ninety-six hour HYSPLIT air-mass back trajectories ending up in our measurement locations were clustered based upon their Euclidian distance (Fig. 4a). The NPF events were most commonly associated with cluster 2 (Fig. 4b), i.e., air blowing from the eastern coast of the Antarctic Peninsula and the Weddell Sea. These same air masses, which blew over the largest fraction of sea-ice covered ocean (Fig. 4c), carried the highest signals of H_2SO_4 (Fig. 4d) and C_2 and C_4 amines (Fig. 4e). The marginal ice zone and adjacent open ocean of the Weddell Sea have already been reported to be a source of DMS and alkylamine emissions from the microbiota of sea ice and plankton[13,14].

Discussion

We show that NPF events around the northern Antarctic Peninsula occurred in association with elevated H_2SO_4 concentrations as a necessary condition (Fig. 1). Elevated concentrations of other acids and oxygenated organics, such as MSA, typically co-occurred with high H_2SO_4 during NPF events due to midday photochemistry, but by themselves, without the latter, they did not lead to measurable particle nucleation and growth (Fig. 2, Supplementary Fig. 7). Therefore, our results confirm previous observations of the essential role of H_2SO_4 in NPF in the Antarctic region[23]. However, unlike the previous work, where ammonia was suggested as the major base for ion-induced

H_2SO_4 nucleation[23], here we show that alkylamines may provide a pivotal role in stabilising H_2SO_4 clusters during nucleation periods. This conclusion is based on a comparison of both the rate of particle formation relative to H_2SO_4 and the ratio of H_2SO_4 monomer:dimer to that seen in CLOUD chamber measurements of H_2SO_4-DMA-H_2O nucleation (Fig. 3), alongside the higher signals of C_2 and C_4 amines compared with methylamine and ammonia during NPF events (Fig. 1). Although not necessary for initial particle formation, the present MSA, HIO_3 and oxygenated organics will be involved in the subsequent growth of particles, this contribution depending upon their abundance and volatility.

These results reveal the complexity of aerosol processes in Antarctica. Alkylamines add to ammonia as important ingredients in H_2SO_4 nucleation, and NPF occurs frequently when air masses blow over regions of extended sea ice marginal zone. These air masses contain elevated concentrations of alkylamines and H_2SO_4, confirming that emissions from marine plankton and sea ice melt play crucial roles in the creation of particles critical to regulation of the Antarctic climate. The novel mechanism observed here represents a highly efficient particle formation pathway, with the amine driven nucleation occurring at formation rates 1,000 times faster than that of ammonia at 278 K, even in the presence of ionising radiation, and with stabilization of H_2SO_4 clusters by amines proceeding at near the kinetic limit with negligible evaporation. For its high potential as an aerosol source, this mechanism should be incorporated in modelling efforts towards CCN number estimations and aerosol-cloud interaction studies. Our results are demonstrative of the poor mechanistic knowledge of ocean-atmosphere interactions in the pristine polar environments, and more broadly, of the aerosol processes likely to have had dominant roles in the pre-industrial climate.

Methods

Field site. Ship measurements took place between 2019-01-25 and 2019-02-04 aboard the RV Hesperides. The cruise began at the South Shetland Islands (around -63º latitude), sailing down to -

68º latitude across several days to Adelaide Island, and then back through to the South Shetland Islands. Frequent ship plume related particle events were seen, and these have been filtered out based on the size distributions and particle concentrations seen. Ground measurements took place between 2019-02-12 and 2019-03-13 at the Spanish research station, Juan Carlos I (-62.66, -60.39). The station is located directly on the coast on the south of Livingston Island in the South Shetland Islands. All measurements were taken approximately 100 meters from the main station at a height of 1 meter, with occasional pollution seen in the SMPS spectra from vehicles, generators or waste incineration. These spectra have been filtered from the dataset.

Instrumental setup. The Aerodyne Nitrate Chemical Ionisation Atmospheric Pressure Interface Time of Flight Mass Spectrometer (CI-APi-ToF) was used to make measurements of neutral oxidised organic compounds, strong acids (HIO_3, H_2SO_4 etc), and their molecular clusters at high time resolution with high resolving power. The ionization system charges molecules by adduct formation, such as in the case of organic compounds with two or more hydrogen bond donor groups[42], or proton transfer in the case of strong acids like H_2SO_4. Hydroxyl or hydroperoxyl functionalities are both common hydrogen bond donating groups, with hydroperoxyl being the more efficient hydrogen bond donor[43]. This instrument has been explained in great detail elsewhere[44], but briefly, the front end consists of a chemical ionisation system where a 15 LPM sample flow is drawn in through the 1 metre length 1" OD stainless steel tubing opening. A secondary flow is run parallel and concentric to this sample flow, rendering the reaction chamber effectively wall-less. A 3 SCCM flow of a carrier gas (N_2) is passed over a reservoir of liquid HNO_3, entraining vapour which is subsequently ionised to NO_3^- via an X-ray source. This flow is then guided into the sample flow. The nitrate ions will then charge molecules either by clustering or proton transfer. The mixed flows travelling at 15 LPM enter the critical orifice at the front end of the instrument at 0.8 LPM and are guided through a series of differentially pumped chambers before reaching the ToF analyser. Two of these chambers contain quadrupoles which focus the ion beam, and can be used to select greater sensitivity for certain mass

ranges, and the voltages across each individual chamber can be tuned to maximise sensitivity and resolution for ions of interest. All data analysis was carried out in the Tofware package (Tofwerk AG, Switzerland) in Igor Pro 7 (Wavemetrics Inc., USA). Normalization was performed using signals for NO_3^-, $H_2ONO_3^-$, $HNO_3NO_3^-$, and $(HNO_3)_2NO_3^-$, corresponding to the ionised nitric acid monomer, nitric acid monomer-water cluster, nitric acid dimer and nitric acid trimer respectively. Signals were normalised by the sum of all of these ions except for the amine signals, which were normalised by the nitrate trimer[45]. Our data have been treated with a calibration coefficient of 10^{10} cm^{-3}, based upon an earlier calibration[46].

A Nano Scanning Mobility Particle Sizer (NanoSMPS) instrument measured particle size distributions at five minute time resolution. The NanoSMPS consists of the 3082 EC, 3085 Nano DMA, 3776 CPC (TSI, USA). This measures the size range 4-65 nm. A condensation particle counter (CPC 3775, TSI, USA) was also run in parallel collecting total particle count ≥ 4 nm. A Particle Size Magnifier (PSM, A10, Airmodus, FN) linked to a CPC (3775, TSI, USA) measured the sub-3 nm size fraction. The PSM was run in stepping mode, operating at four different saturator flows to vary the lowest size cut-off of particles that it will grow (D_{50}). Due to instrument malfunction, there is limited PSM data availability.

Calculations of formation rates and condensation sinks

The condensation sink (CS) represents the rate at which a vapour phase molecule will collide with pre-existing particle surface, and was calculated from the size distribution data as follows:

$$CS = 4\pi D \sum_{d_p} \beta_{m,d_p} d_p N_{d_p} , \quad (1)$$

where D is the diffusion coefficient of the diffusing vapour (assumed H_2SO_4), β_m is a transition regime correction[47], d_p is particle diameter, and N_{dp} is the number of particles at diameter d_p. The formation rate of new particles at size d_p is calculated as follows:

$$J_{d_p} = \frac{dN_{d_p}}{dt} + CoagS_{d_p} . N_{d_p} + \frac{GR}{\Delta d_p} . N_{d_p} \quad (2)$$

Where the first term on the right hand side comprises the rate at which particles enter the size d_p, and the latter two terms represent losses from this size by coagulation and growth respectively. See ref 47 for more information on calculation of coagulation sinks and formation rates, and 48 for calculation of growth rates. As PSM data was not available on all days, the NanoSMPS measurements were extended down to 1.5 nm using the equation of Lehtinen et al., 2007[49]

$$J_1 = J_2 \cdot \exp\left(\frac{CoagS_{d_{p1}}}{GR} \cdot d_{p1} \cdot \gamma\right) \quad (3)$$

where J_1 is the formation rate to be calculated at size D_{p1}, $CoagS_{dp1}$ is the coagulation sink at that size, GR is the growth rate and J_2 is the original particle formation rate. *γ is a factor defined as*

$$\gamma = \frac{1}{m+1}\left[\left(\frac{d_{p2}}{d_{p1}}\right)^{m+1} - 1\right] \quad (4)$$

$$m = \frac{log\left(CoagS_{d_{p2}}/CoagS_{d_{p1}}\right)}{log(d_{p2}/d_{p1})} \quad (5)$$

Back trajectories and sea ice extent

The NOAA HYSPLIT model was used to calculate 4 day back-trajectories for air masses arriving at the sampling sites. Each back trajectory data point was assigned to sea ice concentration percentage on a 12.5 km grid from microwave data, providing a sea ice concentration from 0 – 100% (5% width)[50]. These air masses were then clustered using an angle-based distance matrix to produce the 5 back trajectory clusters.

Definitions

CCN: Cloud condensation nuclei

CI-APi-ToF: Chemical ionization atmospheric pressure interface time of flight mass spectrometer

CN: Condensation nuclei

CPC: Condensation particle counter

CS: Condensation sink

D_{50}: 50% detection limit cutoff for particle counting instrument

DMS: Dimethyl sulphide

HOM: Highly oxygenated multifunctional organic molecules

IIC: Ion induced clustering

MSA: Methanesulphonic acid

NanoSMPS: Nano Scanning Mobility Particle Sizer

PSM: Particle size magnifier

References

1. Turner, J. *et al.* Antarctic climate change during the last 50 years. *Int. J. Climatol.* **25**, 279–294 (2005).
2. Turner, J. *et al.* Absence of 21st century warming on Antarctic Peninsula consistent with natural variability. *Nature* **535**, 411–415 (2016).
3. Siegert, M. *et al.* The Antarctic Peninsula under a 1.5°C global warming scenario. *Front. Environ. Sci.* **7**, 1–7 (2019).
4. Turton, J. V., Kirchgaessner, A., Ross, A. N. & King, J. C. The spatial distribution and temporal variability of föhn winds over the Larsen C ice shelf, Antarctica. *Q. J. R. Meteorol. Soc.* **144**, 1169–1178 (2018).
5. Marshall, G. J. & Bracegirdle, T. J. An examination of the relationship between the Southern Annular Mode and Antarctic surface air temperatures in the CMIP5 historical runs. *Clim. Dyn.* **45**, 1513–1535 (2015).
6. IPCC, 2013: Climate Change 2013. *The Physical Science Basis. Contribution of Working Group I to the Fifth Assessment Report of the Intergovernmental Panel on Climate Change*. *The physical science basis. Contribution of the Working Group 1 to the Fifth Assessment Report (AR5) of the Intergovernmental Panel on Climate Change* (Cambridge University Press, 2014).
7. Seinfeld, J. H. *et al.* Improving our fundamental understanding of the role of aerosol−cloud interactions in the climate system. *Proc. Natl. Acad. Sci. U. S. A.* **113**, 5781–5790 (2016).
8. Carslaw, K. S. *et al.* Large contribution of natural aerosols to uncertainty in indirect forcing. *Nature* **503**, 67–71 (2013).
9. Xie, Y. *et al.* Aerosol optical, microphysical, chemical and radiative properties of high aerosol load cases over the Arctic based on AERONET measurements. *Sci. Rep.* **8**, (2018).
10. Weller, R., Schmidt, K., Teinilä, K. & Hillamo, R. Natural new particle formation at the coastal Antarctic site Neumayer. *Atmos. Chem. Phys* **15**, 11399–11410 (2015).
11. O'Dowd, C. D. *et al.* Biogenic sulphur emissions and inferred non-sea-salt-sulphate particularly during Events of new particle formation in and around Antarctica. *Atlantic* **102**, (1997).
12. Adams, P. J., Seinfeld, J. H. & Koch, D. M. Global concentrations of tropospheric sulfate, nitrate, and ammonium aerosol simulated in a general circulation model. *J. Geophys. Res. Atmos.* **104**, 13791–13823 (1999).
13. Dall'Osto, M. *et al.* Antarctic sea ice region as a source of biogenic organic nitrogen in aerosols. *Sci. Rep.* **7**, 1–10 (2017).
14. Dall'Osto, M. *et al.* Simultaneous Detection of Alkylamines in the Surface Ocean and Atmosphere of the Antarctic Sympagic Environment. *ACS Earth Sp. Chem.* **3**, 854–862 (2019).
15. Dall'Osto, M. *et al.* Arctic sea ice melt leads to atmospheric new particle formation. *Sci. Rep.* **7**, 1–10 (2017).
16. Jang, E. *et al.* New particle formation events observed at the King Sejong Station, Antarctic Peninsula - Part 2: Link with the oceanic biological activities. *Atmos. Chem. Phys.* **19**, 7595–7608 (2019).
17. Lee, S. H. *et al.* New Particle Formation in the Atmosphere: From Molecular Clusters to Global Climate. *J. Geophys. Res. Atmos.* (2019) doi:10.1029/2018JD029356.
18. Chen, H., Varner, M. E., Gerber, R. B. & Finlayson-Pitts, B. J. Reactions of Methanesulfonic Acid with Amines and Ammonia as a Source of New Particles in Air. *J. Phys. Chem. B* **120**, 47 (2016).
19. Wen, H. *et al.* Formation of atmospheric molecular clusters consisting of methanesulfonic acid and sulfuric acid: Insights from flow tube experiments and cluster dynamics simulations. *Atmos. Environ.* **199**, 380–390 (2018).
20. Bork, N., Elm, J., Olenius, T. & Vehkamäki, H. Methane sulfonic acid-enhanced formation

of molecular clusters of sulfuric acid and dimethyl amine. *Atmos. Chem. Phys* **14**, 12023–12030 (2014).
21. Rose, C. *et al.* Observations of biogenic ion-induced cluster formation in the atmosphere. *Sci. Adv.* **4**, 5218 (2018).
22. Sipilä, M. *et al.* Molecular-scale evidence of aerosol particle formation via sequential addition of HIO3. *Nature* **537**, 532–534 (2016).
23. Jokinen, T. *et al.* Ion-induced sulfuric acid–ammonia nucleation drives particle formation in coastal Antarctica. *Sci. Adv.* **4**, eaat9744 (2018).
24. Yao, L. *et al.* Atmospheric new particle formation from sulfuric acid and amines in a Chinese megacity. *Science (80-.).* **361**, 278–281 (2018).
25. Schobesberger, S. *et al.* On the composition of ammonia-sulfuric-acid ion clusters during aerosol particle formation. *Atmos. Chem. Phys.* **15**, 55–78 (2015).
26. Kirkby, J. *et al.* Role of sulphuric acid, ammonia and galactic cosmic rays in atmospheric aerosol nucleation. *Nature* **476**, 429–435 (2011).
27. Almeida, J. *et al.* Molecular understanding of sulphuric acid-amine particle nucleation in the atmosphere. *Nature* **502**, 359–363 (2013).
28. Kirkby, J. *et al.* Ion-induced nucleation of pure biogenic particles. *Nature* **533**, 521–526 (2016).
29. Duplissy, J. *et al.* Effect of ions on sulfuric acid-water binary particleformation: 2. Experimental data and comparison with QC-normalized classical nucleation theory. *J. Geophys. Res. Atmos.* **121**, 1752–1775 (2016).
30. Kyrö, E.-M. *et al.* Antarctic new particle formation from continental biogenic precursors. *Atmos. Chem. Phys* **13**, 3527–3546 (2013).
31. Järvinen, E. *et al.* Sciences ess Atmospheric Chemistry and Physics Climate of the Past Geoscientific Instrumentation Methods and Data Systems Seasonal cycle and modal structure of particle number size distribution at Dome C, Antarctica. *Atmos. Chem. Phys* **13**, 7473–7487 (2013).
32. Dal Maso, M. *et al.* Formation and growth of fresh atmospheric aerosols: Eight years of aerosol size distribution data from SMEAR II, Hyytiälä, Finland. *Boreal Environ. Res.* **10**, 323–336 (2005).
33. Arquero, K. D., Xu, J., Gerber, R. B. & Finlayson-Pitts, B. J. Particle formation and growth from oxalic acid, methanesulfonic acid, trimethylamine and water: A combined experimental and theoretical study. *Phys. Chem. Chem. Phys.* **19**, 28286–28301 (2017).
34. Mcfiggans, G. *et al.* Secondary organic aerosol reduced by mixture of atmospheric vapours. *Nature* 0–6 (2019) doi:10.1038/s41586-018-0871-y.
35. Kupiainen, O., Ortega, I. K., Kurté, T. & Vehkamäki, H. Amine substitution into sulfuric acid-Ammonia clusters. *Atmos. Chem. Phys.* **12**, 3591–3599 (2012).
36. Bousiotis, D., Dall'osto, M., Beddows, D. C. S., Pope, F. D. & Harrison, R. M. Analysis of new particle formation (NPF) events at nearby rural, urban background and urban roadside sites. *Atmos. Chem. Phys* **19**, 5679–5694 (2019).
37. Kim, J. *et al.* New particle formation events observed at King Sejong Station, Antarctic Peninsula - Part 1: Physical characteristics and contribution to cloud condensation nuclei. *Atmos. Chem. Phys.* **19**, 7583–7594 (2019).
38. Chen, H. & Finlayson-Pitts, B. J. New Particle Formation from Methanesulfonic Acid and Amines/Ammonia as a Function of Temperature. *Environ. Sci. Technol.* **51**, 243–252 (2017).
39. Hodshire, A. L. *et al.* The potential role of methanesulfonic acid (MSA) in aerosol formation and growth and the associated radiative forcings. *Atmos. Chem. Phys.* **19**, 3137–3160 (2019).
40. Kürten, A. *et al.* Neutral molecular cluster formation of sulfuric acid–dimethylamine observed in real time under atmospheric conditions. *Proc. Natl. Acad. Sci.* **111**, 15019–15024 (2014).
41. Myllys, N. *et al.* Role of Base Strength, Cluster Structure and Charge in Sulfuric Acid-Driven Particle Formation. *Atmos. Chem. Phys. Discuss.* 1–23 (2019) doi:10.5194/acp-2019-

305.
42. Hyttinen, N. *et al.* Modeling the Charging of Highly Oxidized Cyclohexene Ozonolysis Products Using Nitrate-Based Chemical Ionization. *J. Phys. Chem. A* **119**, 6339–6345 (2015).
43. Møller, K. H., Tram, C. M. & Kjaergaard, H. G. Side-by-Side Comparison of Hydroperoxide and Corresponding Alcohol as Hydrogen-Bond Donors. *J. Phys. Chem. A* **121**, 2951–2959 (2017).
44. Jokinen, T. *et al.* Atmospheric sulphuric acid and neutral cluster measurements using CI-APi-TOF. *Atmos. Chem. Phys.* **12**, 4117–4125 (2012).
45. Simon, M. *et al.* Detection of dimethylamine in the low pptv range using nitrate chemical ionization atmospheric pressure interface time-of-flight (CI-APi-TOF) mass spectrometry. *Atmos. Meas. Tech.* **9**, 2135–2145 (2016).
46. Brean, J. *et al.* Observations of highly oxidised molecules and particle nucleation in the atmosphere of Beijing. *Atmos. Chem. Phys. Discuss.* 1–35 (2019) doi:10.5194/acp-2019-156.
47. Kulmala, M. *et al.* On the formation, growth and composition of nucleation mode particles. *Tellus, Ser. B Chem. Phys. Meteorol.* **53**, 479–490 (2001).
48. Kulmala, M. *et al.* Measurement of the nucleation of atmospheric aerosol particles. *Nat. Protoc.* **7**, 1651–1667 (2012).
49. Lehtinen, K. E. J., Dal Maso, M., Kulmala, M. & Kerminen, V. M. Estimating nucleation rates from apparent particle formation rates and vice versa: Revised formulation of the Kerminen-Kulmala equation. *J. Aerosol Sci.* **38**, 988–994 (2007).
50. Ezraty, R., Girard-Ardhuin, F., Piolle, J. F. & Heygster, L. K. G. *Arctic and Antarctic sea-ice concentration and Arctic sea ice drift estimated from Special Sensor Microwave Imager data. Version 2.1*. (Département d'Océanographie Physique et Spatiale, IFREMER, Brest, France and University of Bremen Germany, 2007).

Acknowledgments

We wish to thank the Spanish Armada, and particularly the captains and crew of the BIO A-33 Hesperides, for their invaluable collaboration. We are also indebted to the UTM, and especially Miki Ojeda, for logistic and technical support on the Antarctic Spanish BAE.

Funding: This study was funded by the Spanish Ministry of Economy (PI-ICE-CTM 2017–89117-R). This work was also supported by the National Centre for Atmospheric Science funded by the U.K. Natural Environment Research Council (R8/H12/83/011).

Author contributions: MDO, JB and DCSB made the field measurements. RS and MD'O organised the campaign and the cruise. JB processed the data and led the data interpretation, and produced the first draft of the paper. Further contributions to the paper were made by RMH, ZS and RS.

Competing financial interests: The authors declare no conflict of interests.

Data and materials availability: Data supporting this publication are openly available from the UBIRA eData repository at https://doi.org/10.25500/edata.bham.00000400

FIGURE LEGENDS

Figure 1: Potential new particle sources on nucleation and non-nucleation days. **(a)** concentrations of gas phase H_2SO_4, MSA, HIO_3 and oxygenated organic molecules, and **(b)** signal intensities for ammonia and amines. Measurements made at the station. Error bars show 1 standard error.

Figure 2: Diurnal cycles between nucleation and non-nucleation days showing **(a)** <10 nm particle count as measured by SMPS, **(b)** H_2SO_4 monomer concentration, and **(c)** MSA concentration. Dashed lines indicate means on each of the respective days.

Figure 3: Nucleation rates and sulphuric acid concentrations in Antarctica and in chambers. **(a)** Particle formation rate as a function of H_2SO_4 monomer concentration, and **(b)** H_2SO_4 dimer as a function of H_2SO_4 monomer concentration. Green circles show ambient Antarctic data aggregated to 1 day, orange squares show the CLOUD data from experiments of H_2SO_4-DMA-H_2O nucleation[40], purple diamonds show CLOUD data from experiments of H_2SO_4-H_2O nucleation, pink triangles show CLOUD data from experiments of H_2SO_4-NH_3-H_2O nucleation[26], and the dashed line shows theoretical concentration of H_2SO_4 dimer produced due to ion induced clustering in the CI-APi-ToF ionisation inlet[24]. All chamber data is recorded at 278 K and 38% RH under GCR conditions, except H_2SO_4-DMA-H_2O data, which includes both GCR and neutral data.

Figure 4: Association between sea ice extent and new particle formation. (a) Clustered 96 hour back trajectories for station measurements, lighter traces showing the unclustered trajectories, (**b**) The association of each back trajectory cluster with sea ice extent, (**c**) the percentage of NPF events associated with each of these back trajectory clusters, and **(d, e)** box plots showing concentrations and signals per cluster for H_2SO_4, and C_2 & C_4 alkylamines, as measured by the CI-APi-ToF.

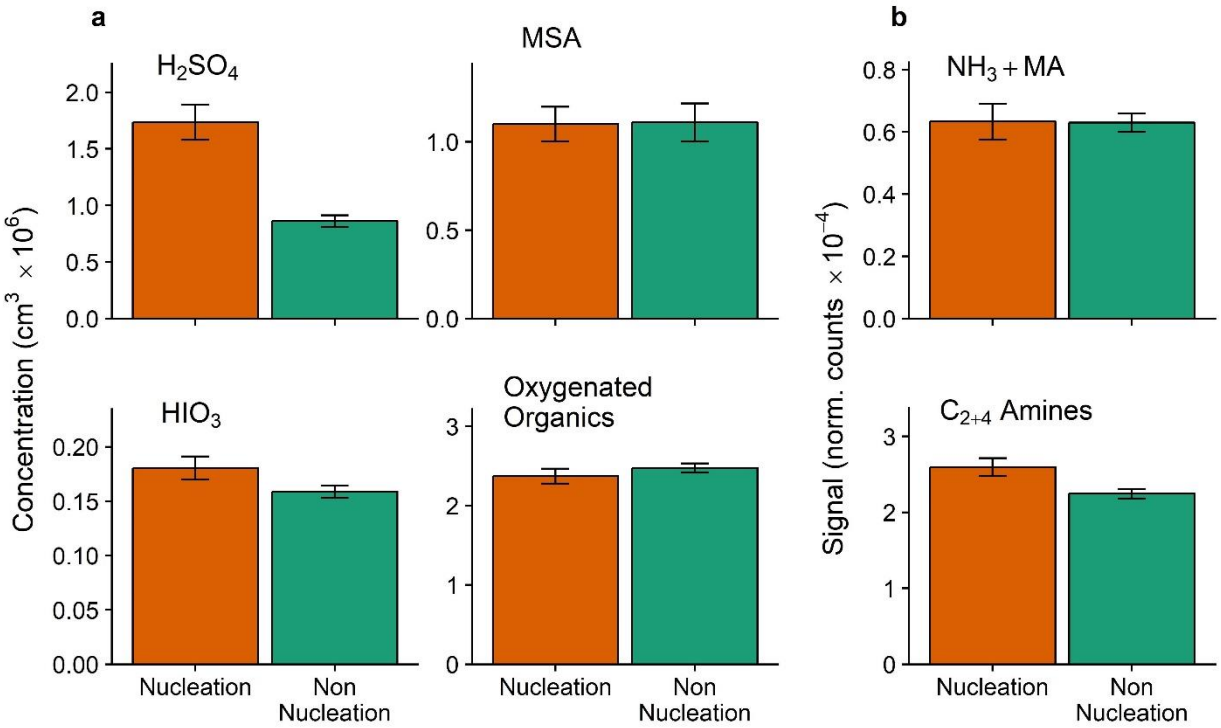

Figure 1: Potential new particle sources on nucleation and non-nucleation days. **(a)** concentrations of gas phase H_2SO_4, MSA, HIO_3 and oxygenated organic molecules, and **(b)** signal intensities for ammonia and amines. Measurements made at the station. Error bars show 1 standard error.

.

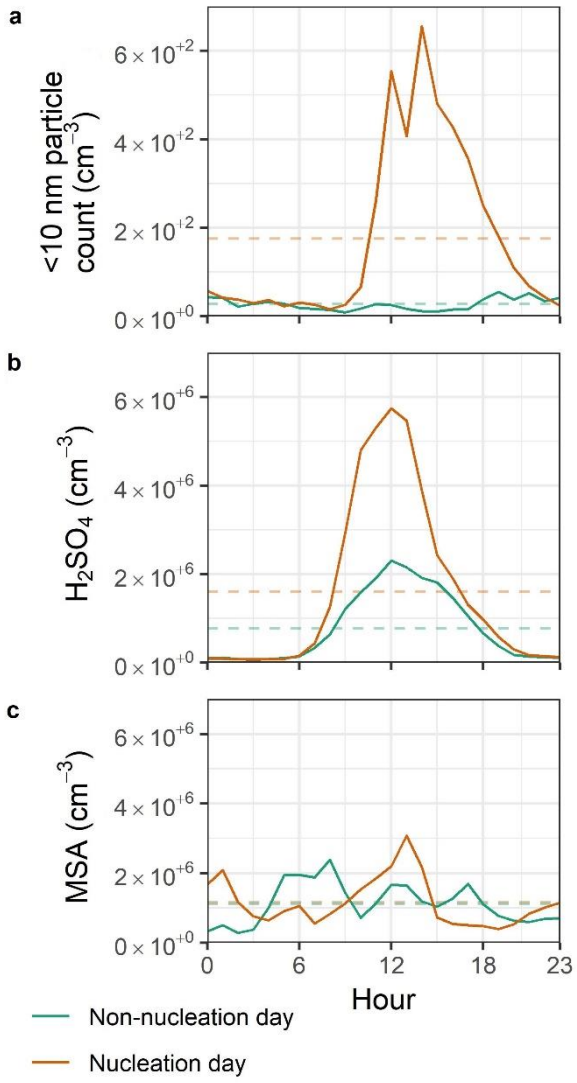

Figure 2: Diurnal cycles between nucleation and non-nucleation days showing **(a)** <10 nm particle count as measured by SMPS, **(b)** H_2SO_4 monomer concentration, and **(c)** MSA concentration. Dashed lines indicate means on each of the respective days.

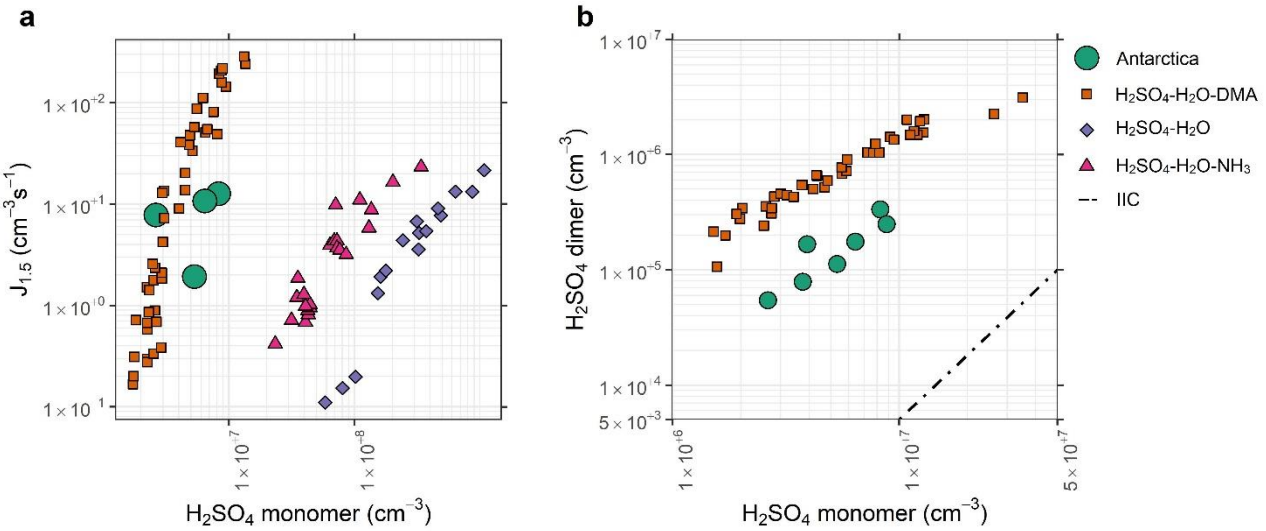

Figure 3: Nucleation rates and sulphuric acid concentrations in Antarctica and in chambers. **(a)** Particle formation rate as a function of H_2SO_4 monomer concentration, and **(b)** H_2SO_4 dimer as a function of H_2SO_4 monomer concentration. Green circles show ambient Antarctic data aggregated to 1 day, orange squares show the CLOUD data from experiments of H_2SO_4-DMA-H_2O nucleation[40], purple diamonds show CLOUD data from experiments of H_2SO_4-H_2O nucleation, pink triangles show CLOUD data from experiments of H_2SO_4-NH_3-H_2O nucleation[26], and the dashed line shows theoretical concentration of H_2SO_4 dimer produced due to ion induced clustering in the CI-APi-ToF ionisation inlet[24]. All chamber data is recorded at 278 K and 38% RH under GCR conditions, except H_2SO_4-DMA-H_2O data, which includes both GCR and neutral data.

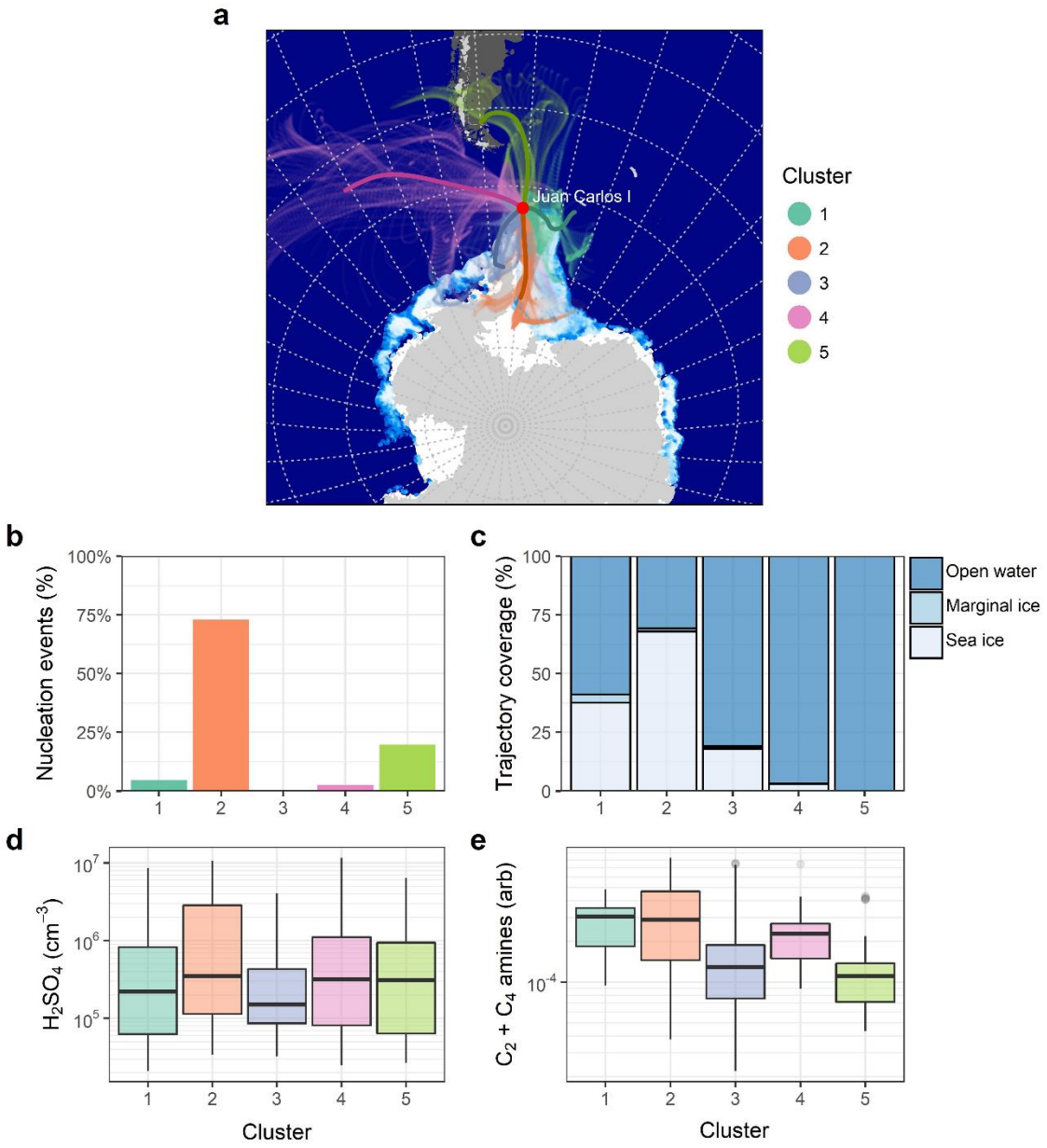

Figure 4: Association between sea ice extent and new particle formation. (a) Clustered 96 hour HYSPLIT back trajectories for station measurements, lighter traces showing the unclustered trajectories, (**b**) the percentage of NPF events associated with each of these back trajectory clusters, (**c**) The association of each back trajectory cluster with regions of sea ice, where 0-20 % sea ice coverage is "open water", 20-80 % sea ice coverage is "marginal ice", and >80 % sea ice coverage is "sea ice", and **(d, e)** box plots showing concentrations and signals per cluster for H_2SO_4, and C_2 & C_4 alkylamines, as measured by the CI-APi-ToF.

Supplementary Information

OPEN OCEAN AND COASTAL NEW PARTICLE FORMATION FROM SULPHURIC ACID AND AMINES AROUND THE ANTARCTIC PENINSULA

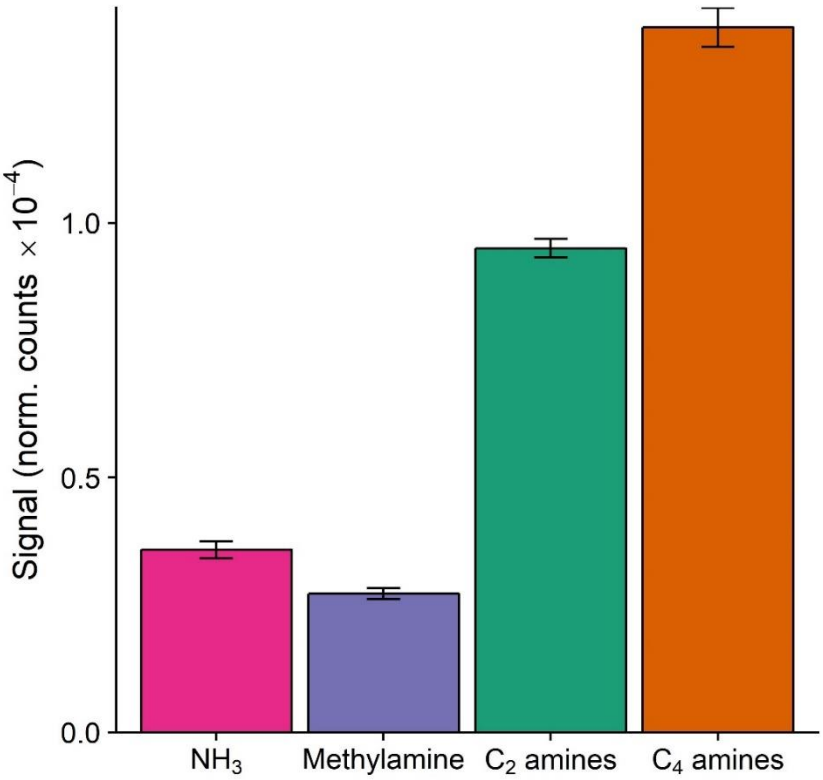

Supplementary Figure 1: Mean ion signals for ammonia and amines. Data is of station measurements; units are normalised counts. Amine and ammonia ion signals have been normalised to the nitrate trimer counts.

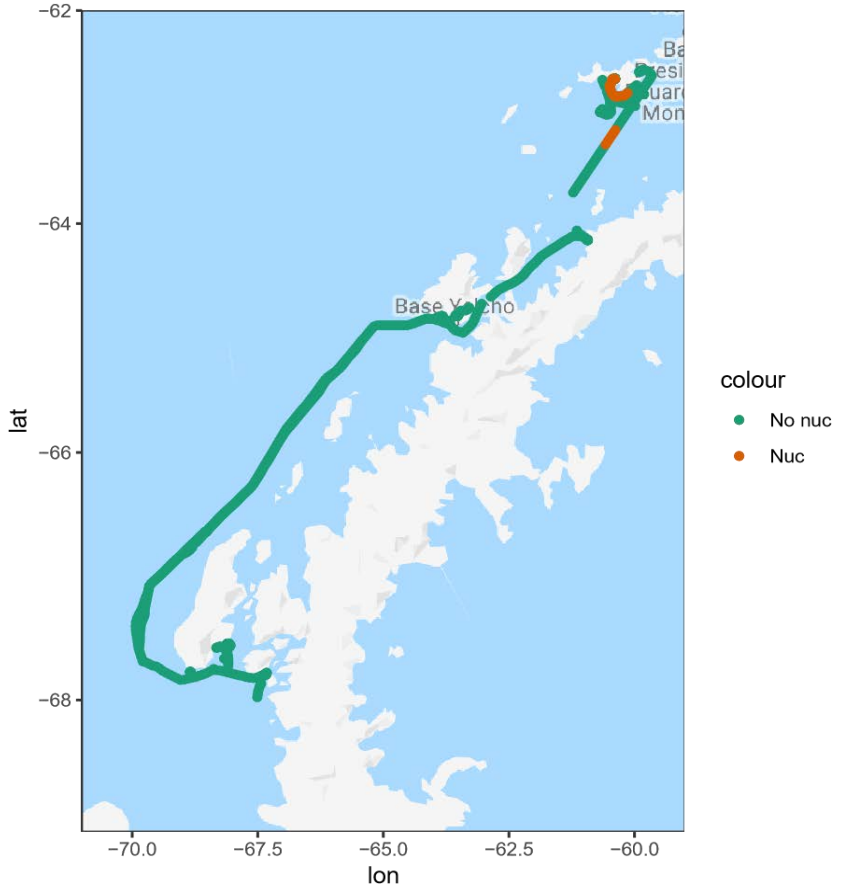

Supplementary Figure 2: Cruise trajectory, coloured by nucleation/non nucleation occurrence.

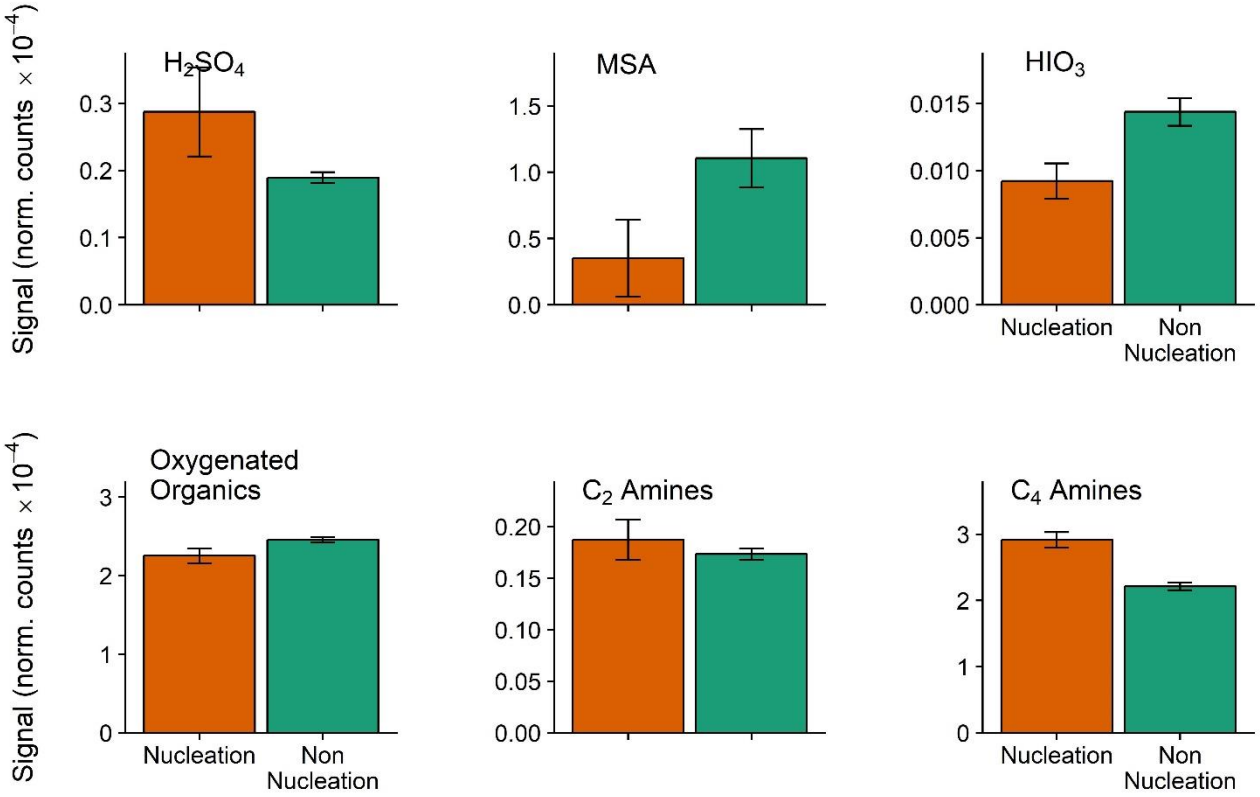

Supplementary Figure 3: Potential new particle sources during nucleation and non-nucleation periods during cruise. Signals of gas phase H_2SO_4, MSA, HIO_3, oxygenated organic molecules, C_2 amines, and C_4 amines. Only the exact NPF periods are labelled as "Nucleation" here, to avoid highlighting midday maxima as NPF events were frequently seen in the evening-time.

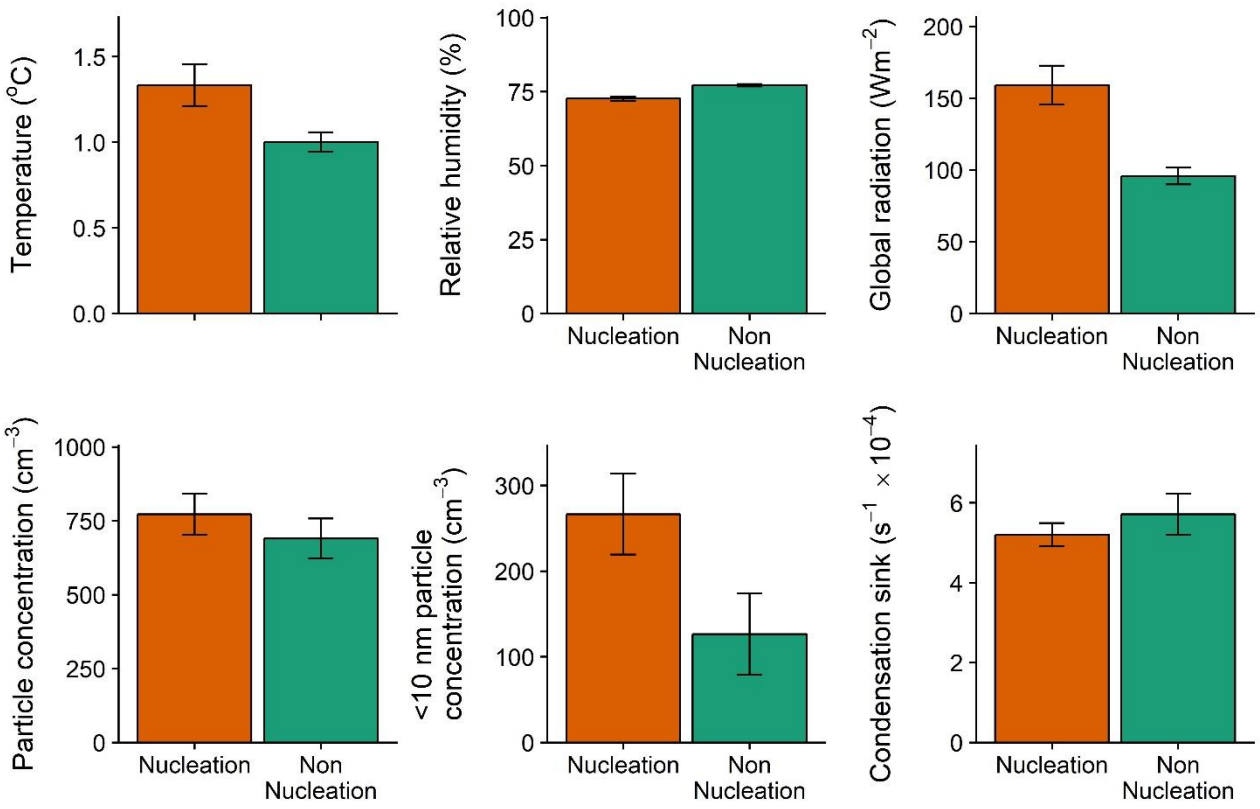

Supplementary Figure 4: Box plots of meteorological and particle count data. Data are segregated by nucleation and non-nucleation days for measurements at the station.

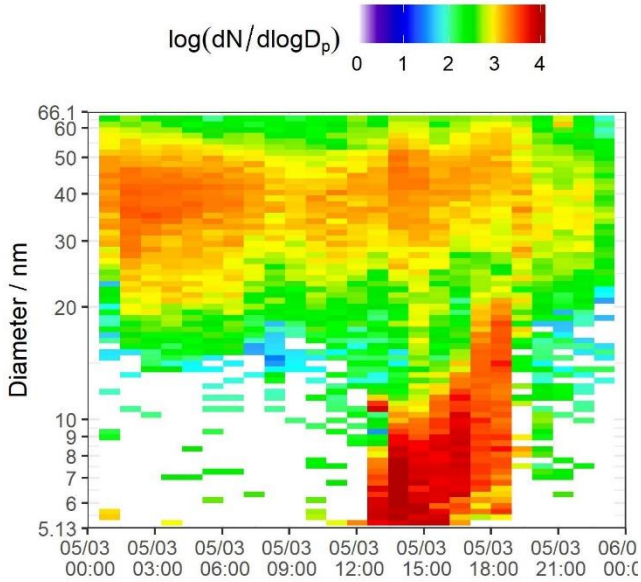

Supplementary Figure 5: Example nucleation event contour. Data taken during a nucleation event on 05/03/2019. White sections refer to particle count of 0 in a particular bin.

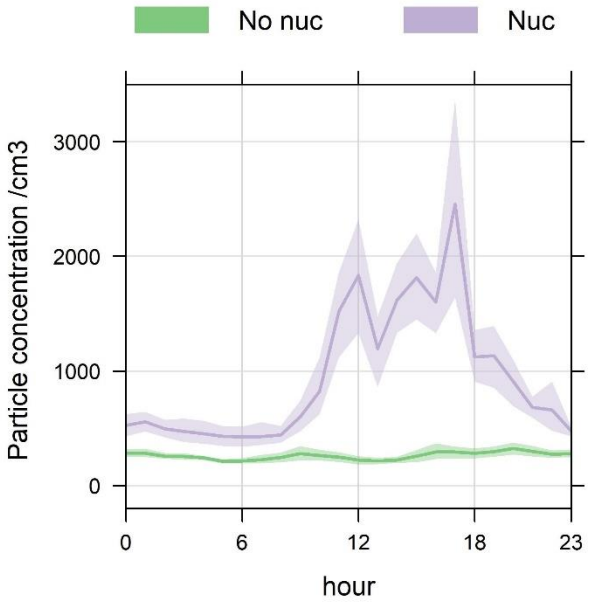

Supplementary Figure 6: Average particle count diurnal cycle for event and non-event days. Data taken from SMPS counts, spikes are seen due to irregular timing of events. Shaded area shows 95% confidence interval on mean

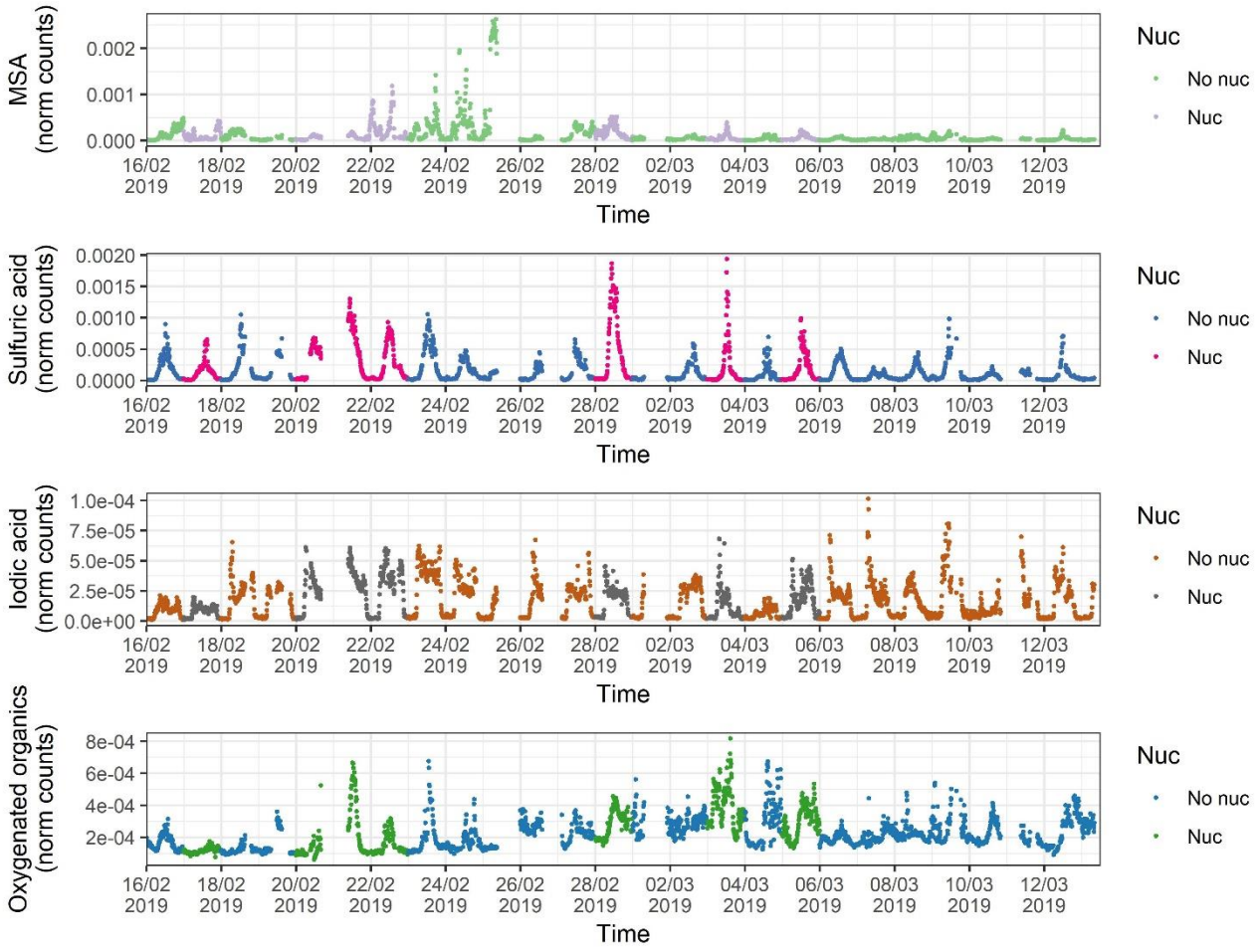

Supplementary Figure 7: Time series of MSA, H_2SO_4 and HIO_3 for the period of station data. Units are of normalised counts. The colours represent nucleation/non-nucleation days. Spikes in MSA and IA signal frequently not coincidental with new particle formation.

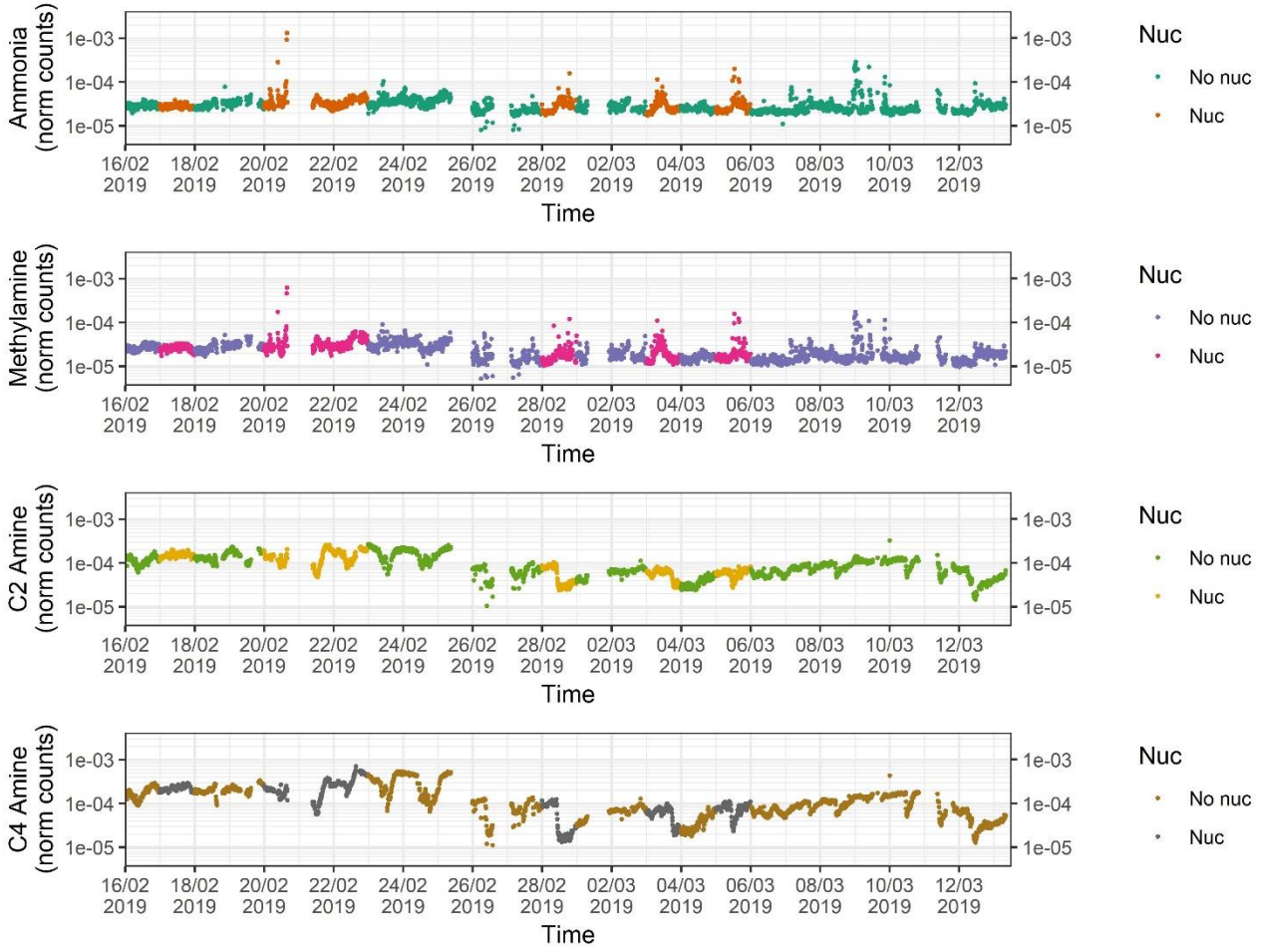

Supplementary Figure 8: Time series of ammonia and amines for the period of station data. Units are of normalised counts. The colours represent nucleation/non-nucleation days.

CHAPTER 5: DISCUSSION

Discussion

The mechanisms driving both aerosol nucleation and growth in urban environments involve a host of acids (most significantly sulphuric acid), bases, and HOMs. Particle formation proceeding in Beijing and Barcelona are inferred to involve sulphuric acid and amines (chapters 2 & 3). This is markedly similar to that seen in Antarctica (chapter 4). The involvement of these small amines in preference to ammonia is expected in environments where mixing ratios of amines of a few pptv are observed, as amines will efficiently replace ammonia in clusters with sulphuric acid[84], and such mechanisms have been observed in urban environments year round[43,81]. Evaporation rates of sulphuric acid-amine clusters at tropospheric temperature ranges are low due to their high binding energies, but their elevation with increasing temperatures result in a reduced particle formation rate at temperatures approaching 298 K[79,81]. This results in significantly enhanced nucleation rates at any given sulphuric acid concentration both in the polar and urban environments studied in this thesis compared to mechanisms involving solely ammonia as a ternary stabilising compound (Figure 6). Involvement of HOMs, iodic acid, methanesulphonic acid, dicarboxylic acids and other present species cannot be ruled out, but are not thought to be dominant processes in the datasets presented in this thesis[66,80,120,127,193] Nucleation driven by sulphuric acid, ammonia and HOMs in conjunction has been shown in the boreal environment, and mirrored in a chamber study[194], and hypothesised in rural Germany[165], where results were similar to those presented in Chapter 3. A prior report from coastal mainland Antarctica shows particle formation proceeding by nucleation of sulphuric acid and ammonia[48], a mechanism significantly less efficient than our observed sulphuric acid-amine mechanism. Chapter 4 is the first report of such a mechanism in the polar environment.

Amines are expected in urban environments with industrial, waste management, and regional agricultural sources[70]. Amines in Antarctica were found to arise from sea-ice influenced regions of ocean, with prior work reporting melting sea ice as a source of amines in both the ocean and secondary aerosols[69,195]. Global models[18,19] currently opt to neglect the role of amine emissions due to their limited sources outside of areas with significant anthropogenic influence, however, this work provides direct

evidence of an oceanic amine source that accelerates particle formation rates significantly (chapter 4). The global role of amine-influenced nucleation may be significant and therefore should not be neglected in these models once such sources are constrained, as sulphuric acid-amine nucleation will compete with the schemes currently considered, such as the sulphuric acid-HOM system. Further, while HOM yields and O:C ratios increase with temperature, the dependence of the rates of sulphuric acid-HOM and pure HOM nucleation on temperature have not yet been investigated[54,120,123]. The rate of sulphuric acid-amine nucleation has been shown to reduce with temperatures approaching 298 K due to cluster evaporation, but will still be an efficient source of new particles[79,81], and therefore this mechanism may be significant in warmer environments should emission fluxes of amines be sufficiently large (i.e., from agriculture[70,165,196]).

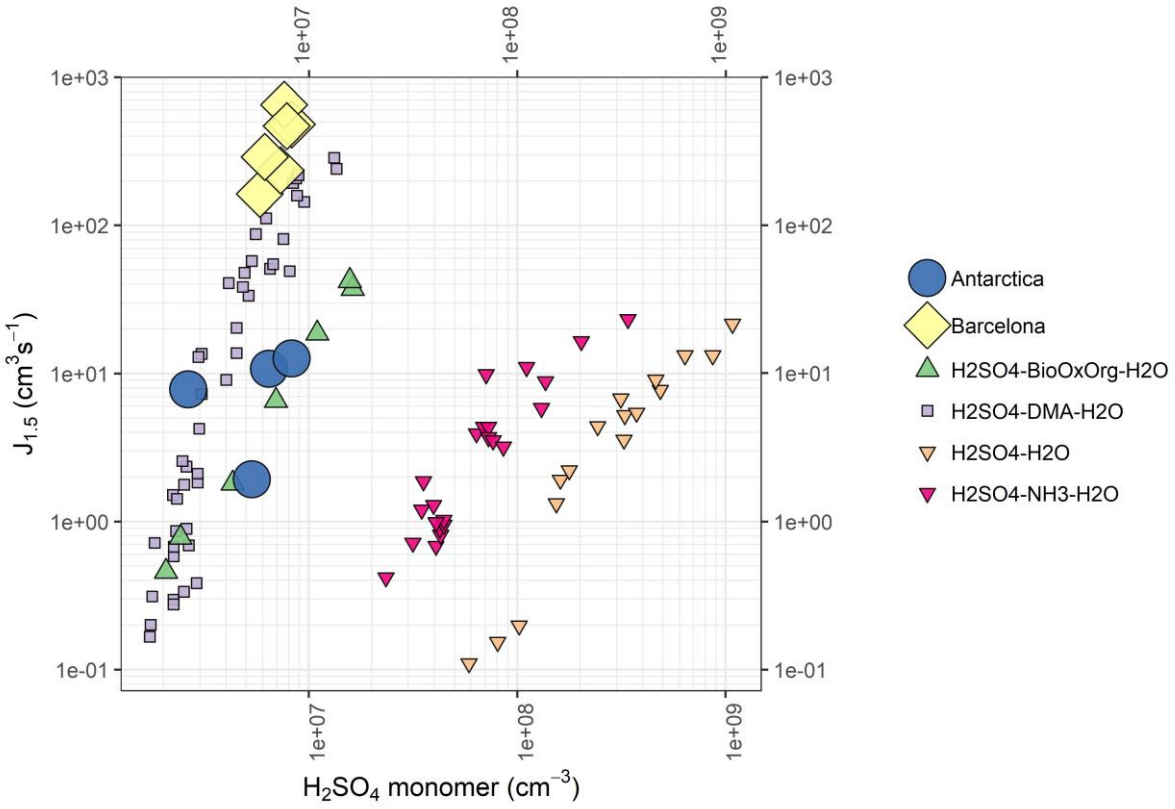

Figure 6: Rates of different mechanisms of sulphuric acid nucleation. Data from two field campaigns (Antarctica: blue circles, Barcelona: yellow diamonds), alongside data from CLOUD chamber experiments under GCR conditions at 278 K[78,79,120]. DMA experiments also include neutral condition experiments, as both GCR and neutral conditions yielded similar results.

Chapters 2 and 3 demonstrate the importance of both the precursor VOC and temperature for generation of HOMs, as well as the significance of NO_x as a peroxy radical terminator, inhibiting both autoxidation and RO_2· dimerization chemistry, limiting generation of large HOMs of high carbon number. NO_x is shown to be significant in adding nitrogen to HOMs, most likely in the form of R-O-NO_2 groups, which can increase saturation vapour pressure due to intramolecular hydrogen bonding, an effect which had been shown prior in chamber studies[197], but not in the urban environment. Despite this, a pivotal role of HOMs in NPF is inferred in Barcelona.

Alkylbenzenes produce most of the observed HOMs in both Beijing and Barcelona due to their significant local sources. With significant reductions in combustion engine vehicle traffic and therefore both alkylbenzene and NO_x emissions expected in coming years, more highly oxygenated HOMs will be expected in cities, but at lower concentrations, which will likely slow later stage particle growth significantly. Very few HOMs were observed in Antarctica (chapter 4) both due to low emission fluxes of any molecules which would efficiently produce HOM upon oxidation, and lower temperatures, although RO_2 lifetimes would undoubtedly be significantly longer than in the urban environment. It is worth note that it is uncertain as to whether HOMs we observe in this work are truly peroxy radical isomerisation products, as species arising from multiple generations of OH· oxidation of alkylbenzenes can have the same molecular formulae as HOMs from peroxy radical isomerisation. These HOMs are seen to be integral for rapid particle growth in Barcelona. Days defined as "burst-event" days were observed to occur under significantly reduced HOM concentrations at the measurement location. However, these events occur across several hours, and therefore ~60 – 120 km southward of the measurement station at a wind speed of ~5 m s^{-1}, extending over the ocean. The lifetime of HOMs under typical urban summertime atmospheric conditions is on the order of seconds with respect to condensation, and tens of minutes with respect to OH oxidation[77]. It is implausible that the HOMs present across the ocean are similar to that seen in the CI-APi-ToF spectra, as this region extends far from direct traffic emissions, although shipping emissions are plausible, and thus unless the event occurs homogeneously over a significant area, the source characteristics seen for the beginning of such an event ~60 – 120 km southwards are likely different to those seen at the measurement location

Table 1: Mean conditions for each sampling campaign

	Beijing	*Barcelona*	*Antarctica*
Temperature (°C)	26.7	11.0	1.67
Global radiation (W m^{-2})	148	302	108
RH (%)	51.0	71.0	77.8
Condensation Sink (s^{-1})	0.12	0.035	0.00056
Particle concentration (cm^{-3})	22580	14968	616
PM2.5 mass (μg m^{-3})	49.4	11	
NO_x (ppb)	23.8	18.1	

Both of the urban environments studied were warm, subject to high insolation, high CS, and high NO_x (Table 1). The effect of the former of these two effects will be faster oxidation chemistry, both in the form of faster autoxidation chemistry, and higher oxidant concentrations. High CS and NO_x inhibit nucleation events by acting as a sink for low volatility vapours and suppressing autoxidation chemistry respectively. Significant sources of nucleating vapours (i.e., sulphuric acid in the form of high SO_2 and $OH^{\cdot}$) are therefore required to drive nucleation in these environments. Primary particle emissions are plentiful, with both high PM2.5 mass and particle number concentrations even in the absence of nucleation. Particle mass and number concentrations were greatest in the substantially more polluted environment of Beijing. Despite this, nucleation was more frequent in Beijing than Barcelona (47% and 30% of days, respectively).

Conversely, the pristine environment of Antarctica was significantly colder, with lower insolation, but also lower condensation sinks, and thus a much more inefficient sink of low volatility vapours. This is offset by both lower concentrations of oxidants arising from weaker incident radiation, and lower concentrations of precursors (i.e., SO_2). Primary particle emissions are scarce, as are emissions of NO_x, with the majority of particulate mass arising from sea spray. Sea spray and NPF pose the two main sources of Antarctic CCN. Nucleation occurred on 17% of measurement days in Antarctica, and particle formation is around two orders of magnitude less rapid than that in Barcelona, with growth around one order of magnitude less rapid, attributable to significantly lower sulphuric acid and HOM concentrations (Figure 7). These rates will also be influenced by temperatures, as well as concentrations of other acids (iodic acid, MSA, small organic acids), and other molecules. The moderate growth limited to ~20 nm

in Antarctica is similar to events seen in Barcelona under low HOM concentrations, where particles fail to grow past the first 10 nm, further solidifying the pivotal role of HOM in particle growth processes in these environments.

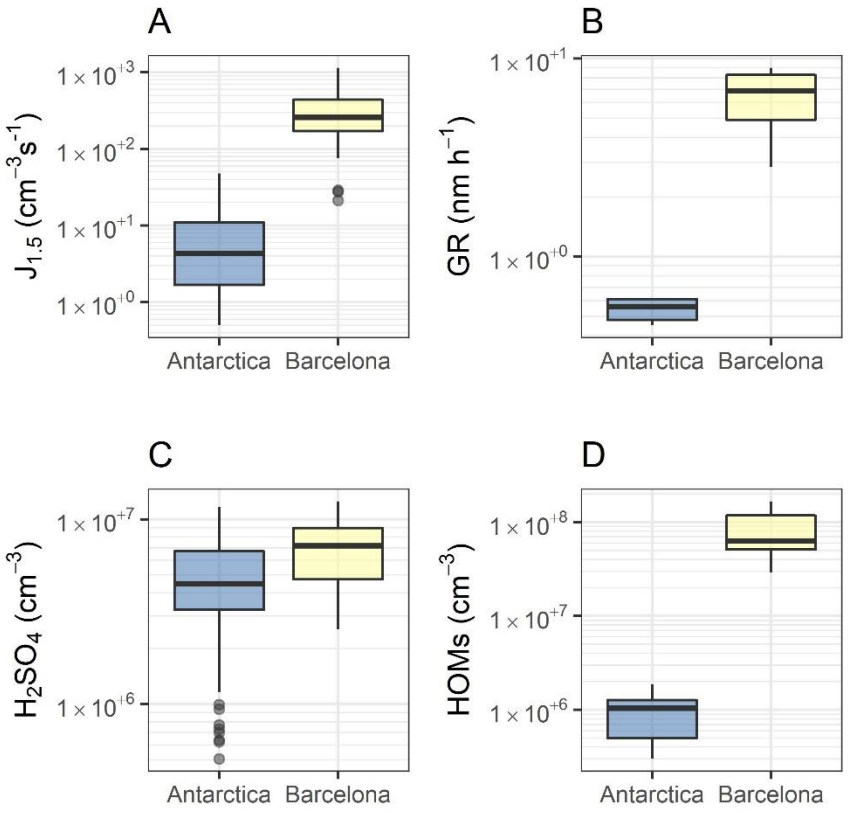

Figure 7: Comparison of events in Antarctica and Barcelona showing (A) formation rates, (B) growth rates, (C) sulphuric acid concentrations during events, and (D) HOM concentrations during events.

Future directions

Research on new particle formation and growth is a field facing challenges arising from a lack of measurements across the diverse host of environments in which NPF occurs, as well as a lack of truly long term measurements of sufficient detail to understand the temporal variability of NPF mechanisms. Understanding such large datasets after their collection also proves an issue, with high mass and temporal resolution measurements of compounds upon the many thousands arising from CI-APi-ToF instruments. Future research will therefore likely rely on the development of robust statistical techniques for source apportionment as applied to CI-APi-ToF data[172]. While mechanistic knowledge of nucleation is improving rapidly, understanding of growth processes is inhibited by a lack of

measurements of the composition of new particles, with the mechanisms of particle growth being mostly the subject of conjecture rather than direct measurement. This understanding will be aided by future improvements to instrumentation, such as the recent development of the EESI-ToF[198]. Further, there still remains great ambiguity when attempting to assign precursor VOC to HOM in regions with multiple VOC of similar carbon number, as there are multiple fragmentation, dimerization, oxidation, H-shift and termination reactions, all of which can produce HOM of overlapping chemical formulae (although at vastly different yields)[111]. While modelling studies of HOM formation are currently sparse[147,199], improved understanding of HOM chemistry from a host of VOCs from chamber and computational studies will help inform future models, and better deconvolve HOM formation in complex urban environments, as will future development of on-line chromatographic techniques capable of separating HOM of the same mass. Integrated studies involving the co-deployment of instruments capable of measuring HOM precursors (PTR-MS), their oxidants (FAGE[52], CIMS[200], BBCAES[201]), and their various oxidation products (iodide CIMS, nitrate CIMS[202]), alongside the resultant changes to aerosol composition (EESI-ToF[203], AMS[134]), while resource intensive, are capable of providing unparalleled insight into the behaviour and dynamics of these molecules.

The regionality of mechanisms of new particle formation events remains a question, with the influence of combustion related VOCs emissions undoubtedly significant in urban background regions (chapters 2 and 3). Whether these influences are much more significant at the roadside, and the degree to which primary sulphuric acid affects nucleation in these areas remains unanswered, as does the question of how the outflow of such anthropogenic emissions affect regional new particle formation and growth. Diversified and simultaneous measurements will be required to fully understand such mechanisms.

Regarding the work of this thesis, while a pivotal role of NO_x in HOM chemistry in Beijing and Barcelona is demonstrated, the exact effect on particle formation and growth processes is not yet clear. Further, while involvement of a wide array of compounds in particle formation is likely in these environments, no direct measurements of such clusters were made due to the limitations of the CI-APi-ToF. Further, while a mechanism of particle formation from sulphuric acid and amines is demonstrated in Antarctica, with amines arising from regions of melting sea ice, the mechanistic origin and spatial

extent of these amines and therefore the regional significance of this mechanism remains unknown. The work of this thesis contributes to the ever-growing body of research on NPF by both evidencing mechanisms of nucleation across a diverse set of environments and providing insight into the nature of HOM formation and growth in polluted urban centres where measurements are sparse.

REFERENCES

1. N. T. K. Thanh, N. Maclean, S. Mahiddine, Mechanisms of nucleation and growth of nanoparticles in solution. *Chem. Rev.* **114**, 7610–7630 (2014).

2. M. Kulmala, I. Riipinen, M. Sipilä, H. E. Manninen, T. Petäjä, H. Junninen, M. D. Maso, G. Mordas, A. Mirme, M. Vana, A. Hirsikko, L. Laakso, R. M. Harrison, I. Hanson, C. Leung, K. E. J. Lehtinen, V.-M. Kerminen, Toward direct measurement of atmospheric nucleation. *Science (80-.).* **318**, 89–92 (2007).

3. M. Kulmala, T. Petäjä, T. Nieminen, M. Sipilä, H. E. Manninen, K. Lehtipalo, M. Dal Maso, P. P. Aalto, H. Junninen, P. Paasonen, I. Riipinen, K. E. J. Lehtinen, A. Laaksonen, V.-M. Kerminen, Measurement of the nucleation of atmospheric aerosol particles. *Nat. Protoc.* **7**, 1651–1667 (2012).

4. J. Kontkanen, T. Olenius, M. Kulmala, I. Riipinen, Exploring the potential of the nano-Köhler theory to describe the growth of atmospheric molecular clusters by organic vapors, 1–31 (2018).

5. M. Wang, W. Kong, R. Marten, X. C. He, D. Chen, J. Pfeifer, A. Heitto, J. Kontkanen, L. Dada, A. Kürten, T. Yli-Juuti, H. E. Manninen, S. Amanatidis, A. Amorim, R. Baalbaki, A. Baccarini, D. M. Bell, B. Bertozzi, S. Bräkling, S. Brilke, L. C. Murillo, R. Chiu, B. Chu, L. P. De Menezes, J. Duplissy, H. Finkenzeller, L. G. Carracedo, M. Granzin, R. Guida, A. Hansel, V. Hofbauer, J. Krechmer, K. Lehtipalo, H. Lamkaddam, M. Lampimäki, C. P. Lee, V. Makhmutov, G. Marie, S. Mathot, R. L. Mauldin, B. Mentler, T. Müller, A. Onnela, E. Partoll, T. Petäjä, M. Philippov, V. Pospisilova, A. Ranjithkumar, M. Rissanen, B. Rörup, W. Scholz, J. Shen, M. Simon, M. Sipilä, G. Steiner, D. Stolzenburg, Y. J. Tham, A. Tomé, A. C. Wagner, D. S. Wang, Y. Wang, S. K. Weber, P. M. Winkler, P. J. Wlasits, Y. Wu, M. Xiao, Q. Ye, M. Zauner-Wieczorek, X. Zhou, R. Volkamer, I. Riipinen, J. Dommen, J. Curtius, U. Baltensperger, M. Kulmala, D. R. Worsnop, J. Kirkby, J. H. Seinfeld, I. El-Haddad, R. C. Flagan, N. M. Donahue, Rapid growth of new atmospheric particles by nitric acid and ammonia condensation. *Nature*. **581**, 184–189 (2020).

6. S. H. Lee, H. Gordon, H. Yu, K. Lehtipalo, R. Haley, Y. Li, R. Zhang, New Particle Formation in the Atmosphere: From Molecular Clusters to Global Climate. *J. Geophys. Res. Atmos.* (2019), doi:10.1029/2018JD029356.

7. R. Zhang, A. Khalizov, L. Wang, M. Hu, W. Xu, Nucleation and growth of nanoparticles in the atmosphere. *Chem. Rev.* **112**, 1957–2011 (2012).

8. M. Kulmala, P. Korhonen, A. Laaksonen, Y. Viisanen, R. McGraw, J. H. Seinfeld, Ternary nucleation of H2SO4, NH3 and H2O. *AIP Conf. Proc.* **534**, 111–114 (2000).

9. M. Kulmala, J. Kontkanen, H. Junninen, K. Lehtipalo, E. Hanna, T. Nieminen, T. Petäjä, M. Sipilä, S. Schobesberger, P. Rantala, A. Franchin, T. Jokinen, E. Järvinen, M. Äijälä, J. Hakala, P. P. Aalto, P. Paasonen, J. Mikkilä, J. Aalto, H. Hakola, U. Makkonen, T. Ruuskanen, L. Roy, M. Iii, J. Duplissy, H. Vehkamäki, J. Bäck, A. Kortelainen, T. Kurtén, M. V Johnston, J. N. Smith, M. Ehn, F. Thomas, K. E. J. Lehtinen, A. Laaksonen, V. Kerminen, D. R. Worsnop, Direct Observations of Atmospheric Aerosol Nucleation. *Science*. **339**, 943–6 (2013).

10. A. A. Lushnikov, M. Kulmala, Dimers in nucleating vapors. *Phys. Rev. E*. **58**, 3157–3167 (1998).

11. M. Kulmala, H. Vehkamäki, T. Petäjä, M. Dal Maso, A. Lauri, V. M. Kerminen, W. Birmili, P.

H. McMurry, Formation and growth rates of ultrafine atmospheric particles: A review of observations. *J. Aerosol Sci.* **35**, 143–176 (2004).

12. V. M. Kerminen, M. Paramonov, T. Anttila, I. Riipinen, C. Fountoukis, H. Korhonen, E. Asmi, L. Laakso, H. Lihavainen, E. Swietlicki, B. Svenningsson, A. Asmi, S. N. Pandis, M. Kulmala, T. Petäjä, Cloud condensation nuclei production associated with atmospheric nucleation: A synthesis based on existing literature and new results. *Atmos. Chem. Phys.* **12**, 12037–12059 (2012).

13. 2013: Climate Change 2013 IPCC, *The Physical Science Basis. Contribution of Working Group I to the Fifth Assessment Report of the Intergovernmental Panel on Climate Change* (Cambridge University Press, Cambridge, 2014).

14. T. Storelvmo, T. Leirvik, U. Lohmann, P. C. B. Phillips, M. Wild, Disentangling greenhouse warming and aerosol cooling to reveal Earth's climate sensitivity. *Nat. Geosci.* **9**, 286–289 (2016).

15. F. Yu, G. Luo, X. Liu, R. C. Easter, X. Ma, S. J. Ghan, Indirect radiative forcing by ion-mediated nucleation of aerosol. *Atmos. Chem. Phys.* **12**, 11451–11463 (2012).

16. J. Kazil, P. Stier, K. Zhang, J. Quaas, S. Kinne, D. O'Donnell, S. Rast, M. Esch, S. Ferrachat, U. Lohmann, J. Feichter, Aerosol nucleation and its role for clouds and Earth's radiative forcing in the aerosol-climate model ECHAM5-HAM. *Atmos. Chem. Phys.* **10**, 10733–10752 (2010).

17. C. E. Scott, A. Rap, D. V. Spracklen, P. M. Forster, K. S. Carslaw, G. W. Mann, K. J. Pringle, N. Kivekäs, M. Kulmala, H. Lihavainen, P. Tunved, The direct and indirect radiative effects of biogenic secondary organic aerosol. *Atmos. Chem. Phys.* **14**, 447–470 (2014).

18. E. M. Dunne, H. Gordon, A. Kürten, J. Almeida, J. Duplissy, C. Williamson, I. K. Ortega, K. J. Pringle, A. Adamov, U. Baltensperger, P. Barmet, F. Benduhn, F. Bianchi, M. Breitenlechner, A. Clarke, J. Curtius, J. Dommen, N. M. Donahue, S. Ehrhart, R. C. Flagan, A. Franchin, R. Guida, J. Hakala, A. Hansel, M. Heinritzi, T. Jokinen, J. Kangasluoma, J. Kirkby, M. Kulmala, A. Kupc, M. J. Lawler, K. Lehtipalo, V. Makhmutov, G. Mann, S. Mathot, J. Merikanto, P. Miettinen, A. Nenes, A. Onnela, A. Rap, C. L. S. Reddington, F. Riccobono, N. A. D. Richards, M. P. Rissanen, L. Rondo, N. Sarnela, S. Schobesberger, K. Sengupta, M. Simon, M. Sipilä, J. N. Smith, Y. Stozkhov, A. Tomé, J. Tröstl, P. E. Wagner, D. Wimmer, P. M. Winkler, D. R. Worsnop, K. S. Carslaw, Global atmospheric particle formation from CERN CLOUD measurements. *Science (80-.).* **354**, 1119–1124 (2016).

19. H. Gordon, K. Sengupta, A. Rap, J. Duplissy, C. Frege, C. Williamson, M. Heinritzi, M. Simon, C. Yan, J. Almeida, J. Tröstl, T. Nieminen, I. K. Ortega, R. Wagner, E. M. Dunne, A. Adamov, A. Amorim, A. K. Bernhammer, F. Bianchi, M. Breitenlechner, S. Brilke, X. Chen, J. S. Craven, A. Dias, S. Ehrhart, L. Fischer, R. C. Flagan, A. Franchin, C. Fuchs, R. Guida, J. Hakala, C. R. Hoyle, T. Jokinen, H. Junninen, J. Kangasluoma, J. Kim, J. Kirkby, M. Krapf, A. Kürten, A. Laaksonen, K. Lehtipalo, V. Makhmutov, S. Mathot, U. Molteni, S. A. Monks, A. Onnela, O. Peräkylä, F. Piel, T. Petäjä, A. P. Praplan, K. J. Pringle, N. A. D. Richards, M. P. Rissanen, L. Rondo, N. Sarnela, S. Schobesberger, C. E. Scott, J. H. Seinfeld, S. Sharma, M. Sipilä, G. Steiner, Y. Stozhkov, F. Stratmann, A. Tomé, A. Virtanen, A. L. Vogel, A. C. Wagner, P. E. Wagner, E. Weingartner, D. Wimmer, P. M. Winkler, P. Ye, X. Zhang, A. Hansel, J. Dommen, N. M. Donahue, D. R. Worsnop, U. Baltensperger, M. Kulmala, J. Curtius, K. S. Carslaw, Reduced anthropogenic aerosol radiative forcing caused by biogenic new particle formation. *Proc. Natl. Acad. Sci. U. S. A.* **113**, 12053–12058 (2016).

20. T. Anttila, P. Vaattovaara, M. Komppula, A. P. Hyvärinen, H. Lihavainen, V. M. Kerminen, A. Laaksonen, Size-dependent activation of aerosols into cloud droplets at a subarctic background site during the second Pallas Cloud Experiment (2nd PaCE): Method development and data evaluation. *Atmos. Chem. Phys.* **9**, 4841–4854 (2009).

21. S. Henning, E. Weingartner, S. Schmidt, M. Wendisch, H. W. Gäggeler, U. Baltensperger, Size-dependent aerosol activation at the high-alpine site Jungfraujoch (3580 m asl). *Tellus B Chem. Phys. Meteorol.* **54**, 82–95 (2002).

22. M. Komppula, H. Lihavainen, V. M. Kerminen, M. Kulmala, Y. Viisanen, Measurements of cloud droplet activation of aerosol particles at a clean subarctic background site. *J. Geophys. Res. D Atmos.* **110**, 1–10 (2005).

23. Z. B. Wang, H. Su, X. Wang, N. Ma, A. Wiedensohler, U. Pöschl, Y. Cheng, Scanning supersaturation CPC applied as a nano-CCN counter for size-resolved analysis of the hygroscopicity and chemical composition of nanoparticles. *Atmos. Meas. Tech.* **7**, 11137–11168 (2014).

24. H. Gordon, J. Kirkby, U. Baltensperger, F. Bianchi, M. Breitenlechner, J. Curtius, A. Dias, J. Dommen, N. M. Donahue, E. M. Dunne, J. Duplissy, S. Ehrhart, R. C. Flagan, C. Frege, C. Fuchs, A. Hansel, C. R. Hoyle, M. Kulmala, A. Kürten, K. Lehtipalo, V. Makhmutov, U. Molteni, M. P. Rissanen, Y. Stozkhov, J. Tröstl, G. Tsagkogeorgas, R. Wagner, C. Williamson, D. Wimmer, P. M. Winkler, C. Yan, K. S. Carslaw, Causes and importance of new particle formation in the present-day and preindustrial atmospheres. *J. Geophys. Res. Atmos.* **122**, 8739–8760 (2017).

25. A. Hamed, W. Birmili, J. Joutsensaari, S. Mikkonen, A. Asmi, B. Wehner, G. Spindler, A. Jaatinen, A. Wiedensohler, H. Korhonen, K. E. J. Lehtinen, A. Laaksonen, Changes in the production rate of secondary aerosol particles in Central Europe in view of decreasing SO2 emissions between 1996 and 2006. *Atmos. Chem. Phys.* **10**, 1071–1091 (2010).

26. A. J. Cohen, M. Brauer, R. Burnett, H. R. Anderson, J. Frostad, K. Estep, K. Balakrishnan, B. Brunekreef, L. Dandona, R. Dandona, V. Feigin, G. Freedman, B. Hubbell, A. Jobling, H. Kan, L. Knibbs, Y. Liu, R. Martin, L. Morawska, C. A. Pope, H. Shin, K. Straif, G. Shaddick, M. Thomas, R. van Dingenen, A. van Donkelaar, T. Vos, C. J. L. Murray, M. H. Forouzanfar, Estimates and 25-year trends of the global burden of disease attributable to ambient air pollution: an analysis of data from the Global Burden of Diseases Study 2015. *Lancet*. **389**, 1907–1918 (2017).

27. C. Sioutas, R. J. Delfino, M. Singh, Exposure assessment for atmospheric Ultrafine Particles (UFPs) and implications in epidemiologic research. *Environ. Health Perspect.* **113**, 947–955 (2005).

28. R. J. Delfino, C. Sioutas, S. Malik, Potential role of ultrafine particles in associations between airborne particle mass and cardiovascular health. *Environ. Health Perspect.* **113**, 934–946 (2005).

29. R. D. Brook, S. Rajagopalan, C. A. Pope, J. R. Brook, A. Bhatnagar, A. V. Diez-Roux, F. Holguin, Y. Hong, R. V. Luepker, M. A. Mittleman, A. Peters, D. Siscovick, S. C. Smith, L. Whitsel, J. D. Kaufman, Particulate matter air pollution and cardiovascular disease: An update to the scientific statement from the american heart association. *Circulation*. **121**, 2331–2378 (2010).

30. A. Shimada, N. Kawamura, M. Okajima, T. Kaewamatawong, H. Inoue, T. Morita, Translocation pathway of the intratracheally instilled ultrafine particles from the lung into the blood circulation in the mouse. *Toxicol. Pathol.* **34**, 949–957 (2006).

31. J. A. Araujo, B. Barajas, M. Kleinman, X. Wang, B. J. Bennett, K. W. Gong, M. Navab, J. Harkema, C. Sioutas, A. J. Lusis, A. E. Nel, Ambient particulate pollutants in the ultrafine range promote early atherosclerosis and systemic oxidative stress. *Circ. Res.* **102**, 589–596 (2008).

32. G. Oberdörster, A. Elder, A. Rinderknecht, Nanoparticles and the brain: cause for concern? *J. Nanosci. Nanotechnol.* **9**, 4996–5007 (2009).

33. R. B. Schlesinger, Toxicological evidence for health effects from inhaled particulate pollution: does it support the human experience? *Inhal. Toxicol.* **7**, 99–109 (1995).

34. A. V. Fedulov, A. Leme, Z. Yang, M. Dahl, R. Lim, T. J. Mariani, L. Kobzik, Pulmonary exposure to particles during pregnancy causes increased neonatal asthma susceptibility. *Am. J. Respir. Cell Mol. Biol.* **38**, 57–67 (2008).

35. M. Reiprich, S. Rudzok, N. Schütze, J. C. Simon, I. Lehmann, S. Trump, T. Polte, Inhibition of endotoxin-induced perinatal asthma protection by pollutants in an experimental mouse model. *Allergy Eur. J. Allergy Clin. Immunol.* **68**, 481–489 (2013).

36. S. Manners, R. Alam, D. Schwartz, M. Gorska, A Mouse Model Links Asthma Susceptibility to Prenatal Exposure to Diesel Exhaust. *J Allergy Clin Immunol*. **134**, 63–72 (2014).

37. Y. Saleh, S. Antherieu, R. Dusautoir, L. Y. Alleman, J. Sotty, C. De Sousa, A. Platel, E. Perdrix, V. Riffault, I. Fronval, F. Nesslany, L. Canivet, G. Garçon, J. M. Lo-Guidice, Exposure to atmospheric ultrafine particles induces severe lung inflammatory response and tissue remodeling in mice. *Int. J. Environ. Res. Public Health*. **16** (2019), doi:10.3390/ijerph16071210.

38. M. Stafoggia, A. Schneider, J. Cyrys, E. Samoli, Z. J. Andersen, G. B. Bedada, T. Bellander, G. Cattani, K. Eleftheriadis, A. Faustini, B. Hoffmann, B. Jacquemin, K. Katsouyanni, A. Massling, J. Pekkanen, N. Perez, A. Peters, U. Quass, T. Yli-Tuomi, F. Forastiere, Association between Short-term Exposure to Ultrafine Particles and Mortality in Eight European Urban Areas. *Epidemiology*. **28**, 172–180 (2017).

39. S. Lanzinger, A. Schneider, S. Breitner, M. Stafoggia, I. Erzen, M. Dostal, A. Pastorkova, S. Bastian, J. Cyrys, A. Zscheppang, T. Kolodnitska, A. Peters, M. Senghaas, J. Fauler, W. Kirch, E. Reichert, G. Löschau, A. Hausmann, H. G. Kath, M. Böttger, A. Peters, S. Breitner, J. Cyrys, U. Geruschkat, T. Kusch, S. Lanzinger, Rückerl, A. Schneider, J. Novák, J. Fiala, J. Šilhavỳ, M. Gobec, Eržen, P. Pavlinec, L. Vlasyk, M. Prodanchuk, T. Kolodnitska, B. Mykhalchuk, Associations between ultrafine and fine particles and mortality in five central European cities - Results from the UFIREG study. *Environ. Int.* **88**, 44–52 (2016).

40. J. Y. Liu, T. C. Hsiao, K. Y. Lee, H. C. Chuang, T. J. Cheng, K. J. Chuang, Association of ultrafine particles with cardiopulmonary health among adult subjects in the urban areas of northern Taiwan. *Sci. Total Environ.* **627**, 211–215 (2018).

41. M. M, Mobility Spectrums of large ions in a New Mexico Semidesert. *J. Geophys. Res.*, 396–413 (1964).

42. V. M. Kerminen, X. Chen, V. Vakkari, T. Petäjä, M. Kulmala, F. Bianchi, Atmospheric new particle formation and growth: Review of field observations. *Environ. Res. Lett.* **13** (2018), doi:10.1088/1748-9326/aadf3c.

43. L. Yao, O. Garmash, F. Bianchi, J. Zheng, C. Yan, J. Kontkanen, H. Junninen, S. B. Mazon, M. Ehn, P. Paasonen, M. Sipilä, M. Wang, X. Wang, S. Xiao, H. Chen, Y. Lu, B. Zhang, D. Wang, Q. Fu, F. Geng, L. Li, H. Wang, L. Qiao, X. Yang, J. Chen, V. M. Kerminen, T. Petäjä, D. R. Worsnop, M. Kulmala, L. Wang, Atmospheric new particle formation from sulfuric acid and amines in a Chinese megacity. *Science (80-.).* **361**, 278–281 (2018).

44. M. Dall'Osto, D. C. S. Beddows, A. Asmi, L. Poulain, L. Hao, E. Freney, J. D. Allan, M. Canagaratna, M. Crippa, F. Bianchi, G. De Leeuw, A. Eriksson, E. Swietlicki, H. C. Hansson, J. S. Henzing, C. Granier, K. Zemankova, P. Laj, T. Onasch, A. Prevot, J. P. Putaud, K. Sellegri, M. Vidal, A. Virtanen, R. Simo, D. Worsnop, C. O'Dowd, M. Kulmala, R. M. Harrison, Novel insights on new particle formation derived from a pan-european observing system. *Sci. Rep.* **8**, 1–11 (2018).

45. Z. J. Wu, M. Hu, S. Liu, B. Wehner, S. Bauer, a M. Ssling, a Wiedensohler, T. Petäjä, M. Dal Maso, M. Kulmala, New particle formation in Beijing, China: Statistical analysis of a 1-year

data set. *J. Geophys. Res.* **112**, D09209 (2007).

46. D. Bousiotis, M. Dall'osto, D. C. S. Beddows, F. D. Pope, R. M. Harrison, Analysis of new particle formation (NPF) events at nearby rural, urban background and urban roadside sites. *Atmos. Chem. Phys*. **19**, 5679–5694 (2019).

47. R. M. Harrison, M. Jones, G. Collins, Measurements of the physical properties of particles in the urban atmosphere. *Atmos. Environ.* **33**, 309–321 (1999).

48. T. Jokinen, M. Sipilä, J. Kontkanen, V. Vakkari, P. Tisler, E.-M. Duplissy, H. Junninen, J. Kangasluoma, H. E. Manninen, T. Petäjä, M. Kulmala, D. R. Worsnop, J. Kirkby, A. Virkkula, V.-M. Kerminen, Ion-induced sulfuric acid–ammonia nucleation drives particle formation in coastal Antarctica. *Sci. Adv.* **4**, eaat9744 (2018).

49. F. Bianchi, J. Tröstl, H. Junninen, C. Frege, S. Henne, C. R. Hoyle, U. Molteni, E. Herrmann, N. Bukowiecki, X. Chen, J. Duplissy, M. Gysel, M. Hutterli, J. Kangasluoma, J. Kontkanen, H. E. Manninen, S. Münch, O. Peräkylä, T. Petäjä, L. Rondo, C. Williamson, E. Weingartner, D. R. Worsnop, M. Kulmala, J. Dommen, U. Baltensperger, New particle formation in the free troposphere : A question of chemistry and timing. *Science (80-.).* **5456**, 1–11 (2016).

50. C. J. Williamson, A. Kupc, D. Axisa, K. R. Bilsback, T. P. Bui, P. Campuzano-Jost, M. Dollner, K. D. Froyd, A. L. Hodshire, J. L. Jimenez, J. K. Kodros, G. Luo, D. M. Murphy, B. A. Nault, E. A. Ray, B. Weinzierl, J. C. Wilson, F. Yu, P. Yu, J. R. Pierce, C. A. Brock, A large source of cloud condensation nuclei from new particle formation in the tropics. *Nature*. **574**, 399–403 (2019).

51. L. K. Whalley, P. M. Edwards, K. L. Furneaux, A. Goddard, T. Ingham, M. J. Evans, D. Stone, J. R. Hopkins, C. E. Jones, A. Karunaharan, J. D. Lee, A. C. Lewis, P. S. Monks, S. J. Moller, D. E. Heard, Quantifying the magnitude of a missing hydroxyl radical source in a tropical rainforest. *Atmos. Chem. Phys.* **11**, 7223–7233 (2011).

52. L. K. Whalley, D. Stone, B. Bandy, R. Dunmore, J. F. Hamilton, J. Hopkins, J. D. Lee, A. C. Lewis, D. E. Heard, Atmospheric OH reactivity in central London: observations, model predictions and estimates of in situ ozone production. *Atmos. Chem. Phys*. **16**, 2109–2122 (2016).

53. H. Junninen, M. Hulkkonen, I. Riipinen, T. Nieminen, A. Hirsikko, T. Suni, M. Boy, S. H. Lee, M. Vana, H. Tammet, V. M. Kerminen, M. Kulmala, Observations on nocturnal growth of atmospheric clusters. *Tellus, Ser. B Chem. Phys. Meteorol.* **60 B**, 365–371 (2008).

54. C. Rose, Q. Zha, L. Dada, C. Yan, K. Lehtipalo, H. Junninen, S. B. Mazon, T. Jokinen, N. Sarnela, M. Sipilä, T. Petäjä, V.-M. Kerminen, F. Bianchi, M. Kulmala, Observations of biogenic ion-induced cluster formation in the atmosphere. *Sci. Adv.* **4**, 5218 (2018).

55. H. Vehkamäki, An improved parameterization for sulfuric acid–water nucleation rates for tropospheric and stratospheric conditions. *J. Geophys. Res.* **107**, 1–10 (2002).

56. R. J. Weber, J. J. Marti, P. H. McMurry, F. L. Eisele, D. J. Tanner, A. Jefferson, Measurements of new particle formation and ultrafine particle growth rates at a clean continental site. *J. Geophys. Res. Atmos.* **102**, 4375–4385 (1997).

57. R. J. Weber, P. H. McMurry, R. L. Mauldin, D. J. Tanner, F. L. Eisele, a. D. Clarke, V. N. Kapustin, New Particle Formation in the Remote Troposphere: A Comparison of Observations at Various Sites. *Geophys. Res. Lett.* **26**, 307 (1999).

58. W. A. Hoppel, G. M. Frick, J. W. Fitzgerald, R. W. Larsen, Marine boundary layer measurements of new particle formation and the effects nonprecipitating clouds have on aerosol size distribution. *J. Geophys. Res.* **99** (1994), doi:10.1029/94jd00797.

59. R. Zhang, I. Suh, J. Zhao, D. Zhang, E. C. Fortner, X. Tie, L. T. Molina, M. J. Molina,

Atmospheric new particle formation enhanced by organic acids. *Science (80-.).* **304**, 1487–1490 (2004).

60. C. D. O'dowd, M. Kulmala, J. L. Jimenez, R. Bahreini, R. C. Flagan, J. H. Seinfeld, K. Hämerl, L. Pirjola, T. Hoffmann, Marine aerosol formation from biogenic iodine emissions. *Nature*. **417**, 632–636 (2002).

61. H. Berresheim, T. Elste, H. G. Tremmel, A. G. Allen, H. C. Hansson, K. Rosman, M. Dal Maso, J. M. Mäkelä, M. Kulmala, C. D. O'Dowd, Gas-aerosol relationships of H2so4, MSA, and OH: Observations in the coastal marine boundary layer at Mace Head, Ireland. *J. Geophys. Res. Atmos.* **107**, 1–12 (2002).

62. T. Kurtén, V. Loukonen, H. Vehkaméki, M. Kulmala, Amines are likely to enhance neutral and ion-induced sulfuric acid-water nucleation in the atmosphere more effectively than ammonia. *Atmos. Chem. Phys.* **8**, 4095–4103 (2008).

63. V. E. Fioletov, C. A. McLinden, N. Krotkov, C. Li, J. Joiner, N. Theys, S. Carn, M. D. Moran, A global catalogue of large SO2 sources and emissions derived from the Ozone Monitoring Instrument. *Atmos. Chem. Phys.* **16**, 11497–11519 (2016).

64. M. Olin, H. Kuuluvainen, M. Aurela, J. Kalliokoski, N. Kuittinen, M. Isotalo, H. J. Timonen, J. V. Niemi, T. Rönkkö, M. Dal Maso, Traffic-originated nanocluster emission exceeds H2SO4-driven photochemical new particle formation in an urban area. *Atmos. Chem. Phys.* **20**, 1–13 (2020).

65. S. Guo, M. Hu, J. Peng, Z. Wu, M. L. Zamora, D. Shang, Z. Du, J. Zheng, X. Fang, R. Tang, Y. Wu, L. Zeng, S. Shuai, W. Zhang, Y. Wang, Y. Ji, Y. Li, A. L. Zhang, W. Wang, F. Zhang, J. Zhao, X. Gong, C. Wang, M. J. Molina, R. Zhang, Remarkable nucleation and growth of ultrafine particles from vehicular exhaust. *Proc. Natl. Acad. Sci.*, 201916366 (2020).

66. M. Sipilä, N. Sarnela, T. Jokinen, H. Henschel, H. Junninen, J. Kontkanen, S. Richters, J. Kangasluoma, A. Franchin, O. Peräkylä, M. P. Rissanen, M. Ehn, H. Vehkamäki, T. Kurten, T. Berndt, T. Petäjä, D. Worsnop, D. Ceburnis, V. M. Kerminen, M. Kulmala, C. O'Dowd, Molecular-scale evidence of aerosol particle formation via sequential addition of HIO3. *Nature*. **537**, 532–534 (2016).

67. A. L. Hodshire, P. Campuzano-Jost, J. K. Kodros, B. Croft, B. A. Nault, J. C. Schroder, J. L. Jimenez, J. R. Pierce, The potential role of methanesulfonic acid (MSA) in aerosol formation and growth and the associated radiative forcings. *Atmos. Chem. Phys.* **19**, 3137–3160 (2019).

68. M. Dall'Osto, J. Ovadnevaite, M. Paglione, D. C. S. Beddows, D. Ceburnis, C. Cree, P. Cortés, M. Zamanillo, S. O. Nunes, G. L. Pérez, E. Ortega-Retuerta, M. Emelianov, D. Vaqué, C. Marrasé, M. Estrada, M. M. Sala, M. Vidal, M. F. Fitzsimons, R. Beale, R. Airs, M. Rinaldi, S. Decesari, M. C. Facchini, R. M. Harrison, C. O'Dowd, R. Simó, Antarctic sea ice region as a source of biogenic organic nitrogen in aerosols. *Sci. Rep.* **7**, 1–10 (2017).

69. M. Dall'Osto, R. L. Airs, R. Beale, C. Cree, M. F. Fitzsimons, D. Beddows, R. M. Harrison, D. Ceburnis, C. O'Dowd, M. Rinaldi, M. Paglione, A. Nenes, S. Decesari, R. Simó, Simultaneous Detection of Alkylamines in the Surface Ocean and Atmosphere of the Antarctic Sympagic Environment. *ACS Earth Sp. Chem.* **3**, 854–862 (2019).

70. X. Ge, A. S. Wexler, S. L. Clegg, Atmospheric amines - Part I. A review. *Atmos. Environ.* **45**, 524–546 (2011).

71. M. Ábalos, J. M. Bayona, F. Ventura, Development of a solid-phase microextraction GC-NPD procedure for the determination of free volatile amines in wastewater and sewage-polluted waters. *Anal. Chem.* **71**, 3531–3537 (1999).

72. S. H. Cadle, P. A. Mulawa, Low-molecular-weight aliphatic amines in exhaust from catalyst-

equipped cars. *Environ. Sci. Technol.* **14**, 718–723 (1980).

73. G. L. Hutchinson, A. R. Mosier, C. E. Andre, Ammonia and Amine Emissions from a Large Cattle Feedlot. *J. Environ. Qual.* **11**, 288–293 (1982).

74. S. H. Lee, J. Uin, A. B. Guenther, J. A. de Gouw, F. Yu, A. B. Nadykto, J. Herb, N. L. Ng, A. Koss, W. H. Brune, K. Baumann, V. P. Kanawade, F. N. Keutsch, A. Nenes, K. Olsen, A. Goldstein, Q. Ouyang, Isoprene suppression of new particle formation: Potential mechanisms and implications. *J. Geophys. Res.* **121**, 14621–14635 (2016).

75. G. Mcfiggans, T. F. Mentel, J. Wildt, I. Pullinen, S. Kang, E. Kleist, S. Schmitt, M. Springer, R. Tillmann, C. Wu, D. Zhao, M. Hallquist, C. Faxon, M. Le Breton, A. M. Hallquist, D. Simpson, R. Bergstro, M. E. Jenkin, M. Ehn, J. A. Thornton, M. R. Alfarra, T. J. Bannan, C. J. Percival, M. Priestley, D. Topping, A. Kiendler-scharr, Secondary organic aerosol reduced by mixture of atmospheric vapours. *Nature*, 0–6 (2019).

76. C. H. Clark, M. Kacarab, S. Nakao, A. Asa-Awuku, K. Sato, D. R. Cocker, Temperature Effects on Secondary Organic Aerosol (SOA) from the Dark Ozonolysis and Photo-Oxidation of Isoprene. *Environ. Sci. Technol.* **50**, 5564–5571 (2016).

77. F. Bianchi, T. Kurtén, M. Riva, C. Mohr, M. P. Rissanen, P. Roldin, T. Berndt, J. D. Crounse, P. O. Wennberg, T. F. Mentel, J. Wildt, H. Junninen, T. Jokinen, M. Kulmala, D. R. Worsnop, J. A. Thornton, N. Donahue, H. G. Kjaergaard, M. Ehn, Highly Oxygenated Organic Molecules (HOM) from Gas-Phase Autoxidation Involving Peroxy Radicals: A Key Contributor to Atmospheric Aerosol. *Chem. Rev.* (2019).

78. J. Kirkby, J. Curtius, J. Almeida, E. Dunne, J. Duplissy, S. Ehrhart, A. Franchin, S. Gagné, L. Ickes, A. Kürten, A. Kupc, A. Metzger, F. Riccobono, L. Rondo, S. Schobesberger, G. Tsagkogeorgas, D. Wimmer, A. Amorim, F. Bianchi, M. Breitenlechner, A. David, J. Dommen, A. Downard, M. Ehn, R. C. Flagan, S. Haider, A. Hansel, D. Hauser, W. Jud, H. Junninen, F. Kreissl, A. Kvashin, A. Laaksonen, K. Lehtipalo, J. Lima, E. R. Lovejoy, V. Makhmutov, S. Mathot, J. Mikkilä, P. Minginette, S. Mogo, T. Nieminen, A. Onnela, P. Pereira, T. Petäjä, R. Schnitzhofer, J. H. Seinfeld, M. Sipilä, Y. Stozhkov, F. Stratmann, A. Tomé, J. Vanhanen, Y. Viisanen, A. Vrtala, P. E. Wagner, H. Walther, E. Weingartner, H. Wex, P. M. Winkler, K. S. Carslaw, D. R. Worsnop, U. Baltensperger, M. Kulmala, Role of sulphuric acid, ammonia and galactic cosmic rays in atmospheric aerosol nucleation. *Nature*. **476**, 429–435 (2011).

79. J. Almeida, S. Schobesberger, A. Kürten, I. K. Ortega, O. Kupiainen-Määttä, A. P. Praplan, A. Adamov, A. Amorim, F. Bianchi, M. Breitenlechner, A. David, J. Dommen, N. M. Donahue, A. Downard, E. Dunne, J. Duplissy, S. Ehrhart, R. C. Flagan, A. Franchin, R. Guida, J. Hakala, A. Hansel, M. Heinritzi, H. Henschel, T. Jokinen, H. Junninen, M. Kajos, J. Kangasluoma, H. Keskinen, A. Kupc, T. Kurtén, A. N. Kvashin, A. Laaksonen, K. Lehtipalo, M. Leiminger, J. Leppä, V. Loukonen, V. Makhmutov, S. Mathot, M. J. McGrath, T. Nieminen, T. Olenius, A. Onnela, T. Petäjä, F. Riccobono, I. Riipinen, M. Rissanen, L. Rondo, T. Ruuskanen, F. D. Santos, N. Sarnela, S. Schallhart, R. Schnitzhofer, J. H. Seinfeld, M. Simon, M. Sipilä, Y. Stozhkov, F. Stratmann, A. Tomé, J. Tröstl, G. Tsagkogeorgas, P. Vaattovaara, Y. Viisanen, A. Virtanen, A. Vrtala, P. E. Wagner, E. Weingartner, H. Wex, C. Williamson, D. Wimmer, P. Ye, T. Yli-Juuti, K. S. Carslaw, M. Kulmala, J. Curtius, U. Baltensperger, D. R. Worsnop, H. Vehkamäki, J. Kirkby, Molecular understanding of sulphuric acid-amine particle nucleation in the atmosphere. *Nature*. **502**, 359–363 (2013).

80. J. Elm, N. Myllys, T. Kurtén, What is Required for Highly Oxidized Molecules to Form Clusters with Sulfuric Acid? *J. Phys. Chem. A*. **121**, 4578–4587 (2017).

81. C. Deng, Y. Fu, L. Dada, C. Yan, R. Cai, D. Yang, Y. Zhou, R. Yin, Y. Lu, X. Li, X. Qiao, X. Fan, W. Nie, J. Kontkanen, J. Kangasluoma, B. Chu, A. Ding, V.-M. Kerminen, P. Paasonen, D. R. Worsnop, F. Bianchi, Y. Liu, J. Zheng, L. Wang, M. Kulmala, J. Jiang, Seasonal Characteristics of New Particle Formation and Growth in Urban Beijing. *Environ. Sci. Technol.*

54, 8547–8557 (2020).

82. W. A. Glasoe, K. Volz, B. Panta, N. Freshour, R. Bachman, D. R. Hanson, P. H. Mcmurry, C. Jen, Sulfuric acid nucleation: An experimental study of the effect of seven bases. *J. Geophys. Res. Atmos.* **175**, 1933–1950 (2015).

83. B. R. Bzdek, D. P. Ridge, M. V. Johnston, Amine exchange into ammonium bisulfate and ammonium nitrate nuclei. *Atmos. Chem. Phys.* **10**, 3495–3503 (2010).

84. O. Kupiainen, I. K. Ortega, T. Kurté, H. Vehkamäki, Amine substitution into sulfuric acid-Ammonia clusters. *Atmos. Chem. Phys.* **12**, 3591–3599 (2012).

85. A. Kürten, T. Jokinen, M. Simon, M. Sipilä, N. Sarnela, H. Junninen, A. Adamov, J. Almeida, A. Amorim, F. Bianchi, M. Breitenlechner, J. Dommen, N. M. Donahue, J. Duplissy, S. Ehrhart, R. C. Flagan, A. Franchin, J. Hakala, A. Hansel, M. Heinritzi, M. Hutterli, J. Kangasluoma, J. Kirkby, A. Laaksonen, K. Lehtipalo, M. Leiminger, V. Makhmutov, S. Mathot, A. Onnela, T. Petäjä, A. P. Praplan, F. Riccobono, M. P. Rissanen, L. Rondo, S. Schobesberger, J. H. Seinfeld, G. Steiner, A. Tomé, J. Tröstl, P. M. Winkler, C. Williamson, D. Wimmer, P. Ye, U. Baltensperger, K. S. Carslaw, M. Kulmala, D. R. Worsnop, J. Curtius, Neutral molecular cluster formation of sulfuric acid–dimethylamine observed in real time under atmospheric conditions. *Proc. Natl. Acad. Sci.* **111**, 15019–15024 (2014).

86. J. F. Pankow, W. E. Asher, SIMPOL 1: a simple group contribution method for predicting vapor pressures and enthalpies of vaporization of multifunctional organic compounds. *Atmos. Chem. Phys*. **8**, 2773–2796 (2008).

87. M. Ehn, H. Junninen, T. Petäjä, T. Kurtén, V. M. Kerminen, S. Schobesberger, H. E. Manninen, I. K. Ortega, H. Vehkamäki, M. Kulmala, D. R. Worsnop, Composition and temporal behavior of ambient ions in the boreal forest. *Atmos. Chem. Phys.* **10**, 8513–8530 (2010).

88. H. Junninen, M. Ehn, Petäjä, L. Luosujärvi, T. Kotiaho, R. Kostiainen, U. Rohner, M. Gonin, K. Fuhrer, M. Kulmala, D. R. Worsnop, A high-resolution mass spectrometer to measure atmospheric ion composition. *Atmos. Meas. Tech.* **3**, 1039–1053 (2010).

89. M. Ehn, E. Kleist, H. Junninen, T. Petäjä, G. Lönn, S. Schobesberger, M. Dal Maso, A. Trimborn, M. Kulmala, D. R. Worsnop, A. Wahner, J. Wildt, T. F. Mentel, Gas phase formation of extremely oxidized pinene reaction products in chamber and ambient air. *Atmos. Chem. Phys.* **12**, 5113–5127 (2012).

90. F. L. Eisele, D. J. Tanner, Measurement of the gas phase concentration of H2SO4 and methane sulfonic acid and estimates of H2SO4 production and loss in the atmosphere. *J. Geophys. Res.* **98**, 9001–9010 (1993).

91. T. Jokinen, M. Sipilä, H. Junninen, M. Ehn, G. Lönn, J. Hakala, T. Petäjä, R. L. Mauldin, M. Kulmala, D. R. Worsnop, Atmospheric sulphuric acid and neutral cluster measurements using CI-APi-TOF. *Atmos. Chem. Phys.* **12**, 4117–4125 (2012).

92. M. Ehn, J. A. Thornton, E. Kleist, M. Sipilä, H. Junninen, I. Pullinen, M. Springer, F. Rubach, R. Tillmann, B. Lee, F. Lopez-Hilfiker, S. Andres, I.-H. Acir, M. Rissanen, T. Jokinen, S. Schobesberger, J. Kangasluoma, J. Kontkanen, T. Nieminen, T. Kurtén, L. B. Nielsen, S. Jørgensen, H. G. Kjaergaard, M. Canagaratna, M. D. Maso, T. Berndt, T. Petäjä, A. Wahner, V.-M. Kerminen, M. Kulmala, D. R. Worsnop, J. Wildt, T. F. Mentel, A large source of low-volatility secondary organic aerosol. *Nature*. **506**, 476–479 (2014).

93. O. Garmash, M. P. Rissanen, I. Pullinen, S. Schmitt, O. Kausiala, R. Tillmann, C. Percival, T. J. Bannan, M. Priestley, Å. M. Hallquist, E. Kleist, A. Kiendler-Scharr, M. Hallquist, T. Berndt, G. McFiggans, J. Wildt, T. Mentel, M. Ehn, Multi-generation OH oxidation as a source for highly oxygenated organic molecules from aromatics. *Atmos. Chem. Phys.* **20**, 515–537 (2020).

94. A. Zaytsev, A. R. Koss, M. Breitenlechner, J. E. Krechmer, K. J. Nihill, C. Y. Lim, J. C. Rowe, J. L. Cox, J. Moss, J. R. Roscioli, M. R. Canagaratna, D. R. Worsnop, J. H. Kroll, F. N. Keutsch, Mechanistic Study of Formation of Ring-retaining and Ring-opening Products from Oxidation of Aromatic Compounds under Urban Atmospheric Conditions. *Atmos. Chem. Phys. Discuss.*, 1–24 (2019).

95. T. F. Mentel, M. Springer, M. Ehn, E. Kleist, I. Pullinen, T. Kurtén, M. Rissanen, A. Wahner, J. Wildt, Formation of highly oxidized multifunctional compounds: Autoxidation of peroxy radicals formed in the ozonolysis of alkenes - Deduced from structure-product relationships. *Atmos. Chem. Phys.* **15**, 6745–6765 (2015).

96. T. Jokinen, M. Sipilä, S. Richters, V. M. Kerminen, P. Paasonen, F. Stratmann, D. Worsnop, M. Kulmala, M. Ehn, H. Herrmann, T. Berndt, Rapid autoxidation forms highly oxidized RO2 radicals in the atmosphere. *Angew. Chemie - Int. Ed.* **53**, 14596–14600 (2014).

97. J. D. Crounse, L. B. Nielsen, S. Jørgensen, H. G. Kjaergaard, P. O. Wennberg, Autoxidation of organic compounds in the atmosphere. *J. Phys. Chem. Lett.* **4**, 3513–3520 (2013).

98. E. Praske, R. V. Otkjær, J. D. Crounse, J. C. Hethcox, B. M. Stoltz, H. G. Kjaergaard, P. O. Wennberg, Atmospheric autoxidation is increasingly important in urban and suburban North America. *Proc. Natl. Acad. Sci.* **115**, 64–69 (2018).

99. L. L. J. Quéléver, K. Kristensen, L. Normann Jensen, B. Rosati, R. Teiwes, K. R. Daellenbach, O. Peräkylä, P. Roldin, R. Bossi, H. B. Pedersen, M. Glasius, M. Bilde, M. Ehn, Effect of temperature on the formation of highly oxygenated organic molecules (HOMs) from alpha-pinene ozonolysis. *Atmos. Chem. Phys*. **19**, 7609–7625 (2019).

100. C. Frege, I. K. Ortega, M. P. Rissanen, A. P. Praplan, G. Steiner, M. Heinritzi, L. Ahonen, A. Amorim, A. K. Bernhammer, F. Bianchi, S. Brilke, M. Breitenlechner, L. Dada, A. Dias, J. Duplissy, S. Ehrhart, I. El-Haddad, L. Fischer, C. Fuchs, O. Garmash, M. Gonin, A. Hansel, C. R. Hoyle, T. Jokinen, H. Junninen, J. Kirkby, A. Kürten, K. Lehtipalo, M. Leiminger, R. Lee Mauldin, U. Molteni, L. Nichman, T. Petäjä, N. Sarnela, S. Schobesberger, M. Simon, M. Sipilä, D. Stolzenburg, A. Tomé, A. L. Vogel, A. C. Wagner, R. Wagner, M. Xiao, C. Yan, P. Ye, J. Curtius, N. M. Donahue, R. C. Flagan, M. Kulmala, D. R. Worsnop, P. Winkler, J. Dommen, U. Baltensperger, Influence of temperature on the molecular composition of ions and charged clusters during pure biogenic nucleation. *Atmos. Chem. Phys.* **18**, 65–79 (2018).

101. D. Stolzenburg, L. Fischer, A. L. Vogel, M. Heinritzi, M. Schervish, M. Simon, A. C. Wagner, L. Dada, L. R. Ahonen, A. Amorim, A. Baccarini, P. S. Bauer, B. Baumgartner, A. Bergen, F. Bianchi, M. Breitenlechner, S. Brilke, S. Buenrostro Mazon, D. Chen, A. Dias, D. C. Draper, J. Duplissy, I. El Haddad, H. Finkenzeller, C. Frege, C. Fuchs, O. Garmash, H. Gordon, X. He, J. Helm, V. Hofbauer, C. R. Hoyle, C. Kim, J. Kirkby, J. Kontkanen, A. Kürten, J. Lampilahti, M. Lawler, K. Lehtipalo, M. Leiminger, H. Mai, S. Mathot, B. Mentler, U. Molteni, W. Nie, T. Nieminen, J. B. Nowak, A. Ojdanic, A. Onnela, M. Passananti, T. Petäjä, L. L. J. Quéléver, M. P. Rissanen, N. Sarnela, S. Schallhart, C. Tauber, A. Tomé, R. Wagner, M. Wang, L. Weitz, D. Wimmer, M. Xiao, C. Yan, P. Ye, Q. Zha, U. Baltensperger, J. Curtius, J. Dommen, R. C. Flagan, M. Kulmala, J. N. Smith, D. R. Worsnop, A. Hansel, N. M. Donahue, P. M. Winkler, Rapid growth of organic aerosol nanoparticles over a wide tropospheric temperature range. *Proc. Natl. Acad. Sci.*, 201807604 (2018).

102. M. Simon, L. Dada, M. Heinritzi, W. Scholz, D. Stolzenburg, A. C. Wagner, A. Kürten, B. Rörup, X. He, J. Almeida, A. Baccarini, P. S. Bauer, L. Beck, A. Bergen, F. Bianchi, S. Brilke, L. Caudillo, D. Chen, B. Chu, A. Dias, C. Danielle, J. Duplissy, I. El Haddad, H. Finkenzeller, C. Frege, L. Gonzalez-, H. Gordon, M. Granzin, J. Hakala, V. Hofbauer, R. Christopher, C. Kim, W. Kong, H. Lamkaddam, C. P. Lee, M. Leiminger, H. Mai, H. E. Manninen, G. Marie, B. Mentler, U. Molteni, L. Nichman, W. Nie, A. Ojdanic, E. Partoll, T. Petäjä, J. Pfeifer, M. Philippov, L. L. J. Quéléver, A. Ranjithkumar, M. Rissanen, S. Schallhart, S. Schobesberger, J. Shen, M. Sipilä, G. Steiner, Y. Stozhkov, C. Tauber, J. Yee, A. R. Tomé, M. Vazquez-pufleau,

A. Vogel, R. Wagner, D. S. Wang, Y. Wang, S. K. Weber, Y. Wu, M. Xiao, C. Yan, Molecular understanding of new-particle formation from alpha-pinene between -50 °C and 25 °C. *Atmos. Chem. Phys. Discuss.*, 1–42 (2020).

103. D. Stolzenburg, M. Simon, A. Ranjithkumar, A. Kürten, K. Lehtipalo, H. Gordon, T. Nieminen, L. Pichelstorfer, X.-C. He, S. Brilke, M. Xiao, A. Amorim, R. Baalbaki, A. Baccarini, L. Beck, S. Bräkling, L. Caudillo Murillo, D. Chen, B. Chu, L. Dada, A. Dias, J. Dommen, J. Duplissy, I. El Haddad, H. Finkenzeller, L. Fischer, L. Gonzalez Carracedo, M. Heinritzi, C. Kim, T. K. Koenig, W. Kong, H. Lamkaddam, C. P. Lee, M. Leiminger, Z. Li, V. Makhmutov, H. E. Manninen, G. Marie, R. Marten, T. Müller, W. Nie, E. Partoll, T. Petäjä, J. Pfeifer, M. Philippov, M. P. Rissanen, B. Rörup, S. Schobesberger, S. Schuchmann, J. Shen, M. Sipilä, G. Steiner, Y. Stozhkov, C. Tauber, Y. J. Tham, A. Tomé, M. Vazquez-Pufleau, A. C. Wagner, M. Wang, Y. Wang, S. K. Weber, D. Wimmer, P. J. Wlasits, Y. Wu, Q. Ye, M. Zauner-Wieczorek, U. Baltensperger, K. S. Carslaw, J. Curtius, N. M. Donahue, R. C. Flagan, A. Hansel, M. Kulmala, R. Volkamer, J. Kirkby, P. M. Winkler, Enhanced growth rate of atmospheric particles from sulfuric acid. *Atmos. Chem. Phys. Discuss.* **2019**, 1–17 (2019).

104. Y. Wang, M. Riva, H. Xie, L. Heikkinen, S. Schallhart, Q. Zha, C. Yan, X. He, O. Peräkylä, M. Ehn, Formation of highly oxygenated organic molecules from chlorine atom initiated oxidation of alpha-pinene. *Atmos. Chem. Phys.* **20**, 5145–5155 (2020).

105. T. Berndt, S. Richters, T. Jokinen, N. Hyttinen, T. Kurtén, R. V. Otkjær, H. G. Kjaergaard, F. Stratmann, H. Herrmann, M. Sipilä, M. Kulmala, M. Ehn, Hydroxyl radical-induced formation of highly oxidized organic compounds. *Nat. Commun.* **7**, 13677 (2016).

106. T. Nah, J. Sanchez, C. M. Boyd, N. L. Ng, Photochemical Aging of α-pinene and β-pinene Secondary Organic Aerosol formed from Nitrate Radical Oxidation. *Environ. Sci. Technol.* **50**, 222–231 (2016).

107. T. Jokinen, T. Berndt, R. Makkonen, V.-M. Kerminen, H. Junninen, P. Paasonen, F. Stratmann, H. Herrmann, A. B. Guenther, D. R. Worsnop, M. Kulmala, M. Ehn, M. Sipilä, Production of extremely low volatile organic compounds from biogenic emissions: Measured yields and atmospheric implications. *Proc. Natl. Acad. Sci.* **112**, 7123–7128 (2015).

108. T. Berndt, S. Richters, R. Kaethner, J. Voigtländer, F. Stratmann, M. Sipilä, M. Kulmala, H. Herrmann, Gas-Phase Ozonolysis of Cycloalkenes: Formation of Highly Oxidized RO2 Radicals and Their Reactions with NO, NO2, SO2, and Other RO2 Radicals. *J. Phys. Chem. A*. **119**, 10336–10348 (2015).

109. S. Wang, R. Wu, T. Berndt, M. Ehn, L. Wang, Formation of Highly Oxidized Radicals and Multifunctional Products from the Atmospheric Oxidation of Alkylbenzenes. *Environ. Sci. Technol.* **51**, 8442–8449 (2017).

110. U. Molteni, F. Bianchi, F. Klein, I. El Haddad, C. Frege, M. J. Rossi, J. Dommen, U. Baltensperger, Formation of highly oxygenated organic molecules from aromatic compounds. *Atmos. Chem. Phys.* **18**, 1909–1921 (2018).

111. F. Bianchi, T. Kurtén, M. Riva, C. Mohr, M. P. Rissanen, P. Roldin, T. Berndt, J. D. Crounse, P. O. Wennberg, T. F. Mentel, J. Wildt, H. Junninen, T. Jokinen, M. Kulmala, D. R. Worsnop, J. A. Thornton, N. Donahue, H. G. Kjaergaard, M. Ehn, Highly Oxygenated Organic Molecules (HOM) from Gas-Phase Autoxidation Involving Peroxy Radicals: A Key Contributor to Atmospheric Aerosol. *Chem. Rev.* **119**, 3472–3509 (2019).

112. C. Mohr, J. A. Thornton, A. Heitto, F. D. Lopez-Hilfiker, A. Lutz, I. Riipinen, J. Hong, N. M. Donahue, M. Hallquist, T. Petäjä, M. Kulmala, T. Yli-Juuti, Molecular identification of organic vapors driving atmospheric nanoparticle growth. *Nat. Commun.* **10**, 1–7 (2019).

113. T. Yli-Juuti, K. Barsanti, L. Hildebrandt Ruiz, A. J. Kieloaho, U. Makkonen, T. Petäjä, T. Ruuskanen, M. Kulmala, I. Riipinen, Model for acid-base chemistry in nanoparticle growth

(MABNAG). *Atmos. Chem. Phys.* **13**, 12507–12524 (2013).

114. T. Kurtén, K. Tiusanen, P. Roldin, M. Rissanen, J. N. Luy, M. Boy, M. Ehn, N. Donahue, α-Pinene Autoxidation Products May Not Have Extremely Low Saturation Vapor Pressures Despite High O:C Ratios. *J. Phys. Chem. A*. **120**, 2569–2582 (2016).

115. J. Tröstl, W. K. Chuang, H. Gordon, M. Heinritzi, C. Yan, U. Molteni, L. Ahlm, C. Frege, F. Bianchi, R. Wagner, M. Simon, K. Lehtipalo, C. Williamson, J. S. Craven, J. Duplissy, A. Adamov, J. Almeida, A. K. Bernhammer, M. Breitenlechner, S. Brilke, A. Dias, S. Ehrhart, R. C. Flagan, A. Franchin, C. Fuchs, R. Guida, M. Gysel, A. Hansel, C. R. Hoyle, T. Jokinen, H. Junninen, J. Kangasluoma, H. Keskinen, J. Kim, M. Krapf, A. Kürten, A. Laaksonen, M. Lawler, M. Leiminger, S. Mathot, O. Möhler, T. Nieminen, A. Onnela, T. Petäjä, F. M. Piel, P. Miettinen, M. P. Rissanen, L. Rondo, N. Sarnela, S. Schobesberger, K. Sengupta, M. Sipilä, J. N. Smith, G. Steiner, A. Tomè, A. Virtanen, A. C. Wagner, E. Weingartner, D. Wimmer, P. M. Winkler, P. Ye, K. S. Carslaw, J. Curtius, J. Dommen, J. Kirkby, M. Kulmala, I. Riipinen, D. R. Worsnop, N. M. Donahue, U. Baltensperger, The role of low-volatility organic compounds in initial particle growth in the atmosphere. *Nature*. **533**, 527–531 (2016).

116. N. M. Donahue, S. A. Epstein, S. N. Pandis, A. L. Robinson, Atmospheric Chemistry and Physics A two-dimensional volatility basis set: 1. organic-aerosol mixing thermodynamics. *Atmos. Chem. Phys*. **11**, 3303–3318 (2011).

117. S. . Epstein, I. Riipinen, N. M. Donahue, A Semiempirical Correlation between Enthalpy of Vaporization and Saturation Concentration for Organic Aerosol. *Environ. Sci. Technol*. **44**, 743–748 (2010).

118. M. Schervish, N. M. Donahue, Peroxy Radical Chemistry and the Volatility Basis Set. *Atmos. Chem. Phys. Discuss* (2019), doi:10.5194/acp-2019-509.

119. O. Peräkylä, M. Riva, L. Heikkinen, L. Quéléver, P. Roldin, M. Ehn, Experimental investigation into the volatilities of highly oxygenated organic molecules (HOM). *Atmos. Chem. Phys. Discuss.*, 1–28 (2019).

120. F. Riccobono, S. Schobesberger, C. Scott, J. Dommen, I. Ortega, L. Rondo, J. Almeida, A. Amorim, F. Bianchi, M. Breitenlechner, A. David, A. Downard, E. Dunne, J. Duplissy, S. Ehrhart, R. Flagan, A. Franchin, A. Hansel, H. Junninen, M. Kajos, H. Keskinen, A. Kupc, A. Kürten, A. Kvashin, A. Laaksonen, K. Lehtipalo, V. Makhmutov, S. Mathot, T. Nieminen, A. Onnela, T. Petäjä, A. Praplan, F. Santos, S. Schallhart, J. Seinfeld, M. Sipilä, D. Van Spracklen, Y. Stozhkov, F. Stratmann, A. Tomé, G. Tsagkogeorgas, P. Vaattovaara, Y. Viisanen, A. Vrtala, P. Wagner, E. Weingartner, H. Wex, D. Wimmer, K. Carslaw, J. Curtius, N. Donahue, J. Kirkby, M. Kulmala, D. Worsnop, U. Baltensperger, Oxidation products of biogenic emissions contribute to nucleation of atmospheric particles. *Science (80-.).* **344**, 717–721 (2014).

121. A. Metzger, B. Verheggen, J. Dommen, J. Duplissy, A. S. H. Prevot, E. Weingartner, I. Riipinen, M. Kulmala, D. V Spracklen, K. S. Carslaw, U. Baltensperger, Evidence for the role of organics in aerosol particle formation under atmospheric conditions. *Proc. Natl. Acad. Sci. U. S. A.* **107**, 6646–51 (2010).

122. S. Schobesberger, H. Junninen, F. Bianchi, G. Lönn, M. Ehn, K. Lehtipalo, J. Dommen, S. Ehrhart, I. K. Ortega, A. Franchin, T. Nieminen, F. Riccobono, M. Hutterli, J. Duplissy, J. Almeida, A. Amorim, M. Breitenlechner, A. J. Downard, E. M. Dunne, R. C. Flagan, M. Kajos, H. Keskinen, J. Kirkby, A. Kupc, A. Kürten, T. Kurtén, A. Laaksonen, S. Mathot, A. Onnela, A. P. Praplan, L. Rondo, F. D. Santos, S. Schallhart, R. Schnitzhofer, M. Sipilä, A. Tomé, G. Tsagkogeorgas, H. Vehkamäki, D. Wimmer, U. Baltensperger, K. S. Carslaw, J. Curtius, A. Hansel, T. Petäjä, M. Kulmala, N. M. Donahue, D. R. Worsnop, Molecular understanding of atmospheric particle formation from sulfuric acid and large oxidized organic molecules. *Proc. Natl. Acad. Sci. U. S. A.* **110**, 17223–17228 (2013).

123. J. Kirkby, J. Duplissy, K. Sengupta, C. Frege, H. Gordon, C. Williamson, M. Heinritzi, M. Simon, C. Yan, J. Almeida, J. Trostl, T. Nieminen, I. K. Ortega, R. Wagner, A. Adamov, A. Amorim, A. K. Bernhammer, F. Bianchi, M. Breitenlechner, S. Brilke, X. Chen, J. Craven, A. Dias, S. Ehrhart, R. C. Flagan, A. Franchin, C. Fuchs, R. Guida, J. Hakala, C. R. Hoyle, T. Jokinen, H. Junninen, J. Kangasluoma, J. Kim, M. Krapf, A. Kurten, A. Laaksonen, K. Lehtipalo, V. Makhmutov, S. Mathot, U. Molteni, A. Onnela, O. Perakyla, F. Piel, T. Petaja, A. P. Praplan, K. Pringle, A. Rap, N. A. D. Richards, I. Riipinen, M. P. Rissanen, L. Rondo, N. Sarnela, S. Schobesberger, C. E. Scott, J. H. Seinfeld, M. Sipila, G. Steiner, Y. Stozhkov, F. Stratmann, A. Tomé, A. Virtanen, A. L. Vogel, A. C. Wagner, P. E. Wagner, E. Weingartner, D. Wimmer, P. M. Winkler, P. Ye, X. Zhang, A. Hansel, J. Dommen, N. M. Donahue, D. R. Worsnop, U. Baltensperger, M. Kulmala, K. S. Carslaw, J. Curtius, Ion-induced nucleation of pure biogenic particles. *Nature*. **533**, 521–526 (2016).

124. Q. Ye, M. Wang, V. Hofbauer, D. Stolzenburg, D. Chen, M. Schervish, A. Vogel, R. L. Mauldin, R. Baalbaki, S. Brilke, J. Duplissy, I. El Haddad, H. Finkenzeller, L. Fischer, X. He, C. Kim, A. Ku, H. Lamkaddam, C. P. Lee, K. Lehtipalo, M. Leiminger, H. E. Manninen, R. Marten, M. Rissanen, S. Schobesberger, B. Mentler, E. Partoll, T. Peta, S. Schuchmann, M. Simon, Y. J. Tham, M. Vazquez-pu, A. C. Wagner, Y. Wang, Y. Wu, M. Xiao, U. Baltensperger, J. Curtius, R. Flagan, J. Kirkby, M. Kulmala, R. Volkamer, P. M. Winkler, D. Worsnop, N. M. Donahue, Molecular Composition and Volatility of Nucleated Particles from α - Pinene Oxidation between − 50 ° C and +25 ° C (2019), doi:10.1021/acs.est.9b03265.

125. J. M. Mäkelä, T. Hoffmann, C. Holzke, M. Väkevä, T. Suni, T. Mattila, P. P. Aalto, U. Tapper, E. I. Kauppinen, C. D. O'Dowd, Biogenic iodine emissions and identification of end-products in coastal ultrafine particles during nucleation bursts. *J. Geophys. Res. Atmos.* **107**, 1–14 (2002).

126. H. Chen, M. E. Varner, R. B. Gerber, B. J. Finlayson-Pitts, Reactions of Methanesulfonic Acid with Amines and Ammonia as a Source of New Particles in Air. *J. Phys. Chem. B*. **120**, 47 (2016).

127. H. Chen, B. J. Finlayson-Pitts, New Particle Formation from Methanesulfonic Acid and Amines/Ammonia as a Function of Temperature. *Environ. Sci. Technol.* **51**, 243–252 (2017).

128. V. Perraud, J. Xu, R. B. Berber, B. J. Finlayson-Pitts, Integrated experimental and theoretical approach to probe the synergistic effect of ammonia in methanesulfonic acid reactions with small alkylamines. *Environ. Sci. Process. Impacts* (2020), doi:10.1039/c9em00431a.

129. N. Bork, J. Elm, T. Olenius, H. Vehkamäki, Methane sulfonic acid-enhanced formation of molecular clusters of sulfuric acid and dimethyl amine. *Atmos. Chem. Phys*. **14**, 12023–12030 (2014).

130. J. Brean, R. M. Harrison, Z. Shi, D. C. S. Beddows, A. F. W Joe, C. Nicholas Hewitt, Observations of highly oxidised molecules and particle nucleation in the atmosphere of Beijing. *Atmos. Chem. Phys. Discuss.*, 1–35 (2019).

131. M. Kulmala, V. M. Kerminen, T. Petäjä, A. J. Ding, L. Wang, Atmospheric gas-to-particle conversion: Why NPF events are observed in megacities? *Faraday Discuss.* **200**, 271–288 (2017).

132. Y. Gong, M. Hu, Y. Cheng, H. Su, D. Yue, F. Liu, A. Wiedensohler, Z. Wang, H. Kalesse, S. Liu, Z. Wu, K. Xiao, P. Mi, Y. Zhang, Competition of coagulation sink and source rate: New particle formation in the Pearl River Delta of China. *Atmos. Environ.* **44**, 3278–3285 (2010).

133. Z. B. Wang, M. Hu, J. Y. Sun, Z. J. Wu, D. L. Yue, X. J. Shen, Y. M. Zhang, X. Y. Pei, Y. F. Cheng, A. Wiedensohler, Characteristics of regional new particle formation in urban and regional background environments in the North China Plain. *Atmos. Chem. Phys.* **13**, 12495–12506 (2013).

134. S. Guo, M. Hu, M. L. Zamora, J. Peng, D. Shang, J. Zheng, Z. Du, Z. Wu, M. Shao, L. Zeng,

M. J. Molina, R. Zhang, Elucidating severe urban haze formation in China. *Proc. Natl. Acad. Sci. U. S. A.* **111**, 17373–8 (2014).

135. E. Herrmann, A. J. Ding, V. M. Kerminen, T. Petäjä, X. Q. Yang, J. N. Sun, X. M. Qi, H. Manninen, J. Hakala, T. Nieminen, P. P. Aalto, M. Kulmala, C. B. Fu, Aerosols and nucleation in eastern China: First insights from the new SORPES-NJU station. *Atmos. Chem. Phys.* **14**, 2169–2183 (2014).

136. Z. Wang, Z. Wu, D. Yue, D. Shang, S. Guo, J. Sun, A. Ding, L. Wang, J. Jiang, H. Guo, J. Gao, H. C. Cheung, L. Morawska, M. Keywood, M. Hu, New particle formation in China: Current knowledge and further directions. *Sci. Total Environ.* **577**, 258–266 (2016).

137. Z. Shi, K. He, X. Yu, Z. Yao, F. Yang, Y. Ma, R. Ma, Y. Jia, J. Zhang, Diurnal variation of number concentration and size distribution of ultrafine particles in the urban atmosphere of Beijing in winter. *J. Environ. Sci. (China)*. **19**, 933–8 (2007).

138. H. Yu, L. Zhou, L. Dai, W. Shen, W. Dai, J. Zheng, Y. Ma, M. Chen, Nucleation and growth of sub-3 nm particles in the polluted urban atmosphere of a megacity in China. *Atmos. Chem. Phys.* **16**, 2641–2657 (2016).

139. X. J. Shen, J. Y. Sun, Y. M. Zhang, B. Wehner, A. Nowak, T. Tuch, X. C. Zhang, T. T. Wang, H. G. Zhou, X. L. Zhang, F. Dong, W. Birmili, A. Wiedensohler, First long-term study of particle number size distributions and new particle formation events of regional aerosol in the North China Plain. *Atmos. Chem. Phys.* **11**, 1565–1580 (2011).

140. J. F. Peng, M. Hu, Z. B. Wang, X. F. Huang, P. Kumar, Z. J. Wu, S. Guo, D. L. Yue, D. J. Shang, Z. Zheng, L. Y. He, Submicron aerosols at thirteen diversified sites in China: Size distribution, new particle formation and corresponding contribution to cloud condensation nuclei production. *Atmos. Chem. Phys.* **14**, 10249–10265 (2014).

141. S. Xiao, M. Y. Wang, L. Yao, M. Kulmala, B. Zhou, X. Yang, J. M. Chen, D. F. Wang, Q. Y. Fu, D. R. Worsnop, L. Wang, Strong atmospheric new particle formation in winter in urban Shanghai, China. *Atmos. Chem. Phys.* **15**, 1769–1781 (2015).

142. S. Liu, M. Hu, Z. Wu, B. Wehner, A. Wiedensohler, Y. Cheng, Aerosol number size distribution and new particle formation at a rural/coastal site in Pearl River Delta (PRD) of China. *Atmos. Environ.* **42**, 6275–6283 (2008).

143. Z. Wu, M. Hu, P. Lin, S. Liu, B. Wehner, A. Wiedensohler, Particle number size distribution in the urban atmosphere of Beijing, China. *Atmos. Environ.* **42**, 7967–7980 (2008).

144. R. Halonen, E. Zapadinsky, T. Kurtén, H. Vehkamäki, B. Reischl, Rate enhancement in collisions of sulfuric acid molecules due to long-range intermolecular forces. *Atmos. Chem. Phys. Discuss.*, 1–17 (2019).

145. G. Isaacman-Vanwertz, P. Massoli, R. O'Brien, C. Lim, J. P. Franklin, J. A. Moss, J. F. Hunter, J. B. Nowak, M. R. Canagaratna, P. K. Misztal, C. Arata, J. R. Roscioli, S. T. Herndon, T. B. Onasch, A. T. Lambe, J. T. Jayne, L. Su, D. A. Knopf, A. H. Goldstein, D. R. Worsnop, J. H. Kroll, Chemical evolution of atmospheric organic carbon over multiple generations of oxidation. *Nat. Chem.* **10**, 462–468 (2018).

146. A. Mutzel, L. Poulain, T. Berndt, Y. Iinuma, M. Rodigast, O. Böge, S. Richters, G. Spindler, M. Sipila¨, T. Jokinen, M. Kulmala, H. Herrmann, Highly Oxidized Multifunctional Organic Compounds Observed in Tropospheric Particles: A Field and Laboratory Study. *Environ. Sci. Technol.* **49**, 7754–7761 (2015).

147. N. Sarnela, T. Jokinen, J. Duplissy, C. Yan, T. Nieminen, M. Ehn, S. Schobesberger, M. Heinritzi, S. Ehrhart, K. Lehtipalo, J. Tröstl, M. Simon, A. Kürten, M. Leiminger, M. J. Lawler, M. P. Rissanen, F. Bianchi, A. P. Praplan, J. Hakala, A. Amorim, M. Gonin, A. Hansel, J.

Kirkby, J. Dommen, J. Curtius, J. N. Smith, T. Petäjä, D. R. Worsnop, M. Kulmala, N. M. Donahue, M. Sipilä, Measurement–model comparison of stabilized Criegee intermediate and highly oxygenated molecule production in the CLOUD chamber. *Atmos. Chem. Phys.* **18**, 2363–2380 (2018).

148. M. P. Rissanen, T. Kurt??n, M. Sipil??, J. A. Thornton, O. Kausiala, O. Garmash, H. G. Kjaergaard, T. Pet??j??, D. R. Worsnop, M. Ehn, M. Kulmala, Effects of chemical complexity on the autoxidation mechanisms of endocyclic alkene ozonolysis products: From methylcyclohexenes toward understanding ??-pinene. *J. Phys. Chem. A*. **119**, 4633–4650 (2015).

149. Y. Wang, M. Riva, H. Xie, L. Heikkinen, Formation of highly oxygenated organic molecules from chlorine atom initiated oxidation of alpha-pinene, 1–31 (2019).

150. T. Kurtén, M. P. Rissanen, K. Mackeprang, J. A. Thornton, N. Hyttinen, S. Jørgensen, M. Ehn, H. G. Kjaergaard, Computational Study of Hydrogen Shifts and Ring-Opening Mechanisms in α-Pinene Ozonolysis Products. *J. Phys. Chem. A*. **119**, 11366–11375 (2015).

151. N. C. Eddingsaas, C. L. Loza, L. D. Yee, M. Chan, K. A. Schilling, P. S. Chhabra, J. H. Seinfeld, P. O. Wennberg, Atmospheric Chemistry and Physics α-pinene photooxidation under controlled chemical conditions-Part 2: SOA yield and composition in low-and high-NO x environments. *Atmos. Chem. Phys*. **12**, 7413–7427 (2012).

152. M. Sarrafzadeh, J. Wildt, I. Pullinen, M. Springer, E. Kleist, R. Tillmann, S. H. Schmitt, C. Wu, T. F. Mentel, D. Zhao, D. R. Hastie, A. Kiendler-Scharr, Impact of NO x and OH on secondary organic aerosol formation from β-pinene photooxidation. *Atmos. Chem. Phys*. **16**, 11237–11248 (2016).

153. J. Hammes, E. Tsiligiannis, T. F. Mentel, M. Hallquist, Effect of NO x on 1,3,5-trimethylbenzene (TMB) oxidation product distribution and particle formation . *Atmos. Chem. Phys. Discuss.*, 1–18 (2019).

154. M. R. Stolzenburg, P. H. McMurry, An ultrafine aerosol condensation nucleus counter. *Aerosol Sci. Technol.* **14**, 48–65 (1991).

155. B. Stacey, R. M. Harrison, F. Pope, Evaluation of Ultrafine Particle Concentrations and Size Distributions at London Heathrow Airport University of Birmingham. *Atmos. Environ.*, 117148 (2019).

156. K. Sellegri, C. Rose, A. Marinoni, A. Lupi, A. Wiedensohler, M. Andrade, P. Bonasoni, P. Laj, New Particle Formation: A Review of Ground-Based Observations at Mountain Research Stations. *Atmosphere (Basel).* **10**, 493 (2019).

157. K. Iida, M. R. Stolzenburg, P. H. McMurry, Effect of working fluid on sub-2 nm particle detection with a laminar flow ultrafine condensation particle counter. *Aerosol Sci. Technol.* **43**, 81–96 (2009).

158. S. Mirme, A. Mirme, The mathematical principles and design of the NAIS - A spectrometer for the measurement of cluster ion and nanometer aerosol size distributions. *Atmos. Meas. Tech.* **6**, 1061–1071 (2013).

159. A. Mirme, E. Tamm, G. Mordas, M. Vana, J. Uin, S. Mirme, T. Bernotas, L. Laakso, A. Hirsikko, M. Kulmala, A wide-range multi-channel air ion spectrometer. *Boreal Environ. Res.* **12**, 247–264 (2007).

160. J. Vanhanen, J. Mikkilä, K. Lehtipalo, M. Sipilä, H. E. Manninen, E. Siivola, T. Petäjä, M. Kulmala, Particle Size Magnifier for Nano-CN Detection. *Aerosol Sci. Technol.* **45**, 533–542 (2011).

161. R. Cai, D. Yang, L. R. Ahonen, L. Shi, F. Korhonen, Y. Ma, T. Petäjä, J. Zheng, J. Kangasluoma,

J. Jiang, J. Jiang, J. Zheng, Data inversion methods to determine sub-3 nm aerosol size distributions using the Particle Size Magnifier, 1–32 (2018).

162. T. Chan, R. Cai, L. R. Ahonen, Y. Liu, Y. Zhou, J. Vanhanen, L. Dada, Y. Chao, Assessment of particle size magnifier inversion methods to obtain particle size distribution from atmospheric measurements. *Atmos. Chem. Phys. Discuss.*, 1–21 (2020).

163. N. Hyttinen, O. Kupiainen-Määtta, M. P. Rissanen, M. Muuronen, M. Ehn, T. Kurtén, Modeling the Charging of Highly Oxidized Cyclohexene Ozonolysis Products Using Nitrate-Based Chemical Ionization. *J. Phys. Chem. A*. **119**, 6339–6345 (2015).

164. K. H. Møller, C. M. Tram, H. G. Kjaergaard, Side-by-Side Comparison of Hydroperoxide and Corresponding Alcohol as Hydrogen-Bond Donors. *J. Phys. Chem. A*. **121**, 2951–2959 (2017).

165. A. Kürten, A. Bergen, M. Heinritzi, M. Leiminger, V. Lorenz, F. Piel, M. Simon, R. Sitals, A. C. Wagner, J. Curtius, Observation of new particle formation and measurement of sulfuric acid, ammonia, amines and highly oxidized organic molecules at a rural site in central Germany. *Atmos. Chem. Phys.* **16**, 12793–12813 (2016).

166. M. Simon, M. Heinritzi, S. Herzog, M. Leiminger, F. Bianchi, A. Praplan, J. Dommen, J. Curtius, A. Kurten, Detection of dimethylamine in the low pptv range using nitrate chemical ionization atmospheric pressure interface time-of-flight (CI-APi-TOF) mass spectrometry. *Atmos. Meas. Tech.* **9**, 2135–2145 (2016).

167. A. Kürten, L. Rondo, S. Ehrhart, J. Curtius, Calibration of a chemical ionization mass spectrometer for the measurement of gaseous sulfuric acid. *J. Phys. Chem. A*. **116**, 6375–6386 (2012).

168. S. Mikkonen, S. Romakkaniemi, J. N. Smith, H. Korhonen, T. Petäjä, C. Plass-Duelmer, M. Boy, P. H. McMurry, K. E. J. Lehtinen, J. Joutsensaari, A. Hamed, R. L. Mauldin, W. Birmili, G. Spindler, F. Arnold, M. Kulmala, A. Laaksonen, A statistical proxy for sulphuric acid concentration. *Atmos. Chem. Phys.* **11**, 11319–11334 (2011).

169. C. Yan, W. Nie, M. Äijälä, M. P. Rissanen, M. R. Canagaratna, P. Massoli, H. Junninen, T. Jokinen, N. Sarnela, S. A. K. Häme, S. Schobesberger, F. Canonaco, L. Yao, A. S. H. Prévôt, T. Petäjä, M. Kulmala, M. Sipilä, D. R. Worsnop, M. Ehn, Source characterization of highly oxidized multifunctional compounds in a boreal forest environment using positive matrix factorization. *Atmos. Chem. Phys.* **16**, 12715–12731 (2016).

170. P. Massoli, H. Stark, M. R. Canagaratna, J. E. Krechmer, L. Xu, N. L. Ng, R. L. Mauldin, C. Yan, J. Kimmel, P. K. Misztal, J. L. Jimenez, J. T. Jayne, D. R. Worsnop, Ambient Measurements of Highly Oxidized Gas-Phase Molecules during the Southern Oxidant and Aerosol Study (SOAS) 2013. *ACS Earth Sp. Chem.* **2**, 653–672 (2018).

171. Y. Zhang, O. Peräkylä, C. Yan, L. Heikkinen, M. Äijälä, K. R. Daellenbach, Q. Zha, M. Riva, O. Garmash, H. Junninen, P. Paatero, D. Worsnop, M. Ehn, A novel approach for simple statistical analysis of high-resolution mass spectra. *Atmos. Meas. Tech*. **12**, 3761–3776 (2019).

172. A. R. Koss, M. R. Canagaratna, A. Zaytsev, J. E. Krechmer, K. Nihill, C. Lim, J. C. Rowe, J. R. Roscioli, N. Keutsch, J. H. Kroll, Dimensionality-reduction techniques for complex mass spectrometric datasets : application to laboratory atmospheric organic oxidation experiments. *Atmos. Chem. Phys. Discuss.*, 1–42 (2019).

173. F. Bianchi, O. Garmash, X. He, C. Yan, S. Iyer, I. Rosendahl, Z. Xu, M. P. Rissanen, M. Riva, R. Taipale, N. Sarnela, T. Petäjä, D. R. Worsnop, M. Kulmala, M. Ehn, H. Junninen, The role of highly oxygenated molecules (HOMs) in determining the composition of ambient ions in the boreal forest. *Atmos. Chem. Phys.* **17**, 13819–13831 (2017).

174. C. Yan, The role of H2SO4-NH3 anion clusters in ion-induced aerosol nucleation mechanisms

in the boreal forest. *Atmos. Chem. Phys.*, 1–20 (2018).

175. M. Dal Maso, M. Kulmala, I. Riipinen, R. Wagner, T. Hussein, P. P. Aalto, K. E. J. Lehtinen, Formation and growth of fresh atmospheric aerosols: Eight years of aerosol size distribution data from SMEAR II, Hyytiälä, Finland. *Boreal Environ. Res.* **10**, 323–336 (2005).

176. J. Kim, Y. Jun Yoon, Y. Gim, J. Hee Choi, H. Jin Kang, K. T. Park, J. Park, B. Yong Lee, New particle formation events observed at King Sejong Station, Antarctic Peninsula - Part 1: Physical characteristics and contribution to cloud condensation nuclei. *Atmos. Chem. Phys.* **19**, 7583–7594 (2019).

177. T. Nieminen, V.-M. Kerminen, T. Petäjä, P. P. Aalto, M. Arshinov, E. Asmi, U. Baltensperger, D. C. S. Beddows, J. P. Beukes, D. Collins, A. Ding, R. M. Harrison, B. Henzing, R. Hooda, M. Hu, U. Hõrrak, N. Kivekäs, K. Komsaare, R. Krejci, A. Kristensson, L. Laakso, A. Laaksonen, W. R. Leaitch, H. Lihavainen, N. Mihalopoulos, Z. Németh, W. Nie, C. O'Dowd, I. Salma, K. Sellegri, B. Svenningsson, E. Swietlicki, P. Tunved, V. Ulevicius, V. Vakkari, M. Vana, A. Wiedensohler, Z. Wu, A. Virtanen, M. Kulmala, Global analysis of continental boundary layer new particle formation based on long-term measurements. *Atmos. Chem. Phys. Discuss.*, 1–34 (2018).

178. M. Vana, M. Ehn, T. Petäjä, H. Vuollekoski, P. Aalto, G. de Leeuw, D. Ceburnis, C. D. O'Dowd, M. Kulmala, Characteristic features of air ions at Mace Head on the west coast of Ireland. *Atmos. Res.* **90**, 278–286 (2008).

179. S. Guo, M. Hu, J. Peng, Z. Wu, M. L. Zamora, D. Shang, Z. Du, J. Zheng, X. Fang, R. Tang, Y. Wu, L. Zeng, S. Shuai, W. Zhang, Y. Wang, Y. Ji, Y. Li, A. L. Zhang, W. Wang, F. Zhang, J. Zhao, X. Gong, C. Wang, M. J. Molina, R. Zhang, Remarkable nucleation and growth of ultrafine particles from vehicular exhaust. *Proc. Natl. Acad. Sci.*, 201916366 (2020).

180. T. Yli-Juuti, N. Riipinen, P. P. Aalto, T. Nieminen, W. Maenhaut, I. A. Janssens, M. Claeys, I. Salma, R. Ocskay, A. Hoffer, K. Lmre, M. Kulmala, Characteristics of new particle formation events and cluster ions at K-puszta, Hungary. *Boreal Environ. Res.* **14**, 683–698 (2009).

181. R. L. Modini, Z. D. Ristovski, G. R. Johnson, C. He, N. Surawski, L. Morawska, T. Suni, M. Kulmala, New particle formation and growth at a remote, sub-tropical coastal location. *Atmos. Chem. Phys.* **9**, 7607–7621 (2009).

182. M. Dal Maso, M. Kulmala, K. E. J. Lehtinen, J. M. M̈kelä, P. Aalto, C. D. O'Dowd, Condensation and coagulation sinks and formation of nucleation mode particles in coastal and boreal forest boundary layers. *J. Geophys. Res. Atmos.* **107** (2002), doi:10.1029/2001JD001053.

183. M. Kulmala, M. Dal Maso, J. M. Mäkelä, L. Pirjola, M. Väkevä, P. Aalto, P. Miikkulainen, K. Hämeri, C. D. O'Dowd, On the formation, growth and composition of nucleation mode particles. *Tellus, Ser. B Chem. Phys. Meteorol.* **53**, 479–490 (2001).

184. R. Cai, D. Yang, Y. Fu, X. Wang, X. Li, Y. Ma, J. Hao, J. Zheng, Aerosol surface area concentration : a governing factor in new particle formation in Beijing, 12327–12340 (2017).

185. J. Julin, P. M. Winkler, N. M. Donahue, P. E. Wagner, I. Riipinen, Near-unity mass accommodation coefficient of organic molecules of varying structure. *Environ. Sci. Technol.* **48**, 12083–12089 (2014).

186. M. D. Allen, O. G. Raabe, Slip correction measurements of spherical solid aerosol particles in an improved millikan apparatus. *Aerosol Sci. Technol.* **4**, 269–286 (1985).

187. N. A. Fuchs, The Mechanics of Aerosols. *Science (80-.).* **146**, 1033–1034 (1964).

188. M. Kulmala, M. Dal Maso, J. M. Mäkelä, L. Pirjola, M. Väkevä, P. Aalto, P. Miikkulainen, K. Hämeri, C. D. O'Dowd, On the formation, growth and composition of nucleation mode particles. *Tellus, Ser. B Chem. Phys. Meteorol.* **53**, 479–490 (2001).

189. J. Leppa, Atmospheric new particle formation: real and apparent growth of neutral and charged particles. *Atmos. Chem. Phys.* **11**, 4939–4955 (2011).

190. T. Nieminen, K. E. J. Lehtinen, M. Kulmala, Sub-10 nm particle growth by vapor condensation-effects of vapor molecule size and particle thermal speed. *Atmos. Chem. Phys.* **10**, 9773–9779 (2010).

191. H. Korhonen, V. M. Kerminen, H. Kokkola, K. E. J. Lehtinen, Estimating atmospheric nucleation rates from size distribution measurements: Analytical equations for the case of size dependent growth rates. *J. Aerosol Sci.* **69**, 13–20 (2014).

192. M. Schervish, N. M. Donahue, Peroxy radical chemistry and the volatility basis set. *Atmos. Chem. Phys.* **20**, 1183–1199 (2020).

193. X. Fang, M. Hu, D. Shang, R. Tang, L. Shi, T. Olenius, Y. Wang, H. Wang, Z. Zhang, S. Chen, X. Yu, W. Zhu, S. Lou, Y. Ma, X. Li, L. Zeng, Z. Wu, J. Zheng, S. Guo, Observational Evidence for the Involvement of Dicarboxylic Acids in Particle Nucleation. *Environ. Sci. Technol. Lett.* (2020), doi:10.1021/acs.estlett.0c00270.

194. K. Lehtipalo, C. Yan, L. Dada, F. Bianchi, M. Xiao, R. Wagner, D. Stolzenburg, L. R. Ahonen, A. Amorim, A. Baccarini, P. S. Bauer, B. Baumgartner, A. Bergen, A.-K. Bernhammer, M. Breitenlechner, S. Brilke, A. Buchholz, S. B. Mazon, D. Chen, X. Chen, A. Dias, J. Dommen, D. C. Draper, J. Duplissy, M. Ehn, H. Finkenzeller, L. Fischer, C. Frege, C. Fuchs, O. Garmash, H. Gordon, J. Hakala, X. He, L. Heikkinen, M. Heinritzi, J. C. Helm, V. Hofbauer, C. R. Hoyle, T. Jokinen, J. Kangasluoma, V.-M. Kerminen, C. Kim, J. Kirkby, J. Kontkanen, A. Kürten, M. J. Lawler, H. Mai, S. Mathot, R. L. Mauldin, U. Molteni, L. Nichman, W. Nie, T. Nieminen, A. Ojdanic, A. Onnela, M. Passananti, T. Petäjä, F. Piel, V. Pospisilova, L. L. J. Quéléver, M. P. Rissanen, C. Rose, N. Sarnela, S. Schallhart, S. Schuchmann, K. Sengupta, M. Simon, M. Sipilä, C. Tauber, A. Tomé, J. Tröstl, O. Väisänen, A. L. Vogel, R. Volkamer, A. C. Wagner, M. Wang, L. Weitz, D. Wimmer, P. Ye, A. Ylisirniö, Q. Zha, K. S. Carslaw, J. Curtius, N. M. Donahue, R. C. Flagan, A. Hansel, I. Riipinen, A. Virtanen, P. M. Winkler, U. Baltensperger, M. Kulmala, D. R. Worsnop, Multicomponent new particle formation from sulfuric acid, ammonia, and biogenic vapors. *Sci. Adv.* **4**, eaau5363 (2018).

195. M. Dall'Osto, D. C. S. Beddows, P. Tunved, R. Krejci, J. Ström, H. C. Hansson, Y. J. Yoon, K. T. Park, S. Becagli, R. Udisti, T. Onasch, C. D. O'dowd, R. Simó, R. M. Harrison, Arctic sea ice melt leads to atmospheric new particle formation. *Sci. Rep.* **7**, 1–10 (2017).

196. M. Van Damme, L. Clarisse, S. Whitburn, J. Hadji-Lazaro, D. Hurtmans, C. Clerbaux, P. F. Coheur, Industrial and agricultural ammonia point sources exposed. *Nature*. **564**, 99–103 (2018).

197. M. P. Rissanen, NO2 Suppression of Autoxidation-Inhibition of Gas-Phase Highly Oxidized Dimer Product Formation. *ACS Earth Sp. Chem.* **2**, 1211–1219 (2018).

198. F. D. Lopez-Hilfiker, V. Pospisilova, W. Huang, M. Kalberer, C. Mohr, G. Stefenelli, J. A. Thornton, U. Baltensperger, A. S. H. Prevot, J. G. Slowik, An Extractive Electrospray Ionization Time-of-Flight Mass Spectrometer (EESI-TOF) for online measurement of atmospheric aerosol particles. *Atmos. Meas. Tech. Discuss.*, 1–40 (2019).

199. X. Qi, A. Ding, P. Roldin, Z. Xu, P. Zhou, N. Sarnela, W. Nie, X. Huang, A. Rusanen, M. Ehn, M. P. Rissanen, T. Petäjä, M. Kulmala, M. Boy, Modelling studies of HOMs and their contributions to new particle formation and growth: comparison of boreal forest in Finland and a polluted environment in China. *Atmos. Chem. Phys*. **18**, 11779–11791 (2018).

200. W. Pu, Z. Zou, W. Wang, D. Tanner, Z. Wang, T. Wang, Development of a chemical ionization mass spectrometry system for measurement of atmospheric OH radical. *Atmos. Meas. Tech. Discuss.* (2020), doi:https://doi.org/10.5194/amt-2020-252.

201. N. Lee Ng, S. S. Brown, A. T. Archibald, E. Atlas, R. C. Cohen, J. N. Crowley, D. A. Day, N. M. Donahue, J. L. Fry, H. Fuchs, R. J. Griffin, M. I. Guzman, H. Herrmann, A. Hodzic, Y. Iinuma, A. Kiendler-Scharr, B. H. Lee, D. J. Luecken, J. Mao, R. McLaren, A. Mutzel, H. D. Osthoff, B. Ouyang, B. Picquet-Varrault, U. Platt, H. O. T. Pye, Y. Rudich, R. H. Schwantes, M. Shiraiwa, J. Stutz, J. A. Thornton, A. Tilgner, B. J. Williams, R. A. Zaveri, Nitrate radicals and biogenic volatile organic compounds: Oxidation, mechanisms, and organic aerosol. *Atmos. Chem. Phys.* **17**, 2103–2162 (2017).

202. M. Riva, P. Rantala, E. J. Krechmer, O. Peräkylä, Y. Zhang, L. Heikkinen, O. Garmash, C. Yan, M. Kulmala, D. Worsnop, M. Ehn, Evaluating the performance of five different chemical ionization techniques for detecting gaseous oxygenated organic species. *Atmos. Meas. Tech.* **12**, 2403–2421 (2019).

203. V. Pospisilova, F. D. Lopez-Hilfiker, D. M. Bell, I. El Haddad, C. Mohr, W. Huang, L. Heikkinen, M. Xiao, J. Dommen, A. S. H. Prevot, U. Baltensperger, J. G. Slowik, On the fate of oxygenated organic molecules in atmospheric aerosol particles. *Sci. Adv.* **6**, 1–12 (2020).

ABBREVIATIONS

AIS: Air ion spectrometer

APi-ToF: Atmospheric pressure interface time of flight mass spectrometer

BSQ: Big segmented quadrupole

CCN: Cloud condensation nuclei

CI-APi-ToF: Chemical ionization atmospheric pressure interface time of flight mass spectrometer

CN: Condensation nuclei

CoagS: Coagulation sink

CPC: Condensation particle counter

CS: Condensation sink

D_{50}: 50% detection limit cutoff for particle counting instrument

DEG: Diethylene glycol

DMA: Dimethylamine

DMS: Dimethyl sulphide

D_p: Diameter of particle

EC: Electrostatic classifier

ELVOC: Extremely low volatility organic compound

GR: Growth rate

HOM: Highly oxygenated multifunctional organic molecules

IIC: Ion induced clustering

LVOC: Low volatility organic compound

MSA: Methanesulphonic acid

NAIS: Neutral cluster and air ion spectrometer

NPF: New Particle Formation

PB: Primary beam

PMF: Positive matrix factorization

PSM: Particle size magnifier

SMPS: Scanning Mobility Particle Sizer

SSQ: Small segmented quadrupole

SVOC: Semi volatile organic compound

ToF: Time-of-flight

ULVOC: Ultra low volatility organic compound

VBS: Volatility basis set

VOC: Volatile organic compound

APPENDIX: OPEN OCEAN AND COASTAL NEW PARTICLE FORMATION FROM SULPHURIC ACID AND AMINES AROUND THE ANTARCTIC PENINSULA (UPDATED)

This is an updated version of the manuscript presented in Chapter 4 for which the review contributions of four reviewers have been integrated.

Authors: James Brean, Manuel Dall'Osto, Rafel Simo, Zongbo Shi, David C.S. Beddows, and Roy M. Harrison

Author contributions: MDO, JB and DCSB made the field measurements. RS and MD'O organised the campaign and the cruise. JB processed the data and led the data interpretation, and produced the first draft of the paper and integrated all review comments. Further contributions to the paper were made by RMH, ZS and RS. R code to produce HYSPLIT back trajectories and CS values was provided by DCSB, alongside sea ice concentrations and Figure 3a.

OPEN OCEAN AND COASTAL NEW PARTICLE FORMATION FROM SULPHURIC ACID AND AMINES AROUND THE ANTARCTIC PENINSULA

James Brean[1], Manuel Dall'Osto[2], Rafel Simó[2], Zongbo Shi[1], David C.S. Beddows[1] and Roy M. Harrison[1*†]

[1]Division of Environmental Health and Risk Management
School of Geography, Earth and Environmental Sciences
University of Birmingham, Edgbaston
Birmingham B15 2TT, United Kingdom

[2]Institute of Marine Science
Consejo Superior de Investigaciones Científicas (CSIC)
Barcelona, Spain

[*]Correspondence author: Roy M. Harrison, Division of Environmental Health and Risk Management, School of Geography, Earth and Environmental Sciences, University of Birmingham Edgbaston, Birmingham B15 2TT, United Kingdom. Email: r.m.harrison@bham.ac.uk
Tele: +44 121 414 3494; Fax: +44 121 414 3709;
ORCID ID: 0000-0002-2684-5226

[†]Also at: Department of Environmental Sciences / Center of Excellence in Environmental Studies, King Abdulaziz University, PO Box 80203, Jeddah, 21589, Saudi Arabia

ABSTRACT

New particle formation is globally one of the major sources of aerosol by number, and therefore a leading factor controlling cloud condensation nuclei (CCN) concentrations. Antarctica is experiencing drastic and variable climate change, and modelling estimates of the regional feedbacks through aerosol direct and indirect radiative forcing are highly uncertain as they are limited by knowledge of aerosol formation mechanisms. Here, we study summertime open ocean and coastal new particle formation in the Antarctic Peninsula region. The rates of particle formation relative to sulphuric acid concentration as well as the sulphuric acid dimer:monomer ratios were similar to those seen for sulphuric acid-dimethylamine-water nucleation. Numerous sulphuric acid-amine peaks were identified during NPF events, evidencing that alkylamines were the bases that facilitated sulphuric acid nucleation. Most new particle formation events occurred in air masses arriving from the ice-covered Weddell Sea and its marginal ice zone, which are a significant source of volatile sulphur and alkylamines. This nucleation mechanism is more efficient than the ion-induced sulphuric acid-ammonia pathway previously observed in Antarctica, and one that can occur rapidly under neutral conditions. This hitherto overlooked pathway to biologically-driven aerosol formation should be considered for estimating aerosol and CCN numbers in ocean – sea ice – aerosols – climate feedback models.

Keywords: New particle formation; Antarctic; nucleation; sulphuric acid; alkylamines

MAIN

The Antarctic Peninsula has shown some of the largest increases in near-surface air temperature measured globally across the last 50 years[1], despite a pause to this increase within the last two decades[2]. Climate models struggle to accurately predict the temperature of the Antarctic Peninsula[3], and this is due in part to uncertainties in both meteorology[4] and the gas and aerosol processes governing radiative forcing. One of the largest areas of uncertainty in the latter is the direct and indirect radiative forcing due to aerosols and clouds[5]. Model studies suggest that natural aerosols contribute disproportionately to uncertainty in indirect forcing[6]. Unlike the Arctic, where anthropogenic contributions to aerosol loadings are considerable, the Antarctic is remote from major emission sources, and particles of natural origin dominate the aerosol population[7]. In such a pristine environment, new particle formation (NPF) makes a major contribution both to the condensation nuclei (CN) count, and more critically to the number of cloud condensation nuclei (CCN), hence influencing both the direct and the indirect radiative forcing. NPF processes in Antarctica have been associated with marine air masses[8] and high fluxes of the trace gas dimethylsulphide (DMS). Indeed, early studies of Antarctic submicron particles found their composition dominated by sulphuric acid (H_2SO_4), largely accompanied by ammonium[9]. Later studies have found a contribution of low molecular weight alkylamines to aerosol mass, arising from air masses passing over areas of melting sea ice[10]. Measurements of amines in seawater further suggest high alkylamine content in or near sea ice, and on-line analysis of Antarctic aerosols show that a significant fraction of aerosol phase alkylamines are secondary in origin, rather than primary[11]. Recent evidence points towards NPF events originating from sympagic biogenic precursors at the sea ice marginal zone, and Antarctic plateau[12], while long term particle size distribution measurements in the Antarctic Peninsula has linked NPF frequency and faster growth rates of nascent aerosols to upwind emissions of DMS by pelagic phytoplankton[8]. DMS is a biogenic volatile organosulphur compound that in the atmosphere oxidises to both H_2SO_4 and methanesulphonic acid (CH_3SO_3H, MSA). The most efficient pathways for these begin with a H-

abstraction, or an addition respectively[13]. H_2SO_4 is thought to be responsible for most nucleation observed in the atmosphere[14]. MSA can also form new particles in the presence of bases[15] and has been shown to accelerate nucleation of H_2SO_4 and dimethylamine (DMA) with which it forms stable clusters in the H_2SO_4-MSA-DMA system[16].

Recent advances in instrumentation have provided new insight into the fundamental steps of NPF in remote boreal forest[17], coastal[18], pristine polar[19] and urban environments[20]. This is backed up by a host of chamber experiments that have revealed the role of ammonia[21] and amines[22,23] in accelerating H_2SO_4-H_2O nucleation, and the influence of galactic cosmic rays (GCR), temperature, and humidity[21–24]. While there have been a number of studies of NPF in Antarctica[7,25,26], only one study[19] has investigated the particle nucleation process at a fundamental level. They reported ion-induced H_2SO_4-NH_3-H_2O nucleation, similar to that observed in laboratory experiments where GCR were seen to significantly enhance the nucleation rates[21], but dissimilar to H_2SO_4-DMA-H_2O nucleation where GCR were less influential[22]. Here we present evidence for a parallel process in particle nucleation involving H_2SO_4 and small alkylamines that can proceed rapidly under charged or neutral conditions. The study involved air sampling both on coastal land and over the open ocean, providing the first ship-borne data on nucleation processes at the molecular level.

RESULTS

Characteristics of new particle formation events

NPF events, defined using the criteria of Dal Maso et al. (2005)[27], were observed at the research station on Livingston Island on 4 of 29 measurement days (13.8 %). Events began concurrently with the rise in H_2SO_4 concentrations, growing to 10 - 20 nm (Figure 1a, 1b). C_2 and C_4 amines were measured in the gas phase. They showed high signals relative to methylamine and ammonia (Figure S1), although this difference may be enhanced by sensitivities which have not yet been quantified for individual bases. Trimethylamine was not measured in the gas phase but was present in

measured sulphuric acid clusters. Clustering between NO_3^- and NH_3 is significantly weaker than that with DMA and hence the sensitivity to NH_3 was likely lower, and the mixing ratio of NH_3 was much higher than that of amines. However, alkylamines have been shown to enhance formation rates at modest mixing ratios[22,23] like those encountered during our NPF events (in the range of a few pptv), which were sufficient to substitute NH_3 in H_2SO_4-NH_3 clusters[28]. Minima of amine signals at midday were driven by either clustering with elevated sulphuric acid, which clusters at roughly a 1:1 ratio if mixing ratios are sufficient[29], uptake onto particle surfaces, or photolysis[30]. Daily peak H_2SO_4 concentrations were on average above a factor of 2 higher on event days, driven by enhanced solar radiation. Although elevated temperatures can inhibit particle formation rates by promoting rapid cluster evaporation, peak temperatures were markedly similar between days (Figure 1c). The growth rates of new particles calculated from SMPS data varied between 0.41 – 0.58 nm h^{-1}, similar to other reports of Antarctic pure sulphuric acid-driven growth[19], but lower than measured in other Antarctic environments[25,26,31], although many of these measurements do not extend below 10 nm. At these rates, growth to CCN size is a process taking place on the order of days. Although we were not able to quantify the contribution of the NPFs to CCN in the studied region, it is likely these new particles eventually grow and contribute to CCN concentration downwind.

MSA concentrations are similar between NPF event and non-event days (Figure S2); other sulphur oxides (SO_3^- and SO_5^-) were measured, and followed similar trends to MSA, both distinct from H_2SO_4. The diurnal patterns of MSA were less pronounced and the mean concentrations on event and non-event days were markedly similar, despite enhanced photochemistry. MSA has been shown to form particles in flow reactors at ppbv concentrations[15], with the number of formed particles increasing at lower temperatures. In our data, however, maximum MSA concentrations did not result in NPF events if concurrent with the absence of H_2SO_4 , indicating that MSA alone could not form particles at an appreciable rate compared to H_2SO_4. A modelling study[32] showed a significant

increase in global particle number counts when MSA participated in ternary nucleation in the same manner as H_2SO_4; however, our results suggest this was not the case. Rather, MSA could have doubled the rates of particle formation from H_2SO_4 and amines at the ambient temperatures encountered[16] or influenced the particle size distribution by condensation on newly formed particles[32].

Iodic acid (HIO_3) was slightly elevated on NPF days, though HIO_3 concentrations were around an order of magnitude lower than those of H_2SO_4 and MSA. Organic compounds were comprised both of small ($\leq C_4$) dicarboxylic acids and larger oxygenated organics with the formula $C_{5\text{-}6}H_{6\text{-}10}O_{4\text{-}7}N_{0\text{-}1}$. Concentrations of both were slightly lower on NPF days. Positive matrix factorisation analyses show that these oxygenated organic molecules had the same oceanic sources as DMS-derived acids. Some dicarboxylic acids were seen to have a local origin from the research station (Figure S3). These organic molecules are too volatile to contribute to nucleation or early stage growth, with $Log_{10}C^*$(273 K) values between $3{\cdot}10^2$ and 10^6 μg m^{-3}, and classing these molecules as intermediate volatility organic compounds[33]. High isoprene mixing ratios can, however, act as $OH^{\cdot}$ sinks resulting in supressed NPF[34]; thus, slight mean elevations of oxygenated organics across non-event days may indicate the role of their precursors as $OH^{\cdot}$ scavengers. Across the whole range of particle sizes NPF events increased particle numbers from a median background of 229 cm^{-3} to 1625 cm^{-3}.

Two NPF events were observed during the cruise aboard the RV Hesperides, one occurring in close proximity to the research station and the other one just slightly south (Figure S4). Here, NPF also occurred under significant elevations of H_2SO_4 and amines, most notably C_4 amines (Figure S5). C_2 and C_4 amines were the only bases measurable aboard the cruise, with no significant signal of NH_3. Events occurred under depletions of both MSA and HIO_3, and unchanged concentrations of oxygenated organics compared to non-event periods.

Our observed elevation of H_2SO_4 relative to MSA and HIO_3 (Figures 1, S2, S6 and S7), as well as the absence of organics that would qualify as ultralow volatility organic compounds (ULVOC), capable of forming new particles in the absence of other acids, suggest that H_2SO_4 was the main driver of NPF in the entire dataset, both at the station and on board the ship. The presence of C_2 and C_4 amines at such high signal relative to NH_3 and methylamine (Figure S1) imply the former two may be of greater importance in stabilising H_2SO_4 clusters.

New particle formation from sulphuric acid and amines

Figure 2a shows particle formation rates plotted against H_2SO_4 monomer concentration. Measurements are compared to the results of the CLOUD consortium experiments in the presence/absence of galactic cosmic rays (GCR)[21,22,29]. Particle formation rates of up to 13 cm^{-3} s^{-1} occurred at over an order of magnitude lower H_2SO_4 concentration than would be expected for H_2SO_4-NH_3-H_2O nucleation at 278 K, and formation rates were greater than those previously observed in Antarctica at higher H_2SO_4 concentrations[19]. The upper bound of the measurement uncertainty on $J_{1.7}$ still falls short of the rates seen in the CLOUD chamber for H_2SO_4-DMA-H_2O nucleation on most days, where high mixing ratios of DMA were utilised. The lower bound of our uncertainty on $J_{1.7}$ is still more efficient than the CLOUD H_2SO_4-NH_3-H_2O system. Temperatures and relative humidity values during our measurements were 274.8 ± 1.7 K and 70 ± 1.3 %, respectively. These differ from those of the CLOUD experiments, but cluster stabilities and nucleation rates have been shown to be mostly stable across this range of conditions for H_2SO_4 and amines[22,23,35].

The H_2SO_4 dimer concentration in the CI-APi-ToF is elevated relative to the monomer by the presence of stabilising bases (H_2SO_4 clusters often lose base upon charging by nitrate ions[22]). Figure 2b shows measured H_2SO_4 dimer against H_2SO_4 monomer concentrations. Also plotted are the ratios seen in the CLOUD chamber for H_2SO_4-DMA-H_2O nucleation experiments[22] as well as the estimated H_2SO_4 dimer formed purely from ion induced clustering (IIC) of H_2SO_4 monomer in the NO_3^- chemical ionisation inlet[20,22]. The positioning of the H_2SO_4 dimer:monomer ratio above the lower IIC

limit indicates that there was a secondary stabilising species present in the system, and likely H_2O as a ternary species. This ratio sits below that measured for the ternary H_2SO_4–DMA–H_2O system, but is similar to that seen for DMA-H_2SO_4 nucleation in Shanghai[20]. Compared to the latter study, though, we measured at markedly lower condensation sinks (10^{-3} – 10^{-4} s^{-1}), to which this ratio is highly sensitive. It is therefore likely that amine concentrations were limiting, or the bases involved were less efficient at stabilising sulphuric acid clusters than DMA, such as methylamine, ethylamine in the case of C_2 amines, or diethylamine in the case of C_4 amines[36].

Figure 2c shows the mass defect plots before, and during a nucleation event on 2019-02-28. Clusters of sulphuric acid and amines with up to three sulphuric acid molecules, and two sulphuric acid molecules with two bases were visible in the CI-APi-ToF spectra. A large range of sulphuric acid-amine peaks were present (Figure S8), alongside a host of other sulphur containing ions. The amines that were clustered with the sulphuric acid dimer ranged from a single C_2 amine (at low signal) through to 2 amines with a combined carbon number of 8. The largest of these peaks is the sulphuric acid dimer clustered with two amines of combined carbon number 4, likely two C_2 amines[23]. These clusters have been shown to be mostly stable against evaporation[29], with the $(H_2SO_4)_2(DMA)_2$ cluster having evaporation rates on the order of 10^{-6} s^{-1} (ref. 37), and to grow by stepwise collisional addition until they reach detectable size by particle counting instruments. A peak for the H_2SO_4-MSA cluster is also observed, which likely has an enhancing effect on nucleation rate[16].

Taking all of this into account, we suggest that the nucleation events we observed around the Antarctic Peninsula were driven by H_2SO_4-amine clusters of $C_{1\text{-}4}$ amines, with H_2O as a ternary stabilising species. The role of ions cannot be ruled out, but is seen to be minimal when nucleation involves a strong alkylamine base[22]. Similarly, MSA likely has a synergistic effect on particle formation rates[16]. These results add to prior evidence for H_2SO_4-NH_3-H_2O nucleation on the coast of mainland

Antarctica[19], where no alkylamines were detected in the clusters and formation rates were in agreement with previous chamber work for H_2SO_4-NH_3-H_2O nucleation.

Links to air mass trajectories

Ninety-six-hour HYSPLIT air-mass back trajectories ending up in our measurement locations were clustered based upon their Euclidian distance (Figure 3a). The NPF events were most associated with cluster 2 (Figure 3b), i.e., air blowing from the eastern coast of the Antarctic Peninsula and the Weddell Sea. These same air masses, which blew over the largest fraction of sea-ice covered ocean (Figure 3c), carried the highest signals of H_2SO_4 (Figure 3d) and C_2 and C_4 amines (Figure 3e). The marginal ice zone and adjacent open ocean of the Weddell Sea have already been reported to be a source of DMS and alkylamine emissions from the microbiota of sea ice and plankton[10,11], and thus we suggest that these regions were the principal providers of the strong acid and base components needed for NPF.

DISCUSSION

We show that NPF events around the northern Antarctic Peninsula occurred in association with elevated H_2SO_4 concentrations as a necessary condition (Figure 1). Elevated concentrations of other acids and oxygenated organics, such as MSA, typically co-occurred with high H_2SO_4 during NPF events due to midday photochemistry, but by themselves without the latter they did not lead to measurable particle formation and growth (Figures S2, S6, and S7). Therefore, our results confirm previous observations of the essential role of H_2SO_4 in NPF in the Antarctic region[19]. Here we show that alkylamines provide a pivotal role in stabilising H_2SO_4 clusters during nucleation periods. This conclusion is based on a comparison of the rate of particle formation relative to H_2SO_4, alongside the ratio of H_2SO_4 dimer:monomer to that seen in CLOUD chamber measurements of H_2SO_4-DMA-H_2O nucleation. Further evidence is provided by the appearance of diverse sulphuric acid-amine clusters during nucleation events (Figure 2). Previous measurements in coastal mainland

Antarctica at Aboa, 2000 km southeast of our sampling location, provide evidence of nucleation proceeding via clustering of H_2SO_4-NH_3-H_2O[19]. Here we provide evidence for H_2SO_4-amine-H_2O nucleation as a dominant process in the Antarctic Peninsula. It is likely that the amines are from regions of sea ice in the Antarctic Peninsula – western Weddell Sea region. Sympagic waters in this region have been shown to be rich in methyl, dimethyl and trimethylamines and their precursors[11], and aerosol originating from iced regions have shown a near 5-fold enhancement in amine concentration[10]. This mechanism will likely to be important in regions where there are substantial amine emissions, such as in the regions where sympagic conditions are similar to those of the Weddell Sea region. Figure 3a shows that sea ice extent around coastal Antarctica is substantial, suggesting that this process may be important in a large area close to these iced regions. Long-term reports of NPF from a station only ~100 km northeast show markedly similar formation rates to our own, and an 11 % elevation to CCN counts following NPF, indicating the potential significance of this mechanism for aerosol-cloud interaction[31]. The presence of a H_2SO_4-MSA cluster in the mass spectrum suggests that concurrent MSA, as well as HIO_3 and oxygenated organics, dependent upon their abundance and volatility, may be involved in the stabilisation of clusters, and subsequent particle growth.

Our results reveal the complexity of aerosol processes in Antarctica. NPF occurs frequently when air masses blow over regions of extended sea ice marginal zone, these air masses contain elevated concentrations of alkylamines and H_2SO_4, confirming that emissions from marine plankton and sea ice melt play crucial roles in the creation of particles critical to regulation of the Antarctic climate. The novel mechanism observed here represents a highly efficient particle formation pathway, with the amine driven nucleation occurring at formation rates 1,000 times faster than that of ammonia at 278 K, even in the presence of ionising radiation, and with stabilization of H_2SO_4 clusters by amines proceeding at near the kinetic limit with negligible evaporation. Due to its high potential as an aerosol source, this mechanism should be incorporated in modelling efforts towards CCN number

estimations and aerosol-cloud interaction studies. Further observations are needed to confirm the spatial and temporal variations in alkylamine emissions and their role in NPF in and around Antarctica. Our results are demonstrative of the need of mechanistic understanding on ocean-atmosphere interactions in the pristine polar environments, and more broadly, of the aerosol processes likely to have had major roles in the pre-industrial climate.

METHODS

Ship measurements took place between 2019-01-25 and 2019-02-04 aboard the RV Hesperides, station measurements were taken aboard the Spanish research station, Juan Carlos I. Size distribution measurements were made using a NanoSMPS (TSI, USA) measuring particles 4.5-65 nm, and 10-157 nm at different periods. A condensation particle counter (CPC 3775, TSI, USA) was also run in parallel collecting total particle count ≥ 4 nm. An Aerodyne Nitrate Chemical Ionisation Atmospheric Pressure Interface Time of Flight Mass Spectrometer (CI-APi-ToF, Aerodyne, USA) was used to make measurements of neutral oxidised organic compounds, strong acids (HIO_3, H_2SO_4 etc.), and their molecular clusters at high time resolution with high resolving power. Further details regarding instrument setup and data analysis are available in the supplementary information.

Data and materials availability: Data supporting this publication are openly available from the UBIRA eData repository at https://doi.org/10.25500/edata.bham.00000400

Definitions

CCN: Cloud condensation nuclei

CI-APi-ToF: Chemical ionization atmospheric pressure interface time of flight mass spectrometer

CN: Condensation nuclei

CPC: Condensation particle counter

CS: Condensation sink

D_{50}: 50% detection limit cutoff for particle counting instrument

DMS: Dimethyl sulphide

IIC: Ion induced clustering

MSA: Methanesulphonic acid

NanoSMPS: Nano Scanning Mobility Particle Sizer

Acknowledgments

We wish to thank the Spanish Armada, and particularly the captains and crew of the BIO A-33 Hesperides, for their invaluable collaboration. We are also indebted to the UTM, and especially Miki Ojeda, for logistic and technical support on the Antarctic Spanish BAE. We also thank A. Sotomayor for help with mapping.

Funding: This study was funded by the Spanish Ministry of Economy (PI-ICE-CTM 2017–89117-R). This work was also supported by the National Centre for Atmospheric Science funded by the U.K. Natural Environment Research Council (R8/H12/83/011).

Author contributions: MDO, JB and DCSB made the field measurements. MD'O organised the campaign and the cruise. JB processed the data and led the data interpretation and produced the first draft of the paper. Further contributions to the paper were made by RMH, ZS and RS.

Competing financial interests: The authors declare no conflict of interests.

REFERENCES

1. Turner, J. *et al.* Antarctic climate change during the last 50 years. *Int. J. Climatol.* **25**, 279–294 (2005).
2. Turner, J. *et al.* Absence of 21st century warming on Antarctic Peninsula consistent with natural variability. *Nature* **535**, 411–415 (2016).
3. Siegert, M. *et al.* The Antarctic Peninsula under a 1.5°C global warming scenario. *Front. Environ. Sci.* **7**, 1–7 (2019).
4. Turton, J. V., Kirchgaessner, A., Ross, A. N. & King, J. C. The spatial distribution and temporal variability of föhn winds over the Larsen C ice shelf, Antarctica. *Q. J. R. Meteorol. Soc.* **144**, 1169–1178 (2018).
5. IPCC, 2013: Climate Change 2013. *The Physical Science Basis. Contribution of Working Group I to the Fifth Assessment Report of the Intergovernmental Panel on Climate Change*. *The physical science basis. Contribution of the Working Group 1 to the Fifth Assessment Report (AR5) of the Intergovernmental Panel on Climate Change* (Cambridge University Press, 2014).
6. Carslaw, K. S. *et al.* Large contribution of natural aerosols to uncertainty in indirect forcing. *Nature* **503**, 67–71 (2013).
7. Weller, R., Schmidt, K., Teinilä, K. & Hillamo, R. Natural new particle formation at the coastal Antarctic site Neumayer. *Atmos. Chem. Phys* **15**, 11399–11410 (2015).
8. Jang, E. *et al.* New particle formation events observed at the King Sejong Station, Antarctic Peninsula - Part 2: Link with the oceanic biological activities. *Atmos. Chem. Phys.* **19**, 7595–7608 (2019).
9. O'Dowd, C. D. *et al.* Biogenic sulphur emissions and inferred non-sea-salt-sulphate particularly during Events of new particle formation in and around Antarctica. *Atlantic* **102**, (1997).
10. Dall'Osto, M. *et al.* Antarctic sea ice region as a source of biogenic organic nitrogen in aerosols. *Sci. Rep.* **7**, 1–10 (2017).
11. Dall'Osto, M. *et al.* Simultaneous Detection of Alkylamines in the Surface Ocean and Atmosphere of the Antarctic Sympagic Environment. *ACS Earth Sp. Chem.* **3**, 854–862 (2019).
12. Lachlan-Cope, T. *et al.* On the annual variability of Antarctic aerosol size distributions at Halley research station. *Atmos. Chem. Phys.* **20**, 4461–4476 (2020).
13. Hoffmann, E. H. *et al.* An advanced modeling study on the impacts and atmospheric implications of multiphase dimethyl sulfide chemistry. *Proc. Natl. Acad. Sci. U. S. A.* **113**, 11776–11781 (2016).
14. Lee, S. H. *et al.* New Particle Formation in the Atmosphere: From Molecular Clusters to Global Climate. *J. Geophys. Res. Atmos.* (2019) doi:10.1029/2018JD029356.
15. Chen, H. & Finlayson-Pitts, B. J. New Particle Formation from Methanesulfonic Acid and Amines/Ammonia as a Function of Temperature. *Environ. Sci. Technol.* **51**, 243–252 (2017).
16. Bork, N., Elm, J., Olenius, T. & Vehkamäki, H. Methane sulfonic acid-enhanced formation of molecular clusters of sulfuric acid and dimethyl amine. *Atmos. Chem. Phys* **14**, 12023–12030 (2014).
17. Rose, C. *et al.* Observations of biogenic ion-induced cluster formation in the atmosphere. *Sci. Adv.* **4**, 5218 (2018).
18. Sipilä, M. *et al.* Molecular-scale evidence of aerosol particle formation via sequential addition of HIO3. *Nature* **537**, 532–534 (2016).
19. Jokinen, T. *et al.* Ion-induced sulfuric acid–ammonia nucleation drives particle formation in coastal Antarctica. *Sci. Adv.* **4**, eaat9744 (2018).
20. Yao, L. *et al.* Atmospheric new particle formation from sulfuric acid and amines in a Chinese megacity. *Science (80-.).* **361**, 278–281 (2018).
21. Kirkby, J. *et al.* Role of sulphuric acid, ammonia and galactic cosmic rays in atmospheric

aerosol nucleation. *Nature* **476**, 429–435 (2011).
22. Almeida, J. *et al.* Molecular understanding of sulphuric acid-amine particle nucleation in the atmosphere. *Nature* **502**, 359–363 (2013).
23. Olenius, T. *et al.* New particle formation from sulfuric acid and amines: Comparison of monomethylamine, dimethylamine, and trimethylamine. *J. Geophys. Res.* **122**, 7103–7118 (2017).
24. Kirkby, J. *et al.* Ion-induced nucleation of pure biogenic particles. *Nature* **533**, 521–526 (2016).
25. Kyrö, E.-M. *et al.* Antarctic new particle formation from continental biogenic precursors. *Atmos. Chem. Phys* **13**, 3527–3546 (2013).
26. Järvinen, E. *et al.* Seasonal cycle and modal structure of particle number size distribution at Dome C, Antarctica. *Atmos. Chem. Phys.* **13**, 7473–7487 (2013).
27. Dal Maso, M. *et al.* Formation and growth of fresh atmospheric aerosols: Eight years of aerosol size distribution data from SMEAR II, Hyytiälä, Finland. *Boreal Environ. Res.* **10**, 323–336 (2005).
28. Kupiainen, O., Ortega, I. K., Kurté, T. & Vehkamäki, H. Amine substitution into sulfuric acid-Ammonia clusters. *Atmos. Chem. Phys.* **12**, 3591–3599 (2012).
29. Kürten, A. *et al.* Neutral molecular cluster formation of sulfuric acid–dimethylamine observed in real time under atmospheric conditions. *Proc. Natl. Acad. Sci.* **111**, 15019–15024 (2014).
30. Ge, X., Wexler, A. S. & Clegg, S. L. Atmospheric amines - Part II. Thermodynamic properties and gas/particle partitioning. *Atmos. Environ.* **45**, 561–577 (2011).
31. Kim, J. *et al.* New particle formation events observed at King Sejong Station, Antarctic Peninsula - Part 1: Physical characteristics and contribution to cloud condensation nuclei. *Atmos. Chem. Phys.* **19**, 7583–7594 (2019).
32. Hodshire, A. L. *et al.* The potential role of methanesulfonic acid (MSA) in aerosol formation and growth and the associated radiative forcings. *Atmos. Chem. Phys.* **19**, 3137–3160 (2019).
33. Bianchi, F. *et al.* Highly Oxygenated Organic Molecules (HOM) from Gas-Phase Autoxidation Involving Peroxy Radicals: A Key Contributor to Atmospheric Aerosol. *Chem. Rev.* **119**, 3472–3509 (2019).
34. Mcfiggans, G. *et al.* Secondary organic aerosol reduced by mixture of atmospheric vapours. *Nature* 0–6 (2019) doi:10.1038/s41586-018-0871-y.
35. Paasonen, P. *et al.* On the formation of sulphuric acid – Amine clusters in varying atmospheric conditions and its influence on atmospheric new particle formation. *Atmos. Chem. Phys.* **12**, 9113–9133 (2012).
36. Glasoe, W. A. *et al.* Sulfuric acid nucleation: An experimental study of the effect of seven bases. *J. Geophys. Res. Atmos.* **175**, 1933–1950 (2015).
37. Ortega, I. K. *et al.* From quantum chemical formation free energies to evaporation rates. *Atmos. Chem. Phys.* **12**, 225–235 (2012).
38. Jokinen, T. *et al.* Atmospheric sulphuric acid and neutral cluster measurements using CI-APi-TOF. *Atmos. Chem. Phys.* **12**, 4117–4125 (2012).
39. Simon, M. *et al.* Detection of dimethylamine in the low pptv range using nitrate chemical ionization atmospheric pressure interface time-of-flight (CI-APi-TOF) mass spectrometry. *Atmos. Meas. Tech.* **9**, 2135–2145 (2016).
40. Brean, J. *et al.* Observations of Highly Oxidised Molecules and Particle Nucleation in the Atmosphere of Beijing. *Atmos. Chem. Phys.* **19**, 14933–14947 (2019).
41. Kulmala, M. *et al.* Measurement of the nucleation of atmospheric aerosol particles. *Nat. Protoc.* **7**, 1651–1667 (2012).
42. Korhonen, H., Kerminen, V. M., Kokkola, H. & Lehtinen, K. E. J. Estimating atmospheric nucleation rates from size distribution measurements: Analytical equations for the case of size dependent growth rates. *J. Aerosol Sci.* **69**, 13–20 (2014).
43. Nieminen, T., Lehtinen, K. E. J. & Kulmala, M. Sub-10 nm particle growth by vapor

condensation-effects of vapor molecule size and particle thermal speed. *Atmos. Chem. Phys.* **10**, 9773–9779 (2010).
44. Kurtén, T., Noppel, M., Vehkamäki, H., Salonen, M. & Kulmala, M. Quantum chemical studies of hydrate formation of H2SO4 and HSO4-. *Boreal Environ. Res.* **12**, 431–453 (2007).
45. Wang, L. Clusters of hydrated methane sulfonic acid CH3so 3H·(H2O)n (n = 1-5): A theoretical study. *J. Phys. Chem. A* **111**, 3642–3651 (2007).
46. Yli-Juuti, T. *et al.* Growth rates of nucleation mode particles in Hyytiälä during 2003-2009: Variation with particle size, season, data analysis method and ambient conditions. *Atmos. Chem. Phys.* **11**, 12865–12886 (2011).
47. Ezraty, R., Girard-Ardhuin, F., Piolle, J. F. & Heygster, L. K. G. *Arctic and Antarctic sea-ice concentration and Arctic sea ice drift estimated from Special Sensor Microwave Imager data. Version 2.1*. (Département d'Océanographie Physique et Spatiale, IFREMER, Brest, France and University of Bremen Germany, 2007).
48. Paatero, P. & Tapper, U. Positive matrix factorization: A non-negative factor model with optimal utilization of error estimates of data values. *Environmetrics* **5**, 111–126 (1994).
49. Massoli, P. *et al.* Ambient Measurements of Highly Oxidized Gas-Phase Molecules during the Southern Oxidant and Aerosol Study (SOAS) 2013. *ACS Earth Sp. Chem.* **2**, 653–672 (2018).

FIGURE LEGENDS

Figure 1: Diurnal cycles on nucleation and non-nucleation days. Panels show **(a)** SMPS contour plots with $J_{1.7}$ values overlaid, nucleation rates peaking at 11:00, **(b)** sulphuric acid and amines. Sulphuric acid reported as concentration in molecules cm^{-3}, and amines reported as ions s^{-1}, here, sulphuric acid also peaks at 11:00, and **(c)**, global radiation and temperature.

Figure 2: Evidence for sulphuric acid-amine nucleation. **(a)** Particle formation rate as a function of H_2SO_4 monomer concentration, and **(b)** H_2SO_4 dimer as a function of H_2SO_4 monomer concentration. Green circles show ambient Antarctic data where 1 data point corresponds to a single NPF event,, orange squares show the CLOUD data from experiments of H_2SO_4-DMA-H_2O nucleation[40], purple diamonds show CLOUD data from experiments of H_2SO_4-H_2O nucleation, pink triangles show CLOUD data from experiments of H_2SO_4-NH_3-H_2O nucleation[26], and the dashed line shows theoretical concentration of H_2SO_4 dimer produced due to ion induced clustering in the CI-APi-ToF ionisation inlet[24]. All chamber data is recorded at 278 K and 38% RH under GCR conditions, except H_2SO_4-DMA-H_2O data, which includes both GCR and neutral data. Error bars represent systematic uncertainties on data. Panel **(c)** shows the mass defect plot before, and during nucleation. Mass defect is defined as the deviation of a peak from the nearest integer mass.

Figure 3: Association between sea ice extent and new particle formation. (a) Clustered 96 hour back trajectories for station measurements, lighter traces showing the unclustered trajectories, (**b**) The association of each back trajectory cluster with regions of sea ice, (**c**) the percentage of NPF events associated with each of these back trajectory clusters, and **(d, e)** box plots showing concentrations and signals per cluster for H_2SO_4, and C_2 & C_4 alkylamines, as measured by the CI-APi-ToF.

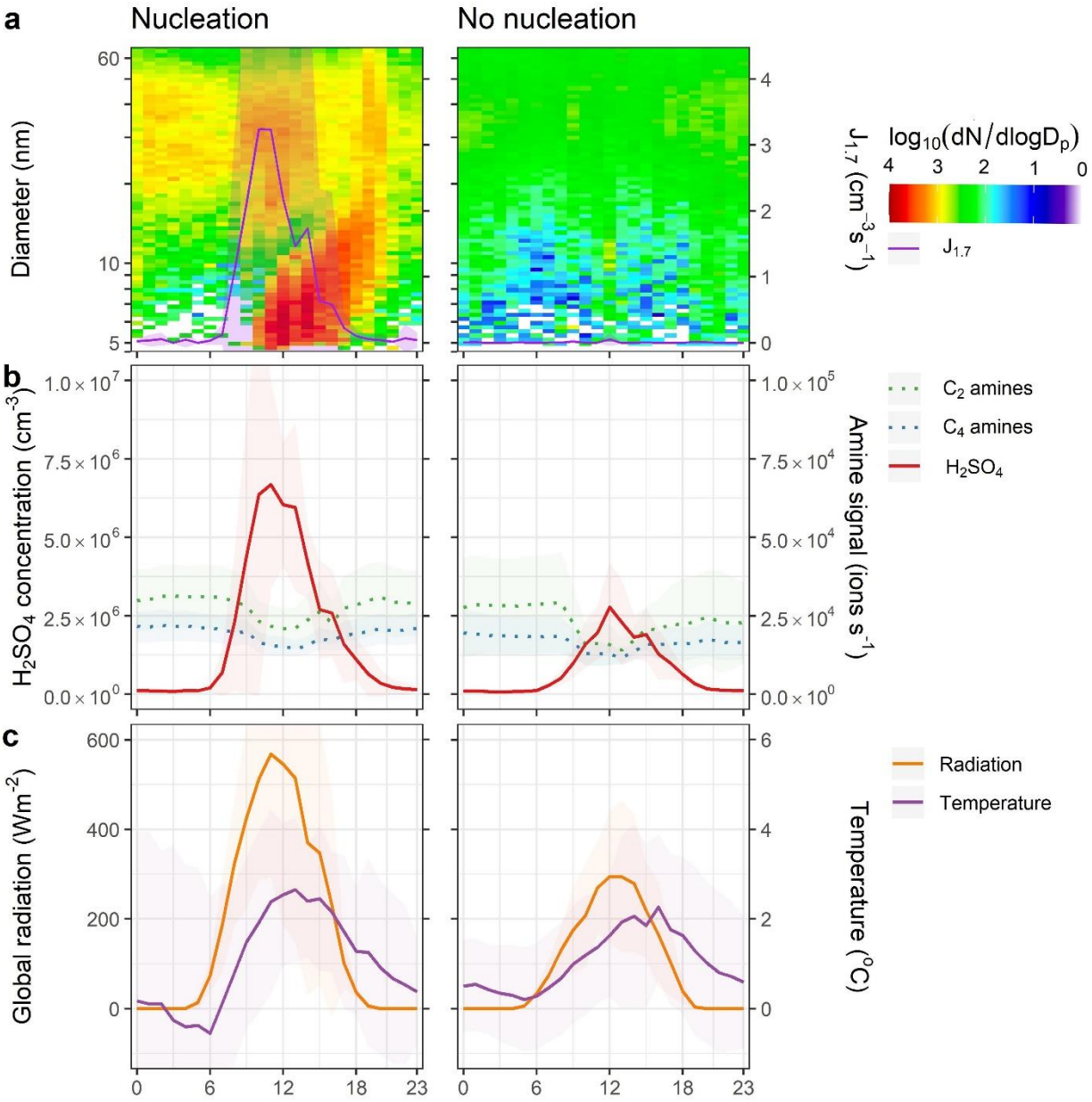

Figure 1: Diurnal cycles on nucleation and non-nucleation days. Shaded regions show 95% confidence intervals on the mean, and do not represent systematic measurement errors. Panels show **(a)** SMPS contour plots with $J_{1.7}$ values overlaid, nucleation rates peaking at 11:00, **(b)** sulphuric acid and amines. Sulphuric acid reported as concentration in molecules cm^{-3}, and amines reported as ions s^{-1}, here, sulphuric acid also peaks at 11:00, and **(c)**, global radiation and temperature.

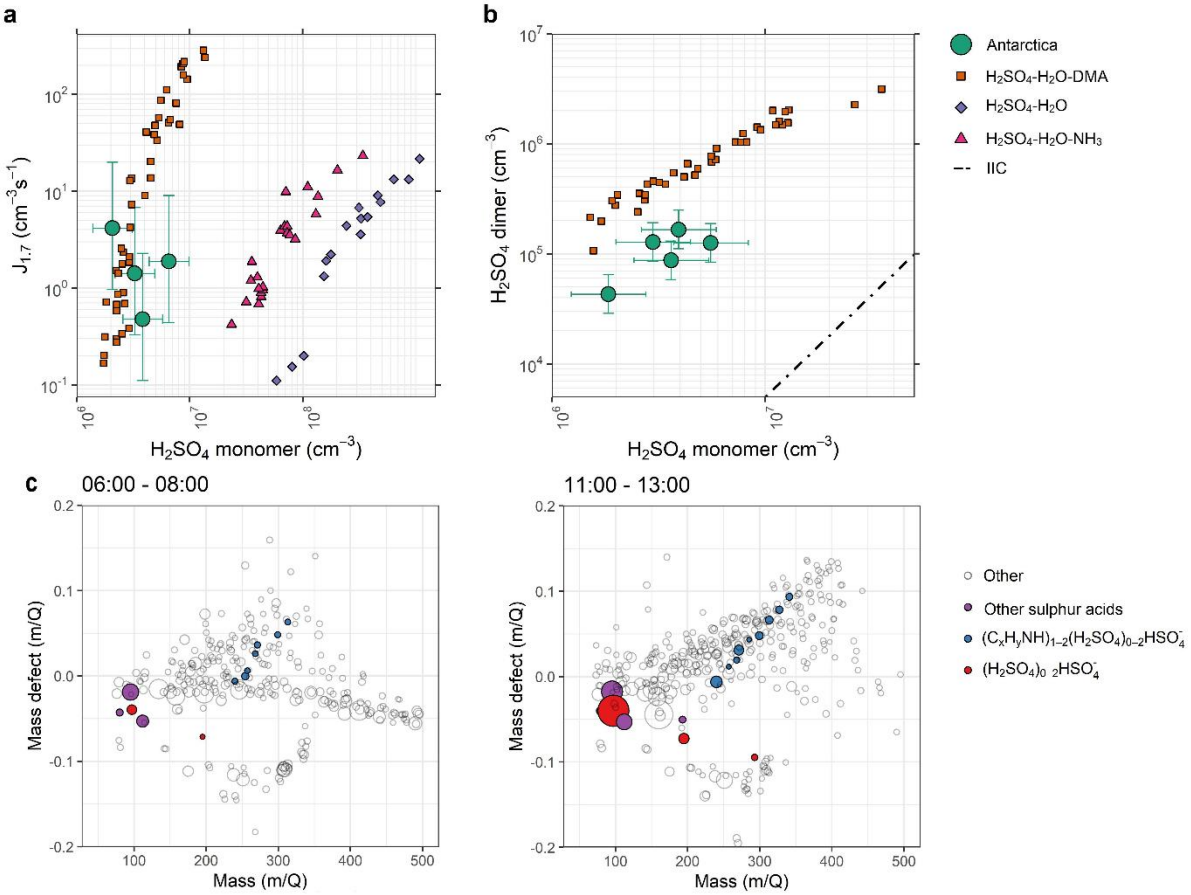

Figure 2: Evidence for sulphuric acid-amine nucleation. **(a)** Particle formation rate as a function of H_2SO_4 monomer concentration, and **(b)** H_2SO_4 dimer as a function of H_2SO_4 monomer concentration. Green circles show ambient Antarctic data where 1 data point corresponds to a single NPF event, orange squares show the CLOUD data from experiments of H_2SO_4-DMA-H_2O nucleation[40], purple diamonds show CLOUD data from experiments of H_2SO_4-H_2O nucleation, pink triangles show CLOUD data from experiments of H_2SO_4-NH_3-H_2O nucleation[26], and the dashed line shows theoretical concentration of H_2SO_4 dimer produced due to ion induced clustering in the CI-APi-ToF ionisation inlet[24]. All chamber data is recorded at 278 K and 38% RH under GCR conditions, except H_2SO_4-DMA-H_2O data, which includes both GCR and neutral data. Error bars represent systematic uncertainties on data. Panel **(c)** shows the mass defect plot before and during nucleation. Mass defect is defined as the deviation of a peak from the nearest integer mass.

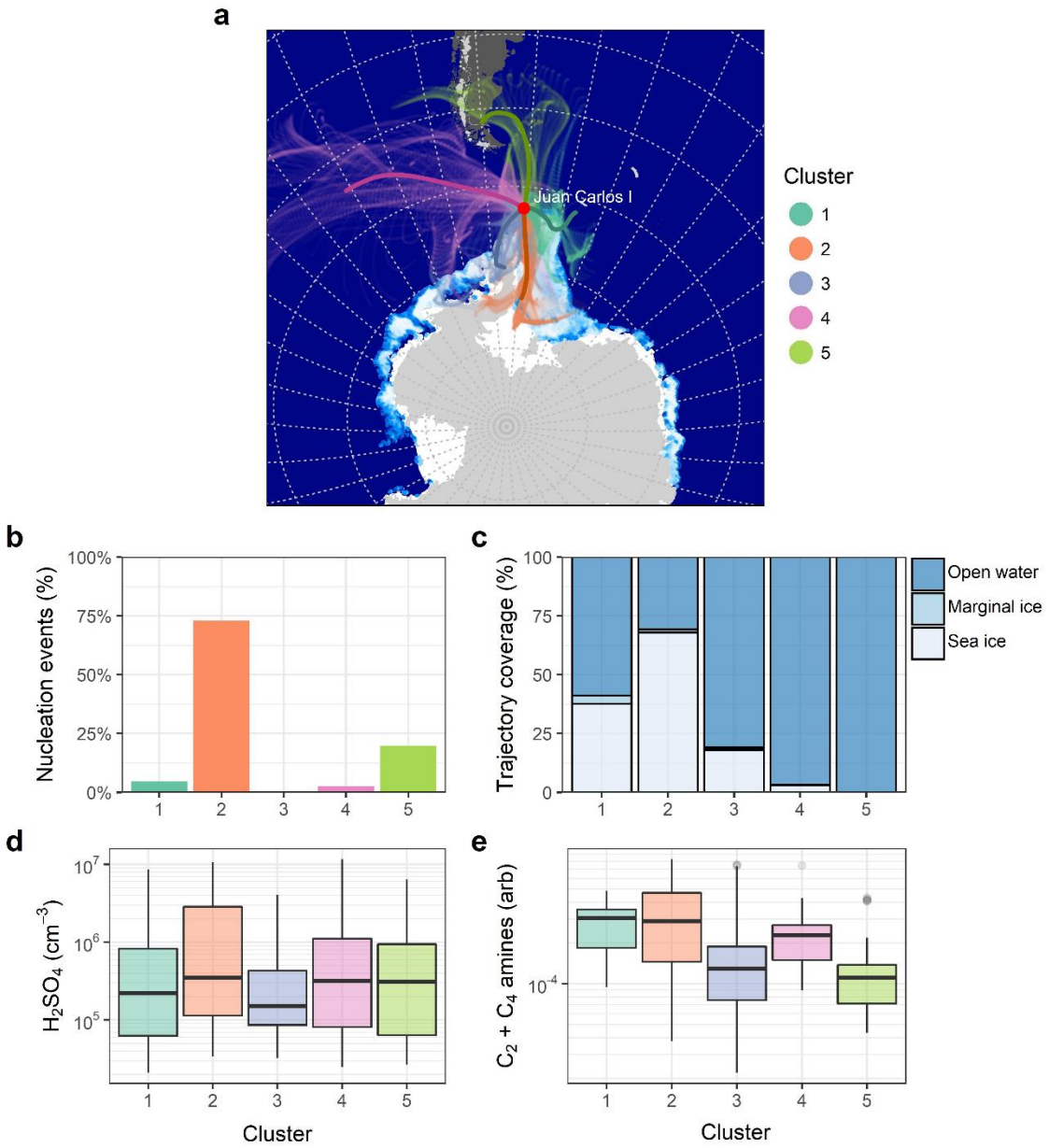

Figure 3: Association between sea ice extent and new particle formation. (a) Clustered 96 hour HYSPLIT back trajectories for station measurements, lighter traces showing the unclustered trajectories, (**b**) the percentage of NPF events associated with each of these back trajectory clusters, (**c**) The association of each back trajectory cluster with regions of sea ice, where 0-20 % sea ice coverage is "open water", 20-80 % sea ice coverage is "marginal ice", and >80 % sea ice coverage is "sea ice", and **(d, e)** box plots showing concentrations and signals per cluster for H_2SO_4, and C_2 & C_4 alkylamines, as measured by the CI-APi-ToF.

Supplementary Information

OPEN OCEAN AND COASTAL NEW PARTICLE FORMATION FROM SULPHURIC ACID AND AMINES AROUND THE ANTARCTIC PENINSULA

METHODS

Field site. Ship measurements took place between 2019-01-25 and 2019-02-04 aboard the RV Hesperides. The cruise began at the South Shetland Islands (around -63º latitude), sailing down to -68º latitude across several days to Adelaide Island, and then back through to the South Shetland Islands. Frequent ship plume related particle events were seen, and these have been filtered out based on the size distributions and particle concentrations seen (Figure S7). Ground measurements took place between 2019-02-12 and 2019-03-13 at the Spanish research station, Juan Carlos I (-62.66, -60.39). The station is located directly on the coast on the south of Livingston Island in the South Shetland Islands. All measurements were taken approximately 100 meters from the main station at a height of 1 meter, with occasional pollution seen in the SMPS spectra from vehicles, generators, or waste incineration. These spectra have been filtered from the dataset (Figure S6). The same instruments were deployed both on the cruise and aboard the ship.

Instrumental setup. The Aerodyne Nitrate Chemical Ionisation Atmospheric Pressure Interface Time of Flight Mass Spectrometer (CI-APi-ToF) was used to make measurements of neutral oxidised organic compounds, strong acids (HIO_3, H_2SO_4 etc.), and their molecular clusters at high time resolution with high resolving power. The ionization system charges molecules by adduct formation, such as in the case of organic compounds with two or more hydrogen bond donor groups, or proton transfer in the case of strong acids like H_2SO_4. Hydroxyl or hydroperoxyl functionalities are both common hydrogen bond donating groups.. This instrument has been explained in great detail elsewhere[38], but briefly, the front end consists of a chemical ionisation system where a 15 LPM sample flow is drawn in through the 1 metre length 1" OD stainless steel tubing opening. A secondary flow is run parallel and concentric to this sample flow, rendering the reaction chamber effectively wall-less. A 3 SCCM flow of a carrier gas (N_2) is passed over a reservoir of liquid HNO_3, entraining vapour which is subsequently ionised to NO_3^- via an X-ray source. Ions are then guided into the sample flow. The nitrate ions will then charge molecules either

by clustering or proton transfer. The mixed flows travelling at 15 LPM enter the critical orifice at the front end of the instrument at 0.8 LPM and are guided through a series of differentially pumped chambers before reaching the ToF analyser. Two of these chambers contain quadrupoles which focus the ion beam and can be used to select greater sensitivity for certain mass ranges, and the voltages across each individual chamber can be tuned to maximise sensitivity and resolution for ions of interest. All data analysis was carried out in the Tofware package (Tofwerk AG, Switzerland) in Igor Pro 7 (Wavemetrics Inc., USA). Normalization was performed using signals for NO_3^-, $H_2ONO_3^-$, $HNO_3NO_3^-$, and $(HNO_3)_2NO_3^-$, corresponding to the ionised nitric acid monomer, nitric acid monomer-water cluster, nitric acid dimer and nitric acid trimer, respectively. Signals were normalised by the sum of all these ions except for the amine signals, which were normalised by the nitrate trimer[39]. Our data have been treated with a calibration coefficient of 10^{10} cm^{-3}, based upon an earlier calibration[40], and presented with a systematic uncertainty of +50%/-33%, in line with other publications. No calibration was applied to the amine data, as calibrations and sensitivities are not currently well constrained. Peak fits and correlations of amines and ammonia in its two measured forms (clustered with the nitrate dimer and trimer) are plotted in Figure S9.

A Nano Scanning Mobility Particle Sizer (NanoSMPS) instrument measured particle size distributions at five minute time resolution. The NanoSMPS consists of the 3082 EC, 3085 Nano DMA, and 3776 CPC (TSI, USA). This measures the size ranges 10-157 nm, and 4.5-65 nm at two periods on the station, and 10-157 nm aboard the ship. A condensation particle counter (CPC 3775, TSI, USA) was also run in parallel collecting total particle count ≥ 4 nm.

Formation rates

The formation rate of new particles at size d_p is calculated as follows:

$$J_{d_p} = \frac{dN_{d_p}}{dt} + CoagS_{d_p} . N_{d_p} + \frac{GR}{\Delta d_p} . N_{d_p} \quad (2)$$

Where the first term on the right-hand side comprises the rate at which particles enter the size d_p, and the latter two terms represent losses from this size by coagulation and growth, respectively. See ref. 41 for more information on calculation of coagulation sinks, growth rates, and formation rates. From our $J_{4.5}$ values, we calculated $J_{1.7}$ using the equation of Korhonen et al., (2014)[42].

$$J_{1.7\,(t)} = J_{x\,(\Delta t+t)} \cdot \exp\left(\frac{CoagS_{d_{p1.7}}}{GR_{1.7}} \cdot d_{p1.7} \cdot \gamma\right) \quad (3)$$

where $J_{1.7}$ is the formation rate to be calculated at 1.7 nm , $CoagS_{dp1.7}$ is the coagulation sink at that size, $GR_{1.7}$ is the growth rate between 1.7 nm and 4.5 nm, J_x is the original particle formation rate, and Δt is determined using a time-delay method using sulphuric acid. γ is a factor defined as

$$\gamma = \frac{1}{m-n+1}\left[\left(\frac{d_{pX}}{d_{p1.7}}\right)^{m-n+1} - 1\right] \quad (4)$$

Where m is a coefficient describing the slope of coagulation sink with diameter, dependent upon the background particle population

$$m = \frac{log\left(CoagS_{d_{px}}/CoagS_{d_{p1.7}}\right)}{log\left(d_{px}/d_{p1.7}\right)} \quad (5)$$

and n is dependent upon the slope of the growth rate (GR) with diameter

$$n = \frac{log\left(GR_{d_{px}}/GR_{d_{p1.7}}\right)}{log\left(d_{px}/d_{p1.7}\right)} \quad (6)$$

Systematic uncertainties on our calculated values of $J_{1.7}$ include a factor of +100% / -50% on the calculated growth rates, a factor of ±25% on dp of the NanoSMPS, and ±50% on the established losses due to condensation sink.

Growth rate

The growth rate of new particles is defined as

$$GR = \frac{ddp}{dt} \quad (7)$$

Two methods to determine the GR of particles were employed here. The first was growth rates determined from the lognormal distribution function method outlined in ref. 41, wherein a

lognormal distribution function was fitted to the new mode of particles. The increase to the geometric mean of the diameter of this mode over time, once corrected for coagulation effects, gives the condensational growth rate. Secondly, as equation 3 requires growth rates from the critical diameter upwards (here presumed 1.7 nm, but is typically estimated 1.5 ± 0.4 nm), we calculated theoretical growth rates due to both H_2SO_4 condensation, and condensation of H_2SO_4, MSA, and HIO_3 through the method of Nieminen et al., 2010[43]. At our measured relative humidity, sulphuric acid favours binding to 3 H_2O molecules[44]. As amine concentrations are likely limited, we presume no mass from amines in the condensing species. For simplicity, the properties of MSA regarding density and hydration[45] were presumed the same as H_2SO_4, whereas HIO_3 was presumed the same, with enhanced density[18].

Calculated rates per day are shown in Figure S10. Measured growth of particles in the range 5-10 nm is within error for both sets of calculations. As the efficiency of condensation of MSA onto particles of size 1.7 nm has not been studied in detail, we utilise our calculations of condensation due to H_2SO_4 for our calculations of $J_{1.7}$. GRs from both size ranges were then input into our formation rate calculations. Calculated growth rates are presented with errors of +100%/-50%[43], and growth rates fitted to SMPS data given an error of ±50% (±25% from fitting, ±25% from instrument errors[46].

Condensation sink

The condensation sink (CS) represents the rate at which a vapour phase molecule will collide with pre-existing particle surface, and was calculated from the size distribution data as follows[41]:

$$CS = 2\pi D \sum_{d_p} \beta_{m,d_p} d_p N_{d_p} , \quad (8)$$

where D is the diffusion coefficient of the diffusing vapour (assumed H_2SO_4), β_m is a transition regime correction, d_p is particle diameter, and N_{dp} is the number of particles at diameter d_p.

Back trajectories and sea ice extent

The NOAA HYSPLIT model was used to calculate 4 day back-trajectories for air masses arriving at the sampling sites. Each back-trajectory data point was assigned to sea ice concentration percentage on a 12.5 km grid from microwave satellite data, providing a sea ice concentration from 0 – 100% (5% width)[47]. These air masses were then clustered using an angle-based distance matrix to produce the 5 back trajectory clusters.

Positive matrix factorisation

Positive matrix factorisation (PMF) was applied to our Nitrate CI-APi-ToF data to identify contaminants. Analyses were performed using the PMF2 algorithm in robust mode[48] using a data matrix of 304 high resolution peaks across 1 week of data at 10 minute time resolution (1000 data points). The error matrix was generated according to Poisson counting statistics as follows[49]

$$\sigma_{ij} = \sqrt{I/t_s} \quad (9)$$

Where I is the ion signal and t_s is the time for integration. After an initial run, an 8 factor solution was chosen. To produce a final 8 factor solution, those species with large scaled residuals (21 of our peaks) had their uncertainties scaled by a factor of 10, and the uncertainties of the rest of the data matrix was scaled by a factor of 1.06, producing a Q/Qexp value of 1.004.

Figure S3 shows the PMF solution for 8 factors. Factors 1 & 2 relate to daytime photochemistry, the latter containing dicarboxylic acids of marine origin, and the former corresponding to daytime oxidation of DMS and VOCs. Due to the mass range selected, deprotonated MSA and H_2SO_4 are not included, but their clusters with NO_3^-, and with other species (MSA-HSO_4^- cluster, HSO_4^- amine clusters etc) are. Contaminant peaks as identified below are absent in these factors, and the dominant wind direction was from the north (the station was located to the south-east) confirming the absence of contaminants in our analysis of nucleation mechanisms, and confirm the role of marine air masses in the production of sulphuric acid, methanesulphonic acid, and oxygenated organics.

The remaining factors belonged to contaminants from either station activities, or from instrument contamination. Most of these factors comprised of just a few large peaks, and thus we identify several contaminant ions through this method. Contaminants arose partially from a narrow wind sector from the station, with factors 3, 4, & 5 being associated with a narrow south easterly air mass band, containing emissions from the nearby station (~250 m distance). Dicarboxylic acids such as the $C_4H_4O_4$-NO_3^- ion, which may be fumaric acid, a food additive, is found in factor 3, and factor 5 contains brominated organic compounds at 305 – 311 m/Q. Other contaminants arose from within the instrument, with factors 6, 7 & 8 containing fluorinated organic compounds, arising from the tubing within the instrument.

Table 1: Nucleation statistics per event. GR_{SMPS} corresponds to measured GRs from the NanoSMPS data, GR_{Acids} corresponds to growth rates from H_2SO_4, MSA and HIO_3, and GR_{H2SO4} corresponds to growth from H_2SO_4 condensation.

Date	H_2SO_4 (10^6 cm^{-3})	J_5 ($cm^{-3}s^{-1}$)	$J_{1.7}$ ($cm^{-3}s^{-1}$)	$GR_{4.8\text{-}10SMPS}$ (nm h^{-1})	$GR_{4.8\text{-}10Acids}$ (nm h^{-1})	$GR_{4.8\text{-}10H2SO4}$ (nm h^{-1})	$GR_{1.7\text{-}4.8H2SO4}$ (nm h^{-1})	Tempera (°C)
21/02/2019	5.84	0.36	1.64	0.58	0.71	0.33	0.42	1.35
22/02/2019	3.67	0.10	0.40	0.55	0.75	0.25	0.33	1.32
28/02/2019	3.04	0.21	1.21	0.41	0.87	0.30	0.39	0.16
05/03/2019	2.00	0.24	3.07	0.41	0.56	0.22	0.28	3.5

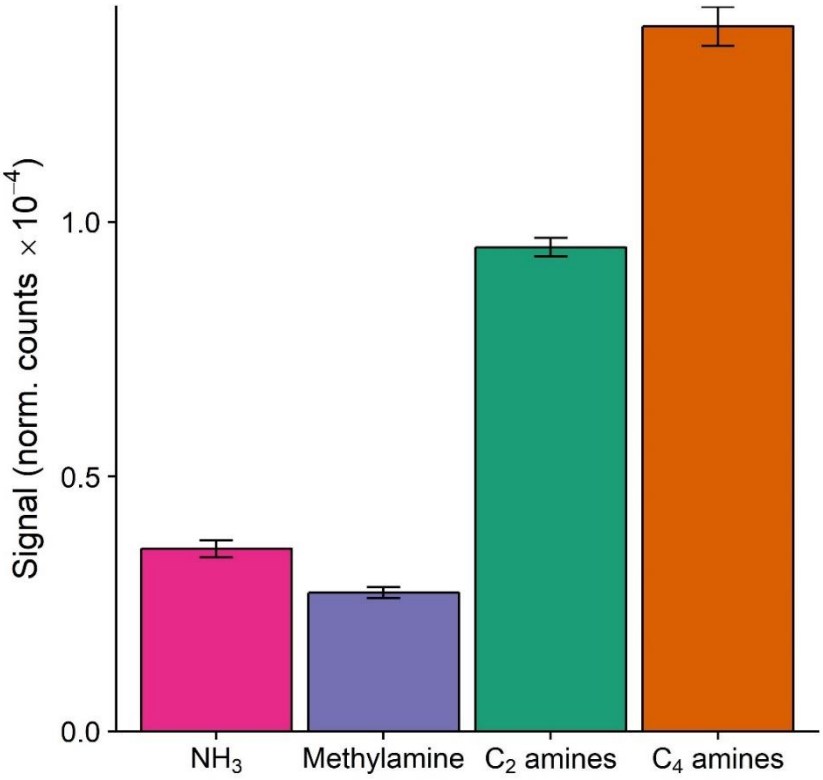

144

145 **Figure S1: Mean ion signals for ammonia and amines**. Data is of station measurements; units are
146 normalised counts. Amine and ammonia ion signals have been normalised to the nitrate trimer
147 counts.
148

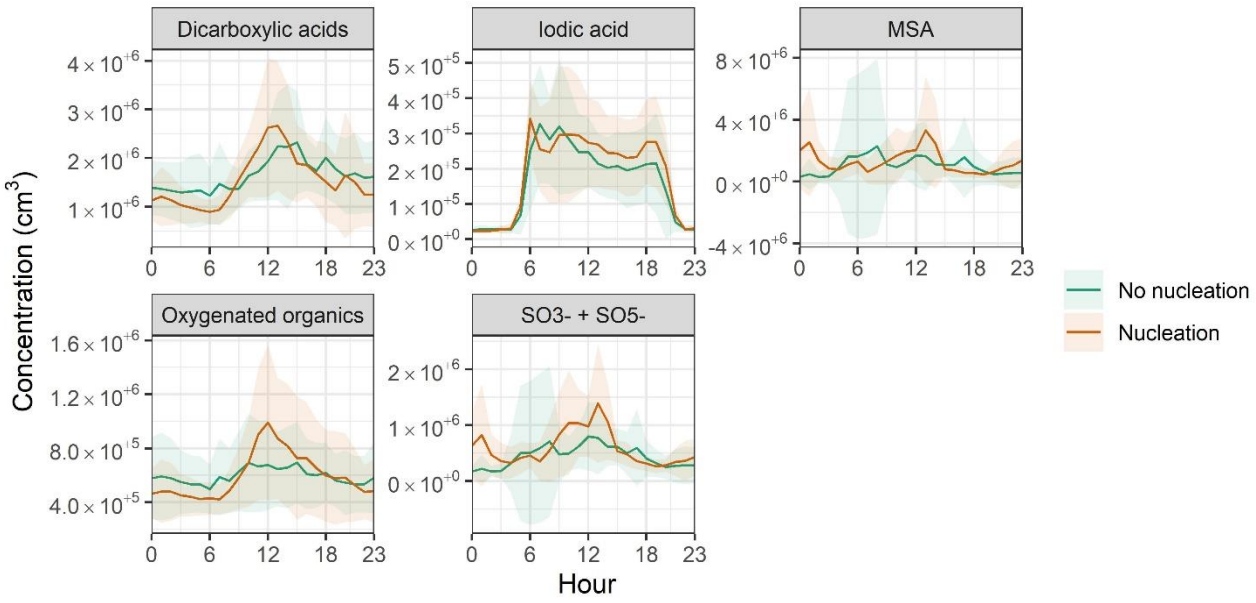

149
150 **Figure S2: Diurnal cycles of ions for station measurements**. In order, dicarboxylic acids, iodic
151 acid, methanesulphonic acid, oxygenated organics, containing C_5 and C_6 oxygenated organics, and
152 SO_3^- and SO_5^- ions. Shaded regions show 95% confidence regions on the mean**.**
153

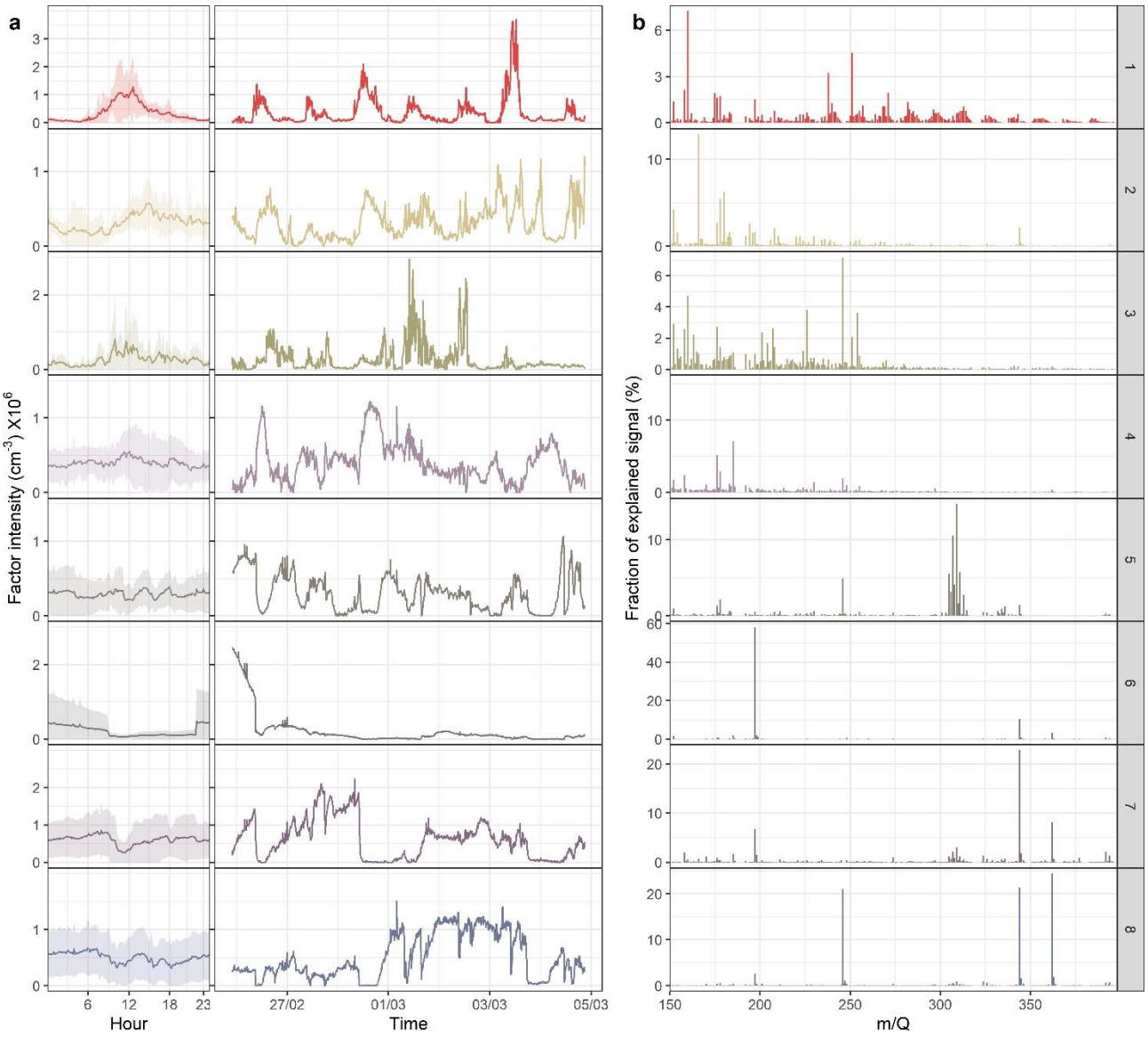

Figure S3: NO_3^- CI-APi-ToF PMF results for 8 factors, showing **(a)** diurnals and time series, where shaded region shows 1 standard deviation on the mean, and **(b)** mass spectra per factor. Data included 300 peaks between 150 – 400 m/Q for 1 week of CI-APi-ToF data. Q/Q_{exp} for this solution = 1.004.

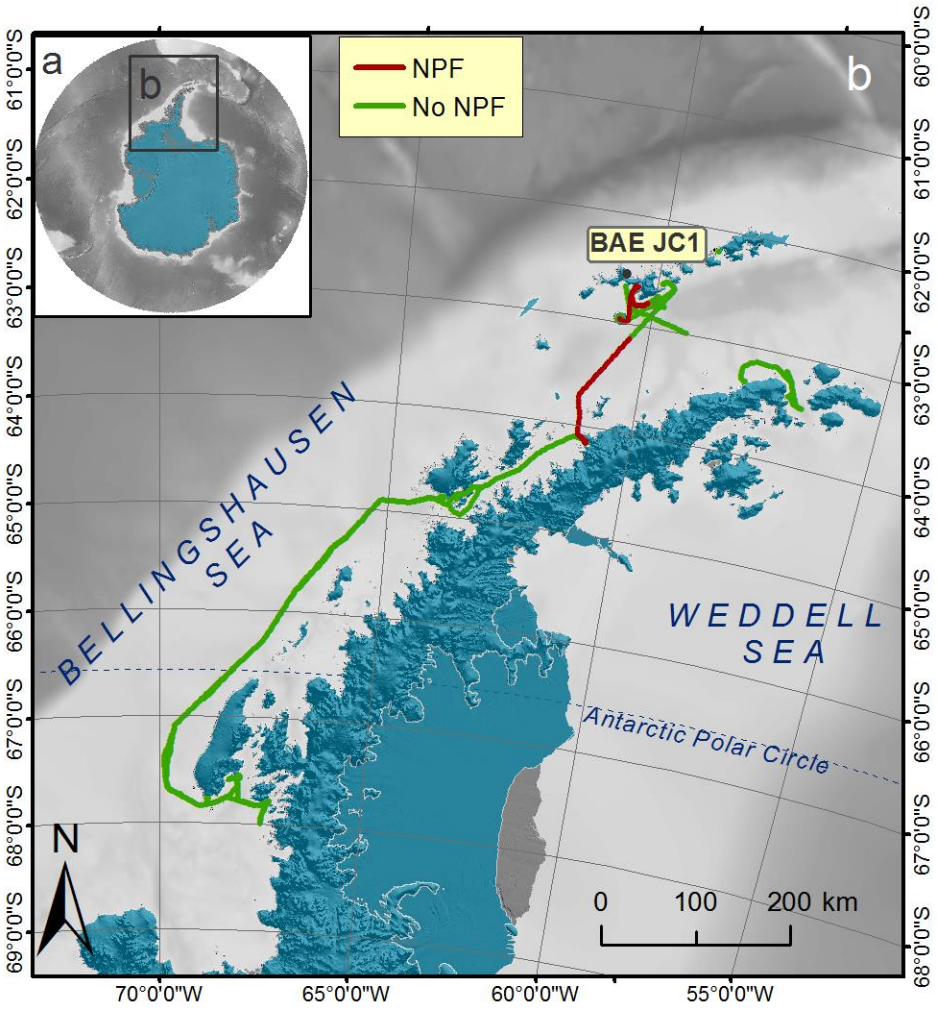

160

161 **Figure S4: Measurement locations**, showing the measurement site **(a)** within Antarctica, and **(b)**
162 within the Antarctic peninsula. BAE JC1 is the location for station measurements, and the coloured
163 line shows the ship track, where red signifies that an NPF event was occurring.
164

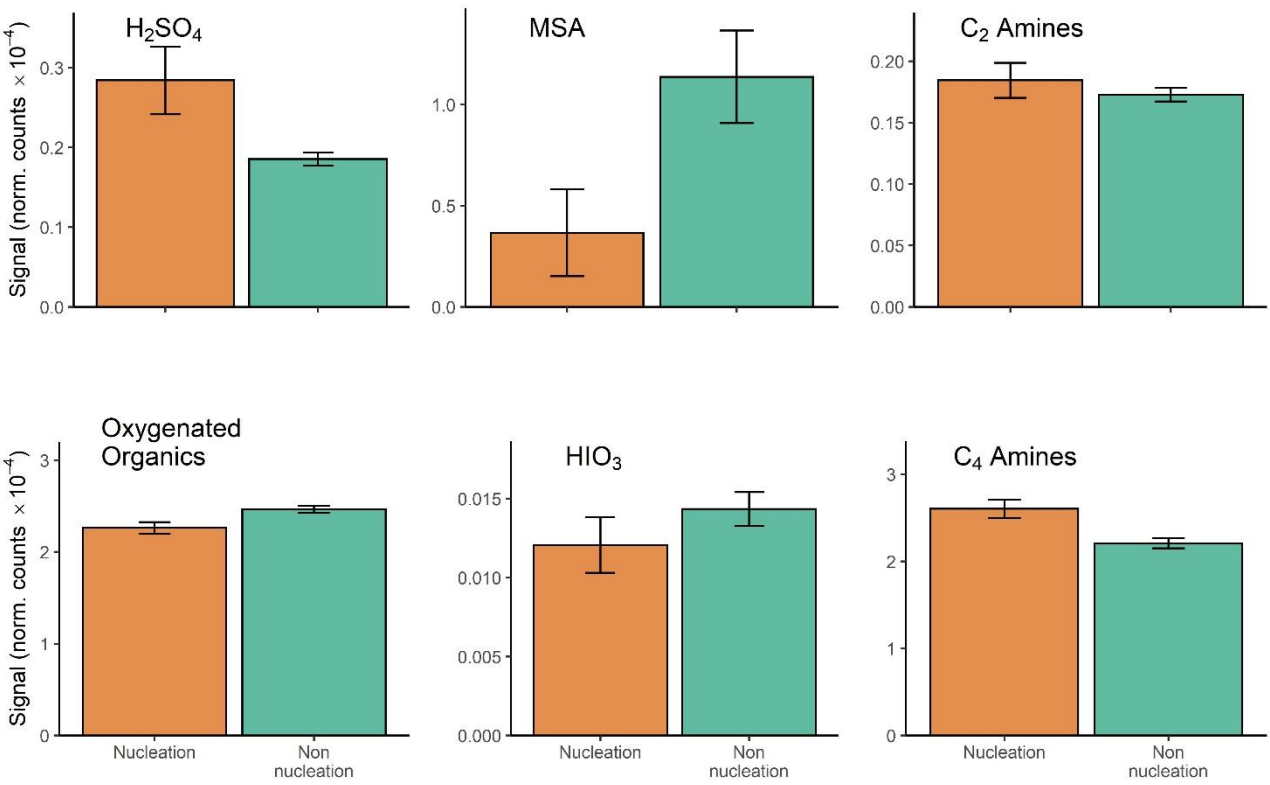

Figure S5: Potential new particle sources during nucleation and non-nucleation periods during cruise. Signals of gas phase H_2SO_4, MSA, HIO_3, oxygenated organic molecules, C_2 amines, and C_4 amines. "Nucleation" refers to periods where NPF was actively occurring (presuming a 0.5 nm h^{-1} growth rate below 4.5 nm), "Non nucleation" refers to the rest of the measurement period. Error bars represent 1 standard error on measured values.

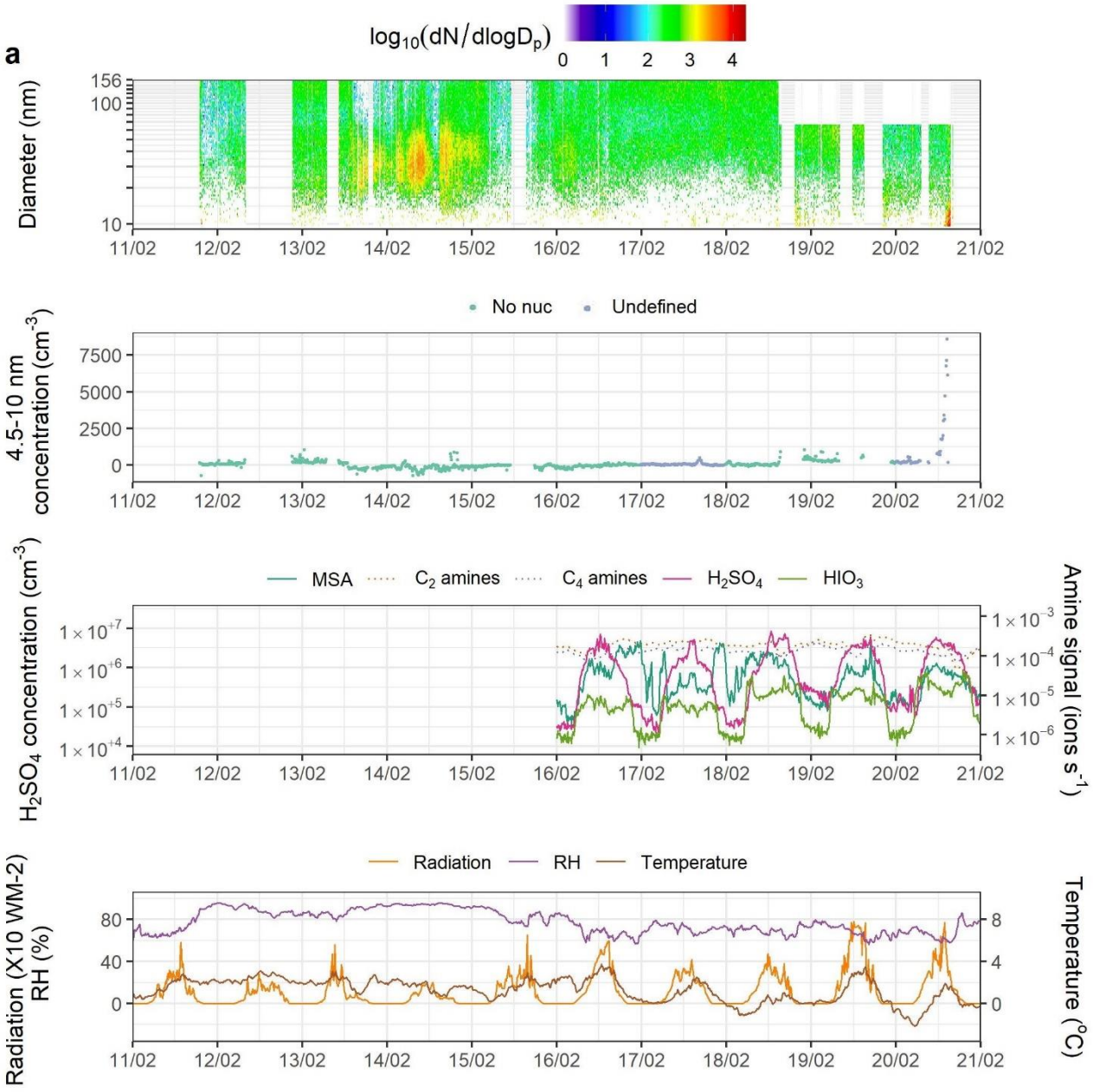
a
log10(dN/dlogDp)
0 1 2 3 4
Diameter (nm)
156
100
10
11/02 12/02 13/02 14/02 15/02 16/02 17/02 18/02 19/02 20/02 21/02
No nuc
Undefined
4.5-10 nm concentration (cm-3)
7500
5000
2500
0
MSA
C2 amines
C4 amines
H2SO4
HIO3
H2SO4 concentration (cm-3)
1×10+7
1×10+6
1×10+5
1×10+4
Amine signal (ions s-1)
1×10-3
1×10-4
1×10-5
1×10-6
Radiation
RH
Temperature
Radiation (X10 WM-2)
RH (%)
80
40
0
Temperature (°C)
8
4
0

174

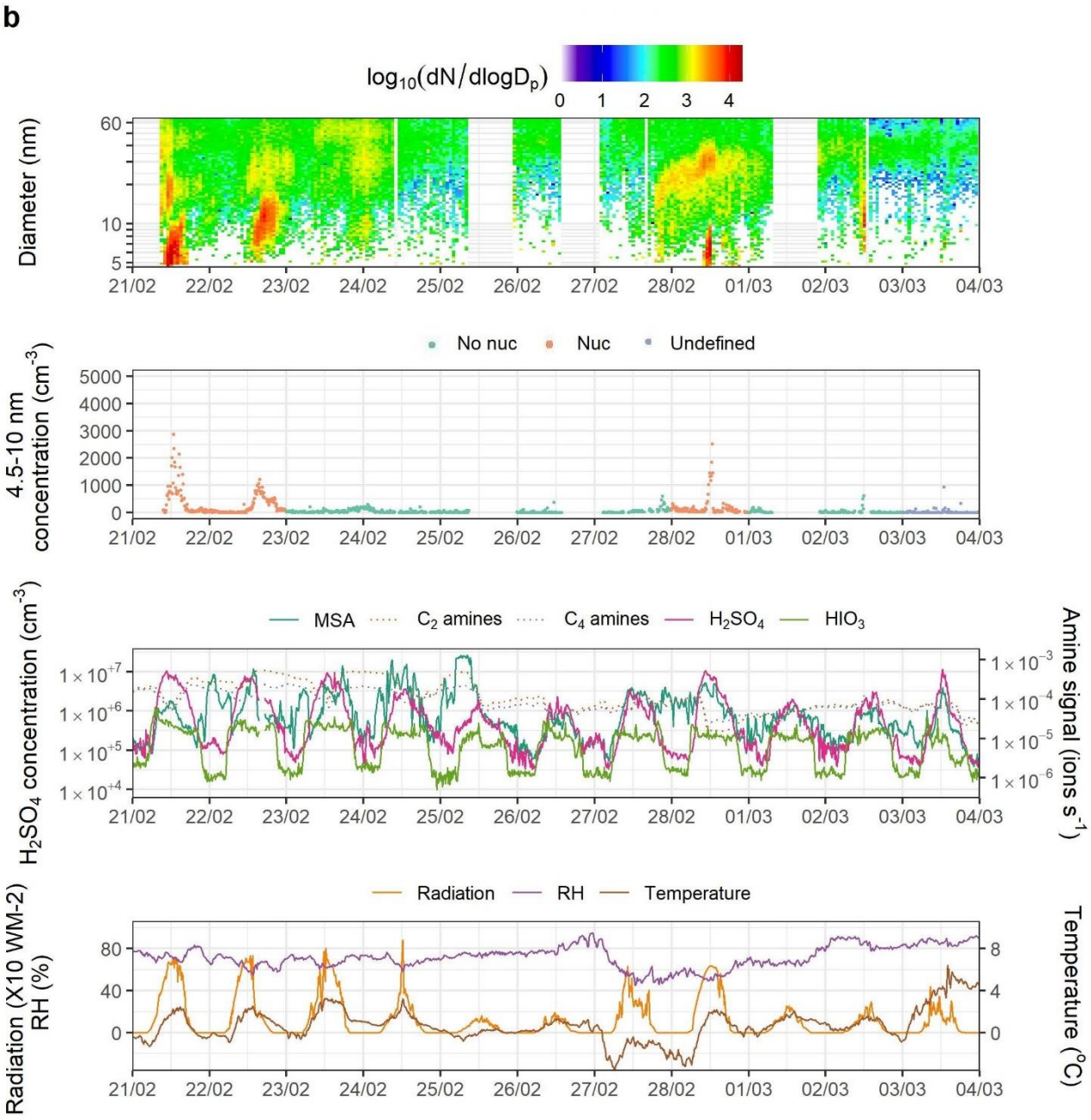
b
log10(dN/dlogDp)
0 1 2 3 4
Diameter (nm)
60
10
5
21/02 22/02 23/02 24/02 25/02 26/02 27/02 28/02 01/03 02/03 03/03 04/03
No nuc
Nuc
Undefined
4.5-10 nm concentration (cm-3)
5000
4000
3000
2000
1000
0
H2SO4 concentration (cm-3)
MSA
C2 amines
C4 amines
H2SO4
HIO3
Amine signal (ions s-1)
Radiation
RH
Temperature
Radiation (X10 WM-2) RH (%)
Temperature (°C)

175

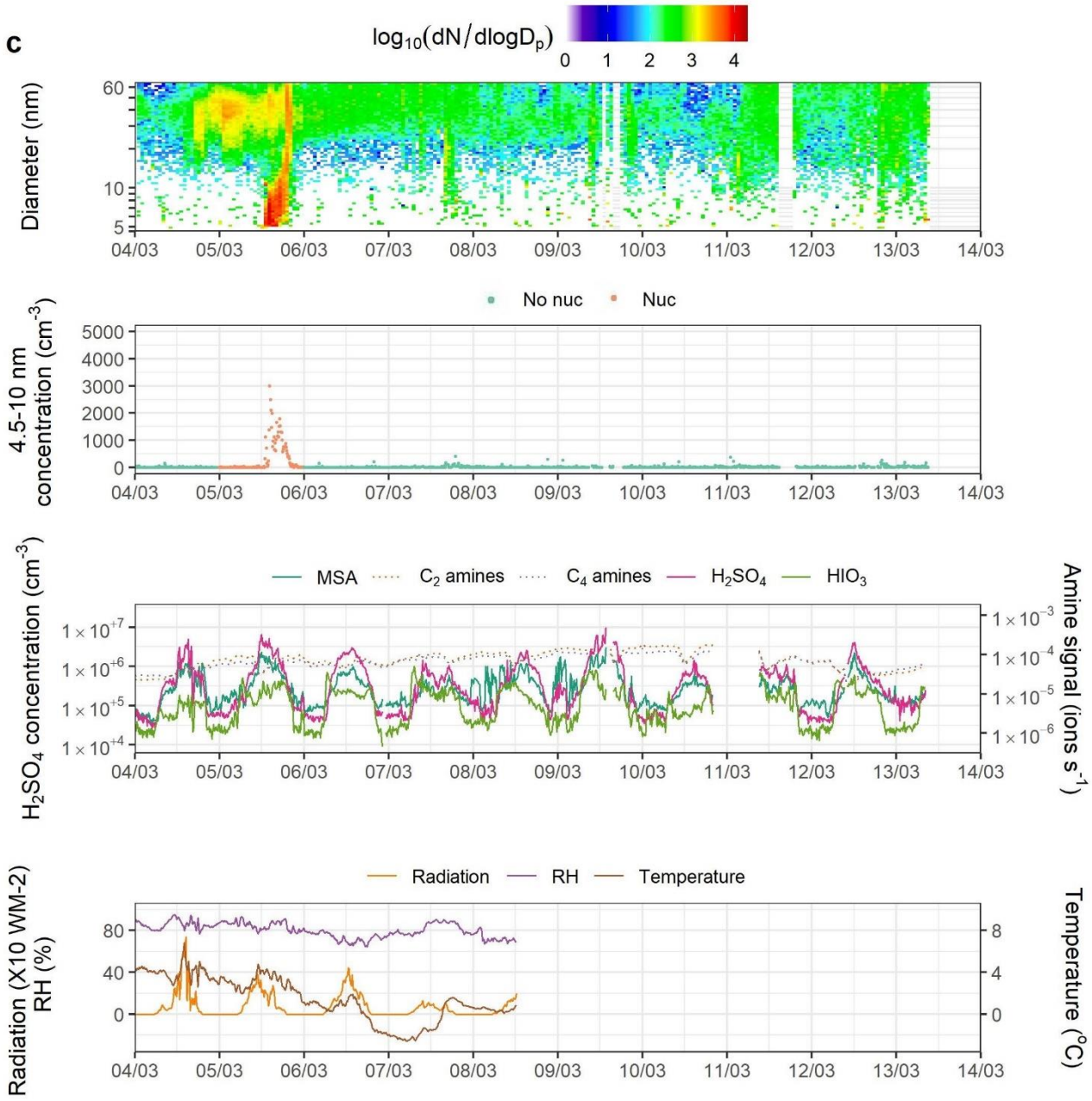

Figure S6: Time series of data during the station measurements, showing SMPS data, 4.5-10 nm particle counts, H_2SO_4, MSA and HIO_3, amines, global radiation, relative humidity, and temperature for three different sections of data. 4.5-10 nm particle count is classified as **(a)** difference between low-flow SMPS and CPC data, and **(b,c)** lower bins of the NanoSMPS. Data have been manually filtered for pollution arising from the nearby station.

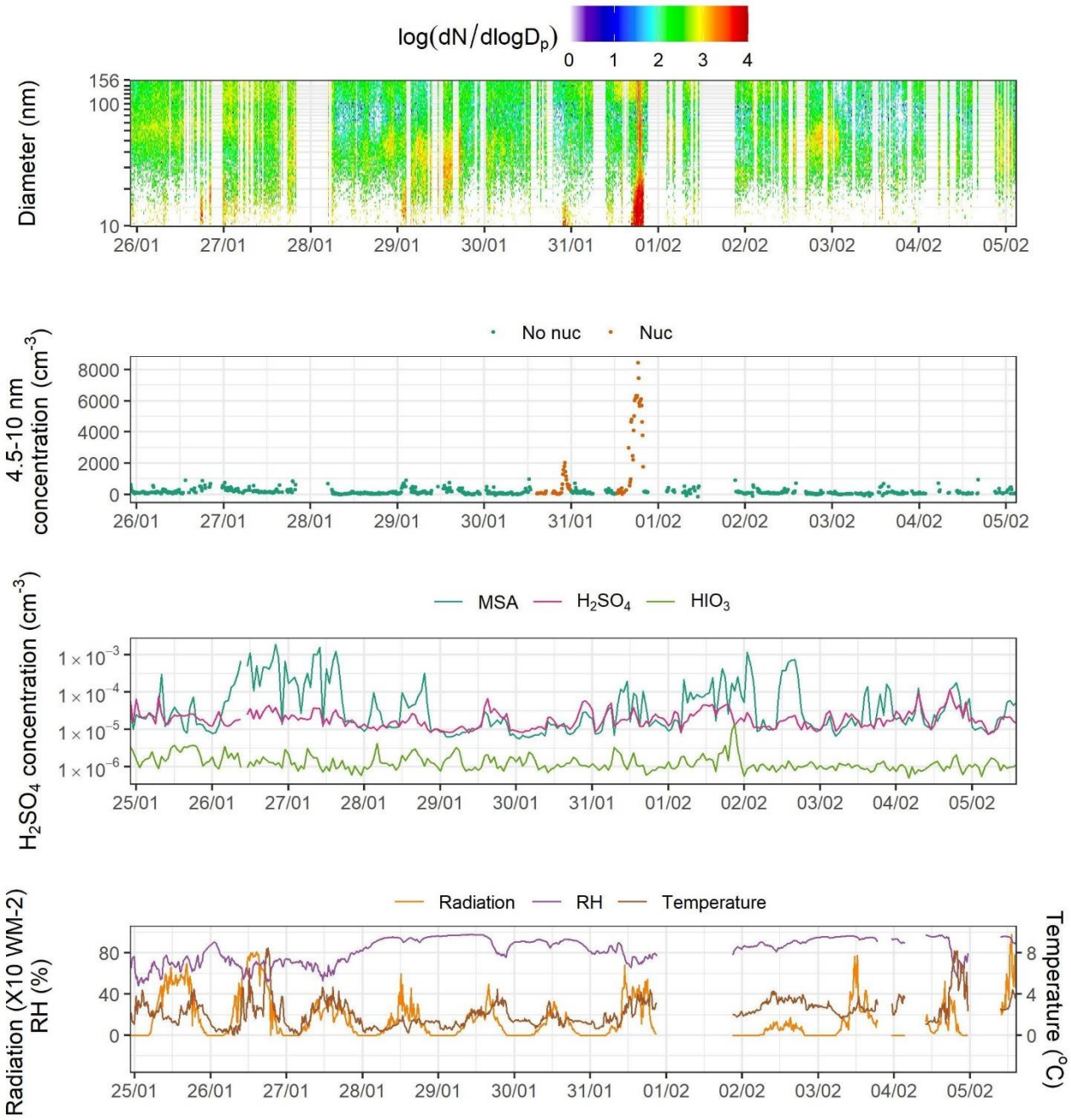

Figure S7: Time series of data during the cruise measurements, showing SMPS data, 4.5-10 nm particle counts, H_2SO_4, MSA and HIO_3, amines, global radiation, relative humidity, and temperature for three different sections of data. 4.5-10 nm particle count is classified as difference between low-flow SMPS and CPC data. Ship plumes have been manually filtered out of the SMPS data.

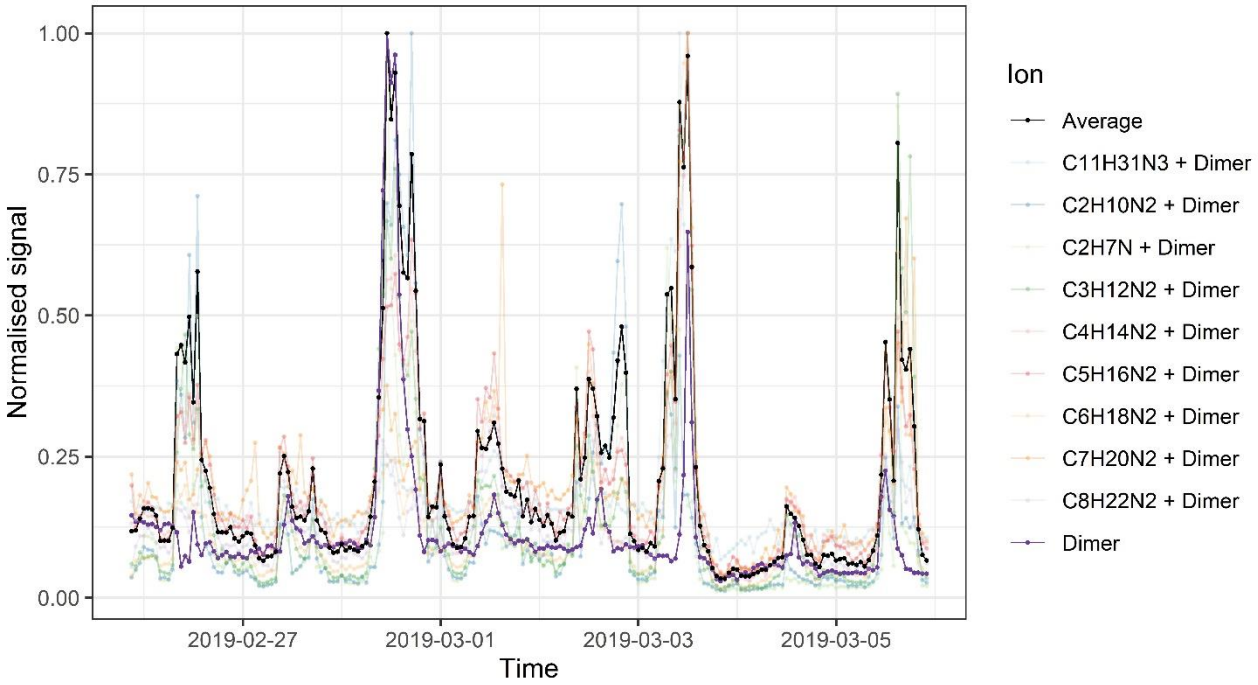

Figure S8: Selected time series of a series of sulphuric acid dimer-amine peaks. Signals for this period have been normalised to a maximum of 1. Purple line shows the sulphuric acid dimer for comparison, and the black line shows the average of all these dimer peaks. Nucleation events occurred on 28/02 and 05/03.

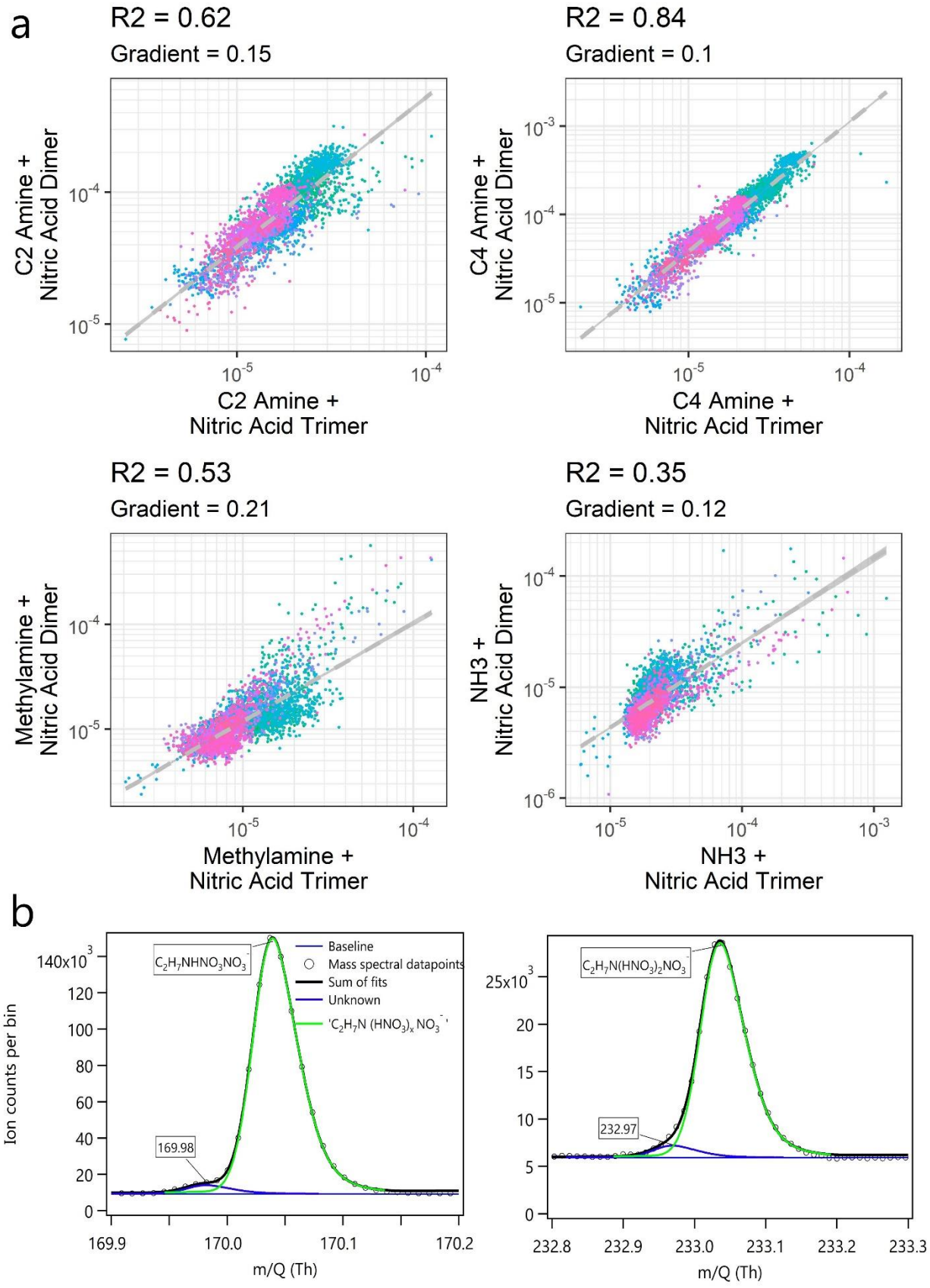

Figure S9: Amine peak characteristics. Showing **(a)** correlations of each ammonia/amine measurement as the form $(Am)(HNO_3)NO_3^-$ and $(Am)(HNO_3)_2NO_3^-$, where Am is NH_3, methylamine, C_2 or C_4 amine. Panel **(b)** shows peak fits for both C_2 amine peaks in our mass spectrum.

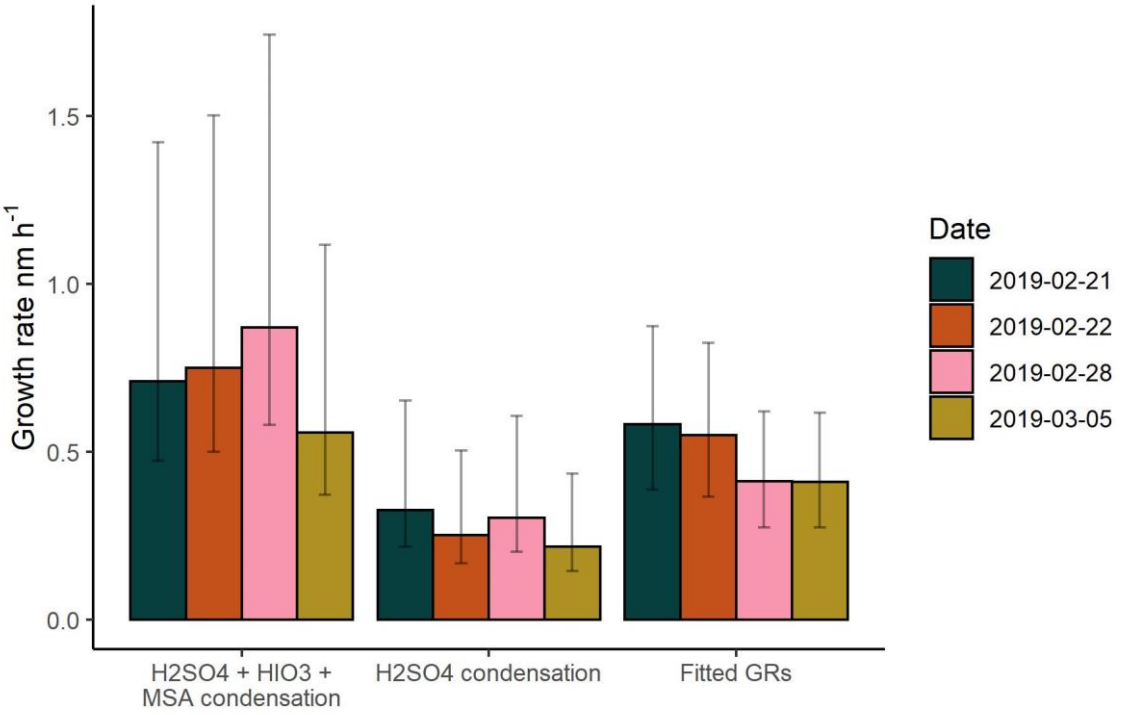

Figure S10: Growth rates by different methods. The leftmost and middle bars represent the theoretical condensation as calculated by ref. 43 due to several vapours, and H_2SO_4 respectively, the rightmost bars show growth rates calculated by the lognormal fitting method applied to NanoSMPS data. Errors on growth rates fitted to SMPS data are ±50%, errors on calculated growth rates are +100%/-50%.